STUDY OF Mg_2Si-BASED THERMOELECTRIC MATERIALS

A Thesis Submitted to the College of

Graduate Studies and Research

In Partial Fulfillment of the Requirements

For the Degree of Doctor of Philosophy

In the Department of Physics and Engineering Physics

University of Saskatchewan

Saskatoon

By

JIANBAO ZHAO

Permission to Use

In presenting this thesis in partial fulfilment of the requirements for a Postgraduate degree from the University of Saskatchewan, I agree that the Libraries of this University may make it freely available for inspection. I further agree that permission for copying of this thesis in any manner, in whole or in part, for scholarly purposes may be granted by the professor or professors who supervised my thesis work or, in their absence, by the Head of the Department or the Dean of the College in which my thesis work was done. It is understood that any copying or publication or use of this thesis or parts thereof for financial gain shall not be allowed without my written permission. It is also understood that due recognition shall be given to me and to the University of Saskatchewan in any scholarly use which may be made of any material in my thesis.

Requests for permission to copy or to make other use of material in this thesis in whole or part should be addressed to:

Head of the Department of Physics and Engineering Physics

116 Science Place

University of Saskatchewan

Saskatoon, Saskatchewan

Canada

S7N 5E2

ABSTRACT

Mg_2Si-based thermoelectrics are currently the most promising, environmentally benign and inexpensive materials for power generation. The objective of this thesis is to characterize Mg_2Si-based thermoelectric materials using state-of-the-art synchrotron radiation techniques including infrared reflectivity/absorption spectroscopy and high resolution X-ray powder diffraction. This is complemented by density functional theory (DFT) calculations. Also reported here is the main research: the analysis of the electronic structure and transport properties of doped Mg_2Si using experimental and theoretical methods.

To enhance the thermoelectric performance, Mg_2Si doped with a single component of Bi or Sb were studied. The investigation showed by doping the electron carrier concentrations were increased. In particular, *dc* conductivities of the doped samples were extracted from the analysis of infrared reflectivity spectra employing the Drude free electron model. We found the conductivity was lower when determined by infrared measurements rather than *in-situ* four point probe measurements of the bulk sample because of the limited penetration depth of infrared (IR) radiation and the very small spot size. In particular, we were able to extract the electrical conductivity, relaxation times and electron effective masses of the samples. DFT calculations reproduced the experimental observations and show a substantial increase in the Seebeck coefficients.

The next step was to study the effect after doping with two different dopants. For this purpose, we investigated the effect of Ge substitute Si in Bi doped Mg_2Si. In particular, the *dc* conductivities of the doped samples were extracted from the analysis of infrared reflectivity spectra. From the IR data, we extracted the relevant parameters for electrical transport. The experimental data were explained with theoretical DFT calculations in which the calculated densities of states (DOS) of the Ge- and Bi-doped Mg_2Si samples were found to be very similar,

and therefore to have comparable Seebeck coefficients. The steep curvatures of the DOS at the Fermi level indicate a light electron band. We found the thermal conductivity of Mg_2Si is substantially lower from 7 $Wm^{-1}K^{-1}$ to 2.7 $Wm^{-1}K^{-1}$ in $Mg_2Si_{0.677}Ge_{0.3}Bi_{0.023}$ at 300 K. A performance figure of merit of 0.7 was achieved at 773 K for this sample.

We further investigated the effect of multi-doping with Sb, Al and Zn on the enhancement of the thermoelectric and electrical transport properties of Mg_2Si. A maximum *ZT* of 0.964 was found for Sb0.5%Zn0.5% doped Mg_2Si ($Mg_{1.995}Zn_{0.005}Si_{0.995}Sb_{0.005}$) at 880 K. This value is comparable to those of PbTe based thermoelectrics which are the currently the materials used in commercial products.

We also studied the effect of pressure on the thermoelectric performance of a Al-doped Mg_2Si sample. From *in-situ* X-ray diffraction, we observed a structural transform in which the electrical conductivity was increased after the phase transition. The experimental observed maximum thermoelectric power at 1.9 GPa was reproduced by DFT calculations and explained by the increase of electronic density of states at the Fermi level.

The effect of multi-wall carbon nanotubes (MWCNTs) to increase the electrical conductivity of $Mg_2Si_{0.877}Ge_{0.1}Bi_{0.023}$ was examined. At 323 K the conductivity was found to increase from 450 $\Omega^{-1}cm^{-1}$ to 500 $\Omega^{-1}cm^{-1}$. However, this effect diminished at higher temperature and the conductivity drop to 470 $\Omega^{-1}cm^{-1}$ at 773 K. Raman study showed the persistent of disorder (D) and tangential (G) mode characteristics of a carbon nanotube in the doped sample indicating that there was no decomposition or substantial chemical reaction of the MWCNTs with $Mg_2Si_{0.877}Ge_{0.1}Bi_{0.023}$.

Finally, we present the results on the analysis of valence electron topologies of Mg_2Si multi-doped with Al, Zn and Sb thermoelectric materials by the Maximum Entropy Method

(MEM) using data obtained from synchrotron X-ray powder diffraction measurements. The results showed the qualitative feature of valence electron distributions were correctly located. However, due to the limited number of Bragg diffraction peaks in the experimental patterns, the effect of the dopants to the core charge density cannot be reliably obtained. An error analysis was performed from the analysis of diffraction pattern of Al-doped Mg_2Si which included high angle Bragg reflections. We concluded that the density maps extracted from MEM analysis of the doped samples were qualitatively correct.

ACKNOWLEDGMENTS

First, I would like to warmly and sincerely thank my supervisor Dr. John S. Tse for the guidance, understanding, patience, and mostly important his continuous and instructive supervision. The thesis has benefited greatly from his guidance. He encouraged me not only to be a physicist but also as an independent researcher with strong motivation and commitment. In particular, I wish to thank him for finding time to help even with an extremely busy schedule.

I would especially like to thank all the faculty members in the Department of Physics and Engineering Physics at University of Saskatchewan. Especially, I am truly grateful to Dr. Tse's group members Xue Yong, Niloofar Zarifi, Jianjun Yang, Hanyu Liu, and Min Wu for their constant supports and help during my research.

Most results in this thesis have been published as academic papers. I would like to thank all the co-authors for their contributions to the manuscripts. In particular to Dr. Holger Kleinke (University of Waterloo) who provided most of samples studied here and Dr. Zhenxian Liu, beamline scientist at U2A, Brookhaven National Laboratory for his instruction to perform far and mid infrared transmission and reflectivity measurements.

I am gratefully indebted to my wife Yang Yang, my parents and my parents-in-law for their everlasting and unconditional love, support, and encouragement during my Ph.D study. In particular, to my baby daughter Emma Zhao, she made me to be a super multitasker.

Last, but certainly not least, I am very grateful to Argonne National Laboratory, Canadian Light Source, Brookhaven National Laboratory, West Grid Canada and AUTO21 for the use of their facilities and the funding supports on my projects.

TABLE OF CONTENTS

LIST OF TABLES

LIST OF FIGURES

LIST OF ABBREVIATIONS

2D	Two-dimensional
3D	Three-dimensional
CNT	Carbon nanotube
DFT	Density functional theory
DOS	Density of states
DSC	Differential scanning calorimetry
EOS	Equation of states
EPMA	Electron-probe microanalysis
EDX	Energy dispersive X-ray
FCC	Face-centered cubic
GGA	Generalized gradient approximation
GB	Grain boundary
GDMS	Glow discharge mass spectrometry
H-K	Hohenberg-Kohn
HBBO	Prototypal oxobenzene-bridged 1,2,3-bisdithiazolyl radical conductor
HAADF	High-angle annular dark-field
HRTEM	High resolution transmission electron microscopy
IR	Infrared
K-K	Kramers–Kronig
LO	Longitudinal-optical
MWCNT	Multi-wall carbon nanotube
MEM	Maximum Entropy Method
Mg_2Si	Magnesium silicide
PAW	Projected augmented wave

PBE	Perdew-Burke-Ernzerhof
PDOS	Projected density of states
PbTe	Lead telluride
SWCNT	Single-wall carbon nanotube
STEM	Scanning transmission electron microscopy
SCD	Differential scanning calorimetry
TE	Thermoelectric
TO	Transverse-optical
TG	Thermogravimetry
VASP	Vienna *Ab-initio* Simulation Package
XC	Exchange-correlation
XEDS	X-ray Spectrometry
XRD	X-ray diffraction
ZT	Figure of merit

CHAPTER 1

INTRODUCTION

With the rapid development of the world's economy in the past few decades, the supply of cheap and clean energy has become the greatest bottleneck to industries and consumers. Meanwhile, the environmental impact of the existing technology of power generation has become severe. For example, with the increased number of vehicles and energy consumption in emerging economies, the associated exhaust emissions have led to a global concern. It is widely recognized that the removal of the emissions or, even more desirable, the conversion of the waste heat into useable energy remains a major challenge and a promising area of research. The purpose of this research is to identify improved thermoelectric materials based on Mg_2Si, which can efficiently convert heat into electricity and *vice versa*.

1.1 Thermoelectric effects and Performance index

Thermoelectric materials are based on two fundamental effects: the Seebeck effect and Peltier effect. The Seebeck effect was first discovered by Thomas Johann Seebeck in the 1800s. The modern day application of this effect is to generate an electrical current by applying a temperature difference between the junctions of *p*- and *n*-doped semiconductors, in which electronic charges from the hot end are diffused to the cold site as illustrated in Fig. 1.1(a). The voltage generated (ΔV) is proportional to the temperature difference (ΔT) and the proportionality constant ($S = -\Delta V/\Delta T$) is defined as the Seebeck coefficient. The Peltier effect is the reverse of the Seebeck effect (Fig. 1.1(b)) and is defined as a temperature difference created by applying a voltage between two connected *n*- and *p*-type semiconductors. When a current (I) is passed between them, heat (Q) is generated or absorbed. The Peltier coefficient (π) is defined as $\pi = Q/I$.

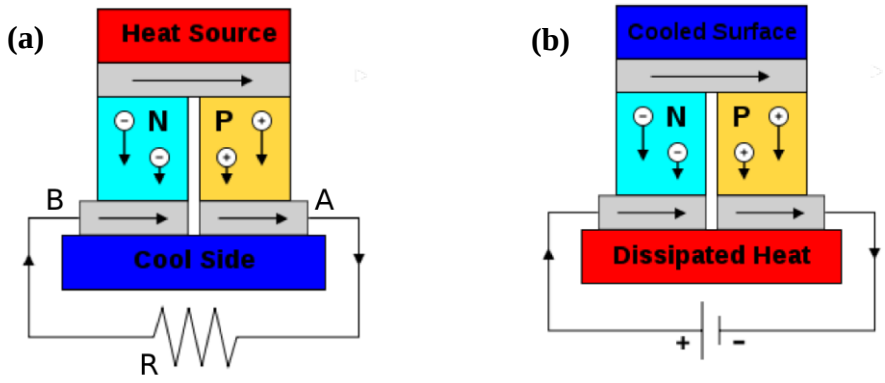

Fig. 1.1 Power generation (a) and refrigeration (b) of thermoelectric modules. [1]

1.2 Figure of merit (ZT)

A thermoelectric converter is a heat engine and its operating principle obeys the laws of thermodynamics. The efficiency (η) of a thermoelectric material is defined as follows,

$$\eta = \frac{energy\ supplied\ to\ the\ load}{heat\ aborbed\ at\ hot\ junction} \tag{1.1}$$

If we assume that the electrical conductivity, thermal conductivity and Seebeck coefficient are the same at both the hot and cold sides, the efficiency (η) can be expressed as:

$$\eta = \frac{I^2R}{\lambda(T_H - T_C) - \frac{1}{2}I^2R} \tag{1.2}$$

where λ is the thermal conductance of hot and cold sides, R is the electrical series resistance of hot and cold ends (p-type and n-type legs are connected in series), and T_H and T_C are the temperature in the hot side and cold side, respectively. [1]

To maximize the efficiency (η) with a function of the temperatures at the hot and cold ends, the differentiation of the efficiency is zero with respect to temperatures. The maximum efficiency (η_{max}) can be written as:

$$\eta_{max}=\frac{(T_H-T_C)}{T_H}\frac{\sqrt{1+ZT}-1}{\sqrt{1+ZT}+T_C/T_H} \tag{1.3}$$

where $T= (T_H+T_C)/2$, and Z is the figure of merit: ($Z=S^2/R\lambda$).

In Eq. 1.3, if the temperatures in the hot and cold sides are held constant, the efficiency is only dependent on Z. Since the unit of Z is K^{-1}, the dimensionless figure-of-merit ZT is defined as:

$$ZT = \frac{S^2\sigma T}{\kappa} \tag{1.4}$$

where S is the Seebeck coefficient, σ is the electrical conductivity and κ is the thermal conductivity of a thermoelectric material.

To achieve high performance efficiency, the ultimate goal is to maximize the ZT of a thermoelectric material. A good thermoelectric material should therefore possess a high Seebeck coefficient, low thermal conductivity as well as a high electrical conductivity. However the Seebeck coefficient (S), electrical conductivity (σ), and thermal conductivity (κ) are not isolated quantities but are related to each other, making these factors difficult to optimize simultaneously. For example, for a single band material, the electrical conductivity can be increased by improving the charge carrier concentration. [2] However, for a free electron-like band structure, the Seebeck coefficient, which is related to the curvature of the electron density of states, is expected to decrease and the electronic contribution to the thermal conductivity will increase as well. [3] The contradictory interplay of these properties presents a significant challenge to

optimizing efficiency. Alternatively, *p*- or *n*-doping with heavy doping atoms will reduce the thermal conductivity (κ), but at the same time the excess charges donated by the dopants will increase the electrical conductivity (σ).

1.3 Mg_2Si-based thermoelectric materials

Several classes of materials are known to be potential thermoelectric generators. [4,5] Among the most promising materials are filled skutterudites [6], clathrates [7], and PbTe-based thermoelectric materials [8]. Recently, the intermetallic compound of Mg_2Si, having the antifluorite structure (*Fm-3m*) and an indirect band gap semiconductor of 0.65 eV, has been proposed as a good high efficiency thermoelectric material from 500 to 800 K in automobiles. [9-13] Subsequent investigations of doped Mg_2Si thermoelectric materials have shown they can achieve a high figure-of-merit (*ZT*) at operating temperatures from 500 K to 800 K. [14] For example, a *ZT* of 1.0 has been found in $Mg_2(Si_{0.3}Sn_{0.7})_{0.975}Sb_{0.025}$ at 640 K [16] and in excess of 1.0 in $Mg_2Si_{0.3925}Sn_{0.6}Sb_{0.0075}$ at 773 K. [15] In comparison, although skutterudites and PbTe-based materials have higher *ZT*s at a higher temperature range, Mg_2Si-based materials have the merit of having a high *ZT* between 500 K and 800 K, which would allow them to be installed in the exhaust systems of vehicles. More importantly, the two components, Mg and Si, are light, non-toxic, sustainable, abundant in the earth and the production cost of Mg_2Si is relatively low in comparison with other thermoelectric materials, such as PbTe and skutterudites. [17,18] In addition, eco-friendly Mg_2Si provides safe handling and operation of devices for practical applications. [19]

A number of researches to enhance the thermoelectric performance of Mg_2Si have focused on doping with various elements or the fabrication of nanostructures. For example, Battiston *et al*. studied Al-doped Mg_2Si with different doping concentrations prepared by ball

milling and spark plasma sintering (SPS). [20] The morphology, composition, crystal structure, and thermoelectric properties of the samples were characterized by field-emission scanning electron microscopy, energy-dispersive spectroscopy, X-ray diffraction, and thermoelectric properties measurements. Al-doped Mg_2Si compounds are usually *n*-type semiconductors. So far, the maximum *ZT* achieved was 0.57 in a sample of Mg_2Si:Al = 1:0.01 at 856 K. It is unfortunate that oxide contaminants often affected the quality of samples. Many researches have suggested the Seebeck coefficient, electrical conductivity and thermal conductivity are strongly affected by Bi doping. [21-23] Bi has a low melting point of 545 K [24] and is easy to fabricate in the spark plasma sintering process. Bi-doped Mg_2Si samples with Bi atoms located in the Si sites are *n*-type semiconductors over a broad temperature range. Since Bi is a Vb group element, the increase in the power factor is due to the enhancement of electrical conductivity by electrons donated by the Bi. Furthermore, Bi-doped Mg_2Si has a lower thermal conductivity than Mg_2Si since Bi atoms are heavier than other *n*-type dopants such as Al and Sb. A maximum *ZT* of 0.86 was found in $Mg_2Si_{0.98}Bi_{0.02}$ at 862 K. This value is 1.5 times higher than that reported for Al-doped Mg_2Si (*ZT* = 0.57 at 856 K). To further enhance the thermoelectric performance, researchers optimized a mixed alloy of $Mg_2Si_{0.4}Sn_{0.6}$ by adding appropriate concentrations of antimony (Sb). A ZT_{max} of 1.1 was achieved with a fairly high charge carrier concentration of 10^{20} cm^{-3}. [25] Another example is $Mg_2Si_{0.6}Ge_{0.4}$ doped with Ag [26-28] in which a maximum *ZT* of 1.68 at 629 K was found. Doping with heavier elements shows the electrical conductivity can be increased with a concomitant reduction in the thermal conductivity. To this day, Sb, Te, Pb, P, Al, Ge, Bi, and Sn have been tried and shown to behave as *n*-type dopants, [29-33] while Cu, Ag, B and Ga have been used as *p*-type dopants with limited success [34,35].

A significant enhancement of the thermoelectric figure of merit of Mg_2Si to 0.7 at 873 K was achieved by double doping with combinations of Bi, Pb, and Sb. These studies show the addition of any two of the doping elements can increase the electrical conductivity due to the excess free electrons provided by the dopants in the conduction band. [36] For example, Jiang *et al*. found that the thermoelectric performance was improved by introducing three types of defects *via* Sb dopants, Mg vacancies, and Mg interstitials, into $Mg_2Si_{0.4}Sn_{0.6-x}Sb_x$ samples. [37] Isoda *et al*. found the highest *ZT* value of 0.94 for Al/Sb double-doped $Mg_2Si_{0.75}Sn_{0.25}$ at 850 K. Therefore, Sb is considered to be an effective dopant to increase the carrier concentration. [38] Previous studies have shown that double or multi-doping is a promising approach to further enhance the thermoelectric figure of merit (*ZT*) of Mg_2Si-based thermoelectric materials. [39-41]

In the past decades, researches have also revealed the application of pressure can help to enhance the thermoelectric properties. [42-48] For example, MoS_2 was found to occur at 25 GPa after a semiconductor-metal transition, in which the thermoelectric performance was found to increase by applying hydrostatic pressure due to the metallization. A large increase in the thermoelectric power of $Sb_{1.5}Bi_{0.5}Te_3$ alloys under non-hydrostatic compression has also been reported. A maximum *ZT* in excess of 2 has been achieved at 2 GPa. [45] If the high pressure form could be recovered, pressure would provide a new route to enhance the thermoelectric performance. [43] Recently, Mg_2Si nominally doped with 1% Al was compressed to 2-3 GPa, and the thermal power was found to increase significantly reaching a maximum value of 8×10^{-3} $W/(K^2m)$. In this case, the increase in the thermoelectric efficiency was also associated with an increase of electrical conductivity and it was suggested that the Al-doped sample became metallic between 5 and 12 GPa. A Raman spectroscopy study also hinted at two possible structural phase transitions at 5-7 GPa and 11-12 GPa. [42]

Yang *et al*. have shown that, using nanotechnology, the *ZT* of nano-Mg_2Si can be increased to 0.36 at 811 K and further increased to 0.8 at 823 K by doping with Bi. [49,50] Fiameni *et al*. have reported that adding single wall carbon nanotube to the Bi-doped Mg_2Si increased considerably the electrical conductivity but also slightly increased the thermal conductivity. [51] Consequently, the best *ZT* was only 0.39 at 327 K for the $Mg_2Si_{0.98}Bi_{0.02}$ with the addition of single wall carbon nanotube.

1.4 Strategies to enhance the efficiency of Mg_2Si-based thermoelectric materials

The motivation for our present research is to further improve the *ZT* of Mg_2Si-based thermoelectric materials. We aim to do this by providing insight into the role of dopants to the electronic band structures, thermoelectric and electrical transport properties, and the crystal structures of single and multiple doped Mg_2Si samples. We first explored the choice of doping elements and their effects on *ZT*. The study aimed at examining dopants having the following characteristics: a similar atomic size to the host Mg or Si atoms, more free electrons to contribute to the electrical conductivity and Seebeck coefficient, and a heavier mass that would help to reduce the lattice thermal conductivity. We employed a convenient synchrotron technique to determine the *dc* conductivities of the doped samples from analysis of their far- and mid-infrared (IR) reflectivity spectra. The advantage of this method was that from the IR data the electron effective masses of the samples could be extracted. To assist interpretation of the experimental results, electronic structures of the doped samples were computed using density functional theory (DFT).

One of the strategies to improve the carrier concentration is through *p*- or *n*-doping of the Mg_2Si crystal. The first project investigated thermoelectric enhancement through doping with a single component. The results show Sb or Bi dopants substitute the Si sites in the crystal. [14,25]

It was expected that the excess electrons from the dopants would help to increase the carrier concentrations and the heavier atoms would reduce thermal conductivities. This expectation was confirmed by experiments and the calculated electronic structure and Seebeck coefficients. The maximum *ZT* achieved was 0.6 at 700 K in a Bi-doped Mg_2Si sample. [52]

A second strategy was to employ multiple doping of Mg_2Si. For this purpose, we studied the effect on the local structure and thermoelectric properties of replacing Si with Ge using different concentrations in Bi-doped Mg_2Si. To understand the role of Ge, the doping level of Bi was fixed at the optimum value so that the effects of different Ge content on the band structure and thermoelectric properties of $Mg_2Si_{0.977-x}Ge_xBi_{0.023}$ ($0.1 \leq x \leq 0.4$) could be studied. [53] In this study, the maximum *ZT* achieved was 0.65 at 700 K, about 8% higher than the single-doped Bi sample. The thermoelectric and electrical transport properties of Mg_2Si multi-doped with Sb, Al and Zn were also examined. At 700 K, *ZT* was found to be 0.7 in $Mg_{1.995}Zn_{0.005}Si_{0.995}Sb_{0.005}$ and $Mg_{1.99}Zn_{0.01}Si_{0.995}Sb_{0.005}$, which is approximately 17% higher than the single-doping method. A maximum *ZT* of 0.946 was found in $Mg_{1.995}Zn_{0.005}Si_{0.995}Sb_{0.005}$ at 880 K. This value is comparable to the *ZT* of PbTe-based thermoelectric materials. [54]

A third strategy was to enhance the thermoelectric performance by compression. Pressure can alter the band structure of a system but it may also induce structural transformation. At ambient pressure and temperature, Mg_2Si has a cubic anti-fluorite structure with the space group of *Fm-3m*. In this investigation, *In-situ* X-ray diffraction and infrared reflectivity measurements up to 17 GPa at room temperature were performed on pure Mg_2Si and Mg_2Si nominally doped with 1% Al ($Mg_{1.99}Al_{0.01}Si$). No structural transformation was observed in pure Mg_2Si. In contrast, a phase transition from cubic anti-fluorite (*Fm-3m*) to orthorhombic (*Pnma*) was observed in the $Mg_{1.99}Al_{0.01}Si$ sample at 10 GPa. The thermal power was found to increase

reaching a maximum value of 8×10^{-3} W/(K^2m) under 2-3 GPa. [55] The enhancement, determined from the analysis of the infrared reflectivity spectra, was mainly due to the increase of electrical conductivity associated with the structural phase transition. The results show the pressure can affect the structures and transport properties and helps to improve the electrical conductivity.

Finally, we attempted to enhance the electrical conductivity of Mg_2Si by adding multi-wall carbon nanotubes (MWCNTs). The key question was to clarify whether there was a chemical interaction between the MWCNTs and $Mg_2Si_{0.877}Ge_{0.1}Bi_{0.023}$. We found that, although there was no indication of such a chemical interaction, nevertheless, the electrical conductivity was increased by 10% in the MWCNT-doped $Mg_2Si_{0.877}Ge_{0.1}Bi_{0.023}$ samples as compared to an undoped sample at 300 K. [56] However, the maximum *ZT* of 0.5 in $Mg_2Si_{0.877}Ge_{0.1}Bi_{0.023}$-0.5 wt% MWCNTs at 700 K is not very attractive for practical applications.

1.5 Thesis organization

This thesis is composed of nine chapters. A general introduction and the motivations for the research are presented in Chapter 1. In Chapter 2, we describe the experimental and theoretical methods employed in this study. In Chapter 3, we report findings of the electrical and thermoelectric properties of single-doped Mg_2Si samples. In Chapters 4 and 5, we address the effects with double- and multi-doped Mg_2Si samples. In Chapter 6, we focus on the study of pressure and its effect on the electrical conductivity and thermopower of Al-doped Mg_2Si. In Chapter 7, we present results of the electrical conductivity and thermoelectric performance by adding multi-wall carbon nanotubes to $Mg_2Si_{0.877}Ge_{0.1}Bi_{0.023}$. In Chapter 8, results of the investigation of the charge density distribution of doped Mg_2Si thermoelectric materials using

the Maximum Entropy Method (MEM) are reported. A brief conclusion of the research performed and a future perspective are given in Chapter 9.

1.6 Research contributions

For this research, Dr. Holger Kleinke, University of Waterloo, Canada and Dr. Kenichi Takarabe, Okayama University of Science, Japan provided the Mg_2Si-based thermoelectric samples. My major responsibilities in the publications were (i) the measurements of infrared absorption/reflectivity spectra; (ii) the analysis of all the spectra to extract the information of electronic band gap energies and electronic transport properties; (iii) structural and electron density characterization using synchrotron X-ray powder diffraction at ambient and high pressure; and (iv) DFT calculations of the electronic structures and Seebeck coefficients to complement the experimental investigation. The majority of the results obtained from the research have been published in five scientific papers listed below. The remaining study on the "Charge Densities of Multi-doped Mg_2Si Thermoelectric Materials using the Maximum Entropy Method" in chapter 8 is under preparation. Other published results 4,7,8, which are not discussed but relevant to this thesis, are also included. In particular, Wong *et al.* report the application of IR transmission and reflectivity to extract band gap and electrical transport properties information.

Publications:

1. J. Zhao, Z. Liu, J. Reid, K. Takarabe, T. Iida, B. Wang, U. Yoshiya, and J. S. Tse, "Thermoelectric properties and electrical transport properties of multi-doped Mg_2Si with Sb Al and Zn," *Journal of Materials Chemistry A*, vol. 3, pp. 19774-19782, 2015.

2. J. Zhao, Z. Liu, R. A. Gordon, K. Takarabe, J. Reid, and J. S. Tse, "Pressure-induced phase transition and electrical properties of thermoelectric Al-doped Mg_2Si," *Journal of Applied Physics*, vol. 118, pp. 145902, 2015.

3. N. Farahi, S. Prabhudev, G. A. Botton, J. Zhao, J. S. Tse, Z. Liu, J. R. Salvador, and H. Kleinke, "Local structure and thermoelectric properties of $Mg_2Si_{0.977-x}Ge_xBi_{0.023}$ ($0.1 \leq x \leq 0.4$)," *Journal of Alloys and Compounds*, vol. 644, pp. 249-255, 2015.

4. M. Sobhan, Q. Xu, J. Zhao, A. Franklin, Y. Hu, J. S. Tse, and P. Wu, "Modification of surface chemistry by lattice Sn doing in $BiFeO_3$ nanofibers," *Europhysics Letters*, vol. 111, pp. 18005, 2015.

5. N. Farahi, S. Prabhudev, M. Bugnet, G. A. Botton, J. Zhao, J. S. Tse, J. R. Salvador, and H. Kleinke, "Enhanced figure of merit in $Mg_2Si_{0.877}Ge_{0.1}Bi_{0.023}$/multi wall carbon nanotube nanocomposites," *RSC Advances*, vol. 5, pp. 65328-65336, 2015.

6. N. Farahi, M. VanZant, J. Zhao, J. S. Tse, S. Prabhudev, G. A. Botton, J. R. Salvador, F. Borondics, Z. Liu and H. Kleinke, "Sb- and Bi- doped Mg_2Si: location of the dopants, micro- and nanostructure, electronic structures and thermoelectric properties," *Dalton Transactions*, vol. 43, pp. 14983-14991, 2014.

7. S. Desgreniers, J. S. Tse, J. Zhao, T. Matsuoka, and Y. Ohishi, "Structural modifications of cold and dense Cesium, Calcium, Barium, and Selenium," *Acta Crystallographica Section A: Foundations and Advances*, vol. A70, pp. C752, 2014.

8. J. W. L. Wong, A. Maiman, K. Lekin, S. M. Winter, W. Yong, J. Zhao, S. V. Garimella, J. S. Tse, R. A. Secco, S. Desgreniers, Y. Ohishi, F. Borondics, and R. T. Oakley, "Pressure Induced Phase Transitions and Metallization of a Neutral Radical Conductor," *Journal of the American Chemical Society*, vol. 136, pp. 1070-1081, 2014.

References

[1] M. Chen, in First-principles Modeling of Thermoelectric Materials, PhD thesis, Theoretical Solid State Chemistry, Vienna University of Technology, Vienna, Austria, 2012.

[2] D. M. Rowe, Thermoelectrics Handbook: Macro to Nano, CRC Press, Taylor & Francis Group, Boca Raton, FL, USA, 2006.

[3] J. H. Lee, J. Wu, and J. C. Grossman, *Physical Review Letters*, 2010, 104, 016602.

[4] L.E. Bell, *Science*, 2008, 321, 1457-1461.

[5] H. Kleinke, *Chem. Mater*., 2010, 22, 604-611.

[6] G. S. Nolas, D. T. Morelli, and T. M. Tritt, *Annu. Rev. Mat. Sci*., 1999, 29, 89-116.

[7] G. S. Nolas, G. A. Slack, and S. B. Schujman, *Semicond. Semimet*., 2001, 69, 255-300.

[8] Z. H. Dughaish, *Phys.B: Cond.Matt*., 2002, 322, 205-223.

[9] R. J. LaBotz, D. R. Mason, and D. F. O'Kane, *J. Electrochem. Soc*., 1963, 110, 127.

[10] T. C. Harman, P. J. Taylor, D. L. Spears, and M. P. Walsh, *J. Electron. Mater*., 2000, 29, L1.

[11] P. M. Lee, *Phys. Rev*., 1964, 135, 1110.

[12] R. G. Morris, R. D. Redin, and G. C. Danielson, *Phys. Rev*., 1958, 109, 1909.

[13] C. R. Whitsett and G.C. Danielson, *Phys. Rev*., 1955, 100, 1261.

[14] V. K. Zaitsev, M. I. Fedorov, E. A. Gurieva, I. S. Eremin, P. P. Konstantinov, A. Y. Samunin, and M. V. Vedernikov, *Phys.B: Cond.Matt*., 2006, 74, 045207/1-045207/5.

[15] Q. Zhang, J. He, T. J. Zhu, S. N. Zhang, X. B. Zhao, and T. M. Tritt, *Appl. Phys. Lett*., 2008, 93, 102109/1-102109/3.

[16] W. Liu, Q. Zhang, X. Tang, H. Li, and J. Sharp, *J. Electr. Matter*., 2011, 40, 1062-1066.

[17] J. Guo, Z. Li, P. Chen, and K. Zhao, *Materials Review*, 2011, 25, 165-168.

[18] X. Luo, H. Liu, W. Xu, and Y. Zhu, *Advanced Materials Research*, 2014, 886, 71-74.

[19] M. Yoshinaga, T. Iida, M. Noda, T. Endo, and Y. Takanashi, *Thin Solid Films*, 2004, 461, 86.

[20] S. Battiston, S. Fiameni, M. Saleemi, S. Boldrini, A. Famengo, F. Agresti, M. Stingaciu, M. S. Toprak, M. Fabrizio, and S. Barison, *Journal of Electronic Materials*, 2013, 42, 1956.

[21] J. Tani and H. Kido, *Physica B*, 2005, 364, 218-224.

[22] S. W. You and I. H. Kim, *Current Apllied Physics*, 2011, 11, S392-S395.

[23] S. M. Choi, K. H. Kim, I. H. Kim, S. U. Kim, and W. S. Seo, *Current Applied Physics*, 2011, 11, S388-S391.

[24] D. R. Lide, CRC Handbook of Chemistry and Physics, 84th ed., CRC Press, New York, 2003, pp. 4–132.

[25] E. N. Nikitin, V. G. Bazanov, and V. I. Tarasov, *Sov. Phys. Solid State*, 1961, 3, 2648-2652.

[26] Y. Noda, H. Kon, Y. Furukawa, N. Otsuka, I. A. Nishida, and K. Masumoto, *Mater. Trans*., 1992, 33, 845-850.

[27] T. Sakamoto, T. Lida, A. Matsumoto, Y. Honda, T. Nemoto, J. Sato, T. Nakajima, H. Taguchi, and Y. Takanashi, *Journal of Electronic Materials*, 2010, 39, 1708.

[28] K. Mars, H. Ihou-Mouko, G. Pont, J. Tobola, and H. Scherrer, *Journal of Electronic Materials*, 2009, 38, 1360.

[29] S. Muthiah, J. Pulikkotil, A. K. Srivastava, A. Kumar, B. D. Pathak, A. Dhar, and R. C. Budhani, *Applied Physics Letters*, 2013, 103, 053901.

[30] T. Saskamoto, T. Lida, Y. Taguchi, S. Kurosaki, Y. Hayatsu, K. Nishio, Y. Kogo, and Y. Takanashi, *Journal of Electronic Materials*, 2012, 41, 1429.

[31] J. I. Tani and H. Kido, *Japanese Journal of Applied Physics*, 2007, 46, 3309-3314.

[32] M. Ioannou, G. Polymeris, E. Hatzikraniotis, A. U. Khan, K. M. Paraskevopoulos, and TH. Kyratsi, *Journal of Electronic Materials*, 2013, 42, 1827.

[33] S. W. You, K. H. Park, I. H. Kim, S. M. Choi, W. S. Seo, and S. U. Kim, *Journal of Electronic Materials*, 2012, 41, 1675.

[34] D. Cederkrantz, N. Farahi, K. A. Borup, B. B. Iversen, M. Nygren, and A. E. C. Palmqvist, *J. Appl. Phys*., 2012, 111, 023701.

[35] H. Ihou-Mouko, C. Mercier, J. Tobola, G. Pont, and H. Scherrer, *J. Alloys Comp*., 2011, 509, 6503.

[36] S. Muthiah, B. Sivaiah, B. Gahtori, K. Tyagi, A. K. Srivastava, B. D. Pathak, A. Dhar, and R. C. Budhani, *Journal of Electronic Materials*, 2014, 43, 2035.

[37] G. Jiang, J. He, T. Zhu, C. Fu, X. Liu, L. Hu, and X. Zhao, *Advanced Functional Materials*, 2014, 24, 3776.

[38] Y. Isoda, M. Held, S. Tada, and Y. Shinohara, *Journal of Electronic Materials*, 2014, 43, 2053.

[39] H. Gao, T. Zhu, X. Liu, L. Chen, and X. Zhao, *Journal of Materials Chemistry*, 2011, 21, 5933.

[40] W. Liu, X. Tang, H. Li, J. Sharp, X. Zhou, and C. Uher, *Chemistry of Materials*, 2011, 23, 5256-5263.

[41] T. Sakamoto, T. Lida, S. Kurosaki, K. Yano, H. Taguchi, K. Nishio, and Y. Takanashi, *Journal of Electronic Materials*, 2011, 40, 629.

[42] N. V. Morozova, S. V. Ovsyannikov, I. V. Korobeinikov, A. E. Karkin, K. Takarabe, Y. Mori, S. Nakamura, and V. V. Shchennikov, *Journal of Applied Physics*, 2014, 115, 213705.

[43] H. Guo, T. Yang, P. Tao, Y. Wang, and Z. Zhang, *Journal of Applied Physics*, 2013, 113, 013709.

[44] G. Yang, H. Cui, D. Ma, and C. He, *Journal of Applied Physics*, 2014, 116, 223709.

[45] D. A. Polvani, J. F. Meng, N. V. Chandra Shekar, J. Sharp, and J. V. Badding, *Chem. Mater*., 2001, 13, 2068-2071.

[46] V. V. Shchennikov, S. V. Ovsyannikov, and A. Y. Manakov, *Journal of Physics and Chemistry of Solids*, 2010, 71, 1168-1174.

[47] S. V. Ovsyannikov, V. V. Shchennikov, G. V. Vorontsov, A. Y. Manakov, A. Y. Likhacheva, and V. A. Kulbachinskii, *Journal of Applied Physics*, 2008, 104, 053713.

[48] R. R. Bourassa, D. Lazarus, and D. A. Blackburn, *Physical Review*, 1968, 165, 853.

[49] M. J. Yang, Q. Shen, and L. M. Zhang, *China Phys. B*, 2011, 20, 106202.

[50] M. J. Yang, W. J. Luo, and Q. Shen, *Rare Met. Mater. Eng*., 2009, S2, 1055-1059.

[51] S. Fiameni, S. Battiston, S. Boldrini, A. Famengo, F. Agresti, S. Barison, and M. Fabrizio, *Journal of Solid State Chemistry*, 2012, 193, 142-146.

[52] N. Farahi, M. VanZant, J. Zhao, J. S. Tse, S. Prabhudev, G. A. Botton, J. R. Salvador, F. Borondics, Z. Liu and H. Kleinke, *Dalton Transactions*, 2014, 43, 14983-14991.

[53] N. Farahi, S. Prabhudev, G. A. Botton, J. Zhao, J. S. Tse, Z. Liu, J. R. Salvador, and H. Kleinke, *Journal of Alloys and Compounds*, 2015, 644, 249-255.

[54] J. Zhao, Z. Liu, J. Reid, K. Takarabe, T. Iida, B. Wang, U. Yoshiya, and J. S. Tse, *Journal of Materials Chemistry A*, 2015, 3, 19774-19782.

[55] J. Zhao, Z. Liu, R. A. Gordon, K. Takarabe, J. Reid, and J. S. Tse, *Journal of Applied Physics*, 2015, 118, 145902.

[56] N. Farahi, S. Prabhudev, M. Bugnet, G. A. Botton, J. Zhao, J. S. Tse, J. R. Salvador, and H. Kleinke, *RSC Advances*, 2015, 5, 65328-65336.

CHAPTER 2

EXPERIMENTAL AND THEORETICAL METHODS

The focus of the research presented in this thesis is to explore different means to increase the efficiency of Mg_2Si-based materials for thermoelectric applications. This requires the characterization of crystal structures, electrical transport properties and thermoelectric properties. The experiments were performed with two synchrotron radiation-based techniques: infrared absorption/reflectivity spectroscopy and high resolution X-ray powder diffraction. To complement the experiments, density functional theory (DFT) calculations were performed to characterize the electronic structures and Seebeck coefficients.

2.1 Experimental methods

2.1.1 Infrared reflectivity spectra measurement

Infrared light is an electromagnetic radiation with wavelength between 700 nm to 1 nm. Traditionally it is divided into near, mid, and far infrared regions according to the wavelengths. Near infrared radiation with frequency of 400-10 cm^{-1} is often used for rotational spectroscopy or the probing of lattice vibrations in solids. Mid-infrared radiation with frequency between 4000-400 cm^{-1} can be used to study the fundamental vibrations. Infrared radiation with frequency of 14000-4000 cm^{-1} can be used to excite electrons for low band gap materials. This phenomenon is exploited in the present experimental studies. Infrared spectroscopy has played an important role in the field of industrial, academicals, and medical research.

In condensed matter physics and material science, optical methods are important for the quantitative determination of the electronic band structure and the dielectric function of solid. The infrared reflectivity spectra can be described by a frequency dependent dielectric function using the Drude-Lorentz model. Drude model is a free electron model often used for metals or

doped semiconductors. The extension, Lorentz model is a bound electron model used for semiconductors or insulators with large band gaps. The dielectric function of a material is directly related to the frequency dependent conductivity (optical conductivity), static *dc* conductivity, plasma frequency, carrier concentration, and electron effective mass in the sample. [1] The frequency dependent reflectivity of metals is a complex response function and can be described by the complex dielectric function. However, the real and imaginary part of the dielectric function is related by the Kramers-Kronig (K-K) relationship. The K-K relations enable us to determine the real part of the dielectric function from the information on the imaginary part, and *vice versa*. It is often difficult to measure the phase $\theta(\omega)$ of the reflected wave, but the K-K procedure allows it to be calculated if the reflectance $R(\omega)$ is known at all frequencies.

The phase angle of the reflected beam is related to the reflectivity by,

$$\theta(\omega) = -\frac{1}{2\pi}\int_0^\infty \ln\frac{|s+\omega|}{|s-\omega|}\frac{d\ln R(s)}{ds}ds \qquad (2.1)$$

where ω and s represent the complex variables of angular frequencies.

On the other hand, the complex dielectric function, ε, is related to the real and imaginary parts of the complex refractive index n and k

$$\varepsilon = \varepsilon_1 + i\varepsilon_2 = (n+ik)^2 \qquad \begin{cases} \varepsilon_1 = n^2 - k^2 \\ \varepsilon_2 = 2nk \end{cases} \qquad (2.2)$$

The reflectivity can then be computed from the refractive index,

$$R = \frac{(n-1)^2+k^2}{(n+1)^2+k^2} \tag{2.3}$$

where the frequency dependent conductivity σ can then be evaluated from,

$$\varepsilon(\omega) = \varepsilon_0 + \frac{4\pi i\sigma}{\omega} \tag{2.4}$$

Finally the optical conductivity is related to the concentration of the charge carrier *N*.

$$\sigma(\omega) = \frac{Ne^2\tau}{m^*(1-i\omega\tau)} \tag{2.5}$$

When the frequency dependent optical conductivity is extrapolated to zero frequency ($\omega \rightarrow 0$) gives the *dc* conductivity of the material. Eq. 2.1-2.5 show that once the dielectric function is known, the optical conductivity, σ, can be evaluated.

A common and useful feature in the reflectivity spectrum of a doped semiconductor is a "dip" in the reflectivity spectrum known as the plasma reflection edge or plasma dip. [1] According to the Drude model, for doped semiconductors, the energy at the energy minimum (plasma frequency ω_p) is related to the carrier concentration (N) and the lectron effective (m^*), $\omega_p^2 = Ne^2/\varepsilon\varepsilon_0 m^*$ where ε is the dielectric constant of the material, and ε_0 is the vacuum permittivity. Therefore, the effective mass (m^*) of electrons in a doped semiconductor can be extracted from the plasma frequency (ω_p) provided the electron concentration (N) is known. This latter quantity can be obtained from separate Hall coefficient measurement.

The mid-infrared reflectance spectra presented in this thesis were measured at the side-station of the U2A beamline, National Synchrotron Radiation Facility, Brookhaven National Laboratory. Powder samples were prepared and loaded into a stainless steel gasket placed

between two 300 μm culets of a Sintek mini type IIa diamond anvil cell. The spectra were recorded on a Bruker Vertex 80v FTIR spectrometer and a Hyperion 2000 IR microscope attached with a liquid nitrogen cooled HgCdTe detector. In order to make a thin film, we closed the diamond anvil cell and pressed the two opposing faces with hand pressure, and then recovered the flatten sample. Half of the sample was removed exposing the diamond face. IR reflectance of the exposed diamond face was as the reference from the purpose of scaling the measured reflectance to absolute unit. Then the IR reflectance of sample (~100 μm) was measured. Spectral data were collected with a resolution of 4 cm^{-1} and accumulated for 512 scans.

The reflectance is converted to absolute reflectivity by normalization to the known reflectance of the diamond substrate measured under identical experimental conditions. For a linear system [2] the optical conductivity was obtained by Kramers-Kronig (K-K) analysis of data obtained from normal incidence reflectivity measurements, and then fitted using a variational K-K constrained dielectric function, as implemented in the RefFIT code The *dc* conductivity is obtained from fitting the data to the Drude-Lorentz (DL) model and extrapolated to zero frequency. To determine the quality of the fit, the sum of the squared difference between observed and the fitted, divided by the expected data (χ^2) was computed. There are four adjustable parameters in the Drude-Lorentz model (equation 2.6). They are the high frequency dielectric constant ε_∞, plasma frequency ω_p, the transverse frequency (eigenfrequency) ω_0, and the linewidth (scattering rate) γ, respectively. We set the transverse frequency ω_0 to zero, since it only describes the response of the unbound or free charge carriers of a metal and therefore not needed in the analysis of semiconductors. [2]

$$\varepsilon(\omega) = \varepsilon_\infty + \sum_i \frac{{\omega^2}_{pi}}{{\omega^2}_{oi} - \omega^2 - i\gamma_i\omega} \qquad (2.6)$$

In Equation 2.6, $\varepsilon(\omega)$ is the frequency dependent dielectric function, which can be expressed as the absolute reflectivity according to Fresnel formula. [1] The Drude-Lorentz fits were performed with the RefFIT code. In the Drude-Lorentz model, the Drude model is related to the free electron, and the Lorentz term is related to dipole oscillators. The initial guesses of the four parameters, the plasma frequency (ω_p) was set to about 2000 cm^{-1}, ω_0 was fixed into zero for metal and doped semiconductor, the high frequency dielectric constant (ε_∞) was adjusted into about 10, and the scattering rate (γ) was valued to 1000 cm^{-1}. This is followed by several iterative cycles until the difference in the calculated and computed reflectivity satisfied the convergence criterion, *i.e* the total χ^2 did not vary significantly during the last few iterations. [2] If the fit is satisfactory, the optical conductivity is calculated and information on *dc* conductivity can be determined.

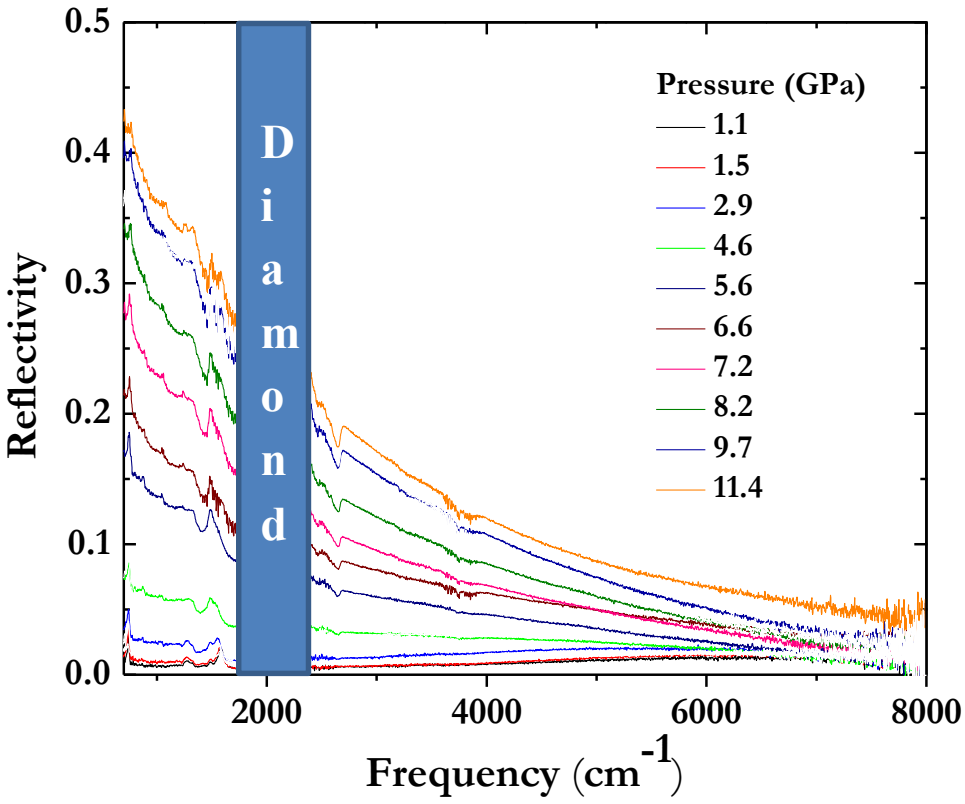

Fig. 2.1 Infrared reflectivity spectra measurement of HBBO under different pressures. (The band marble "Diamond" was undesirable contribution of the C-C stretch from the diamond anvils.)

To test this method, we have extracted the *dc* conductivity from the reflectance spectrum in the metallic phase of the thiazyl radical conductor (HBBO) in a diamond anvil cell. The results of the measurements are shown in Fig. 2.1. The reflectivity spectra of HBBO were analyzed with the software RefFIT based on the Drude-Lorentz and other physical models to extract the frequency dependent dielectric functions, from which the optical conductivity can be calculated. The *dc* conductivities obtained from extrapolation to zero frequency ($\omega \rightarrow 0$) are compared with results obtained from *in-situ* direct *ac* measurements in Fig. 2.3. The general trend of the two set of results are consistent with each other. As shown in Fig. 2.2 & 2.3, both measurements show a sudden increase of conductivity at 4 GPa, indicating a pressure-induced insulator to metal transition. In addition, we have also performed reflectivity measurements upon the release of pressure (hollow circle). The results in Fig. 2.2 show the metallic character can be partially quench-recovered.

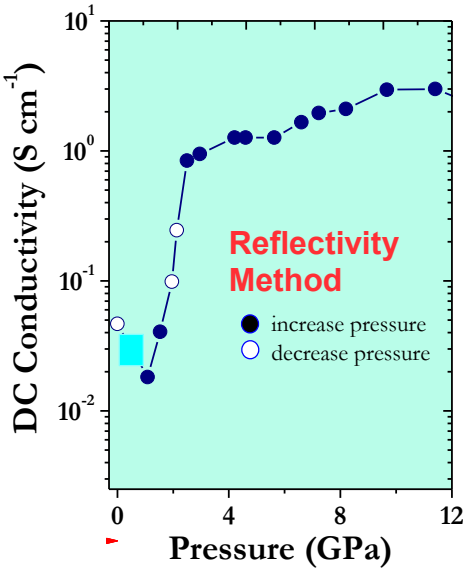

Fig. 2.2 (left) *dc* conductivity calculated of HBBO from the reflectance as a function of pressure.

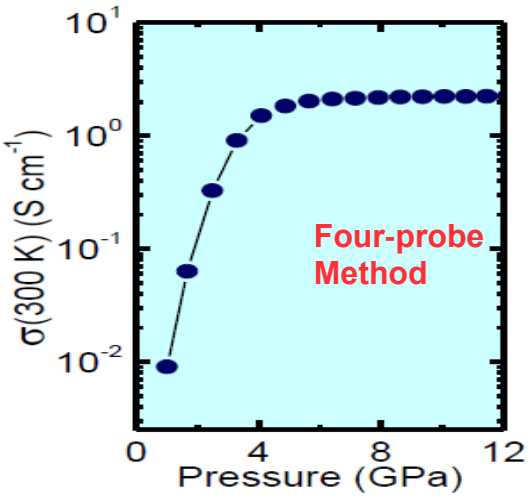

Fig. 2.3 (right) *ac* conductivity measured of HBBO by four probe method as a function of pressure.

2.1.2 Infrared absorption spectra measurement

Infrared absorption spectrum can be used to determine the band gap of a semiconductor. [3] For a direct band gap, the intensity (absorptivity) is proportional to the square root of the photon energy. On the other hand, for indirect band the absorptivity is proportional to the square of the photon energy. In addition, there is a contribution to the absorptivity associated with the energy of the phonon that assist the electronic transition from the valence to the conduction band. [4]

Experiments were performed at room temperature using mid infrared (560-8000cm^{-1}) radiation at IR beamline of the Canadian Light Source Inc. Typically a thin packed powder sample *ca.* 100 μm was loaded on the diamond face of a 300 μm culets Sintek mini type IIa diamond anvil cell. Spectra were recorded on a Hyperion 3000 IR microscope with a liquid nitrogen cooled MCT detector. The IR spectrum of uncovered diamond surface was measured as background. Spectrum was collected with an instrument resolution of 4 cm^{-1}. For example, the measured IR absorption spectrum of pure Mg_2Si is shown in Fig. 2.4. The two arrows in the spectrum show the energies for the creation and annihilation of a phonon associated with the indirect gap excitation. (Fig. 2.4) The absorption feature indicates that the band gap is indirect. [4] In this case, the mean value gives an indirect band gap energy of 0.65 eV and the estimated phonon energy of 0.06 eV is comparable to the lattice vibration frequency of Mg_2Si of 0.04 eV. [4]

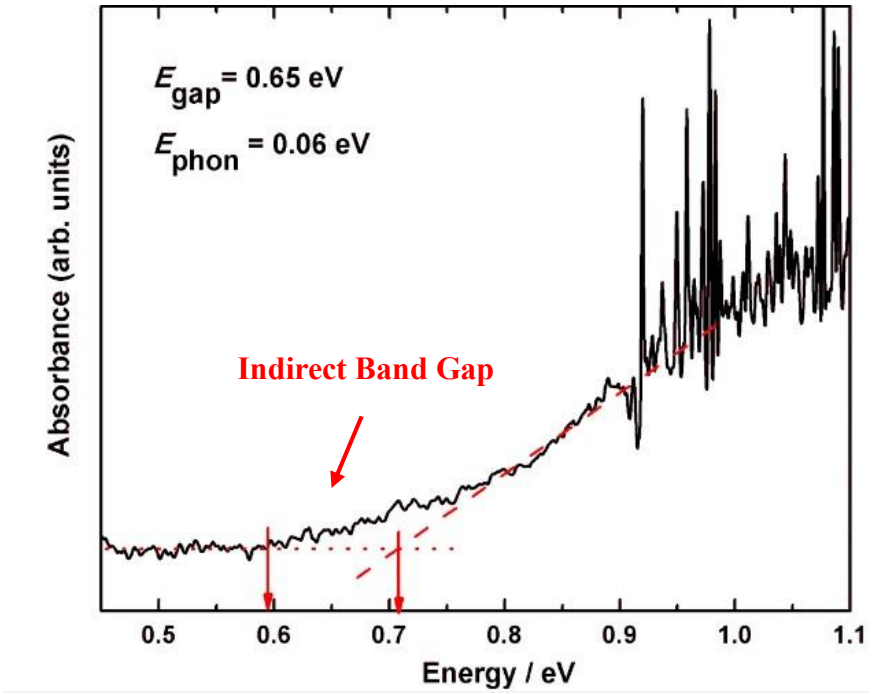

Fig. 2.4 Infrared absorption spectra of pure Mg_2Si.

2.1.3 Synchrotron Powder X-ray diffraction measurements

Powder X-ray diffraction can be used to determine the crystal structure and obtain information on the occupation and location of the dopant sites. Crystals are consisted of regular arrays of atoms and when the wavelength of the X-ray is comparable to the interatomic distances in the crystal, the phenomena of X-ray diffraction occurs. The basic principle of scattering of X-ray in crystal is given by the Bragg's Law: $n\lambda=2d\sin\theta$, where n is the order of reflection, λ is the wavelength of incident ray; d is the interplanar spacing of the crystal; and θ is the angle of incidence and the reflected X-ray (see Fig. 2.5). A diffraction pattern provides information on the intensities and positions of the reflection Bragg peaks. A comparison of the Bragg peaks of the diffraction patterns can reveal whether the dopants have changed the crystal structure of the host Mg_2Si.

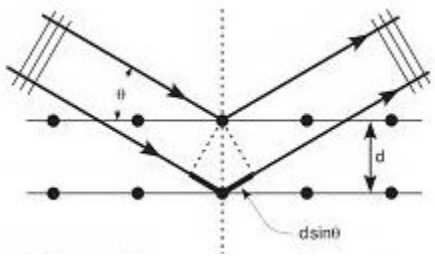

Fig. 2.5 Bragg's Law.

High resolution powder diffraction patterns were measured with synchrotron X-ray from a bending magnet to monochromatized to 18 keV (0.68801 Å) using a double crystal monochromator at the CMCF beamline of the Canadian Light Source. The diffraction patterns were measured in the Debye-Scherrer configuration with an ACCEL MD2 micro-diffractometer equipped with a MarMosaic mx300 CCD X-ray detector. LaB_6 was used as the standard to calibrate the sample to detector distance, tilt angle of detector, and the X-ray wavelength. The program Fit2D V12.043 was used to convert 2D image of diffraction pattern into 1D profile. Diffraction pattern with high energy (shorter wavelength) X-ray and including higher angle diffraction peaks were measured at the HXMA beamline.

2.1.4 Maximum Entropy Method (MEM)

To characterize and better understand the effect of the dopants on the electron density distribution in the host lattice of Mg_2Si crystal, the maximum entropy analysis, which is known to give qualitatively correct electron topology from X-ray diffraction pattern with a limited number of Bragg reflections and without the knowledge of the atom positions, [5,8] were performed.

The scattering intensity (I) is proportional to the square of structure factor (F) in Eq. 2.7.

$$I \propto |F|^2 \tag{2.7}$$

The structure factor (F_{hkl}) can provide the structure information of the sample and it can be given by

$$F_{hkl} = \sum_i g_i f_i(d) t_i exp[2\pi i(hx + ky + lz)] \quad (2.8)$$

where (x, y, z) is atom position d is the d-spacing, g_i is the site occupation factor for atom i, t_i is the temperature factor for atom i, and f_i is the atomic scattering factor for atom i.

Another way to write the structure factor is consider atoms as a continuous distribution of electron density at point (r). In this case, the expression of the structure factor (F_{hkl}) is the function of electron density ρ (r).

$$F_{hkl} = \int_{unit\ cell} \rho\ (r) exp[2\pi i(hx + ky + lz)] dV \quad (2.9)$$

where h k l are Miller indices, x y z are the atomic positions, and V is the volume of unit cell.

From equation (2.9), the electron density ρ (r) is the Fourier transform of the structure factors. Thus, the electron density ρ (r) can be extracted from Eq. 2.10.

$$\rho(x, y, z) = \frac{1}{V} \sum_{hkl} F_{hkl}\ exp[-2\pi i(hx + ky + lz)] \quad (2.10)$$

Therefore, in principle electron density can be calculated from the structure factor by Fourier transform. However, due to the incompleteness of diffraction information, this procedure always suffer from series termination error and this created undesirable random background on the extracted electron density.

The Maximum Entropy Method (MEM) of the information and probability theory is an alternative way to extract the electron density. It was shown by Collins in 1982 electron density distribution can be also calculated by using MEM from a limited diffraction data set. [5]

Compared to the traditional Fourier analysis, MEM avoid a series termination error. In this thesis, due to the limited diffraction data sets obtained from powder diffraction, MEM is a useful way to extract the electron densities of the doped samples.

The information entropy (*S*) is defined as

$$S = -\sum_{i=1}^{N} \rho_i \ln\left(\frac{\rho_i}{\tau_i}\right) \tag{2.11}$$

where τ_i is normalized electron density at i^{th} pixel derived from prior information. [6]

The unit cell is divided into *N* pixels of equal size and normalized electron density (ρ_i) with each pixel considered as probability distribution of independent events.

The most probable electron density distribution in the unit cell is obtained by maximizing the information entropy (S) subject to the following three constraints,

$$(i)\ \ \rho_i > 0 \tag{2.12}$$

$$(ii)\ \ C_F = \sum_{j=1}^{M_F} \frac{|F_c - F_o|^2}{{\sigma_j}^2} = M_F$$

$$and\ (iii) \sum_{i=1}^{N} \rho_i = 1$$

where M_F is the number of observed reflections, F_c and F_o are the calculated and observed structure factors, respectively. σ_j is the estimated standard deviation in the observed structure factor, and C_F is defined as *F*-constraints.

Demonstrated in several recent studies, [7,8] the MEM method is particularly suitable to extract valence electron densities when only low angle Bragg reflections were available. The reason is that the low angle Bragg reflections are mainly due to X-ray scattering from the valence electrons. The form factor (scattering power), $f(\vec{q})$ of an atom as a function of the momentum transfer $\vec{q}$ (= $\frac{4\pi sin\theta}{\lambda}$) is given by,

$$f(\vec{q}) = \int_0^\infty r^2 \rho\,(r) \frac{\sin \vec{q}.\vec{r}}{\vec{q}.\vec{r}} dr \qquad (2.13)$$

The integration can be divided into two regions, *via* the core (<R_c) and the valence,

$$f(\vec{q}) = \int_0^{R_c} r^2 \rho\,(r) \frac{\sin \vec{q}.\vec{r}}{\vec{q}.\vec{r}} dr + \int_{R_c}^\infty r^2 \rho\,(r) \frac{\sin \vec{q}.\vec{r}}{\vec{q}.\vec{r}} dr \qquad (2.14)$$

All low scattering angle should be $\vec{q}.\vec{R}_c \ll \vec{q}.\vec{R}_v$, where R_v is the radius of the valence orbital, since $\vec{R}_v \gg \vec{R}_c$. Therefore, the intensities of the Bragg reflections at low angle (small θ) are more affected by the valence electrons.

The electron density distribution and local structure of Mg_2Si have been studied and analyzed by the MEM method from laboratory X-ray powder diffraction data. [9] In this work, the 3D electron density distribution of Mg_2Si plotted in the form of iso-surface in the unit cell is correctly reproduced as shown in Fig. 2.6. The calculated electronic charges are expected for the Si and Mg atoms in the unit cell. It is interesting to note that no apparent difference in the size of the core regions was visible due to the same number of core electrons in Si and Mg.

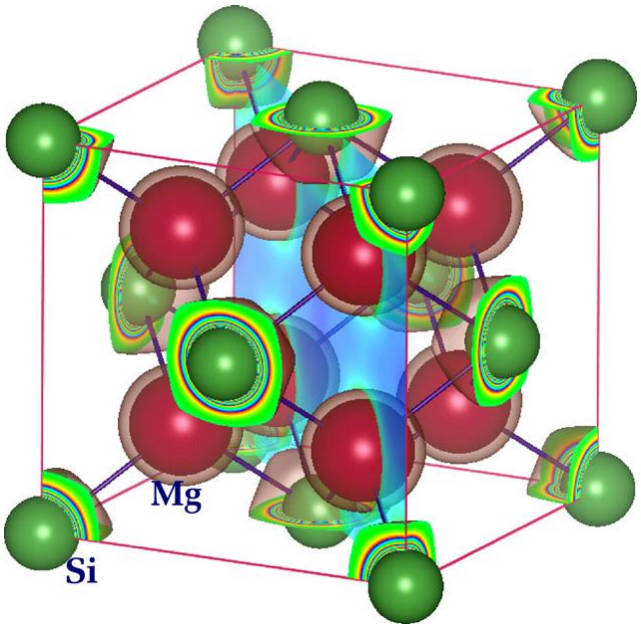

Fig. 2.6 3D iso-surface of the electron density of Mg_2Si in the unit cell superimposed on the structure of Mg_2Si. (Si atom is at the origin). The eight Mg atoms are seen inside the cubic unit cell at ±(1/4 1/4 1/4).Figure taken from ref. [9]

In this thesis, the lattice parameters and the intensities of the Bragg reflections were extracted from the diffraction patterns using the JANA 2006 software package by Le Bail fit. The electron density distribution of the dopants in the crystal are then analyzed from the diffraction patterns using the Maximum Entropy Method implemented in the "Dysnomia" code [10].

2.2 Theoretical methods

First-principles computational electronic structure methods, based on laws of quantum mechanics, are one of the most powerful research tools in physical sciences. In this thesis, electronic structure calculations of thermoelectric materials are based on Density Function Theory (DFT) [11-13], implemented in the Vienna *ab initio* Simulation Package (VASP) [14, 15]. The temperature dependent Seebeck coefficient $S(T)$ relevant to the thermoelectric

performance can then be calculated from the electronic wave functions obtained with first-principles calculations by the Boltzmann transport theory. [16]

2.2.1 Density functional theory (DFT)

Microscopically, any materials are a collection of atoms constructed from nuclei and electrons. According to quantum mechanics, to calculate the physical quantity of a physical system, we only need to solve the many-body Schrödinger equation. The many-body Hamiltonian ($\widehat{H}$) (in atomic unit) is given as,

$$\widehat{H} = -\frac{1}{2}\sum_i \frac{\nabla^2_{\boldsymbol{R}_i}}{M_n} - \frac{1}{2}\sum_i \nabla^2_{\boldsymbol{r}_i} + \sum_{i<j} \frac{Z_i Z_j}{|\boldsymbol{R}_i - \boldsymbol{R}_j|} - \sum_{i,j} \frac{Z_i}{|\boldsymbol{R}_i - \boldsymbol{r}_i|} + \sum_{i<j} \frac{1}{|\boldsymbol{r}_i - \boldsymbol{r}_j|} \qquad (2.15)$$

where M_n and m_e are the masses of the nucleus and electrons, respectively. In this equation, the first two terms are kinetic energies, and the last three terms describe the nucleus-nucleus, electron-nucleus and electron-electron Coulomb interactions, respectively. To simplify the many-body problems, the motions of electrons are separated from the nuclei by assuming that the nuclei is fixed and acting as an external potential, since nuclei are much heavier than electrons *i.e.*, $M_n \gg m_e$. This approximation is known as the Born-Oppenheimer approximation. [17].

Density functional theory (DFT) is the most widely used computational electronic theory as the theory simplifies the description of many electrons system by just using the electron density. Using DFT, the total energy of a system is a functional of the electron density. The total energy can be determined by solving the many-body Schrödinger equation.

According to the Hohenberg-Kohn (HK) theorems, [18] the total energy of the Hamiltonian is a functional of the electron density, $E = E[n(\boldsymbol{r})]$. The principle of HK theorems is summarized as follows:

The ground states energy of a system of interacting electrons is a unique functional of the charge density. For a system with fixed number of electrons, the functional has its minimum value for the correct ground state energy for variations in the charge density. [18]

The total energy functional of a many-electron system under an effective potential V_{eff} in atomic unit is given by,

$$V_{eff}(\boldsymbol{r}) = V_{ext}(\boldsymbol{r}) + \int \frac{n(\boldsymbol{r'})}{|\boldsymbol{r}-\boldsymbol{r'}|} d^3r' + \frac{\delta E_{xc}[n(\boldsymbol{r})]}{\delta n(\boldsymbol{r})} \tag{2.16}$$

where V_{ext} ($\boldsymbol{r}$) is the external potential due to the nuclei, the second term is the electron-density interaction, and by the last term is the exchange-correlation.

A single particle Schrödinger equation (in atomic unit) is used to describe the interactions of each individual electron with the mean field created by rest of the system is,

$$\left(-\frac{1}{2}\nabla^2 + V_{eff}(\boldsymbol{r})\right)\varphi_i(\boldsymbol{r}) = \epsilon_i \varphi_i(\boldsymbol{r}) \tag{2.17}$$

where φ_i ($\boldsymbol{r}$) is the single particle wave function.

The ground state total energy of a solid can be expressed in terms of a functional of the electron density $n(\boldsymbol{r})$ and energy of nuclei,

$$E_{total}[n] = E_{electron}[n] + E_{ion} \tag{2.18}$$

Applying the Born-Oppenheimer approximation, the ground state energy of an interacting electron system is given by the Kohn-Sham equation (in atomic unit),

$$E_{electron}[n(\boldsymbol{r})] = T_0[n(\boldsymbol{r})] + \frac{1}{2}\iint \frac{n(\boldsymbol{r})n(\boldsymbol{r'})}{|\boldsymbol{r}-\boldsymbol{r'}|} d^3r d^3r' + \int V_{ext} n(\boldsymbol{r}) d^3r + E_{xc}[n(\boldsymbol{r})] \tag{2.19}$$

$$T_0[n(\boldsymbol{r})] = \sum_i \int d^3r \varphi_i^*(\boldsymbol{r}) \left(-\frac{1}{2}\nabla^2\right)\varphi_i(\boldsymbol{r}). \tag{2.20}$$

In the Kohn-Sham equation, the exchange correlation functional $E_{xc}[n(\boldsymbol{r})]$ is unknown. It is essential to approximate the exchange and correlation energies by the electron density $n(\boldsymbol{r})$, and more accurately on the derivatives of the electron density $\nabla n(\boldsymbol{r})$. This method is known as

the generalized gradient approximation (GGA). [18] GGA has been demonstrated to be success in many solid-states calculations with reliable results.

$$E_{xc}^{GGA}[n] = \int d^3 r n(\boldsymbol{r}) \varepsilon_{xc}^{GGA}[n, \nabla n] \quad (2.21)$$

In the calculations, Blöchl's projector-augmented wave (PAW) potentials were used to mimic the core electrons of the atoms. [19] The PAW potentials were constructed with the Perdew-Burke-Ernzerhof (PBE) functional. [20]

2.2.2 Electronic structure calculation-Electronic density of states (DOS) and Projected electronic density of states (PDOS)

The electronic density of states (DOS) of a solid is defined as number of electronic states per unit volume per unit energy and is also a function that when multiplied by an interval of energy. When the electronic density of states is projected to the atomic orbitals of the atoms (PDOS), it can provide information on the contributions of the different orbitals to the electronic states. The DOS and PDOS of a system are useful quantities to characterize the electronic structure. Furthermore, the calculated DOS is essential to the input Seebeck coefficient calculations. In this thesis, the electronic structure calculations were performed using density functional theory (DFT) with the Perdew–Burke–Ernzerhof (PBE) generalized gradient approximation (GGA) as implemented in the Vienna *ab initio* simulation package (VASP) code. The projector-augmented wave (PAW) method, a real quantum potential, was adopted with $3s^2$ and $3s^2 3p^2$ as valence electrons for the Mg and Si atoms.

2.2.3 *GW* approximation (*GWA*)

It is well known that the current GGA functional is not appropriate for the accurate prediction of the band gap energy, due to the neglect of Coulomb repulsion and electron correlation of the interacting electrons in the system. [21] *GW* approximation (*GWA*) has been

used to impose the electronic structure by including the effects of the electronic band structure. In the *GWA*, *G* is the one-particle Green's function and *W* is the screened Coulomb interaction. [22-25] The *GWA* method was employed to calculate accurate band gap energy of pure Mg_2Si at ambient and high pressure.

2.2.4 Temperature dependent Seebeck coefficient *S*(*T*) calculation

The Seebeck coefficient can be calculated from the density of states obtained in the electronic structure calculation using the VASP code with the V2Boltz program. [26] This program computed the temperature dependent Seebeck coefficient *S*(*T*) for *n*-doped Mg_2Si-based thermoelectric materials within the rigid band approximation based on the semi-classical Boltzmann transport theory with the DOS as the only input.

The electrical conductivity $\sigma_0(T)$ of a solid can be calculated from the band structure by the energy integral, [27]

$$\sigma_0(T) = \frac{e^2}{3\hbar}\int \left[-\frac{\partial N(E)}{\partial E}\right] N(E)v^2(E)\tau(E,T)dE \qquad (2.22)$$

where *e*, τ, *N*, and ν are electron charge, electronic relaxation time, electron density of states, and Fermi velocity, respectively.

The temperature dependent Seebeck coefficient *S*(*T*) is the ratio of the 0th and 1st moment of the integral,

$$S(T) = \frac{1}{eT}\frac{I^1}{I^0} \qquad (2.23)$$

where $I^x(T) = \int \left[-\frac{\partial N(E)}{\partial E}\right] N(E)v^2(E)\tau(E,T)(E-E_F)^x dE$, and E_F is the Fermi energy.

Inspection of Eq. 2.23 shows a high efficient thermoelectric material should have a high electronic density of states near the Fermi level and a reasonable electrical conductivity. The temperature dependent Seebeck coefficient *S*(*T*) of the doped Mg_2Si sample can be estimated

from the ground state band structure using the rigid band model by shifting the energy of the Fermi level according to the number of electrons donated by the dopant. Thus, an ideal thermoelectric material with the large predicted Seebeck coefficient at low doping concentration will have a high Fermi velocity and high electron density of states (DOS) at the Fermi energy. Generally a high DOS indicates the electron band dispersions near the Fermi level must be fairly flat. [27]

References

[1] M. Fox, Optical Properties of Solids, Oxford University Press, New York City, NY, USA, 2010.

[2] A. B. Kuzmenko, *Rev. Sci. Instrum.*, 2005, 76, 083108.

[3] A. Akrap, M. Tran, A. Ubaldini, J. Teyssier, E. Giannini, and D. V. D. Marel, *Physical Review B*, 2012, 86, 235207.

[4] W. B. Whitten, P. L. Chung, and G. C. Danielson, *Journal of Physics and Chemistry of Solids*, 1965, 26, 49-56.

[5] D. M. Collins, *Nature*, 1982, 298, 49-51.

[6] C. J. Gilmore, *Acta Cryst. A*, 1996, 52, 561-589.

[7] J. S. Tse, M. Hanfland, R. Flacau, S. Desgreniers, Z. Li, K. Mende, K. Gilmore, A. Nyrow, M. M. Sala, and C. Sternemann, *J. Phys. Chem. C.*, 2014, 118, 1161-1166.

[8] R. Li, J. Liu, L. Bai, J. S. Tse, and G. Shen, *Applied Physics Letters*, 2015, 107, 072109.

[9] R. Saravanan and M. C. Robert, *Journal of Alloys and Compounds*, 2009, 479, 26-31.

[10] K. Momma, T. Ikeda, A. A. Belik and F. Izumi, *Powder Diffraction*, 2013, 28, 184-193.

[11] P. Hohenberg and W. Kohn, *Phys. Rev. B*, 1964, 136, B864.

[12] W. Kohn and L. J. Sham, *Phys. Rev.*, 1965, 140, A1133.

[13] I. Gilbert, *Phys. Rev. B*, 1975, 1, 2112.

[14] G. Kresse and J. Furthmüller, *Computational Materials Science*, 1996, 6, 15-50.

[15] G. Kresse and J. Furthmüller, *Phys. Rev. B*, 1996, 54, 11169.

[16] G. K. H. Madsen and D. J. Singh, *Computer Physics Communications*, 2006, 175, 67-71.

[17] M. Born and R. Oppenheimer, *Annalen der Physik*, 1927, 389, 457-484..

[18] J. P. Perdew, K. Burke, and M. Ernzerhof, *Phys. Rev. Lett*., 1996, 77, 3865-3868.

[19] P. E. Blöchl, *Phys. Rev. B*, 1994, 50, 17953.

[20] G. Kresse and D. Joubert, *Phys. Rev. B*, 1999, 59, 1758.

[21] L. J. W. Aulbur and J. Wilkins, *Solid State Physics*, 2000, 54, 1.

[22] L. Hedin, *Phys. Rev*., 1965, 139, A796–A823.

[23] P. Garcia–Gonzalez and R. W. Godby, *Phys. Rev. B*, 2011, 63, 075112.

[24] F. Aryasetiawan and O. Gunnarsson, *Physical Review Letters*, 1995, 74, 3221.

[25] S. V. Faleev, M. V. Schilfgaarde, and T. Kotani, *Physical Review Letters*, 2004, 93, 126406.

[26] M. Chen, in First-principles Modeling of Thermoelectric Materials, PhD thesis, Theoretical Solid State Chemistry, Vienna University of Technology, Vienna, Austria, 2012.

[27] J. S. Tse and D. D. Klug, "Thermoelectrics Handbook: Macro to Nano," ed. D.M. Rowe, CRC Press.

CHAPTER 3

Sb- AND Bi- DOPED Mg_2Si: LOCATION OF THE DOPANTS, MICRO- AND NANOSTRUCTURES, ELECTRONIC STRUCTURES AND THERMOELECTRIC PROPERTIES

Although the potential of Mg_2Si as a thermoelectric material was recognized in 1961, [11] systematic optimization of its properties only began in the last decade. The Mg_2Si-based materials composed of non-toxic, abundant and affordable elements are very attractive for large-scale industrial applications. Previous researches have focused on replacing the Si site with Ge and/or Sn to lower its thermal conductivity, or by doping with Sb or Bi. Unfortunately, despite substantial efforts, the thermoelectric performance remains relatively low. For example, ball-milled and hot-pressed as well as spark-plasma-sintered (SPS) Bi-doped Mg_2Si has been reported to reach ZT_{max} = 0.7~0.86 at around 800 K. [12,13] Unfortunately, a significant amount of Mg_3Bi_2, an undesirable side product after SPS, was always present. [14] Further improvement has been achieved by multiple doping. For example, Sb-doped $Mg_2Si_{0.4}Sn_{0.6}$ has attained a ZT_{max} = 1.1 at 800 K, [16] and melt-spinning of $Mg_2Si_{0.4}Sn_{0.6}Bi_{0.03}$ followed by SPS has improved it to a ZT_{max} = 1.2 at 573 K. [17]

This chapter presents results of the characterization of Mg_2Si-based thermoelectric materials by adding single dopants, Sb or Bi, to Mg_2Si. The compounds studied were $Mg_2Si_{0.98}Sb_{0.02}$ and $Mg_2Si_{0.98}Bi_{0.02.}$ The *dc* conductivities of the doped samples were extracted from the analysis of infrared (IR) reflectivity spectra employing the Drude free electron model. We found infrared (IR) measurements of the *dc* conductivity systematically lower than the *in-situ* four probe measurements of the bulk sample because of the limited penetration depth and very small spot size of the IR radiation. The electron effective masses in the samples were also extracted from the "plasma dip" according to the procedure described in equations 2.1-2.5 of

Chapter 2. Furthermore, the band gap of undoped Mg_2Si as determined by infrared absorption spectrum was found to be indirect with a gap energy of 0.65 eV. This result is in excellent agreement with previous studies. [31-35] To help explain the experimental observation, the electron densities of states of Sb- and Bi-doped Mg_2Si were calculated with the DFT method. The most significant observation is that, even with localized defect atoms (*i.e.* Sb or Bi), electrons donated by the dopants were delocalized over the entire crystal and did not appear as a localized band between the energy gap of Mg_2Si. This observation confirms the validity of the rigid band approximation used by shifting the Fermi level according to the number of electrons donated by the dopant in the calculation of the Seebeck coefficients using the semiclassical Boltzmann transport theory. The calculations predicted negative Seebeck coefficients for the doped samples, consistent with the consequence of *n*-doping. The absolute magnitude of Seebeck coefficients was found to decrease with the dopant concentration. Experimentally, the highest absolute value of Seebeck coefficient was found to be -170 μVK^{-1} at 800 K for $Mg_2Si_{0.99}Sb_{0.01}$ and the highest ZT = 0.6 at 700 K was achieved for $Mg_2Si_{0.98}Bi_{0.02}$.

The results of this study have been published in

N. Farahi, M. VanZant, J. Zhao, J. S. Tse, S. Prabhudev, G. A. Botton, J. R. Salvador, F. Borondics, Z. Liu and H. Kleinke, "Sb- and Bi- doped Mg_2Si: location of the dopants, micro- and nanostructure, electronic structures and thermoelectric properties," *Dalton Transactions*, vol. 43, pp. 14983-14991, 2014.

The authors' contributions are as follows:

- N. Farahi, M. VanZant and H. Kleinke synthesized the samples and performed the thermoelectric property measurements.

- J. Zhao and J. S. Tse performed infrared absorption and reflectivity measurements, performed analysis to extract the dielectric functions and transport properties, and computed the electronic structures and Seebeck coefficients.
- S. Prabhudev and G. A. Botton performed the STEM measurement.
- J. R. Salvador performed the Hall measurement.
- F. Borondics and Z. Liu assisted in performing infrared experiments at CLS and BNL, respectively.
- All authors contributed to the writing and editing of the manuscript.

Abstract

Due to increasing global energy concerns, alternative sustainable methods to create energy such as thermoelectric energy conversion have become increasingly important. Originally, research into thermoelectric materials was focused on tellurides of bismuth and lead because of the exemplary thermoelectric properties of Bi_2Te_3 and PbTe. These materials, however, contain toxic lead and tellurium, which is also scarce and thus expensive. A viable alternative material may exist in Mg_2Si, which needs to be doped and alloyed in order to achieve reasonable thermoelectric efficiency. Doping is a major problem, as *p*-type doping has thus far not produced competitive efficiencies, and *n*-type doping is problematic because of the low solubility of the typical dopants Sb and Bi. This investigation shows experimentally that these dopants can indeed replace Si in the crystal lattice, and excess Sb and Bi atoms are present in the grain boundaries in the form of Mg_3Sb_2 and Mg_3Bi_2. As a consequence, the carrier concentration is lower than the formal Sb/Bi concentration suggests, and the thermal conductivity is significantly reduced. DFT calculations are in good agreement with the experimental data,

including the band gap and the Seebeck coefficient. Overall, this results in competitive efficiencies despite the low carrier concentration. While ball-milling was previously shown to enhance the solubility of the dopants and thus the carrier concentration, this did not lead to enhanced thermoelectric properties.

3.1 Introduction

Thermoelectric energy conversion is receiving increasing attention, while the global energy resources are declining. Thermoelectric (TE) materials can generate electricity out of heat (more precisely: out of a temperature gradient), which may be used to turn waste heat into useful electrical energy, such as in automotives. [1] The thermoelectric conversion efficiency increases with increasing thermoelectric figure of merit, defined as $ZT = TS^2\sigma\kappa^{-1}$. Therein, S is the Seebeck coefficient, σ the electrical conductivity, κ the thermal conductivity, and T the absolute temperature. This figure of merit needs to be improved to enhance the conversion efficiency, as is required for this technology to become economically viable, for example in automotives.

Typically, heavy metal tellurides and antimonides dominate the best thermoelectric materials, including materials based on doped Bi_2Te_3, [2,3] PbTe, [4-6] Tl_9SbTe_6 [7] and Tl_9BiTe_6, [8] $La_{0.4}Yb_{13.6}MnSb_{11}$, [9] and skutterudites including $Ba_{0.08}La_{0.05}Yb_{0.04}$- Co_4Sb_{12}. [10] While using these heavy materials has its advantages, most notably the high figure of merit, in excess of unity, in part related to low thermal conductivity, three serious problems are associated with using tellurium, antimony, lead, thallium and lanthanides in large-scale applications. These problems are toxicity, availability, and cost. Therefore, alternative materials comprised of non-toxic, abundant and affordable elements are very attractive, though they may end up being less efficient. From this point of view, Mg_2Si - adopting the anti-fluorite structure type - appears as a perfect candidate. While its potential as a thermoelectric was already discussed in 1961, [11]

systematic optimization of its properties really began only in the last decade or so, by alloying Si with Ge and/or Sn to lower its thermal conductivity, and by doping it, mostly with Sb or Bi. For example, ball-milled and hot-pressed as well as spark-plasma-sintered (SPS) Bi-doped Mg_2Si was reported to reach ZTmax = 0.7 at 775 K [12] and 0.86 at 862 K, [13] respectively, and 0.74 at 840 K with significant amounts of Mg_3Bi_2 as a side product after SPS. [14] Additional alloying on the Si site, typically with Ge and/or Sn, can further enhance ZT by lowering the thermal conductivity, the weakest point of these materials, and simultaneously improving the power factor by convergence of conduction bands: [15] Sb-doped $Mg_2Si_{0.4}Sn_{0.6}$ attained ZT_{max} = 1.1 at 800 K, [16] and melt-spinning of $Mg_2Si_{0.4}Sn_{0.6}Bi_{0.03}$ followed by spark-plasma-sintering yielded ZT_{max} = 1.2 at 573 K. [17] To further shine light on the thermoelectric properties of Sb- and Bi-doped Mg_2Si, we present here comprehensive detailed studies on the location of the dopants, both with respect to the crystallographic location and the macrostructure.

3.2 Experiment

3.2.1 Syntheses and phase purity analyses

The Mg (99.8%, Alfa Aesar, -20 + 100 mesh), Si (99.9%, Alfa Aesar, -100 mesh), Sb (99.5%, Alfa Aesar, -100 mesh) and Bi (99.5%, Alfa Aesar, -325 mesh) powders were mixed according to the required stoichiometry ratio in a glove box under an argon atmosphere. Excess Mg (4%) was used to counter the effect of magnesium evaporation during the reaction, thus the starting ratios were 2.08Mg : (1 - x)Si : xSb and 2.08Mg : (1 - x) Si : xBi. The reaction mixtures were placed into alumina crucibles, which were then placed into fused silica tubes. The tubes were then heated at 823 K in a resistance furnace for 3.5 days. The products were crushed and reheated at around 873 K for 5 days, and then cooled down to room temperature naturally by switching off the furnace. For phase purity analysis, an Inel powder X-ray diffractometer with

Cu-Kα_1 radiation and a position sensitive detector was used. For x = 0.02, the samples appeared to contain only $Mg_2Si_{1-x}Sb_x$ and $Mg_2Si_{1-x}Bi_x$, respectively, with traces of MgO, *i.e*. no unreacted Si, Sb or Bi were detected. Larger amounts of Sb or Bi resulted in noticeable formation of Mg_3Sb_2 or Mg_3Bi_2.

Additional powder X-ray diffraction experiments on Mg_2Si and $Mg_2Si_{0.98}Bi_{0.02}$ were performed at the CMCF-II beamline at the Canadian Light Source. Synchrotron radiation from a bending magnet port was monochromatized to 18 keV (0.68801 Å) with a double crystal monochromator and focused to the sample with a toroidal mirror. Powder diffraction patterns were measured in the Debye–Scherrer configuration with a versatile ACCEL MD2 micro-diffractometer and MarMosaic mx300 CCD X-ray detector. These experiments confirmed the results obtained from the Inel diffractometer, and showed evidence of a small unit cell expansion upon doping with Bi, namely from a = 6.33504(5) Å to a = 6.34227(6) Å, as shown in Fig. A.1 in the ESI.

To investigate the microstructure homogeneity of the samples, energy dispersive X-ray (EDX) analysis was performed on a piece of the hot-pressed pellets using a Zeiss ULTRA plus electron microscope associated with an EDX device, EDAX Pegasus 1200. The EDX results confirmed the existence of Sb and Bi in the samples with some Sb- and Bi-rich regions, respectively; the analysis of different crystals resulted in an average ratio of 2.05Mg : 0.94Si : 0.01Bi.

Differential scanning calorimetry (DSC) was used to examine the thermal stability of the samples with x = 0.02. The DSC measurement was performed under argon flow by using the NETZSCH STA 409PC Luxx instrument with a heating rate of 10 K min^{-1} from 300 K to 1073

K. No phase transition was detected, and the weight loss was <2%, possibly within experimental error. The plots are presented in Fig. A.2 in the ESI.

3.2.2 Transmission electron microscopy

Atomic-scale structural characterization and elemental analyses were performed using scanning transmission electron microscopy (STEM) operating in a high-angle annular dark-field imaging (HAADF) mode and energy dispersive X-ray Spectrometry (XEDS). Conventional TEM is primarily a broad-beam based technique, wherein all the scattered electrons, upon interacting with the specimen, are collected over a large illumination area on the specimen. In these conditions, images are strongly dependent on the thickness of the sample and objective lens-focus conditions. As opposed to this, STEM-HAADF employs a raster scanning electron probe to collect electrons that are elastically scattered at high angles. Upon converging the electron beam into a sub-angstrom probe, an atomic-scale image of materials can be obtained. The high angle annular dark field (HAADF) detector, as the name suggests, is a detector designed with an annular geometry and placed in a diffraction plane below the sample so as to collect electrons emerging from the specimen at high scattering angles. Since the intensity of these high-angle scattered electrons is directly related to the atomic number of scattering atoms under the electron beam, the resulting STEM-HAADF image provides an atomic number "*Z*"-contrast image with intensities proportional to $Z^{1.6}$. For instance, in the case of the Mg_2Si sample doped with Bi, the atomic columns containing Bi (Z = 83) are expected to appear significantly brighter compared to the bulk of the matrix crystal.

Atomically-resolved STEM-HAADF images were acquired using a FEI-Titan cubed TEM, equipped with two hexapole-design spherical aberration correctors of the probe and image forming lenses. The microscope was operated in the STEM mode at an accelerating voltage of

300 kV and the images were acquired using a Fischione Instruments HAADF detector. Image simulations were carried out using the multislice method by implementing the Kirkland code [18] in order to validate the structural model and deductions of the dopant site preference.

For STEM characterization, the samples were thinned by mechanical polishing to 180 μm thickness, then dimple-ground with a diamond paste to a central thickness of 20 μm and finally ion milled (using a Gatan PIPS model) to electron transparency.

3.2.3 Electronic structure calculations

The electronic structure calculations were performed using density functional theory (DFT) with the Perdew-Burke-Ernzerhof (PBE) generalized gradient approximation (GGA) [19] as implemented in the Vienna *ab initio* simulation package (VASP) code. [20-23] To obtain a more accurate band gap, additional calculations were performed *via* the *GW* approximation (*GWA*), which utilizes the one-particle Green's function and the screened Coulomb interaction W. [24,25] For the GGA calculation, the projector-augmented wave (PAW) [26,27] method was adopted with $2p^6 3s^2$ and $3s^2 3p^2$ as valence electrons for the Mg and Si atoms, respectively. An energy cut-off of 332 eV and an appropriate Monkhorst-Pack scheme was employed for the Brillouin zone with a dense *k*-mesh of 25 × 25 × 25 for the Seebeck coefficient calculation. The band structure was calculated with the VASP code with a 16 × 16 × 16 *k*-point set. For doping with Sb and Bi, a 2 × 2 × 2 supercell was created from the Mg_2Si crystal structure, where one out of 32 Si atoms was replaced either with an Sb or a Bi atom. The stoichiometry of the doped model is thus approximately $Mg_2Si_{0.97}Pn_{0.03}$ (Pn = Sb, Bi). For the Bi case, spin–orbit coupling was included in the calculation. By using VASP output and symmetry, the V2Boltz program [28] was applied on the basis of semiclassical Boltzmann transport theory to calculate the temperature

dependent Seebeck coefficient $S(T)$ for *n*-doped Mg_2Si-based thermoelectric materials within the rigid band approximation. [29]

3.2.4 Physical property measurements

To verify the band gap, an infrared transmission spectrum was obtained from a ground sample of undoped Mg_2Si at room temperature using a Fourier transform IR spectrometer, utilizing the Mid Infrared (560-8000 cm^{-1}) Spectromicroscopy beamline at the Canadian Light Source Inc. The sample was loaded on the 300 μm culets of a Sintek mini type IIa diamond anvil cell. The spectra were recorded on a Hyperion 3000 IR microscope with a liquid nitrogen cooled MCT detector. For the measurement, the diamond was firstly measured as a background spectrum. After extracting the background, the sample of ~100 μm was focused by microscopy and measured. Spectral data collection employed a resolution of 4 cm^{-1} and 512 scans.

The mid- and far-infrared reflectance spectra of undoped Mg_2Si and Mg_2Si doped with Bi or Sb were measured at the National Synchrotron Radiation Facility, Brookhaven National Laboratory. The sample preparation procedure was the same as described above. Far-infrared reflectivity experiments were performed at the side-station of the U2A beamline. Mid-infrared reflectivity was measured with a Bruker Vertex 80v FTIR spectrometer and a Hyperion 2000 IR microscope attached to a liquid nitrogen cooled HgCdTe detector. A conventional globar source was used to minimize any intensity fluctuation during the measurements. The intensity of the source was calibrated against the synchrotron ring current using a gold foil. A KBr beam splitter was used to cover the mid-IR region, and the spectral resolution of 4 cm^{-1} applied to all spectra. The reflectance was converted to absolute reflectivity by normalization to the reflectance diamond substrate measured under identical experimental conditions. Optical conductivity was

obtained by Kramers-Kronig (K-K) analysis of data obtained from normal incidence reflectivity measurements, then fit using a variational K-K constrained dielectric function, as implemented in the REFFIT code. [30] The *dc* conductivity is obtained from fitting to the Drude model and extrapolated to zero frequency. Since the mid and far-infrared spectra were recorded on different detectors, the reflectances in the two regions were connected manually by matching to the mid-infrared reflectance at 600 cm^{-1} (0.75 eV).

The doped Mg_2Si samples were ground and then consolidated in an argon atmosphere under a pressure of 32 MPa at 973 K by using an Oxy-Gon hot press to obtain a cylindrical pellet of 12.7 mm diameter and 3 mm thickness. The pressure was released after heating for 2 hours to eliminate strain on the pellets during the cool-down procedure. Thermal diffusivity (α) measurements were performed on the polished pressed samples under argon flow by using an Anter Flashline FL3000 thermal properties analyzer between 350 K and 670 K. For calculating the thermal conductivity (κ), the density (d) of the pellets was measured via the Archimedes method, and the Dulong–Petit approximation was applied for determining specific heat (C_P) values. The thermal conductivity was then calculated according to $\kappa = \alpha d C_P$.

Rectangular bars with dimensions of approximately 10 × 2 × 2 mm, cut from the same hot-pressed pellets, were used for electrical conductivity (σ) and Seebeck coefficient (S) measurements. These measurements were performed simultaneously under a helium atmosphere by using the ULVAC-RIKO ZEM-3 apparatus between 300 K and 800 K.

The Hall measurements were recorded from 5 K to 300 K using a cryostat equipped with a 5 T magnet and a linear research AC resistance bridge. Ohmic contacts were made by using

silver paint. The Hall mobility, μ_H, was calculated from the relation $\mu_H = \sigma n^{-1} e^{-1}$, where n = carrier concentration and e = electron charge.

3.3 Results and discussion

3.3.1 Micro- and nanostructure

Low-magnification TEM imaging revealed the polycrystalline nature of the sample with grain sizes of the order of 7 μm. We did not observe any formation of Bi-rich precipitates in the matrix. Additionally, STEM-HAADF characterization was performed at an atomic resolution to locate the doped Bi atoms. The principal regions of interest included the bulk of the sample, and the grain boundaries. Fig. 3.1a shows the atomic-resolution STEM-HAADF image from the bulk of the $Mg_2Si_{0.98}Bi_{0.02}$ sample, oriented along the [110] zone axis. A significant number of atomic columns with brighter intensity are distributed randomly over the lattice. Due to the *Z*-dependence in these imaging conditions, we infer that these bright atomic columns correspond to columns containing Bi dopant atoms located on the original Si atoms, deduced from the image simulations discussed further below. The relative variation in the intensities among the bright atomic columns indicates that these columns could contain single Bi dopants or possibly more Bi atoms. However, due to the lack of information on the location of the Bi atoms in the thickness of the sample, we cannot extract further quantitative information on the number of atoms within one column due to the sensitivity of the image intensity upon the precise location of the scattering atoms.

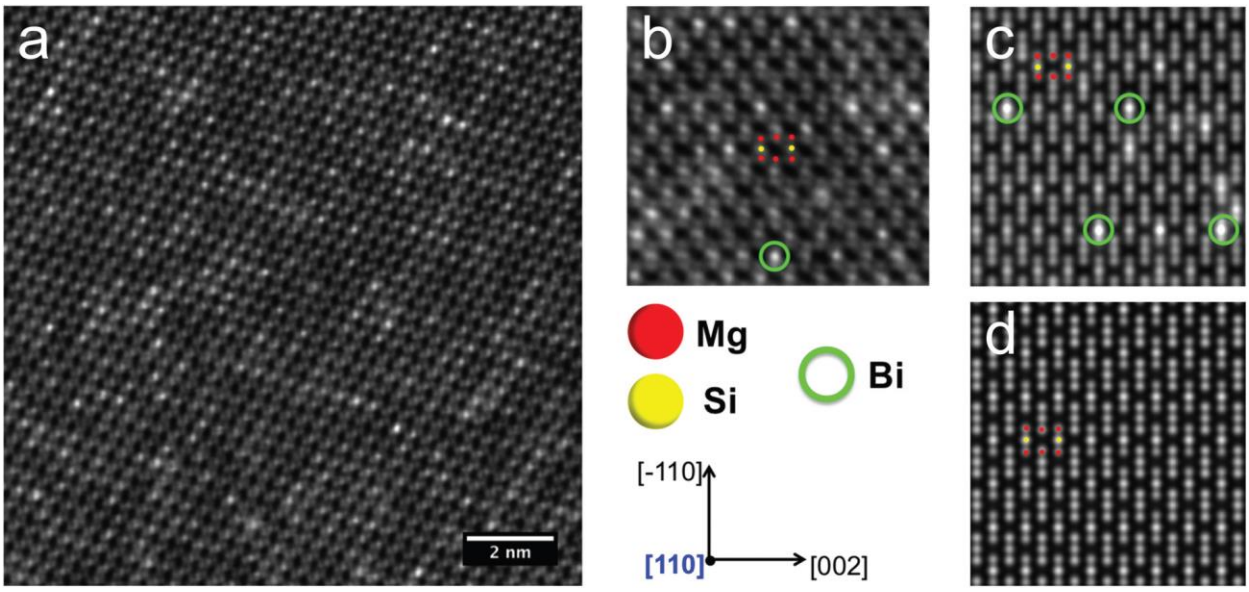

Fig. 3.1 (a) and (b) STEM-HAADF image of $Mg_2Si_{0.98}Bi_{0.02}$. (c) and (d) Multi-slice simulation results obtained for $Mg_2Si_{0.98}Bi_{0.02}$ and Mg_2Si along the [110] zone axis, respectively.

In order to further confirm these deductions, we performed multi-slice image simulations for the $Mg_2Si_{0.98}Bi_{0.02}$ bulk matrix and pure Mg_2Si. These simulations utilized atomic models created from a (10 × 10 × 10 atoms) supercell viewed along the [110] zone axis, in which the Bi dopants were randomly included as substitutional atoms on the Si sites. The resulting images obtained upon entering this structural model into the multi-slice simulations are shown in Fig. 3.1c and 3.1d. Therein, the atomic columns with brighter intensities correspond to those containing Bi-dopants. Unlike $Mg_2Si_{0.98}Bi_{0.02}$ (Fig. 3.1c), the bulk of pure Mg_2Si (Fig. 3.1d) does not reveal strong intensity fluctuations within the matrix, confirming our dopant atom deductions derived from the experimental STEM-HAADF image shown in Fig. 3.1a.

From the STEM-HAADF images acquired from grain boundaries (Fig. 3.2a and 3.2b), it is clear that the Bi dopants also segregate - most likely in the form of Mg_3Bi_2 as sometimes found in the X-ray diagrams at grain boundaries as deduced from the increased intensity of the image. This is further confirmed from XEDS line scans recording the signal of the Bi $L\alpha_1$ peak as a function of position (Fig. 3.2c).

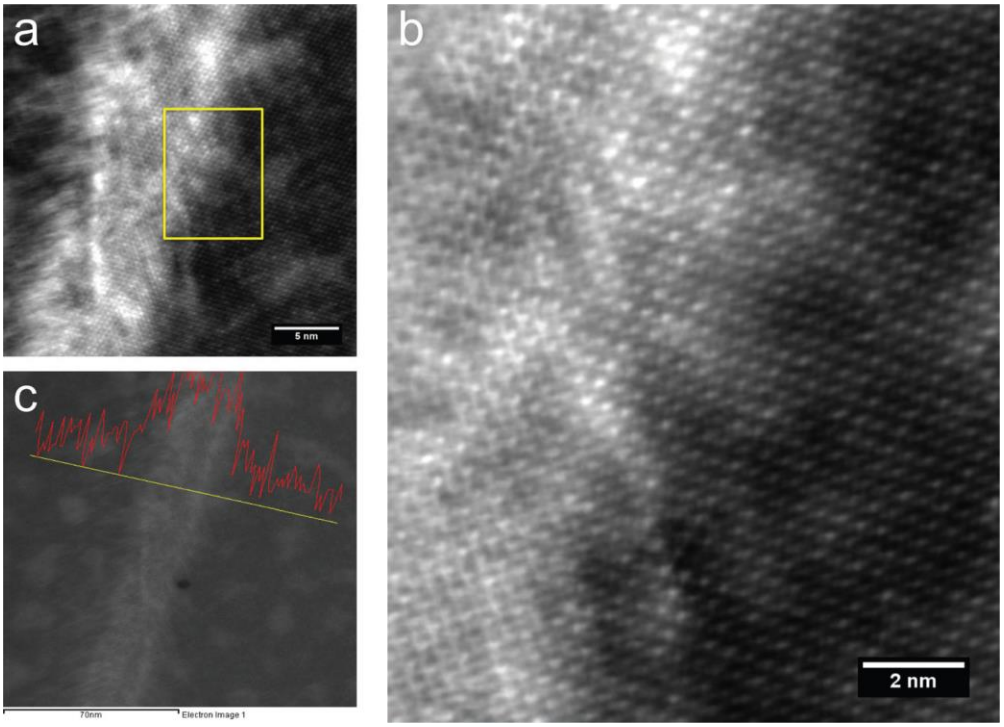

Fig. 3.2 (a) Atomic-resolution STEM-HAADF image of $Mg_2Si_{0.98}Bi_{0.02}$ demonstrating Bi segregation at the grain boundary (GB). (b) STEM-HAADF image acquired from the region marked in yellow in (a). (c) EDX line-scan for Bi (red) over the same area marked in yellow.

3.3.2 Electronic structure

The densities of states calculated via the GGA *vs*. the *GW* approach are depicted in Fig. 3.3 (left). In each case, a narrow gap separates the valence band, mostly comprising Si-*p* states from the conduction band, dominated by Mg states. The use of the screening correction (*GW*) did not change the valence band, but shifted the empty states uniformly towards higher energies. As a result, the calculated band gap increased from 0.2 eV to 0.67 eV, ultimately in agreement with experimental data. [31] The band structures are shown in Fig. A.3 (ESI), revealing the indirect band gap. Similarly, a computed (indirect) band gap of 0.6 eV [32] was obtained after employing the modified Becke–Johnson local density functional (mBJLDA), [33,34] and applying the *GW* corrections to selected *k*-points yielded a computed gap of 0.65 eV. [35]

The IR transmission spectrum of undoped Mg_2Si is shown in Fig. 3.3 (right). The two arrows in the IR transmission spectrum indicate energies of creation and annihilation of a phonon associated with the gap excitation. The sloping feature of the transmittance indicates that the band gap is indirect with an energy of 0.65 eV, confirming the results of the *GW* modified DFT calculations discussed above. The phonon energy is estimated to be 0.06 eV. This can be compared to the maximum IR absorption frequency of a lattice vibration of Mg_2Si of 0.04 eV.

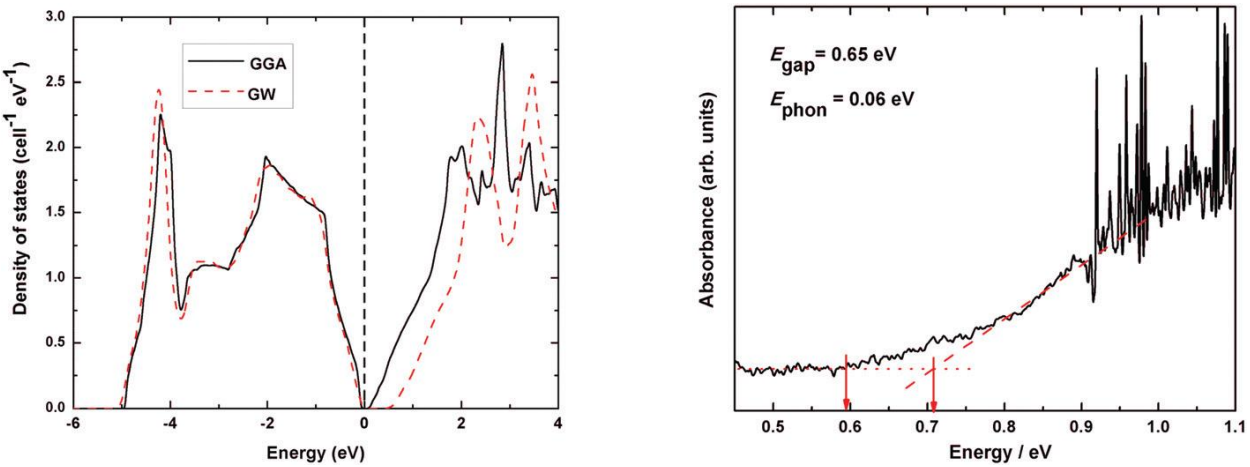

Fig. 3.3 Density of states (left) and absorbance spectrum (right) of Mg_2Si.

The densities of states of Sb- and Bi-doped Mg_2Si are compared in Fig. 3.4. The composition is $Mg_{64}Si_{31}P_n$ (P_n = Sb, Bi), which corresponds to $Mg_2Si_{0.97}P_{n0.03}$, *i.e.* a 3% doping level of P_n on the Si site. The total densities of states for both systems are very similar to that of pure Mg_2Si shown in Fig. 3.3. The most significant observation is that, even with a localized defect atom (*i.e.* Sb or Bi), the density of states projected to the P_n states shows that the electrons from the dopant are spread over the entire crystal and are not localized in the region of the band gap. This observation confirms that one can apply the rigid band approximation for calculating the Seebeck coefficient. The relatively sharp peaks below −5 eV can be attributed to the interaction between the P_n atoms and the surrounding Mg and Si atoms. At a 3% dopant

concentration, the excess electron occupied the conduction band orbitals up to 0.5 eV above the valence band edge.

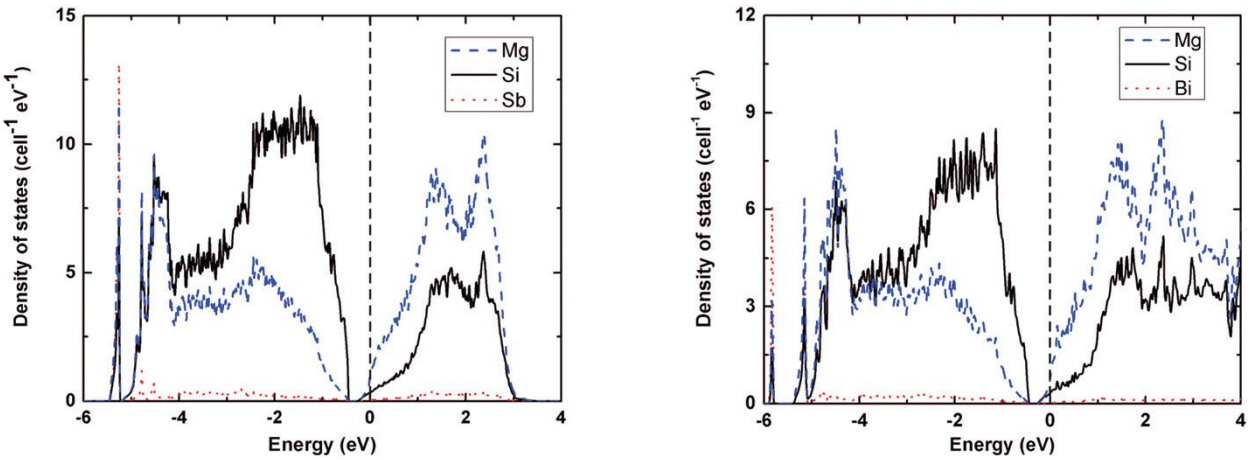

Fig. 3.4 Density of states of $Mg_{64}Si_{31}Sb$ (left) and $Mg_{64}Si_{31}Bi$ (right).

The thermopower can be estimated from the ground state band structure using the rigid band model by simply shifting the energy of the Fermi level according to the number of electrons donated by the dopants. Calculations on pure Mg_2Si and at several doping concentrations of Sb have been performed (Fig. 3.5). The negative Seebeck coefficient of doped Mg_2Si is simply a consequence of *n*-doping. The absolute magnitudes of the Seebeck coefficients were found to decrease with dopant concentration. At a given dopant concentration, the absolute value increases smoothly with increasing temperature, *e.g.* for the $Mg_2Si_{0.98}Sb_{0.02}$ model, from -60 μVK^{-1} at 300 K to -150 μVK^{-1} at 800 K, and for the $Mg_2Si_{0.99}Sb_{0.01}$ model from -80 μVK^{-1} at 300 K to -170 μVK^{-1} at 800 K. The large Seebeck coefficient at low dopant concentration is due to the very sharp slope at the bottom of the conduction band, indicating that the electron bands are fairly flat. At higher dopant concentrations the dopant electrons must populate the more free-electron-like parabolic conduction bands, and therefore the Seebeck coefficient is reduced.

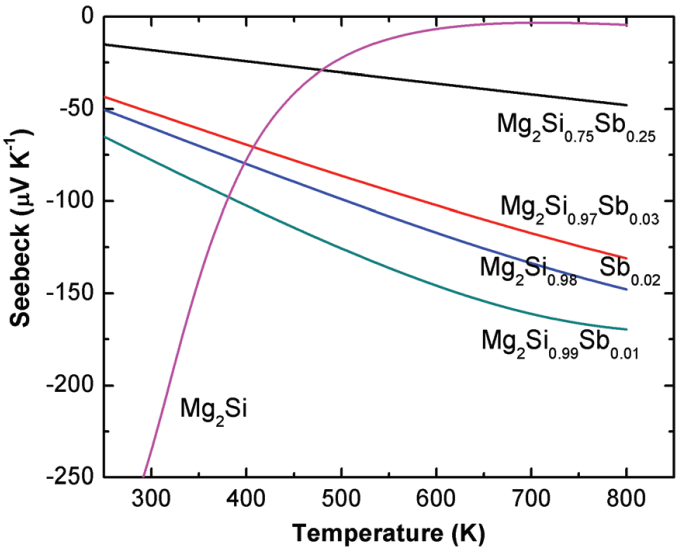

Fig. 3.5 Calculated Seebeck coefficients of $Mg_2Si_{1-x}Sb_x$.

3.3.3 Physical properties

The reflectivity spectra and the optical conductivity are shown in Fig. 3.6. As an undoped, narrow gap semiconductor, Mg_2Si has lower reflectivity than the doped samples. The extrapolated zero frequency reflectivities for Mg_2Si, Sb-doped and Bi-doped samples are 0.5, 0.6 and 0.7, respectively. The *dc* conductivity obtained from K-K analysis is 166 $\Omega^{-1}cm^{-1}$ for the Sb and 177 $\Omega^{-1}cm^{-1}$ for the Bi case. These values are significantly lower than the ones obtained from four-probe measurements on the hot-pressed pellets (discussed below), most likely because of IR's limited penetration depth and spot size (about 400 μm^2), and are thus influenced more by the surface character.

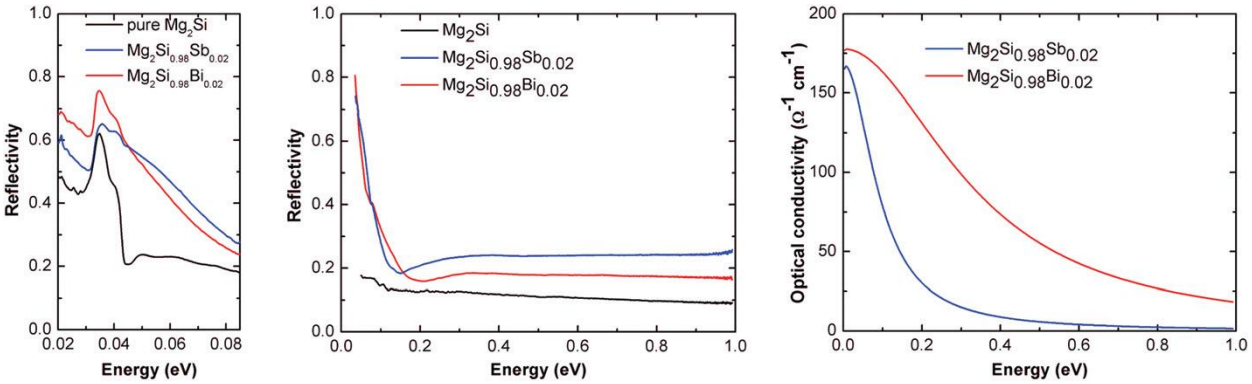

Fig. 3.6 Reflectivity spectra (left and center) and optical conductivity (right) of $Mg_2Si_{0.98}Sb_{0.02}$ and $Mg_2Si_{0.98}Bi_{0.02}$.

A unique feature in the reflectivity curves of the doped samples is the occurrence of a "dip" in their IR spectra. The minimum in the reflectivity is characteristic of a doped semiconductor and is known as the plasma reflection edge. According to the Drude model, the energy at the minimum corresponds to the plasma frequency, ω_P, which is related to the carrier concentration, n, and the electron effective, m^*, *via* $\omega_P^2 = ne^2\varepsilon^{-1}m^{*-1}$, where ε is the dielectric constant of the material. [36] The observed plasma energies for Sb- and Bi-doped Mg_2Si are 0.15 eV and 0.21 eV, respectively. The electron effective mass of in Bi-doped Mg_2Si may be twice as high, *e.g.* determined to be $1.1m_e$ [12] *vs.* $0.47m_e$, [37] where m_e = electron mass. Thus, the carrier concentration in the Bi-doped Mg_2Si is estimated to be roughly four times as high as that of the Sb-doped sample.

The high quality of the IR measurement is reflected in the observation of reflectivity at the longitudinal-optical (LO) and transverse-optical (TO) phonon absorption branch in the far-IR region. The peak at 0.036 eV with a shoulder on the high energy side is caused by the *Reststrahlen* band due to the zone center LO and TO phonon absorptions. The result is in good agreement with a previous measurement on a single crystal. [38] From the envelope of the band, the TO-LO splitting can be estimated. [39] For undoped Mg_2Si, the LO-TO splitting is 71.4 meV

or 58 cm^{-1}. This is comparable to the previously measured value on a single crystal of 60 cm^{-1}. The *Reststrahlen* bands of Bi- and Sb-doped Mg_2Si samples are somewhat broader, giving splitting energies of 63 cm^{-1} and 67 cm^{-1}, respectively. Furthermore, the frequency of the TO vibration in $Mg_2Si_{0.98}Bi_{0.02}$ is 8 meV (6.6 cm^{-1}) lower than that of the pure sample.

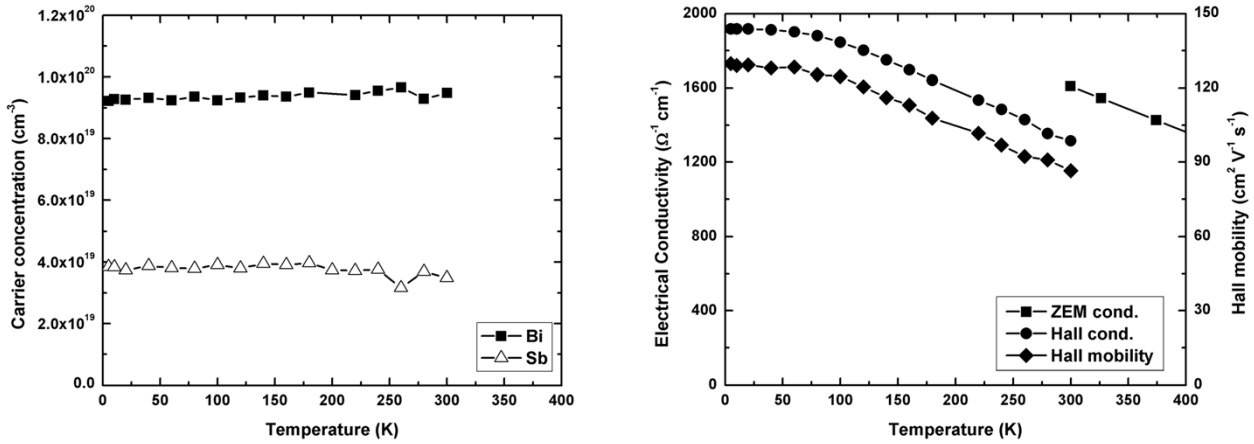

Fig. 3.7 Carrier concentration (left) and Hall mobility and electrical conductivity (right) of $Mg_2Si_{0.98}Sb_{0.02}$ (white symbols) and $Mg_2Si_{0.98}Bi_{0.02}$ (black symbols).

The carrier concentration, mobility and electrical conductivity are depicted in Fig. 3.7 for both $Mg_2Si_{0.98}Sb_{0.02}$ and $Mg_2Si_{0.98}Bi_{0.02}$. Between 5 K and 300 K, no noticeable temperature dependence of the Hall coefficient, R_H, (and thus the carrier concentration) was detected, *e.g.* for Bi-doped Mg_2Si, R_H ranged from −0.0677 cm^3C^{-1} at 5 K to −0.0658 cm^3C^{-1} at 300 K, the negative sign being indicative of the expected *n*-type character of the carriers. The carrier concentrations of $n = 3.5 \times 10^{19}$ electrons per cm^3 and 9.5×10^{19} electrons per cm^3 for Sb and Bi-doped Mg_2Si, respectively, are in qualitative agreement with our TEM and electronic structure studies: replacing Si with P_n = Sb or Bi increases the valence electron count, but not all P_n atoms replaced Si, as we found Mg_3P_{n2} in the grain boundaries. Nominally, replacing 2% of Si with P_n would result in an extrinsic charge carrier concentration of $n = 3.1 \times 10^{20}$ cm^{-3}, considering that each P_n atom comprises one more valence electron than Si. Furthermore, this is in good

agreement with the estimated ratio of the carrier concentration from the reflectance spectroscopy experiments, where the Bi sample appeared to have a much higher carrier concentration.

Similarly, Nolas *et al*. determined $n = 1.5 \times 10^{20}$ cm^{-3} for the same Sb content, [37] and Tani *et al*. found $n = 1.5 \times 10^{20}$ cm^{-3} for the same Sb [40] and $n = 1.1 \times 10^{20}$ cm^{-3} for the same Bi concentration, [13] while Bux *et al*. [12] were able to use all extra electrons from Bi after ball-milling, followed by spark-plasma-sintering, resulting in a value of $n = 3.2 \times 10^{20}$ cm^{-3} (Tables 3.1 and 3.2).

Table 3.1 Thermoelectric properties of $Mg_2Si_{0.98}Sb_{0.02}$ at 300 K-320 K (first value) and at ≈800 K (second value).

Property	Our work	Nolas *et al.*[37]	Tani *et al.*[40]	Ioannou *et al.*[42]
σ (Ω^{-1}cm^{-1})	493-217	1000	1980-650	2850-1200
-α (μVK^{-1})	116-229	75	90-195	62-130
κ (Wm^{-1}K^{-1})		6.7	6.58-3.72	8.53-N/A
n (cm^{-3})	3.5×10^{19}	1.2×10^{20}	1.5×10^{20}	2.5×10^{20}
μ (cm^{2}V^{-1}s^{-1})		50	83	72
ZT		0.03	0.006-0.51	0.05-0.32

Table 3.2 Thermoelectric properties of $Mg_2Si_{0.98}Bi_{0.02}$ at 300 K-320 K (first value) and at ≈800 K (second value).

Property	Our work	Bux *et al.*[12]	Tani *et al.*[13]	Choi *et al.*[14]
σ ($\Omega^{-1}cm^{-1}$)	1610-640	3125-1520	1150-540	1985-850
$-\alpha$ (μVK^{-1})	94-198	72-130	100-240	88-190
κ ($Wm^{-1}K^{-1}$)	7.26-2.95[a]	6.51-4.18	6.35-3.58	6.15-4.05
n (cm^{-3})	9.5×10^{19}	3.2×10^{20}	1.1×10^{20}	
μ ($cm^2V^{-1}s^{-1}$)	87	58	64	
ZT	0.08-0.56[a]	0.05-0.46	0.05-0.78	0.05-0.64

[a] Properties at 660 K.

As expected, the mobility, μ, decreases with increasing temperature, and therefore the electrical conductivity, σ, decreases in parallel. Around 300 K, we obtained μ = 87 $cm^2V^{-1}s^{-1}$ and thus σ = 1315 $\Omega^{-1}cm^{-1}$. The slope of the electrical conductivity determined from the Hall data well matches that obtained from the same pellet using the ULVAC ZEM-3, and the absolute value at 300 K of σ = 1610 $\Omega^{-1}cm^{-1}$ differs by 22%. Tani and Bux found lower values for the mobility, *e.g.* at 300 K in the case of Bi doping, μ = 64 $cm^2V^{-1}s^{-1}$ (Tani) and μ = 58 $cm^2V^{-1}s^{-1}$ (Bux). The mobilities of the Sb-doped samples are of the same order of magnitude, ranging from μ = 50 $cm^2V^{-1}s^{-1}$ (Nolas) [37] to μ = 83 $cm^2V^{-1}s^{-1}$ (Tani). [40]

Fig. 3.8 compares the electrical conductivities (left) and Seebeck coefficients (right) of $Mg_2Si_{0.98}Sb_{0.02}$ and $Mg_2Si_{0.98}Bi_{0.02}$ from 300 K to 840 K, measured using the ZEM-3. The electrical conductivity of $Mg_2Si_{0.98}Bi_{0.02}$ continues to decrease throughout this temperature range, as does the σ of $Mg_2Si_{0.98}Sb_{0.02}$. The latter is significantly smaller (σ = 490 $\Omega^{-1}cm^{-1}$ at 300 K), mostly because of the smaller carrier concentration by a factor of roughly 3. This difference causes, in turn, the absolute Seebeck coefficient of the Sb-doped material to be larger, *e.g.* S = −116 μVK^{-1} *vs.* −94 μVK^{-1} at 300 K. The calculated Seebeck coefficient was smaller, because the calculation assumed that all extra electrons from Sb were available as charge carriers. That the carrier concentration is the main cause for these differences is supported by the similarities of carrier concentration, electrical conductivity, and Seebeck coefficient of $Mg_2Si_{0.98}Bi_{0.02}$ with Tani's sample, [13] while Bux's sample has a higher carrier concentration and electrical conductivity, and a lower Seebeck coefficient. [12]

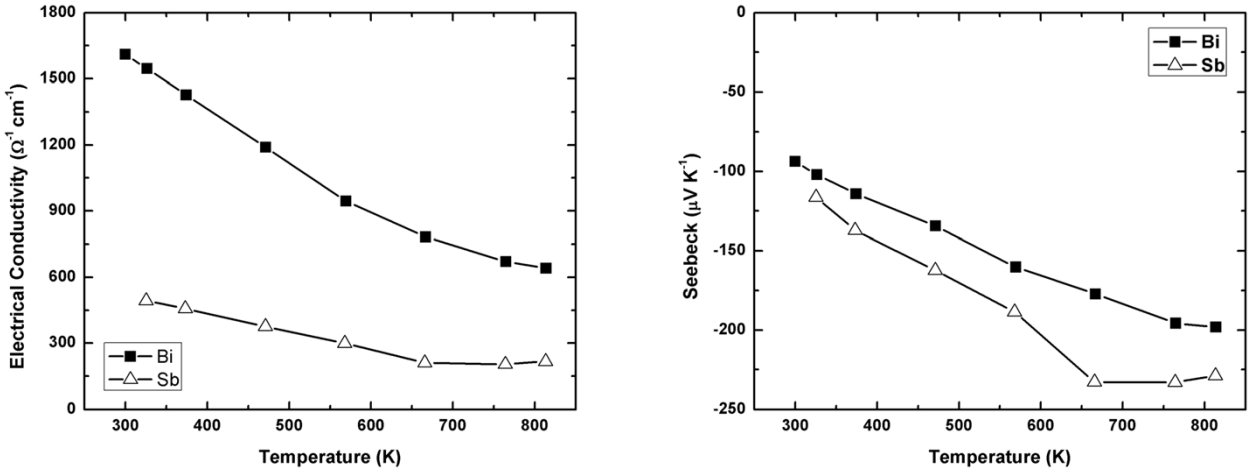

Fig. 3.8 Electrical conductivity (left) and Seebeck coefficient (right) of $Mg_2Si_{0.98}Sb_{0.02}$ (white symbols) and $Mg_2Si_{0.98}Bi_{0.02}$ (black symbols).

From the Seebeck coefficient, one can derive the electron effective mass, if the carrier concentration is known and assuming energy independent scattering and parabolic bands, *via* $S = 8/3\pi k_B^2 e^{-1} h^{-2} m^* T(1/3\pi n^{-1})^{2/3}$. [41] At 300 K, this results in $m^* = 0.62 m_e$ for the Sb case and m^*

= 1.06m_e for the Bi case, in qualitative agreement with Nolas' 0.50m_e for Sb and Bux's 1.1m_e for Bi. Relating this to the plasma frequencies discussed above with our experimental values for the carrier concentration, we calculate $m^*(\mathrm{Bi})/m^*(\mathrm{Sb}) = n(\mathrm{Bi})\omega_P(\mathrm{Bi})^{-2}/\{n(\mathrm{Bi})\omega_P(\mathrm{Bi})^{-2}\} = 1.38$, compared to 1.06/0.62 = 1.71 from the Seebeck data.

Finally, the thermal conductivity, κ, of a second $Mg_2Si_{0.98}Bi_{0.02}$ sample was determined up to 660 K, yielding decreasing values from 7.3 W $m^{-1}K^{-1}$ at 300 K to 3.0 $Wm^{-1}K^{-1}$ at 660 K (Fig. 3.9, left). These numbers, being significantly lower than those of undoped Mg_2Si, agree well with those of other authors working on this system (Table 3.2). Assuming these two Bi-doped materials have the same carrier concentration, as they were prepared the same way, this results in comparable (estimated) figure-of-merit values, *e.g.* ZT = 0.56 at 660 K (Fig. 3.9, right), with the Bi sample from Tani (0.54 at 660 K), [13] which exhibited roughly the same carrier concentration. On the other hand, the Bi-doped material from Bux *et al.*, with its higher carrier concentration, exhibited smaller ZT values, *e.g.* 0.38 at 660 K. [12]

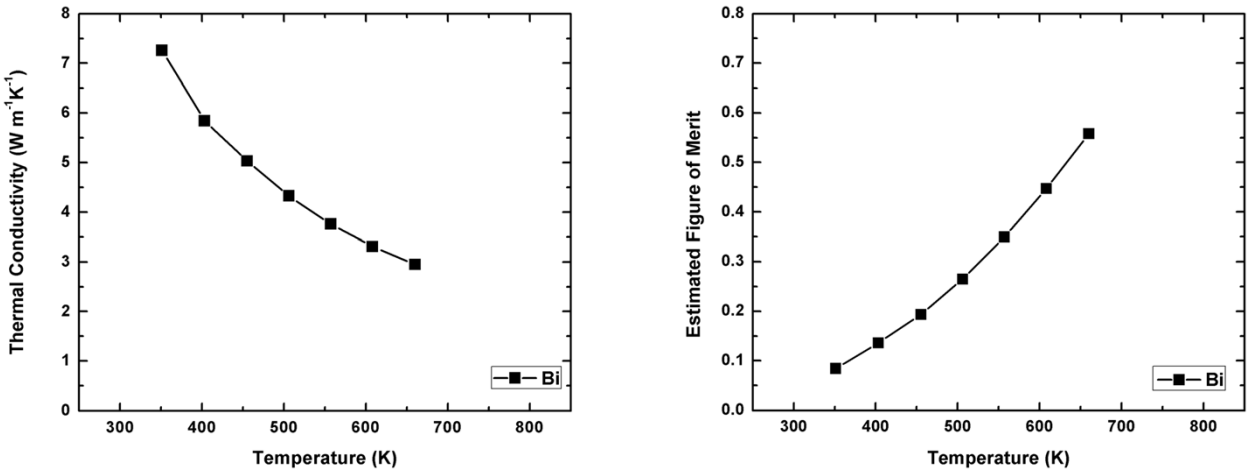

Fig. 3.9 Thermal conductivity (left) and estimated figure of merit (right) of $Mg_2Si_{0.98}Bi_{0.02}$.

3.4 Conclusions

We have prepared Sb- and Bi-doped Mg_2Si samples *via* annealing, followed by hot-pressing. Part of the dopants replace Si, as shown via STEM-HAADF, while the rest form Mg_3Sb_2 and Mg_3Bi_2, found between the grains of doped Mg_2Si particles.

DFT calculations were performed both on pure and doped Mg_2Si models, resulting in the correct band gap size after *GW* correction, in accordance with the results from absorbance spectroscopy. These calculations also showed the validity of the rigid band approximation for calculating the transport properties in dependence of the electron concentration.

As the addition of Sb and Bi only partly led to Si substitution, the experimentally determined carrier concentration was lower than originally expected. These findings support those of Tani *et al*., who used a different synthesis and consolidation method (spark-plasma-sintering *vs*. hot-pressing), whereas Bux *et al*. obtained higher carrier concentration at the same nominal Bi concentration after incremental ball-milling. Therefore, Bux *et al*. found larger electrical conductivity and a smaller Seebeck coefficient, yet ultimately smaller *ZT* values at the 2% doping level.

In conclusion, the presence of Sb and Bi between the grains of doped Mg_2Si may well be advantageous with respect to the thermoelectric performance.

Acknowledgements

This work was sponsored by AUTO21 (Network Centres of Excellence) and General Motors. The use of U2A beamline was supported by COMPRES under NSF Cooperative Agreement EAR 11-57758 and CDAC (DE-FC03-03N00144). The National Synchrotron Light Source, Brookhaven National Laboratory, is supported by the U.S. Department of Energy, Office

of Science, Office of Basic Energy Sciences under Contract No. DE-AC02- 98CH10886. Synchrotron work at the Canadian Light Source was made possible by support from NSERC, NRC, CIHR, and the University of Saskatchewan.

References

[1] J. Yang and F. R. Stabler, *J. Electron. Mater*., 2009, 38, 1245–1251.

[2] D. M. Rowe, Thermoelectrics Handbook: Macro to Nano, CRC Press, Taylor & Francis Group, Boca Raton, FL, USA, 2006.

[3] L. E. Bell, *Science*, 2008, 321, 1457–1461.

[4] M. G. Kanatzidis, *Chem. Mater*., 2010, 22, 648–659.

[5] Y. Pei, A. LaLonde, S. Iwanaga and G. J. Snyder, *Energy Environ. Sci*., 2011, 4, 2085–2089.

[6] K. Biswas, J. He, I. D. Blum, C.-I. Wu, T. P. Hogan, D. N. Seidman, V. P. Dravid and M. G. Kanatzidis, *Nature*, 2012, 489, 414–418.

[7] Q. Guo, M. Chan, B. A. Kuropatwa and H. Kleinke, *Chem. Mater*., 2013, 25, 4097–4104.

[8] B. Wölfing, C. Kloc, J. Teubner and E. Bucher, *Phys. Rev. Lett*., 2001, 86, 4350–4353.

[9] E. S. Toberer, S. R. Brown, T. Ikeda, S. M. Kauzlarich and G. J. Snyder, *Appl. Phys. Lett*., 2008, 93, 062110.

[10] X. Shi, J. Yang, J. R. Salvador, M. Chi, J. Y. Cho, H. Wang, S. Bai, J. Yang, W. Zhang and L. Chen, *J. Am. Chem. Soc*., 2011, 133, 7837–7846.

[11] E. N. Nikitin, V. G. Bazanov and V. I. Tarasov, *Sov. Phys. Solid State*, 1961, 3, 2648–2652.

[12] S. K. Bux, M. T. Yeung, E. S. Toberer, G. J. Snyder, R. B. Kaner and J.-P. Fleurial, *J. Mater. Chem*., 2011, 21, 12259–12266.

[13] J.-i. Tani and H. Kido, *Physica B*, 2005, 364, 218–224.

[14] S.-M. Choi, K.-H. Kim, I.-H. Kim, S.-U. Kim and W.-S. Seo, *Curr. Appl. Phys*., 2011, 11, S388–S391.

[15] W. Liu, X. Tan, K. Yin, H. Liu, X. Tang, J. Shi, Q. Zhang and C. Uher, *Phys. Rev. Lett*., 2012, 108, 166601.

[16] V. K. Zaitsev, M. I. Fedorov, E. A. Gurieva, I. S. Eremin, P. P. Konstantinov, A. Y. Samunin and M. V. Vedernikov, *Phys. Rev. B: Condens. Matter*, 2006, 74, 045207.

[17] X. Zhang, H. Liu, Q. Lu, J. Zhang and F. Zhang, *Appl. Phys. Lett*., 2013, 103, 063901.

[18] E. J. Kirkland, Image Simulation in Transmission Electron Microscopy, Cornell University, Ithaca, NY, USA, 2006, pp. 1–14.

[19] J. P. Perdew, K. Burke and M. Ernzerhof, *Phys. Rev. Lett*., 1996, 77, 3865–3868.

[20] G. Kresse and J. Hafner, *Phys. Rev. B: Condens. Matter*, 1993, 47, 558–561.

[21] G. Kresse and J. Hafner, *Phys. Rev. B: Condens. Matter*, 1994, 49, 14251–14269.

[22] G. Kresse and J. Furthmüller, *Comput. Mater. Sci*., 1996, 6, 15–50.

[23] G. Kresse and J. Furthmüller, *Phys. Rev. B: Condens. Matter*, 1996, 54, 11169–11186.

[24] L. Hedin, *Phys. Rev*., 1965, 139, A796–A823.

[25] P. García-González and R. W. Godby, *Phys. Rev. B: Condens. Matter*, 2001, 63, 075112.

[26] P. E. Blöchl, *Phys. Rev. B: Condens. Matter*, 1994, 50, 17953– 17979.

[27] G. Kresse, *Phys. Rev. B: Condens. Matter*, 1999, 59, 1758– 1775.

[28] M. Chen, in First-principles Modeling of Thermoelectric Materials, PhD thesis, Theoretical Solid State Chemistry, Vienna University of Technology, Vienna, Austria, 2012.

[29] G. K. H. Madsen and D. J. Singh, *Comput. Phys. Commun*., 2006, 175, 67–71.

[30] A. B. Kuzmenko, *Rev. Sci. Instrum*., 2005, 76, 083108.

[31] A. Stella, A. D. Brothers, R. H. Hopkins and D. W. Lynch, *Phys. Status Solidi*, 1967, 23, 697–702.

[32] P. Boulet and M.-C. Record, *J. Chem. Phys*., 2011, 135, 234702.

[33] F. Tran and P. Blaha, *Phys. Rev. Lett*., 2009, 102, 226401.

[34] J. J. Pulikkotil, D. J. Singh, S. Auluck, M. Saravanan, D. K. Misra, A. Dhar and R. C. Budhani, *Phys. Rev. B: Condens. Matter*, 2012, 86, 155204.

[35] B. Arnaud and M. Alouani, *Phys. Rev. B: Condens. Matter*, 2001, 64, 033202.

[36] M. Fox, Optical Properties of Solids, Oxford University Press, New York City, NY, USA, 2010.

[37] G. S. Nolas, D. Wang and M. Beekman, *Phys. Rev. B: Condens. Matter*, 2007, 76, 235204.

[38] D. McWilliam and D. W. Lynch, *Phys. Rev*., 1963, 130, 2248–2252.

[39] P. Y. Yu and M. Cardona, Fundamentals of Semiconductors: Physics and Materials Properties, Springer, New York, NY, USA, 1998.

[40] J.-i. Tani and H. Kido, *Intermetallics*, 2007, 15, 1202– 1207.

[41] M. Cutler, J. F. Leavy and R. L. Fitzpatrick, *Phys. Rev*., 1964, 133, A1143–A1152.

[42] M. Ioannou, G. Polymeris, E. Hatzikraniotis, A. U. Khan, K. M. Paraskevopoulos and T. Kyratsi, *J. Electron. Mater*., 2013, 42, 1827–1834.

CHAPTER 4

LOCAL STRUCTURE AND THERMOELECTRIC PROPERTIES OF $Mg_2Si_{0.977-x}Ge_xBi_{0.023}$ ($0.1 \leq x \leq 0.4$)

In Chapter 3, we demonstrate that enhancement of the thermoelectric performance can be achieved by adding single dopant Sb or Bi to the Mg_2Si with a best *ZT* of about 0.6 at 700 K for $Mg_2Si_{0.98}Bi_{0.02}$. A recent report shows Sb and Bi are promising dopants in the $Mg_2Si_{1-x}(Ge,Sn)_x$ system reaching *ZT* values of 1.2 and 1.4 at 823 K respectively [21]. More recently, Kim *et al.* published a study of the $Mg_2Si_{0.7}Ge_{0.3}$ system with different Bi concentrations. It was shown that through doping with heavier Bi the thermal conductivity was lowered to 2.2 $Wm^{-1}K^{-1}$ in $Mg_2Si_{0.7}Ge_{0.3}Bi_{0.02}$ at 823 K; consequently, a maximum *ZT* of 0.79 was obtained. [22].

For this chapter, we investigated the thermoelectric properties of multiple-doped Mg_2Si. For this purpose, we replaced Si by Ge in Bi-doped Mg_2Si to study the effects on the local structure, electrical transport and thermoelectric properties at different Ge concentrations. To understand the role of Ge, the concentration of Bi was fixed at the optimum *ZT* value of $Mg_2Si_{0.977-x}Ge_xBi_{0.023}$ ($0.1 \leq x \leq 0.4$). In this way, the effects of Ge contents on the band structure and thermoelectric properties could be systematically studied by experimental and theoretical methods. Once again, *dc* conductivities of the doped samples were extracted from the analysis of infrared reflectivity spectra employing the Drude free-electron model. As shown in the previous chapter, we found the *dc* conductivity determined by infrared measurements was lower than that obtained from *in-situ* four probe measurements on the bulk sample. We attributed the discrepancy to the consequence of non-uniform distribution of the dopants in the samples. In addition, we extracted the electron effective masses of the samples. To augment the interpretation of the experimental results, electronic structures of the doped samples were computed using density functional theory (DFT). The slopes of electronic densities of states

(DOS) at the Fermi level of the Ge- and Bi-doped Mg_2Si samples were found to be similar. The results indicate that both Ge- and Bi-doped samples should have had comparable Seebeck coefficients. Finally, experimentally it was found that $Mg_2Si_{0.677}Ge_{0.3}Bi_{0.023}$ at 300 K has a thermal conductivity of 2.7 $Wm^{-1}K^{-1}$, which is slightly lower than that of the pure Mg_2Si: 7 $Wm^{-1}K^{-1}$. A performance figure of merit *ZT* of 0.65 was achieved at 700 K in the $Mg_2Si_{0.677}Ge_{0.3}Bi_{0.023}$ sample. This is about 8% higher than the single-doped sample at 700 K.

The results of this study have been published in

N. Farahi, S. Prabhudev, G. A. Botton, J. Zhao, J. S. Tse, Z. Liu, J. R. Salvador, and H. Kleinke, "Local structure and thermoelectric properties of $Mg_2Si_{0.977-x}Ge_xBi_{0.023}$ ($0.1 \leq x \leq 0.4$)," *Journal of Alloys and Compounds*, vol. 644, pp. 249-255, 2015.

The authors' contributions are as follow:

- N. Farahi and H. Kleinke synthesized the samples and performed the thermoelectric property measurements.
- J. Zhao and J. S. Tse collected infrared transmission and reflectivity spectrum, performed the analysis to extract the dielectric function and transport properties, and calculated the electronic structures.
- S. Prabhudev and G. A. Botton performed the STEM measurement.
- J. R. Salvador performed the Hall measurement.
- Z. Liu assisted in performing infrared experiments at BNL.
- All authors contributed to the writing and editing of the manuscript.

Abstract

We investigated the effect of germanium substitution for silicon in bismuth doped Mg_2Si. This alloying reduces the thermal conductivity from above 7 $Wm^{-1}K^{-1}$ to 2.7 $Wm^{-1}K^{-1}$ at around 300 K in part due to the added mass contrast. High resolution transmission electron microscopy (HRTEM) revealed the presence of Ge-rich domains within the $Mg_2(Si,Ge,Bi)$ particles, contributing to decreasing thermal conductivity with increasing Ge content up to 0.3 Ge per formula unit. The electrical conductivity also decreases with Ge alloying because of the increasing amount of scattering centers, while the Seebeck coefficient increased only very slightly. In total, the positive effect of Ge substitution on the thermoelectric properties of Bi doped Mg_2Si resulted in a figure of merit of 0.7 at 773 K for $Mg_2Si_{0.677}Ge_{0.3}Bi_{0.023}$ sample. The optimum amount of Bi seems to be 0.023 per formula unit (0.77 at%), since lower Bi content resulted in electrical conductivity that is too low, and higher Bi content generated the Mg_3Bi_2 intermetallic phase.

4.1 Introduction

Undoubtedly, energy is one of the biggest challenges that mankind faces in this era. With simultaneous reduction of fossil fuel resources and increase in population around the world, reliance on consuming fossil fuels would not be feasible without proper energy management. Different strategies are being pursued to reduce the dependency on fossil fuels, through the development of a variety of alternative and renewable energy sources. To convert waste heat into useful energy, thermoelectric (TE) materials are inimitable due to their unique ability to convert heat into electricity. As one of the emerging technologies, certain obstacles such as efficiency, profusion and toxicity of these materials need to be addressed before establishing them for industrial applications.

The criteria for evaluating the efficiency of a thermoelectric material is its figure of merit *ZT*, which is expressed as $ZT = TS^2\sigma\kappa^{-1}$. S, σ, κ and *T* represent the Seebeck coefficient, electrical conductivity, thermal conductivity and absolute temperature, respectively. Many of the current state-of-the-art thermoelectric materials are based on toxic elements such as lead [1,2] and thallium [3], or on rare elements such as ytterbium [4] or tellurium [5]. To be applicable to large scale industrial production, new, highly efficient, TE materials should be comprised of low cost, non-toxic and abundant elements. To that end, magnesium silicide has attracted enormous attention as a potential, next generation, high efficiency TE material, especially in medium temperature range applications such as in the automotive waste heat recovery [6].

One of the main features of materials with high *ZT* is their low thermal conductivity, which can be achieved through phonon engineering [7], resonant bonding [8], lone pair electrons [9], solid solutions [10], and by introducing more grain boundary interfaces via nano-structuring [11-13]. Magnesium silicide shows great compositional flexibility as evidenced by its formation of solid solutions with tin [14] or germanium [15-18] on the silicon position. Introducing these heavy elements reduced the room temperature thermal conductivity of Mg_2Si from around 10 $Wm^{-1}K^{-1}$ [19] to approximately 3 Wm^{-1} K^{-1} [18]. Although the powder patterns of compounds with tin or germanium appear to be pure phases within the limit of the technique, microstructural investigations performed by scanning electron microscopy reveal the existence of Ge/Sn rich regions. This indicates that the larger elements will not completely substitute for Si, or that reaching equilibrium compositions require prohibitively long annealing times due to sluggish solid state diffusion processes.

To enhance the figure of merit, the electrical conductivity needs to be increased simultaneously with κ reduction, which may be achieved through doping. So far, Sb, Fe, In, Al

and Au have been shown to behaved as *n*-type dopants for $Mg_2Si_{0.6}Ge_{0.4}$, while Cu, Ag, B and Ga were used as *p*-type dopants with limited success [18,20]. Sb and Bi have proven to be promising dopants in the $Mg_2Si_{1-x}(Ge,Sn)_x$ system by enhancing *ZT* to 1.2 and 1.4 at 823 K, respectively [21]. To better understand the role of Ge, the doping level of bismuth was fixed in the present study at its optimum value, and the effects of the different Ge content on the band structure, thermoelectric properties as well as the micro- and nano-structure of $Mg_2Si_{0.977-x}Ge_xBi_{0.023}$ ($0.1 \leq x \leq 0.4$) were investigated. During our investigations, Kim *et al.* published a study of the $Mg_2Si_{0.7}Ge_{0.3}$ system with different Bi additions [22].

4.2 Experiment

Bismuth-doped $Mg_2Si_{1-x}Ge_x$ samples were synthesized starting from the elements in a tantalum crucible according to the nominal stoichiometric ratio in an argon-filled glove box. We used Mg chips (99.98%, Sigma Aldrich, 4-30 mesh), Si powder (99.9%, Alfa Aesar, -100 mesh), Ge pieces (99.9999+%, Alfa Aesar, ≤2 cm) and Bi granules (99.99%, Sigma Aldrich). The tantalum crucibles were sealed under argon with an arc melter, and then placed into silica tubes. After sealing under vacuum, the tubes were heated in a resistance furnace at 923 K for a week. Then the furnaces were switched off to allow for fast cooling down to room temperature. To obtain pure products, the samples were ground and then annealed at 1173 K for another week and thereafter cooled down by turning off the furnace. The purity of the synthesized samples was examined by using an Inel powder X-ray diffractometer with Cu $K\alpha_1$ radiation and a position sensitive detector (available as Fig. B.1 in the Supporting Information). All samples were pure, except for traces of MgO as also observed by others [21,23,24]. In the end, we settled on 0.023 Bi per formula unit, because using 0.03 or more Bi resulted in the formation of Mg_3Bi_2, as found in the X-ray powder diffraction patterns. Lattice parameter refinements yielded a smooth

increase with increasing Ge content as expected based on the Si/Ge size ratio, resulting in a = 6.3670(2) Å (0.1 Ge), 6.37011(9) Å (0.2 Ge), 6.37363(4) Å (0.3 Ge), and 6.37648(6) Å (0.4 Ge).

To be able to perform the physical property measurements on fully dense specimens, the annealed samples were ground and then hot pressed for two hours at 973 K under 56 MPa in an argon atmosphere using an Oxy-Gon hot press. The pressure was released after sintering to reduce strain and stress on the pellets during cooling. The hot-pressed billets were 12.7 mm in diameter and 3 mm thick. These preparation methods are different from those used by Kim, who used 773 K for annealing for six hours, followed by hot-pressing for two hours at 1073 K under 70 MPa [22], *i.e*. using a higher temperature and pressure in the last step.

To determine the thermal conductivity (κ) of the pressed samples, thermal diffusivity (α) measurements were carried out under flowing Ar by using Anter Flashline FL3000 thermal properties analyzer between 300 K and 800 K. The obtained thermal diffusivity values were then multiplied by the density (d) of the pellets, as measured via the Archimedes method, and the specific heat (C_p) of the compounds, as calculated from the Dulong–Petit approximation, to yield $\kappa = \alpha\ d\ C_p$. In order to verify the suitability of the Dulong–Petit approximation, specific heat measurements were performed on the samples with high Ge content (Fig. B.2) using a Netzsch 404 C differential scanning calorimeter, and the measured values were in good agreement with our approximation.

To obtain the electrical conductivity (σ) and Seebeck coefficient (S) of the samples, the above-mentioned pellets were cut into rectangular bars with the dimensions of approximately 12 × 2 × 2 mm. The measurements were performed under a static helium atmosphere between 300 K and 800 K by using an ULVAC-RIKO ZEM-3 system.

The reflectance spectra were measured at the National Synchrotron Radiation Facility, at Brookhaven National Laboratory as described before [25]. The reflectance was converted to absolute reflectivity by normalization to the reflectance of a diamond substrate measured under identical experimental conditions. Optical conductivity was obtained by Kramers-Kronig (K-K) analysis of data collected from normal incidence reflectivity measurements, then fitted using a variational K-K constrained dielectric function, as implemented in the REFFIT code [26]. The dc conductivity is obtained from a Drude model by extrapolation to zero frequency [27].

To examine the homogeneity of the samples at the micron level, energy dispersive X-ray (EDX) analysis was performed on parts of selected pressed pellets using a Zeiss ULTRA electron microscope associated with an EDX device, EDAX Pegasus 1200 with an acceleration voltage of 25 kV. For this analysis, the pellets were broken into smaller pieces, and the fracture surfaces were then analyzed without further treatments. The EDX results verified the existence of Bi in the samples with some Ge-rich regions. The analysis of different crystals resulted in good agreement between $Si/Si_{nominal}$ and $Ge/Ge_{nominal}$ ratios of 92-100% and 85-93%, respectively.

Atomic-scale structural characterization was performed on pieces of the hot-pressed pellets using aberration corrected scanning transmission electron microscopy (STEM) operating in a high-angle annular dark-field imaging (HAADF) mode. Conventional TEM is primarily a broad-beam based technique, wherein upon interacting with the specimen, all the scattered electrons, are collected over a large illumination area on the specimen. In these conditions, images are strongly dependent on the thickness of the sample and objective lens-focus conditions. As opposed to this, STEM-HAADF employs a raster scanning electron probe to collect electrons that are elastically scattered at high angles. Upon converging the electron beam

into a sub-angstrom probe, an atomic-scale image of materials can be obtained. The high angle annular dark field (HAADF) detector, as the name suggests, is a detector designed in an annular geometry and placed in a diffraction plane below the sample so as to collect electrons emerging from the specimen at high scattering angles. Since the intensity of these high-angle scattered electrons is directly proportional to the atomic number of scattering atoms under the electron beam, the resulting STEM-HAADF image provides an atomic number ‘‘*Z*’’-contrast image with intensities proportional to $Z^{1.6}$. For instance, in the case of the Mg2Si sample alloyed with Ge (Z = 32) and Bi (Z = 83), the atomic columns containing the Ge and Bi atoms are expected to appear significantly brighter compared to the bulk of the matrix crystal.

Atomically-resolved STEM-HAADF images were acquired using a FEI-Titan cubed TEM, equipped with two hexapole-design spherical aberration correctors of the probe and image forming lenses. The microscope was operated in STEM mode at an accelerating voltage of 300 kV and the images were acquired using a Fischione Instruments HAADF detector. For STEM characterization, the samples were thinned by mechanical polishing to 180 μm thickness, then dimple-ground with a diamond paste to a central thickness of 20 μm and finally ion milled (using Gatan PIPS model) to electron transparency.

Density functional theory (DFT) with the Perdew-Burke-Ernzerhof (PBE) generalized gradient approximation (GGA) [28] as applied in the Vienna *ab initio* simulation package (VASP) code was used for performing the electronic structure calculations [29-32]. For the GGA calculation, the projector-augmented wave (PAW) [33,34] method was selected with $2p^6 3s^2$ and $3s^2 3p^2$ as valence electrons for the Mg and Si atoms, respectively. A 4 × 4 × 4 *k*-point mesh was used for the band structure calculation. For bismuth and germanium additions, a 2 × 2 × 2 supercell was generated from the Mg_2Si crystal structure, where one out of 32 Si atoms was

replaced with a Bi atom together with three, six, nine and twelve of 32 Si atoms replaced with Ge atoms. The compositions of the different models are thus $Mg_{64}Si_{31-x}GexBi$ with x = 3, 6, 9 and 12.

4.3 Results and discussion

Fig. 4.1 shows the density of states (DOS) of the $Mg_2Si_{0.969-x}Ge_xBi_{0.031}$ ($0.094 \leq x \leq 0.375$) models. Because of the excess electron stemming from the Bi atoms, the conduction band is occupied to a small degree in each case. A slight reduction of the band gap with increasing Ge content confirms the same experimental observation of $Mg_2Si_{1-x}Ge_x$ in NMR studies [23]. Close to the Fermi level, the slope of the density of states of all the samples is very similar, which should result in comparable Seebeck coefficient values. The magnitude of the slope is indicative of a light band.

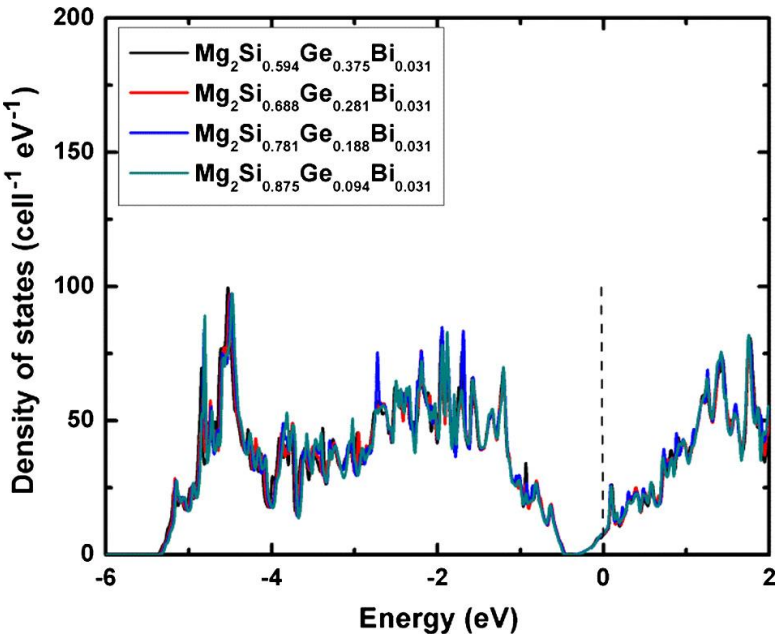

Fig. 4.1 Density of states of $Mg_2Si_{0.969-x}Ge_xBi_{0.031}$ ($0.094 \leq x \leq 0.375$).

To better understand the nature of defects that could stem from the introduction of Ge, high resolution transmission electron microscopy (HRTEM, operating under scanning mode) was performed on the $Mg_2Si_{0.777}Ge_{0.2}Bi_{0.023}$ sample. Fig. 4.2a displays a low magnification STEM (Scanning transmission electron microscopy)-HAADF (High-angle annular dark-field) image of the polycrystalline sample. Regions with bright intensities consist of atoms with higher atomic number (Ge: 32, Bi: 83) compared to the matrix (Mg: 14, Si: 12). The concentration of heavy atoms is higher near the outer edges of the grains, demonstrated in Fig. 4.2b and c that depict the areas marked red and green in Fig. 4.2a, respectively. Because of the low Bi concentration (0.77 at%) in the sample compared to Ge (6.67 at%), it is postulated that the majority of the segregated atoms are Ge atoms, *i.e.* a Ge-rich domain is present at the edge of the Mg_2(Si,Ge,Bi) grains. The strain originating from the larger size of the heavier Ge atoms can be better accommodated along the grain boundaries, causing this concentration gradient.

Fig. 4.2d shows the STEM–HAADF image corresponding to the region marked in 4.2b. The image had a band-pass filter applied for enhanced visibility of segregated atoms. In addition to the Ge-rich domains, as shown by the blue lines, there are atoms, most likely Mg^{2+} because of its small size, occupying interstitial sites as highlighted by the lines marked in red. Consequently, this affects the local strain distribution at the grain boundaries.

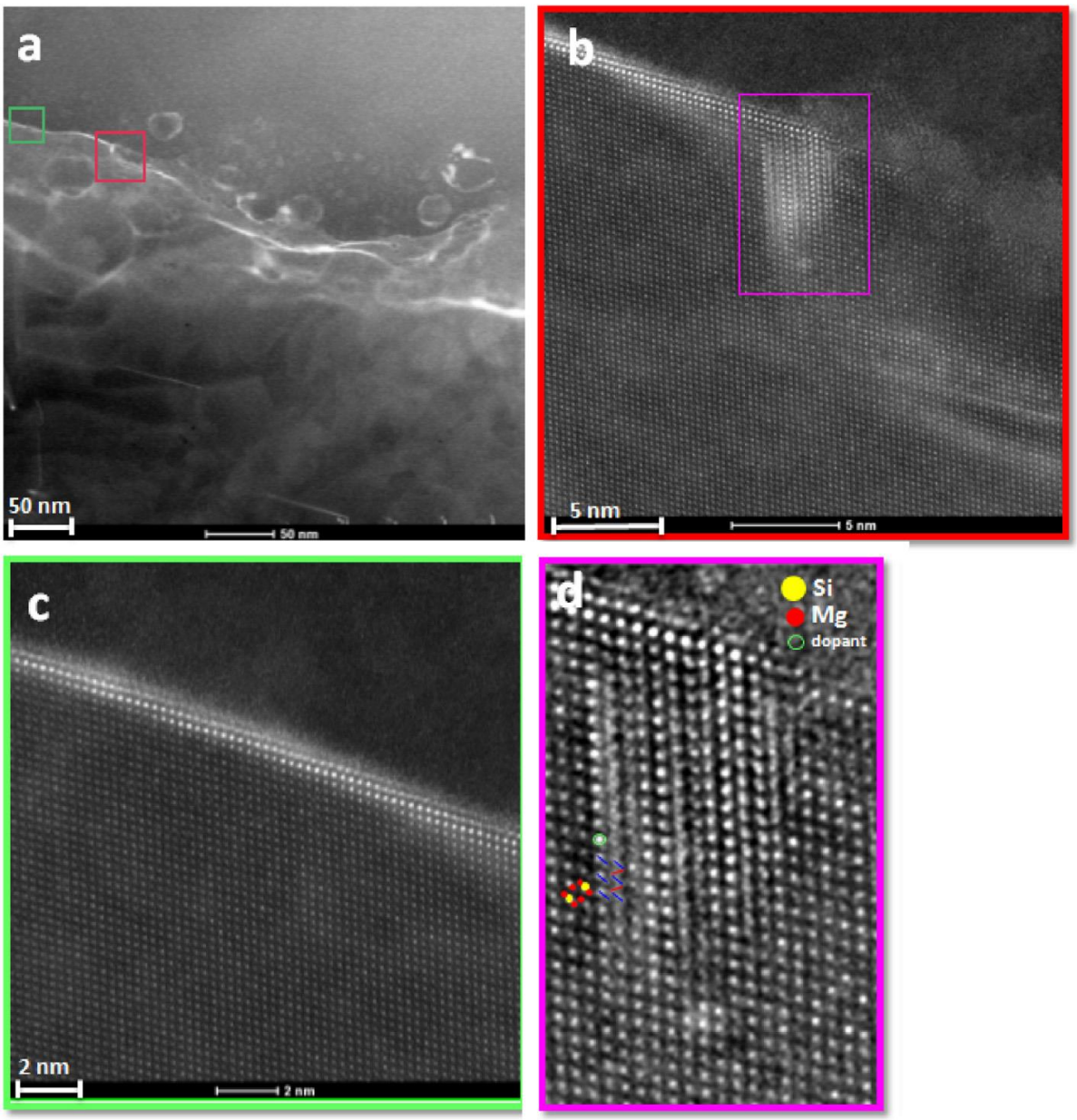

Fig. 4.2 Low-magnification STEM-HAADF image of $Mg_2Si_{0.777}Ge_{0.2}Bi_{0.023}$. (b) and (c) STEM-HAADF image obtained from the red and green marked areas in (a) displaying the higher concentration of heavy atoms. (d) STEM-HAADF image corresponding to the region marked in (b) together with atomic simulation results showing the occupation of interstitial sites marked by red lines as well as the heavy atom segregation on Si sites marked by blue lines. (For interpretation of the references to color in this figure legend, the reader is referred to the web version of this article.)

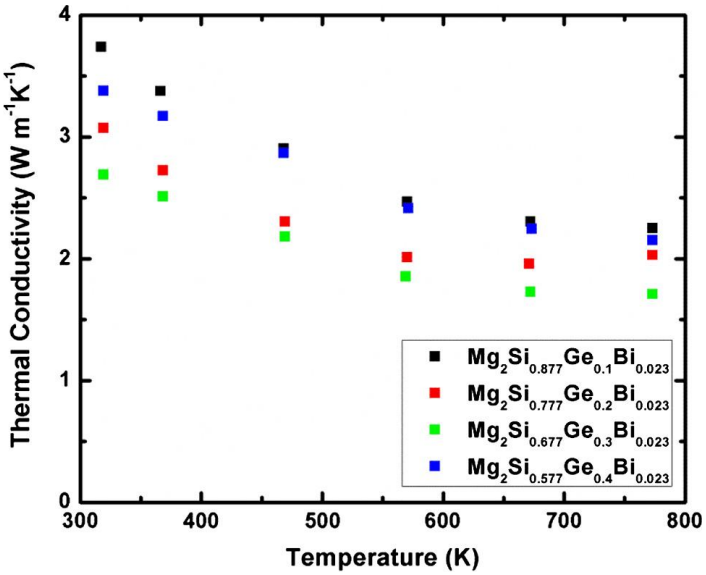

Fig. 4.3 Thermal conductivity of $Mg_2Si_{0.977-x}Ge_xBi_{0.023}$ ($0.1 \leq x \leq 0.4$).

The thermal conductivity of all the samples decreases with increasing temperature due to acoustic phonon scattering (Fig. 4.3). The $Mg_2Si_{0.677}Ge_{0.3}Bi_{0.023}$ sample showed the lowest thermal conductivity of κ = 1.7 $Wm^{-1}K^{-1}$, compared to 3.9 $Wm^{-1}K^{-1}$ at 773 K obtained for Bi doped Mg_2Si [35]. Higher numbers of 2.5 $Wm^{-1}K^{-1}$, 2.3 $Wm^{-1}K^{-1}$ and 2.3 $Wm^{-1}K^{-1}$ were obtained for $Mg_2Si_{0.7}Ge_{0.3}$, $Mg_2Si_{0.7}Ge_{0.3}$:$Sb_{0.02}$ and $Mg_2Si_{0.7}Ge_{0.3}$:$Bi_{0.02}$ by Kim *et al.*, respectively [22,36,37]. All these values are drastically lower than the 7.3 $Wm^{-1}K^{-1}$ (at 320 K) to 3.0 $Wm^{-1}K^{-1}$ (at 660 K) we determined for the Bi-doped binary Mg_2Si [25]. Introducing germanium into the silicon position reduces the thermal conductivity especially at low temperatures, due to the increase in phonon scattering through mass fluctuation point defect scattering between these two elements [38,39] as well as the presence of Ge-rich domains. The decrease in κ with increasing mass contrast was also observed in other solid solutions such as $PbTe_{1-x}Se_x$ [40] and $Mg_2Si_{1-x}Sn_x$ [41,42].

The higher thermal conductivity of the $Mg_2Si_{0.577}Ge_{0.4}Bi_{0.023}$ sample, compared to $Mg_2Si_{0.677}Ge_{0.3}Bi_{0.023}$, *e.g.* 2.2 $Wm^{-1}K^{-1}$ *vs.* 1.7 $Wm^{-1}K^{-1}$ at 773 K (Table 4.1), can in part be

explained by its higher relative density (98%, compared to 96% of the other samples), which facilitates both phonon and electron transportation. The extent of this effect may be estimated *via* the Maxwell-Eucken correction (Eq. (4.1)):

$$\kappa_p = \kappa_0 \frac{1-P}{1+\beta P} \tag{4.1}$$

Therein, κ_P is the measured thermal conductivity with a porosity P, and κ_0 the theoretical thermal conductivity at full density, *i.e.* $P = 0$.With porosities of 4% for the 0.3 Ge sample and 2% for the 0.4 Ge sample and setting $\beta = 2$ for spherical pores, we calculated κ_0 values of 1.9 $Wm^{-1}K^{-1}$ and 2.3 $Wm^{-1}K^{-1}$ at 773 K, respectively. Thusly, the different density cannot explain the large difference of 17% in κ alone; an additional explanation might be the possible existence of small amounts of unreacted Ge in the sample with the higher Ge amount, noting that elemental Ge has a thermal conductivity of the order of 60 $Wm^{-1}K^{-1}$ (and that each measured κ value has an experimental error of the order of ±5%).

The lattice thermal conductivity, κ_L, was calculated through $\kappa_L = \kappa - \kappa_e$, where κ_e is the electronic thermal conductivity, which is derived from the measured electrical conductivity, σ, via the Wiedemann–Franz relationship $\kappa_e = L\sigma T$. The Lorenz numbers L were calculated by applying the single parabolic band and elastic carrier scattering approximation *via* Eq. (4.2),

$$L = \left(\frac{k_B}{e}\right)^2 \left\{\frac{(1+\lambda)(3+\lambda)F_\lambda(\eta)F_{2+\lambda}(\eta) - (2+\lambda)^2 F^2{}_{1+\lambda}(\eta)}{(1+\lambda)^2 F^2{}_\lambda(\eta)}\right\} \tag{4.2}$$

where $F_i(\eta)$ represents the Fermi integral of order i, the reduced Fermi energy (η) is equal to $E_F/(k_BT)$, where E_F is the Fermi energy, and it can be calculated as a function of temperature from measured values of the Seebeck coefficient using Eq. (4.3). k_B is the Boltzmann constant

and *e* the electron charge. Acoustical phonon scattering (λ = 0) can be assumed as the dominant factor limiting charge carrier mobility [43].

$$S = \frac{k_B}{e}\left\{\frac{(2+\lambda)F_{1+\lambda}(\eta)}{(1+\lambda)F_{\lambda}(\eta)} - \eta\right\} \tag{4.3}$$

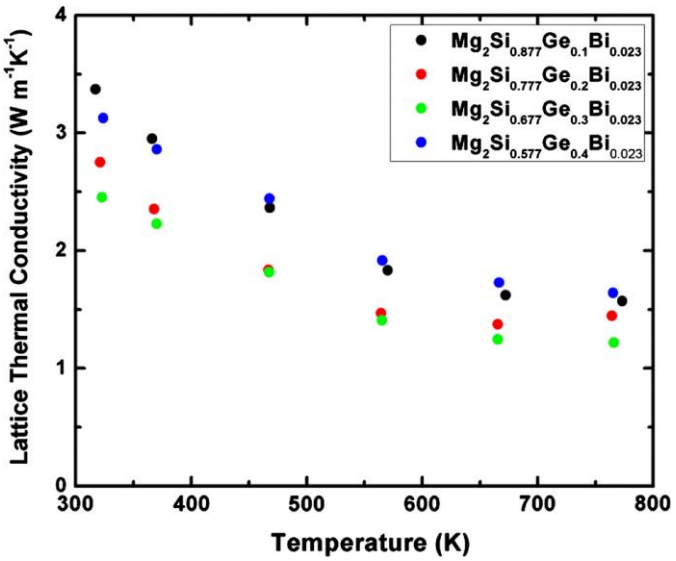

Fig. 4.4 Lattice thermal conductivity of $Mg_2Si_{0.977-x}Ge_xBi_{0.023}$ ($0.1 \leq x \leq 0.4$).

The calculated Lorenz numbers range from $L = 1.94 \times 10^{-8}$ V^2K^{-2} for the 0.1 Ge sample at 323 K to $L = 1.62 \times 10^{-8}$ V^2K^{-2} for the 0.4 Ge sample at 773 K (a complete list of all calculated values and their temperature dependence is available in the Supporting Information as Fig. B.3). The calculated values for the lattice thermal conductivity are presented in Fig. 4.4, which follow the same trends as the total thermal conductivity data. The lowest value of κ_L = 1.2 $Wm^{-1}K^{-1}$ occurs at 773 K for $Mg_2Si_{0.677}Ge_{0.3}Bi_{0.023}$.

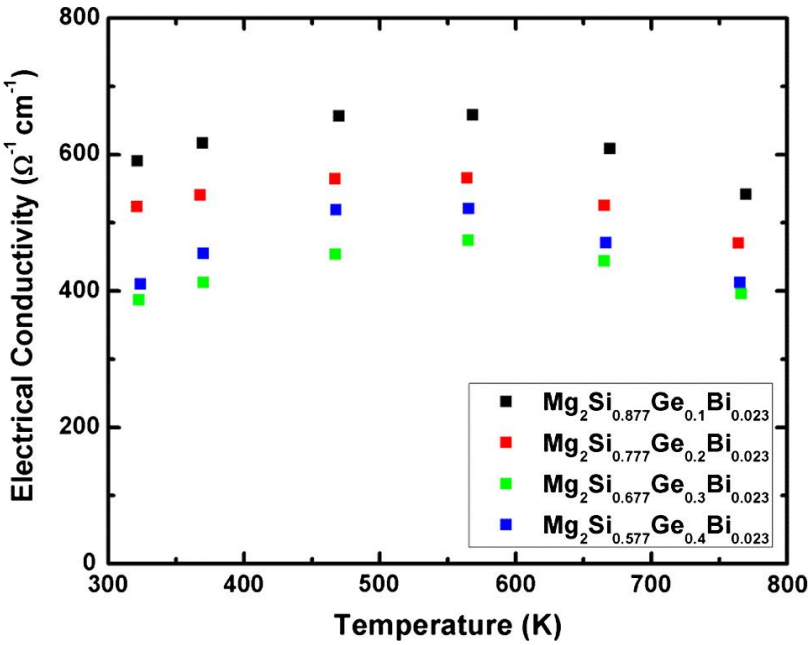

Fig. 4.5 Electrical conductivity of $Mg_2Si_{0.977-x}Ge_xBi_{0.023}$ ($0.1 \leq x \leq 0.4$).

The electrical conductivity data are shown in Fig. 4.5. For all the samples, electrical conductivity increases with temperature up to around 500 K and then decreases. The reduction at higher temperature can be attributed to higher lattice vibration and an increase in acoustical phonon scattering *via* electron phonon interactions. Introducing germanium increases not only phonon scattering but also charge carrier scattering, which results in a reduction in σ from 590 Ω^{-1}cm^{-1} (0.1 Ge) to 390 Ω^{-1}cm^{-1} (0.3 Ge) at room temperature. As was the case in the thermal conductivity data, the sample with 0.4 Ge stands out from this trend. Using again the Maxwell–Eucken correction (Eq. (4.4)) with β = 2, we find corrected values at 773 K for the hypothetical fully dense samples of 446 Ω^{-1} cm^{-1} instead of 396 Ω^{-1}cm^{-1} for the 0.3 Ge sample and of 437 Ω^{-1}cm^{-1} instead of 412 Ω^{-1}cm^{-1} for the 0.4 Ge sample. In contrast to the thermal conductivity, where the different porosities only explained part of the trend, the change in electrical conductivity from 0.3 to 0.4 Ge can thus be fully understood based on the decrease in porosity. This

observation is in accord with the suspected trace amounts of unreacted Ge not increasing the electrical but the thermal conductivity.

$$\sigma_p = \sigma_0 \frac{1-P}{1+\beta P} \tag{4.4}$$

All the Bi doped samples presented here with values between σ = 400 $\Omega^{-1}cm^{-1}$ and 540 $\Omega^{-1}cm^{-1}$ at 773 K exhibit higher electrical conductivity than the one doped with Sb with σ = 300 $\Omega^{-1}cm^{-1}$, while Kim's $Mg_2Si_{0.7}Ge_{0.3}$:$Bi_{0.02}$ sample had higher electrical conductivity of σ = 590 $\Omega^{-1}cm^{-1}$ at 773 K (and smaller Seebeck coefficient) (Table 4.1).

Table 4.1 Thermoelectric properties of $Mg_2Si_{0.97-x}Ge_xBi_{0.023}$ ($0.1 \leq x \leq 0.4$) at 773 K in comparison to literature data.

	x = 0.1	x = 0.2	x = 0.3	x =0.4	$Mg_2Si_{0.7}Ge_{0.3}$:$Bi_{0.02}$ [22]
σ ($\Omega^{-1}cm^{-1}$)	541	470	396	412	590
S (μVK^{-1})	-190	-194	-200	-202	-189
κ ($Wm^{-1}K^{-1}$)	2.25	2.03	1.71	2.15	2.27
L (10^{-8} V^2K^{-2})	1.63	1.63	1.62	1.62	1.61
κ_L ($Wm^{-1}K^{-1}$)	1.57	1.44	1.22	1.64	1.54
μ ($cm^2V^{-1}s^{-1}$)[a]	n/a	n/a	33	40	18
n (10^{19} cm^{-3})[a]	n/a	n/a	6.9	6.8	14
ZT	0.67	0.67	0.71	0.60	0.71

[a] Obtained at 300 K.

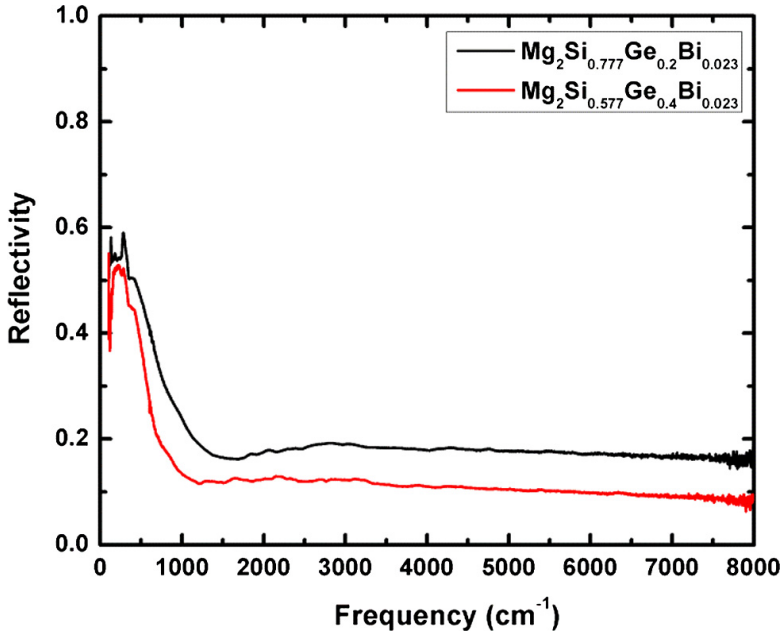

Fig. 4.6 Reflectivity spectra of $Mg_2Si_{0.977-x}Ge_xBi_{0.023}$ (x = 0.2, 0.4).

The reflectivity spectra of samples with 0.2 and 0.4 Ge are depicted in Fig. 4.6. The *dc* conductivity values were calculated from the Kramers-Kronig analysis using the Drude model to be 170 $\Omega^{-1}cm^{-1}$ for the sample with 0.2 Ge and 99 $\Omega^{-1}cm^{-1}$ for 0.4 Ge. These calculated values are drastically lower than the ones measured on the pressed pellets *via* four point-probe measurements, and the reason or the discrepancy is most likely due to the limited spot size (about 400 μm^2) and penetration depth of the infrared radiation. The result of these instrumental limitations is that the signal used to extract the *dc* conductivity values is overly influenced by the character of the surface states.

One of the characteristics of a doped semiconductor is the plasma reflection edge, which is seen as a minimum in the reflectivity. Based on the Drude model, the corresponding energy at the reflectivity minimum is related to the plasma frequency, ω_P, which can be expressed as ω_P^2 =

$ne^2\varepsilon_0^{-1}\varepsilon^{-1}m^{*-1}$, where n, m^*, ε_0 and ε are carrier concentration, electron effective mass, vacuum permittivity and dielectric constant of the material, respectively [27]. We obtained a plasma frequency of 1460 cm^{-1} for 0.2 Ge sample, and 1165 cm^{-1} for 0.4 Ge, corresponding to energies of 0.18 eV and 0.14 eV, respectively. Earlier we reported 0.21 eV for $Mg_2Si_{0.98}Bi_{0.02}$ [25]. The different values for the two Ge samples are likely caused by a different effect mass (thus mobility), as the nominal dopant concentrations are equivalent. Higher frequency/energy correlates with lower effective mass, thus higher mobility, in accord with the higher room temperature conductivity of the 0.2 Ge sample as compared to 0.4 Ge.

To gain more understanding of the transport properties, Hall measurements were carried out on the samples with high Ge content (0.3 and 0.4 Ge per formula unit). The carrier concentrations (n) of both samples are nearly the same, $n \sim 7 \times 10^{19}$ per cm^3, consistent with them both having the same doping level, and are both nearly temperature independent (Fig. 4.7). Interestingly, these concentrations are significantly lower than the one determined by Kim *et al*. on $Mg_2Si_{0.7}Ge_{0.3}$:$Bi_{0.02}$ (1.4×10^{20} cm^{-3}), which is also consistent with their higher electrical conductivity and lower Seebeck coefficient [22]. The different carrier concentration may be a consequence of the lower temperature and pressure used in the consolidation process, which might have resulted in less efficient Bi doping. For example, 0.023 Bi per formula unit would hypothetically add 3.6×10^{20} electrons per cm^3, while we found only 6.9×10^{19} cm^{-3}, compared to Kim's 1.4×10^{20} cm^{-3}. On the other hand, Kim's Sb-doped sample exhibited an unexplained high carrier concentration of 22×10^{20} cm^{-3}, *i.e*. 6 times higher than expected based on the nominal composition.

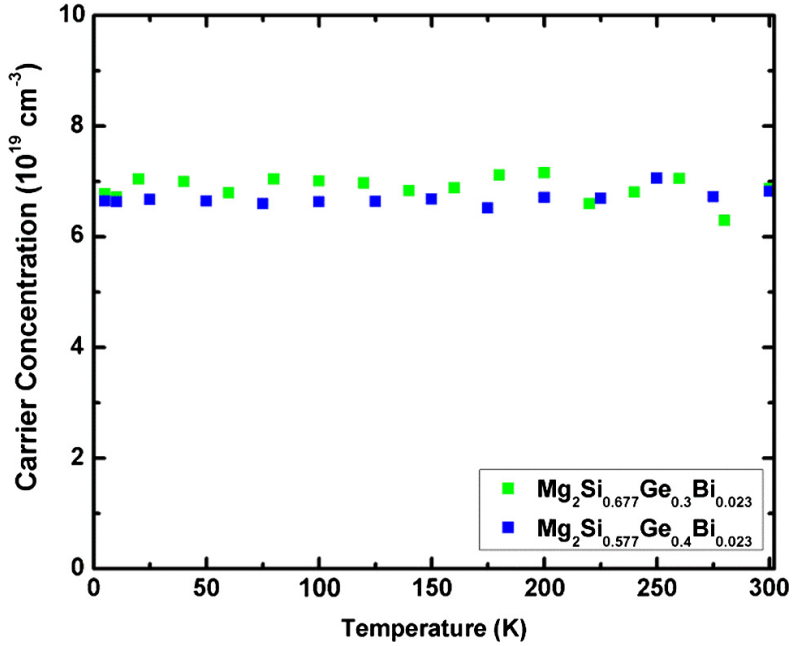

Fig. 4.7 Carrier concentration of $Mg_2Si_{0.977-x}Ge_xBi_{0.023}$ (x = 0.3, 0.4).

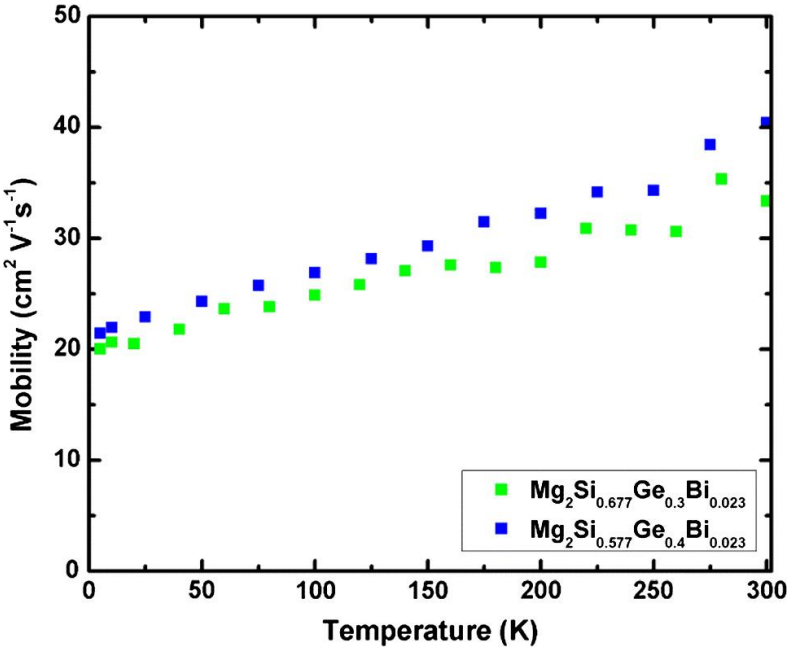

Fig. 4.8 Hall mobility of $Mg_2Si_{0.977-x}Ge_xBi_{0.023}$ (x = 0.3, 0.4).

Fig. 4.8 shows an increase in the mobility (μ) of both samples with temperature. This temperature dependence of the mobility was also observed in Sb-doped Mg_2Si, where this effect was attributed to an activated process, which originated from the presence of MgO at the grain boundaries [44]. The increasing mobility at constant carrier concentration (as measured up to 300 K) causes the electrical conductivity to increase up to about 500 K. The slightly higher mobility of the sample containing 0.4 Ge per formula unit, *e.g.* μ = 40 $cm^2V^{-1}s^{-1}$ *vs*. 33 $cm^2V^{-1}s^{-1}$ for 0.3 Ge at 300 K, is most likely a consequence of the higher relative density as above-mentioned. Kim's $Mg_2Si_{0.7}Ge_{0.3}$:$Bi_{0.02}$ exhibited only μ = 18 $cm^2V^{-1}s^{-1}$ [22], likely caused by the higher carrier concentration.

The Seebeck coefficient as a function of temperature for all the samples is shown in Fig. 4.9. Replacing one Si atom with one Bi will add one electron per atom to the system, which results in a negative Seebeck coefficient. The room temperature Seebeck coefficient is around *S* = -100 μVK^{-1} for all the Bi-doped samples investigated here, in accord with the similar slope of the DOS around the Fermi level, and similar carrier concentration for at least the 0.3 Ge and 0.4 Ge samples. The *S* increases with temperature reaching a maximum value of -200 μVK^{-1} at 773 K behavior typical for a degenerate semiconductor.

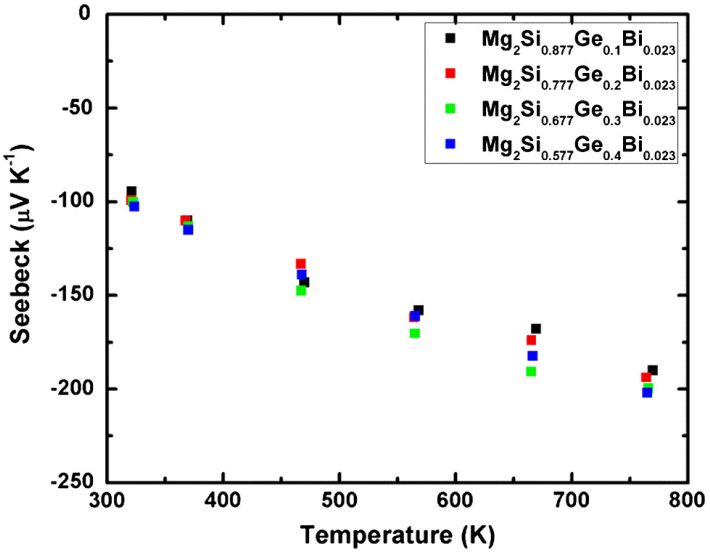

Fig. 4.9 Seebeck coefficient of $Mg_2Si_{0.977-x}Ge_xBi_{0.023}$ ($0.1 \leq x \leq 0.4$).

The similarities of all Seebeck coefficient values also indicate that the carrier concentrations are nearly the same for all the samples. Assuming energy-independent scattering and carriers from a single parabolic band, we calculated the effective mass from the Seebeck coefficient and the carrier concentration *via* Eq. (4.5),

$$S = \frac{8\pi^2 {k_B}^2}{3eh^2} m^* T \left(\frac{\pi}{3n}\right)^{2/3} \tag{4.5}$$

with k_B = Boltzmann constant, h = Planck constant. We obtained $m^* = 0.83\ m_e$ for 0.3 Ge and $m^* = 0.85\ m_e$ for 0.4 Ge (m_e = electron mass). Effective mass values on the order of m_e are common for *n*-type Mg_2Si materials: for example, Kim *et al*. found $m^* = 1.1\ m_e$ for $Mg_2Si_{0.7}Ge_{0.3}$:$Bi_{0.02}$ [22].

The thermoelectric figure of merit *ZT* was calculated from the data discussed above, and compared to Kim's $Mg_2Si_{0.7}Ge_{0.3}$:Bi0.02 and $Mg_2Si_{0.7}Ge_{0.3}$:Sb0.02 (Fig. 4.10). In each case, *ZT* increases with increasing temperature, and the $Mg_2Si_{0.677}Ge_{0.3}Bi_{0.023}$ sample culminates in the highest value of 0.7 at 773 K. This ZT_{max} value is around 50% higher than the $ZT = 0.48$ of its

Sb-doped counterpart. The $Mg_2Si_{0.677}Ge_{0.3}Bi_{0.023}$ sample is also superior to $Mg_2Si_{0.7}Ge_{0.3}$:$Bi_{0.02}$ over the entire temperature range with the exception of our last data point at 773 K, where both 0.3 Ge samples equally exhibit ZT = 0.71: the averaged ZT values over the measured temperature range are ZT_{ave} = 0.35 for $Mg_2Si_{0.677}Ge_{0.3}Bi_{0.023}$ and 0.30 for $Mg_2Si_{0.7}Ge_{0.3}$:$Bi_{0.02}$ [22].

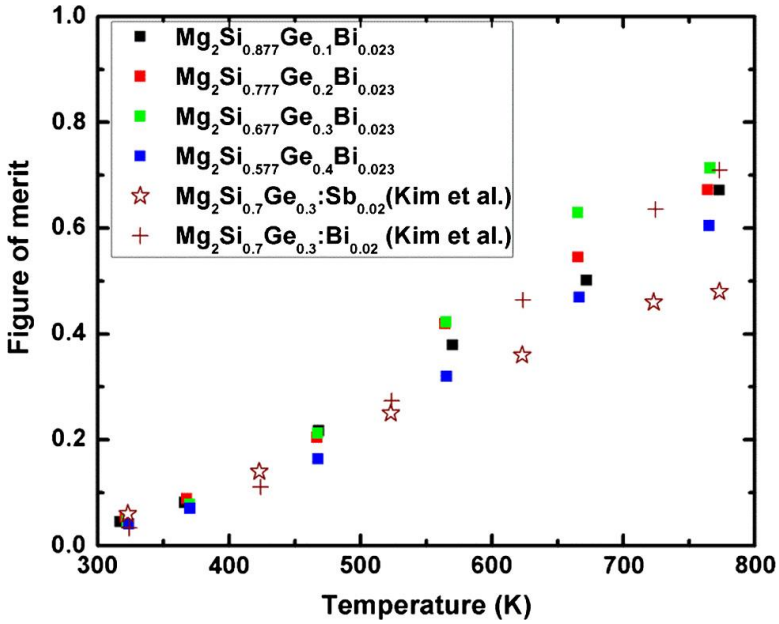

Fig. 4.10 Figure of merit of $Mg_2Si_{0.977-x}Ge_xBi_{0.023}$ ($0.1 \leq x \leq 0.4$).

4.4 Conclusions

By adding germanium to Mg_2Si doped with Bi, the thermal conductivity of alloyed magnesium silicide was reduced from about κ > 7 $Wm^{-1}K^{-1}$ down to values below 4 $Wm^{-1}K^{-1}$ at room temperature. The lowest κ was obtained for $Mg_2Si_{0.677}Ge_{0.3}Bi_{0.023}$ with a value of 1.7 $Wm^{-1}K^{-1}$ at 773 K, and a lattice thermal conductivity of κ_L = 1.2 $Wm^{-1}K^{-1}$. TEM results indicate interstitial sites partly occupied with Mg as well as the presence of Ge-rich domains within the Mg_2(Si,Ge,Bi) particles, which further contribute to a lower thermal conductivity in addition to the alloying effect/increased mass fluctuation. A significant decrease in the electrical

conductivity also occurred with increasing Ge content, but the net effect to the thermoelectric figure of merit is positive.

All in all, bismuth appears to be a more effective dopant than antimony in this system, reflected in a significant enhancement (~48% higher) of thermoelectric figure of merit *ZT* at 773 K, compared to Kim's Sb-doped sample. The same trend exists between Kim's Bi- and Sb-doped samples, which were both prepared by the same methods (though different than ours, as above-mentioned).

Further optimization can be performed on this system by changing the doping level, the pressing conditions, adding tin and studying the effect of nano-structuring, *e.g*. *via* ball milling or forming composites.

Acknowledgements

The authors thankfully acknowledge AUTO21 (Network Centres of Excellence) and General Motors for financial support of this work. JST and JZ wish to thank Westgrid for providing the computing facilities and NSLS-I, Brookhaven National Laboratory, for synchrotron beamtime.

References

[1] Y. Pei, J. Lensch-Falk, E. S. Toberer, D. L. Medlin, and G. J. Snyder, *Adv. Funct. Mater*., 2011, 21, 241.

[2] K. Biswas, J. He, I. D. Blum, C.-I. Wu, T.P. Hogan, D. N. Seidman, V. P. Dravid, and M. G. Kanatzidis, *Nature*, 2012, 489, 414.

[3] J. P. Heremans, B. Wiendlocha, and A. M. Chamoire, *Energy Environ. Sci*., 2012, 5, 5510.

[4] S. R. Brown, S. M. Kauzlarich, F. Gascoin, and G. J. Snyder, *Chem. Mater*., 2006, 18, 1873.

[5] Y. Pei, A. D. LaLonde, N. A. Heinz, and G. J. Snyder, *Adv. Energy Mater*., 2012, 2, 670.

[6] J. Yang and F. R. Stabler, *J. Electron. Mater*., 2009, 38, 1245.

[7] E. S. Toberer, A. Zevalkink, and G. J. Snyder, *J. Mater. Chem*., 2011, 21, 15843.

[8] S. Lee, K. Esfarjani, T. Luo, J. Zhou, Z. Tian, and G. Chen, *Nat. Commun*., 2014, 5, 3525/1.

[9] M. D. Nielsen, V. Ozolins, and J. P. Heremans, *Energy Environ. Sci*., 2013, 6, 570.

[10] P. F. P. Poudeu, J. D'Angelo, H. Kong, A. Downey, J. L. Short, R. Pcionek, T. P. Hogan, C. Uher, and M. G. Kanatzidis, *J. Am. Chem. Soc*., 2006, 128, 14347.

[11] D. L. Medlin and G. J. Snyder, *Curr. Opin. Colloid Interface Sci*., 2009, 14, 226.

[12] A. J. Minnich, M. S. Dresselhaus, Z. F. Ren, and G. Chen, *Energy Environ. Sci*., 2009, 2, 466.

[13] W. Liu, Z. Ren, G. Chen, in: K. Koumoto, T. Mori (Eds.), *Thermoelectr. Nanomater., Springer-Verlag*, Berlin, Heidelberg, 2013, pp. 255–285.

[14] V. K. Zaitsev, *Thermoelectr. Handb*., CRC Press, 2005, pp. 12–29.

[15] R. J. LaBotz, D. R. Mason, and D. F. O'Kane, *J. Electrochem. Soc*., 1963, 110, 127.

[16] M. I. Fedorov, V. K. Zaitsev, G. N. Isachenko, I. S. Eremin, E. A. Gurieva, A. T. Burkov, P. P. Konstantinov, and A .A. Shabaldin, in: ICT 2005. 24th Int. Conf. Thermoelectr. 2005., IEEE, 2005, pp. 110–113.

[17] Y. Noda, H. Kon, Y. Furukawa, I. A. Nishida, and K. Masumoto, *Mater. Trans*., 1992, JIM 33, 851.

[18] Y. Noda, H. Kon, Y. Furukawa, N. Otsuka, I.A. Nishida, K. Masumoto, *Mater. Trans*., 1992, JIM 33, 845.

[19] D. Cederkrantz, N. Farahi, K. A. Borup, B. B. Iversen, M. Nygren, and A. E. C. Palmqvist, *J. Appl. Phys*., 2012, 111, 023701.

[20] H. Ihou-Mouko, C. Mercier, J. Tobola, G. Pont, and H. Scherrer, *J. Alloys Comp*., 2011, 509, 6503.

[21] A. U. Khan, N. Vlachos, and T. Kyratsi, *Scr. Mater*., 2013, 69, 606.

[22] S.-W. You, D.-K. Shin, and I.-H. Kim, *J. Korean Phys. Soc*., 2014, 65, 57.

[23] E. Ratai, M. P. Augustine, and S. M. Kauzlarich, *J. Phys. Chem. B*, 2003, 107, 12573.

[24] T. Ikeda, L. Haviez, Y. Li, and G. J. Snyder, *Small*, 2012, 8, 2350.

[25] N. Farahi, M. VanZant, J. Zhao, J. S. Tse, S. Prabhudev, G. Botton, J. R. Salvador, F. Borondics, Z. Liu, and H. Kleinke, *Dalt. Trans*., 2014, 43,14983.

[26] A. B. Kuzmenko, *Rev. Sci. Instrum*., 2005, 76, 083108/1.

[27] M. Fox, *Optical Properties of Solids*, second ed., Oxford University Press, New York City, NY, USA, 2010.

[28] J. P. Perdew, K. Burke, and M. Ernzerhof, *Phys. Rev. Lett*., 1996, 77, 3865.

[29] G. Kresse, *Phys. Rev. B*, 1996, 54, 11169.

[30] G. Kresse and J. Hafner, *Phys. Rev. B*, 1994, 49, 14251.

[31] G. Kresse and J. Hafner, *Phys. Rev. B*, 1993, 47, 558.

[32] G. Kresse and J. Furthmüller, *Comput. Mater. Sci*., 1996, 6, 15.

[33] P.E. Blöchl, *Phys. Rev. B*, 1994, 50, 17953.

[34] G. Kresse, *Phys. Rev. B*, 1999, 59, 1758.

[35] J. Tani and H. Kido, *Phys. B Condens. Matter*., 2005, 364, 218.

[36] S.-W. You and I.-H. Kim, *J. Korean Phys. Soc*., 2014, 64, 690.

[37] S.-W. You, D.-K. Shin, and I.-H. Kim, *J. Korean Phys. Soc*., 2014, 64, 1346.

[38] T. M. Tritt, *Thermal Conductivity*, Springer, New York City, NY, 2004.

[39] C. Kittel, *Introduction to Solid State Physics*, seventh ed., John Wiley & Sons Inc, New York City, NY, 1996.

[40] H. Wang, A. D. LaLonde, Y. Pei, and G. J. Snyder, *Adv. Funct. Mater*., 2013, 23, 1586.

[41] M. I. Fedorov, D. A. Pshenay-Severin, V. K. Zaitsev, S. Sano, and M. V. Vedernikov, in: Proc. ICT'03. 22nd Int. Conf. Thermoelectr. (IEEE Cat. No.03TH8726), IEEE, 2003, pp. 142–145.

[42] A. Y. Samunin, V. K. Zaitsev, P. P. Konstantinov, M. I. Fedorov, G. N. Isachenko, A. T. Burkov, S. V. Novikov, and E. A. Gurieva, *J. Electron. Mater*., 2012, 42, 1676.

[43] V. I. Fistul', *Heavily Doped Semiconductors*, Springer New York, Boston, MA, 1995.

[44] J. de Boor, T. Dasgupta, H. Kolb, C. Compere, K. Kelm, and E. Mueller, *Acta Mater*., 2014, 77, 68.

CHAPTER 5

THERMOELECTRIC AND ELECTRICAL TRANSPORT PROPERTIES OF Mg_2Si MULTI-DOPED WITH Sb, Al AND Zn

In Chapters 3 and 4, we show that Mg_2Si and $Mg_2Si_{1-x}Ge_x$ doped with a single element such as Sb and Bi led to favourable enhancement of the thermoelectric figure of merit. In 2010, Isoda *et al*. investigated $Mg_2Si_{0.25}Sn_{0.75}$ doped with Li and Ag. [12] They found that, compared to the undoped sample, the presence of Li (20,000 ppm) and Ag (5000 ppm) increased the Seebeck coefficients to a maximum value of 250 μVK^{-1} at 500 K. In comparison with the single Li-doped Mg_2Si, Sn double-doping further doubled the carrier concentration. [13] Sb-doped $Mg_2Si_{0.5}Sn_{0.5}$ compound has been synthesized with a peak power factor of 3.2×10^{-3} $Wm^{-1}K^{-2}$ at 610 K and a maximum ZT >0.9. This is a very promising result as the performance of this class of compound is comparable to the current commercial PbTe-based thermoelectric materials. [14] Furthermore, more recently Du *et al*. also report a maximum ZT of 0.85 obtained at 700 K for $Mg_{2(1+x)}Si_{0.38}Sn_{0.6}Sb_{0.02}$ (x = 0.1) and found that the carrier concentration and electrical conductivity were significantly enhanced. [15] Liu *et al*. also obtained high thermoelectric performance for $Mg_{2(1+x)}Si_{0.45}Sn_{0.537}Sb_{0.013}$ (x = 0.04-0.12) with a best ZT value of 1.0 at 725 K for x = 0.08 and a carrier concentration of $1.9\text{-}10^{20}$ cm^{-3}. [16] Khan *et al*. report that an even higher figure of merit of 1.4 can be obtained at 800 K for $Mg_2Si_{0.55}Sn_{0.4}Ge_{0.05}$ doped with Bi. [17] le-Quoc reports Hall-effect measurements at room temperature on a thin film of Sb doped $Mg_2Si_{1-x}Sn_x$ (x = 0.4, 0.5, 0.6) and shows the Sb acted as an electron donor but the carrier concentration increased non-linearly with the Sb content. The electrical conductivity of the Sb-doped films, however, was still low with a charge carrier concentration less than 10^{19} electron-cm^{-3}. [18] A significant enhancement of the thermoelectric figure of merit of Mg_2Si to 0.7 at 873 K was achieved more recently by double-doping the sample with a combination of Bi, Pb, and

Sb. It was observed that the addition of any two of the doping elements could increase the electrical conductivity because of the increased free electrons from the dopants in the conduction band. [19] For example, Jiang *et al*. found the thermoelectric performance was improved by introducing three types of defects: Sb dopants, Mg vacancies, and Mg interstitials into $Mg_2Si_{0.4}Sn_{0.6-x}Sb_x$ samples. [20] Isoda *et al*. found the highest *ZT* value of 0.94 for the Al/Sb double-doped $Mg_2Si_{0.75}Sn_{0.25}$ at 850 K. Therefore, Sb is considered to be an effective dopant to increase the carrier concentration. [21]

For this chapter, the thermoelectric and electrical transport properties of Mg_2Si were investigated by multi-element-doping with Sb, Al and Zn. The compounds we studied were $Mg_{1.99}Al_{0.005}Zn_{0.005}Si_{0.995}Sb_{0.005}$ (Mg_2Si:Sb0.5%Al0.5%Zn0.5%), $Mg_{1.99}Al_{0.01}Si_{0.995}Sb_{0.005}$ (Mg_2Si:Sb0.5%Al1.0%), $Mg_{1.995}Zn_{0.005}Si_{0.995}Sb_{0.005}$ (Mg_2Si:Sb0.5%Zn0.5%), and $Mg_{1.99}Zn_{0.01}Si_{0.995}Sb_{0.005}$ (Mg_2Si:Sb0.5%Zn1.0%). Once again, the electrical transport properties of the samples were studied by mid-infrared (IR) reflectivity measurements. In addition, the electrical resistivity and Hall coefficients were also measured by the conventional quasi-four-probe method. Combining IR reflectivity data and independently measured Hall coefficients, the static (*dc*) conductivities, effective masses and carrier concentrations of the samples studied were determined. Our experimental collaborators also measured the temperature dependence of the Seebeck coefficient (S), electrical conductivity (σ), and thermal conductivity (κ). From the results, the figure of merit (*ZT*) and power factor ($S^2\sigma\times T$) of Sb, Al, and Zn multi-doped Mg_2Si samples were calculated. At 700 K, the *ZT* was found to be 0.7 in Mg_2Si:Sb0.5%Zn0.5% and Mg_2Si:Sb0.5%Zn1.0%. This value is approximately 17% higher than single-doped Mg_2Si. A maximum *ZT* of 0.964 was found for Mg_2Si:Sb0.5%Zn0.5% at 880 K. This value is also comparable to the PbTe-based thermoelectrics.

The results of this investigation were published in

J. Zhao, Z. Liu, J. Reid, K. Takarabe, T. Iida, B. Wang, U. Yoshiya, and J. S. Tse, "Thermoelectric properties and electrical transport properties of multi-doped Mg_2Si with Sb Al and Zn," *Journal of Materials Chemistry A*, vol. 3, pp. 19774-19782, 2015.

The authors' contributions are as follow:

- J. Zhao and J. S. Tse performed powder X-ray diffraction and mid-infrared reflectivity experiments, and performed the analysis of all the experimental data.
- Z. Liu assisted in performing mid-infrared reflectivity experiments at BNL.
- J. Reid assisted in performing powder X-ray diffraction experiments at CLS.
- K. Takarabe, T. Iida, B. Wang, and U. Yoshiya provided the samples, and performed the thermoelectric properties measurements in Japan.
- All authors contributed to the writing and editing of the manuscript.

Abstract

Enhanced thermoelectric and electrical transport properties of Mg_2Si-based thermoelectric materials have been achieved by multi-doping with Sb, Al and Zn. Results on the investigation of the electrical transport and thermoelectric properties of multi-doped samples prepared using the spark plasma sintering technique are reported. Synchrotron radiation powder X-ray diffraction was used to characterize the structures of the doped samples. The electrical transport properties were determined from mid-infrared reflectivities, Hall effect and conventional quasi-four probe conductivity measurements. Using the electron concentrations (N) determined from the Hall coefficients, the effective masses (m^*) were calculated from the

frequency of the plasma edge (ω_P) of the infrared reflectivities. The thermoelectric performance and thermoelectric figure of merits (*ZT*) in the temperature range of 300 K to 900 K of the doped Mg_2Si compounds were calculated from the measured temperature dependent electrical conductivity (σ), Seebeck coefficient (*S*), and thermal conductivity (κ). A maximum *ZT* of 0.964 was found for Sb0.5%Zn0.5% doped Mg_2Si at 880 K. This value is comparable to those of PbTe based thermoelectric materials.

5.1 Introduction

Doped magnesium silicide (Mg_2Si)-based alloys have been suggested to be a new generation of high performance and environmentally friendly thermoelectric materials. [1-4] Compared to lead-based thermoelectric materials, Mg_2Si-based alloys have the merits of non-toxicity, sustainability and low production cost. The efficiency of thermoelectric materials can be enhanced through *p*- or *n*-type doping. [5-9] Dopants can increase the carrier concentration and mobility of the conduction electrons. Doping with heavy atoms can also affect the lattice vibrations and help to lower the thermal conductivity. It was reported that in the presence of Sb and Bi, Mg_2Si had exhibited good thermoelectric performance. [10] For example, Akasaka *et al.* had found that the figure of merit for Bi-doped and Ag-doped, *n*- and *p*-doping, respectively, was 0.65 at 840 K and 0.1 at 566 K. [11]

More recently, *p*-type and *n*-type Mg_2Si thermoelectric materials multi-doped with more than one element have led to further enhancement of the thermoelectric figure of merit. In 2010, $Mg_2Si_{0.25}Sn_{0.75}$ doped with Li and Ag was investigated by Isoda *et al*. [12] Compared to the single-doped samples, for double doped $Mg_2Si_{0.25}Sn_{0.75}$ with Li (20 000 ppm) and Ag (5000 ppm) the Seebeck coefficients have increased and maximized to 250 μVK^{-1} at 500 K. The previous Seebeck coefficients were found to be positive, indicating *p*-type doping with holes as

conduction carriers. In comparison with single Li-doped Mg_2Si, double doping increased the carrier concentration to more than double. [13] In 2011, the Sb doped $Mg_2Si_{0.5}Sn_{0.5}$ compound was synthesized and the peak power factor of the sample reached 3.2×10^{-3} $Wm^{-1}K^{-2}$ at 610 K with a maximum ZT >0.9, comparable to those of PbTe based thermoelectric materials. [14] In addition, Du *et al*. reported that a maximum *ZT* of 0.85 was obtained at 700 K for $Mg_{2(1+x)}Si_{0.38}Sn_{0.6}Sb_{0.02}$ (x = 0.1), and found that the carrier concentration and electrical conductivity were significantly enhanced by the Mg in the interstitial sites. [15] Moreover, Liu *et al*. also found high thermoelectric performance for $Mg_{2(1+x)}Si_{0.45}Sn_{0.537}Sb_{0.013}$ (x = 0.04-0.12) with a maximum *ZT* of 1.0 at 725 K for x = 0.08 and a carrier concentration of $1.9\text{-}10^{20}$ cm^{-3}. [16] Khan *et al*. reported that an even higher figure of merit (*ZT*) of 1.4 can be obtained at 800 K for the multi-doped compound of $Mg_2Si_{0.55}Sn_{0.4}Ge_{0.05}$ doped with Bi. [17] le-Quoc reported Hall effect measurements at room temperature on a thin film of Sb doped $Mg_2Si_{1-x}Sn_x$ (x = 0.4, 0.5, 0.6) and showed that Sb acted as an electron donor but the carrier concentration increased non-linearly with the Sb content. The electrical conductivity of the Sb doped films, however, is still low with a charge carrier concentration less than 10^{19} cm^{-3}. [18] In 2014, a significant enhancement of the thermoelectric figure of merit of Mg_2Si to 0.7 at 873 K was achieved by double-doping with a combination of Bi, Pb, and Sb. It was observed that the addition of any two of the doping elements can increase the electrical conductivity due to the excess free electrons in the conduction band. [19] For example, Jiang *et al*. found that the thermoelectric performance was improved by introducing three types of point defects, Sb dopants, Mg vacancies, and Mg interstitials, into $Mg_2Si_{0.4}Sn_{0.6-x}Sb_x$ samples. [20] Isoda *et al*. found the highest *ZT* value of 0.94 for the Al/Sb double-doped $Mg_2Si_{0.75}Sn_{0.25}$ at 850 K. Therefore, Sb is considered to be an effective dopant to increase the carrier concentration. [21] Previous studies have shown that

double or multi-doping is a promising approach to further enhance the thermoelectric figure of merit (ZT) of Mg_2Si-based thermoelectric materials.

The objective of this paper is to characterize and to better understand the effect of multi-dopants on the host lattice of Mg_2Si crystals. For this purpose, Sb, Al, and Zn multi-element-doped Mg_2Si samples were synthesized by using the spark plasma sintering technique. The electrical transport properties were studied by mid-infrared reflectivity measurements. Since the reflectivity is related to the dielectric function, frequency dependent optical conductivity can be extracted from the analysis. Static (dc) conductivity is obtained by extrapolation to zero photon energy. In addition, the electrical resistivity and Hall coefficient were also measured by the conventional quasi-four- probe method. The thermoelectric properties of the multi-doped Mg_2Si samples were determined from the temperature dependence of the Seebeck coefficient (S), electrical conductivity (σ), and thermal conductivity (κ). The figure of merit (ZT) and power factor ($S^2\sigma \times T$) of Sb, Al, and Zn multi-doped Mg_2Si samples were then calculated.

The layout of the paper is as follows. First, details on the experimental procedure will be described. The diffraction patterns of multi-element-doped Mg_2Si are compared with those of pure Mg_2Si. This is followed by a discussion on the electrical properties extracted from mid-IR reflectivity and the conventional quasi-four probe method. Finally, the thermoelectric properties were characterized from the results of the temperature dependence of the Seebeck coefficient (S), electrical conductivity (σ), and thermal conductivity (κ). The figure of merit (ZT) and power factor ($S^2\sigma \times T$) were calculated and discussed.

5.2 Experimental details

5.2.1 Synthesis and the sintering process for doped Mg_2Si sample preparation

Crystal growth of polycrystalline Mg_2Si was performed using an electric furnace by lowering the temperature from slightly beyond the melting point (1378 K) of Mg_2Si, and was initiated from stoichiometric melts with Mg : Si = 2 : 1. The starting materials, Mg and Si, were placed in an alumina crucible under argon-hydrogen forming gas (0.08 MPa). Intentional impurities of antimony (Sb) and aluminium (Al), and an isoelectric impurity of zinc (Zn) were incorporated in order to increase the electronic carrier concentrations and phonon scattering. The Sb and Al dopants predominantly substitute Si and Mg, respectively, which act as donors, and Zn is expected to show isoelectric characteristics at the Mg site, *i.e.*, no contribution to carrier generation but an influence over phonon behaviour, bringing about reduction in thermal conductivity. These donor and isoelectric dopants were incorporated during the all-molten synthesis process at 1378 K, and the resultant polycrystalline Mg_2Si was pulverized to powder with a size of 25-75 μm, then placed into a graphite die and sintered by using a plasma-activated sintering (PAS) technique using an ELENIX Ed-PAS-III-Es. Sintering was basically performed at 1123 K for 10 min with a pressure of 40 MPa in an Ar (0.06 MPa) atmosphere and the sintering temperature and time were varied depending on the type of dopant that was used to obtain a dense material. The compositions of the samples were analyzed by electron-probe microanalysis (EPMA) using a JEOL JXA-8900. The concentration of the dopant impurities in the samples was estimated by glow discharge mass spectrometry (GDMS) using a V.G. Scientific VG-9000.

5.2.2 Powder X-ray diffraction measurements

Powder Mg_2Si was purchased from Alfa Products with a purity of 99.5%. Mg_2Si was doped with nominal 0.5 at% of Sb, 0.5-1.0 at% of Al, and 0.5-1.0 at% of Zn by using the spark plasma sintering technique. The four materials studied were Mg_2Si with nominal at% of Sb0.5% Al0.5% Zn0.5%, Sb0.5% Al1.0%, Sb0.5% Zn0.5%, and Sb0.5% Zn1.0%. Synchrotron X-ray diffraction experiments on the pure standard and doped Mg_2Si samples were performed at CMCF-II, Canadian Light Source (CLS), using synchrotron radiation (λ = 0.68880 Å). The diffraction patterns were analyzed using the JANA 2006 software package with the lattice parameters determined by the Le Bail fit. [22,23]

5.2.3 Mid-infrared reflectivity measurements

Mid-infrared normal-incidence reflectance spectra of pure and Sb Zn Al multi-doped Mg_2Si samples were measured at the side-station of the U2A beamline, National Synchrotron Radiation Facility, Brookhaven National Laboratory. Mid-infrared spectra were recorded on a Bruker Vertex 80v FTIR spectrometer and a Hyperion 2000 IR microscope attached with a liquid nitrogen cooled HgCdTe detector. Powder samples were prepared and placed in the 300 μm culet of a Sintek mini type IIa diamond anvil cell. After loading the sample the DAC is closed by hand compression to flatten the powder sample. After re-opening the DAC, one half of the flattened sample was removed leaving half of the clean diamond face exposed. In this way, the orientation of the sample surface and diamond support is ensured to be the same. This is critical for the conversion of the reflectance to absolute reflectivity. The procedure is as follows: the reflectance of the diamond phase (I_d) and the sample (I_{sa}) was measured. The reflectance of the sample was then converted to absolute reflectivity by normalization to the reflectance of the diamond surface. From the known reflectivity of diamond, the reflectivity of the sample-air interface (R_{sa})

was calculated as $R_{sa} = (I_{sa}/I_d) \times (I_d/I_0)$, where I_d/I_0 is a constant of 0.185. All the spectral data were collected at a resolution of 4 cm^{-1} and accumulated for 512 scans.

Frequency dependent optical conductivity was obtained by Kramers-Kronig (K-K) analysis of the reflectivity data by fitting with a variational K-K constrained dielectric function, implemented in the RefFIT code. [24,25] The frequency dependent optical conductivity was derived from the fit to a Drude-Lorentz (DL) model and the *dc* conductivity obtained from extrapolation to zero frequency.

5.2.4 Electrical transport property and thermoelectric property measurements

Polycrystalline Mg_2Si fabricated by an all-molten synthesis method was used as the source material. The Sb, Al and Zn dopants were incorporated during a melt synthesis process at 1378 K, and the resultant polycrystalline Mg_2Si was pulverized to powder with a size of 25-75 μm, then placed into a graphite die and sintered by using a plasma-activated sintering (PAS) technique using an ELENIX Ed-PAS-III-Es. Sintering was performed at a pressure of 40 MPa in an Ar (0.06 MPa) atmosphere and the sintering temperature and time were varied depending on the type of dopant that was used to obtain a dense material. The temperature-dependent thermoelectric properties were measured using an ULVAC-RIKO ZEM2 to determine the Seebeck coefficient and the electrical resistivities, and an ULVACRIKO TC-7000H to determine the thermal conductivity over a temperature range from 300 K to 900 K. Electrical resistivity below room temperature was measured by the standard four-probe method using a commercial Quantum Design Physical Property Measurement System (PPMS) (1.8 K *T* 400 K, 0 *H* 70 kOe). The Hall effect was measured at fixed temperature by changing the magnetic field strength from -5 T to 5 T.

5.3 Results and discussion

High resolution synchrotron angle dispersive X-ray diffraction patterns of pure Mg_2Si, Mg_2Si doped with Sb0.5%Al0.5% Zn0.5%, Sb0.5%Al1.0%, Sb0.5%Zn0.5%, and Sb0.5%Zn1.0% were measured with a photon energy of 18 keV (λ = 0.68880 Å) on the CMCF-II beamline, Canadian Light Source Inc. at room temperature (Fig. 5.1). The lattice constants were determined from the full profile Le Bail fit to the diffraction patterns from 5º to 40º using the JANA 2006 package. The X-ray diffraction pattern of pure Mg_2Si can be indexed readily to the cubic anti-fluorite (CaF_2) structure with space group $Fm\bar{3}m$. On increasing the diffraction angle, the Miller indices (*hkl*) of the Bragg peaks are identified as (111), (200), (220), (311), (222), (400), (331), (420), (422), (511), (440), (531) and (600) reflections. The diffraction patterns of Mg_2Si doped with Sb, Zn and Al all share the same profile as pure Mg_2Si except the Bragg peaks that have shifted noticeably to lower angles. The observation indicated that even with a small dopant concentration (0.5-1.0%) the cubic lattice of Mg_2Si is expanded. Fig. 5.2(a) and (b) summarize the experimental lattice parameters and unit cell volumes of pure Mg_2Si and doped Mg_2Si. The cubic cell parameter of pure Mg_2Si a = 6.2843(9) Å is increased to 6.3506(9) Å to 6.3634(9) Å by the addition of the dopants (Zn, Al, and Sb). This can be rationalized as the atomic sizes of Zn and Al dopants are larger than Mg, and Sb, which replaces Si, also has a bigger size. We can conclude unequivocally that the cubic cells of all the doped samples are larger than pure Mg_2Si. The observations also lend support to the expectation that Al and Zn dopants will occupy the Mg sites, while Sb replaced Si in the Mg_2Si crystal structure. If this is the case, Al, Zn, and Sb doped Mg_2Si are *n*-type semiconductors. As will be shown later, this assignment is in agreement with the negative Hall coefficients.

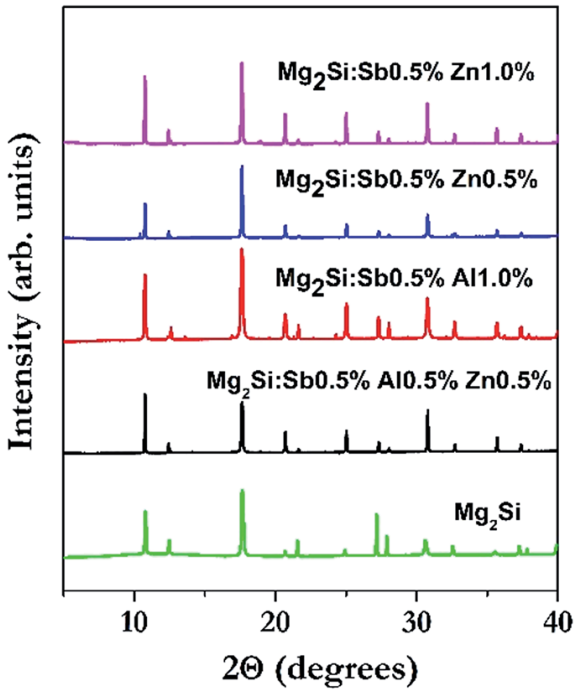

Fig. 5.1 Angle dispersive X-ray diffraction patterns of pure Mg_2Si and doped Mg_2Si measured at room temperature.

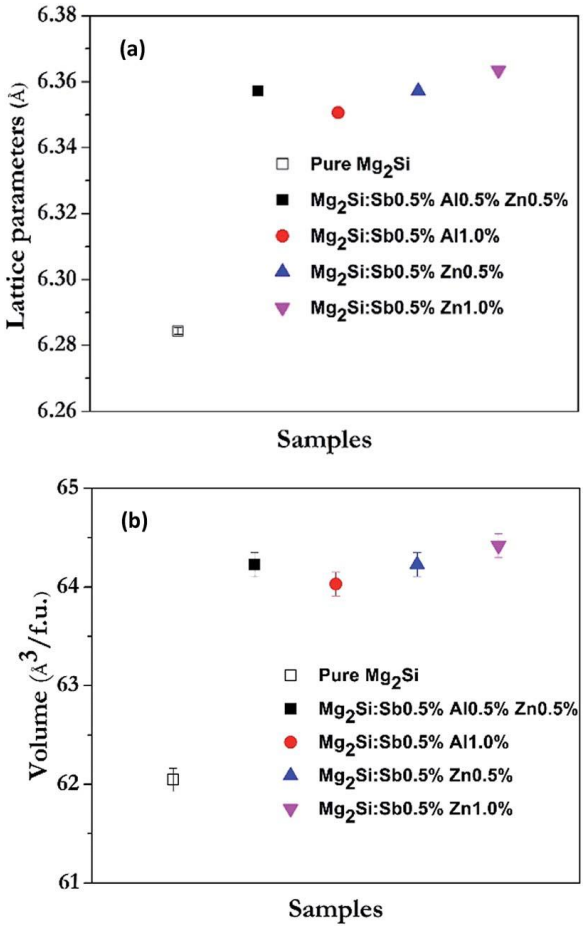

Fig. 5.2 (a) Lattice parameters of pure and doped Mg_2Si; (b) the volume per formula of pure and doped Mg_2Si.

Further analysis of the lattice constants of the doped samples show, for instance, when compared with Mg_2Si:Sb0.5% Zn0.5%, that the lattice constants of Mg_2Si:Sb0.5% and Zn1.0% are expanded, possibly due to the higher doping concentration of Zn. On the other hand, between Mg_2Si:Sb0.5%Zn1.0% and Mg_2Si:Sb0.5%Al1.0%, the only difference is the doped element (*i.e.* Zn *vs*. Al). The lattice parameter in Mg_2Si:Sb0.5%Zn1.0% is slightly larger, as the size of Zn is larger than Al. In comparison, the lattice parameter of Mg_2Si:Sb0.5%Zn0.5% is comparable with Mg_2Si:Sb0.5%Al0.5%Zn0.5%, suggesting that Al has a weaker effect on the expansion of the crystal lattice, probably due to the similar atom sizes of Al and Mg atoms.

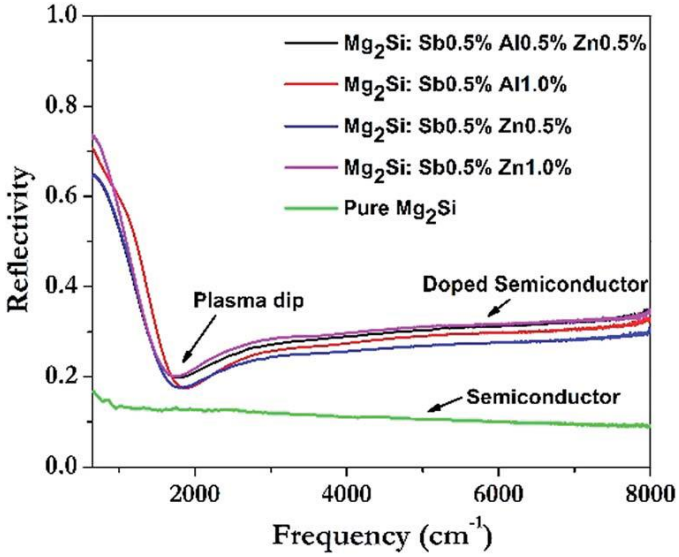

Fig. 5.3 Mid-infrared reflectivity spectra of pure and doped Mg_2Si.

Infrared reflectivity experiments can provide information on the electrical transport of a material. Mid-infrared reflectivity spectra were measured with an internal Globar radiation source (600-8000 cm^{-1}) installed at the U2A beamline on pure Mg_2Si and Mg_2Si multi-doped with Sn Zn and Al. The electronic transport properties of the doped samples were extracted. The experimental reflectivities of pure and multi-doped Mg_2Si are compared in Fig. 5.3. The infrared reflectivity of all the doped Mg_2Si samples exhibits a Drude-like behavior at low frequency

indicative of doped semiconductors. In comparison, the undoped Mg_2Si sample does not have the free electron-like feature, indicating that it is a semiconductor with a small band gap. This is to be expected as Mg_2Si is a semiconductor with a small indirect band gap of 0.6 eV. [27] In comparison to the flat and featureless reflectivity of pure Mg_2Si, the reflectivities of the multi-doped samples extrapolated to zero frequency are much higher. Note that a good conductor, such as copper or aluminum, has a reflectivity close to unity at zero frequency.

The Sb, Zn, Al-doped Mg_2Si samples show a common feature in the reflectivity curves around 1800 cm^{-1}. It is the appearance of a "dip" in the spectra. The minimum in the reflectivity is the characteristic of a doped semiconductor and is known as the plasma reflection edge or plasma dip. [28] According to the simple Drude model, the energy at the energy minimum (plasma frequency ω_P) is related to the carrier concentration (N) and the effective mass (m^*), $\omega_P^2 = Ne^2/\varepsilon\varepsilon_0 m^*$ where ε is the dielectric constant of the material, and ε_0 is the vacuum permittivity. [29] Therefore, the effective mass (m^*) of electrons in a doped semiconductor can be extracted from the plasma frequency (ω_P) provided the electron concentration (N) is known. Detailed results will be reported, analyzed and discussed below.

The frequency dependence conductivity, the optical conductivity, can be obtained by performing a Kramers-Kronig (K-K) analysis on the reflectivity data. [25] The procedure is as follows: the optical conductivity obtained from a variational K-K transformation is fitted to a Drude Lorentz (DL) model and the *dc* conductivity is estimated by extrapolation to zero frequency. A comparison illustrating the quality of the fit is shown in Fig. 5.5. In the figure, the raw and fitted infrared reflectivity spectra of 0.5% Sb&0.5% Zn doped Mg_2Si sample are compared. The *dc* conductivities of the doped samples obtained by this procedure are reported in Table 5.1. The Mg_2Si:Sb0.5% Zn1.0% sample is found to have the highest *dc* conductivity of

767 S cm^{-1} and an extrapolated reflectivity of ~0.73 at zero frequency. The trend of the *dc* conductivities extracted from infrared reflectivity agrees qualitatively with bulk electrical measurements. [26]

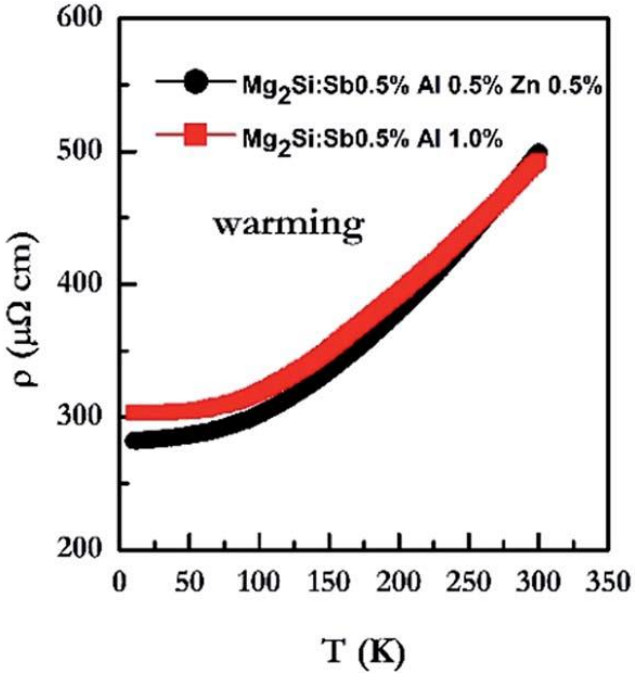

Fig. 5.4 Temperature dependent electrical resistivity of doped Mg_2Si by the conventional quasi-four-probe method.

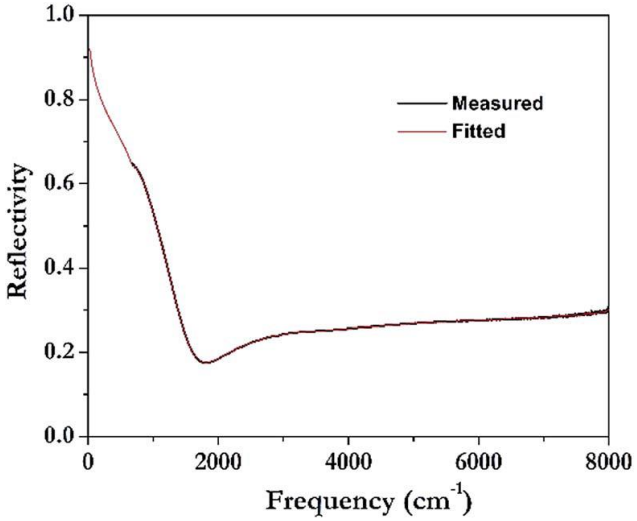

Fig. 5.5 A comparison of measured and fitted infrared reflectivity spectra of 0.5% Sb & 0.5% Zn doped Mg_2Si.

Table 5.1 Summary of the *dc* conductivity (σ_0) & carrier relaxation time (τ) of doped Mg_2Si.

Compound	σ_0 (Scm^{-1})	τ (s)
Mg_2Si:Sb0.5%Al0.5%Zn0.5%	507	3.72×10^{-14}
Mg_2Si:Sb0.5%Al1.0%	627	3.94×10^{-14}
Mg_2Si:Sb0.5% Zn0.5%	480	3.77×10^{-14}
Mg_2Si:Sb0.5%Zn1.0%	767	5.57×10^{-14}

The static *dc* conductivity increased dramatically from pure Mg_2Si, due to the larger concentration of free electrons in the conduction band by doping with Zn, Al, and Sb. From the free electron model, dc conductivity is proportional to the electron concentration (*N*) and scattering time (τ). The electron scattering time (τ) is a parameter in the Drude-Lorentz model and can be obtained from the fitting of the reflectivity data. [28] The fitted relaxation times of doped Mg_2Si samples are tabulated in Table 5.1. The derived relaxation times of *ca*. 10^{-14} s are consistent with other doped semiconductors. The electron concentration (*N*) in a doped semiconductor is the density of the mobile electrons or holes (*n*- or *p*-doped). Since the host crystal Mg_2Si is the same for all samples, the *dc* conductivity depends only on the nature of the dopants. The dramatic enhancement of the *dc* conductivity by the dopants is due to the occupation of the free electron-like conduction bands. In spite of the simplicity of the Drude-Lorentz model and the neglect of low frequency (<600 cm^{-1}) absorption which is not accessible by mid-infrared radiation, the results indicate that the *dc* conductivity can be improved by addition of the (Zn, Al and Sb) dopants.

Although the trend of increasing electrical resistivity and reflectivity is the same from IR reflectivities and four-probe conductivity measurements, the comparison of the absolute magnitude is less satisfactory (Fig. 5.6). The *dc* conductivities derived from infrared reflectivity has the same order of magnitude as the bulk measurements, but are approximately four times smaller. One contributing factor may be the infrared beam only surveyed a very small region (20 × 20 μm^2) within a couple of microns into the sample surface. This is different from the quasi-four-probe conductivity method which is a bulk sensitive technique. At the sample surface the atom density is less than the bulk and the chemical bonding in the surface is also stronger. [30,31] Therefore, there are less free electrons near the sample surface thus reducing the electrical conductivity. Although plausible, this effect cannot satisfactorily explain the discrepancy observed here. Since the *dc* conductivity was obtained from the extrapolation of the frequency dependent conductivity to zero frequency, it is not certain if the omission of reflectivity at very low energy (*i.e.* <600 cm^{-1}) may have an effect. From the past experience, we expect that the *dc* conductivity derived from an IR measurement should agree within an order of the magnitude of the value obtained from the bulk technique. [10,32] We found no systematic error in the experiment and on the treatment of the data. In a previous study, we have also compared the *dc* conductivity derived from IR reflectivities to bulk measurements on doped Mg_2Si and the agreements were favorable. [10] We suspect that the most likely source of the disagreement may be related to a precise knowledge on the concentration of the dopants. The doped samples used in this study were synthesized by the plasma spark sintering method. It is very difficult to control the precise stoichiometry. Another possible source of the discrepancy may be due to the non-uniform distribution of dopants in the sample. In a study of Sb and Bi doped-Mg_2Si, it was found by high resolution transmission microscopy (TEM) that due to the

limited solubility excess Sb and Bi atoms are present in the grain boundaries that may enhance the conductivity of the bulk sample. [10] In comparison, IR measurements only examine a very small spot of *ca*. 20 × 20 μm^2 of the sample so this may produce different results. Finally, the formation of a thin oxide layer on the surface may also contribute to the lower conductivity derived from the IR experiments. A careful characterization of both samples is critical to resolve the discrepancy.

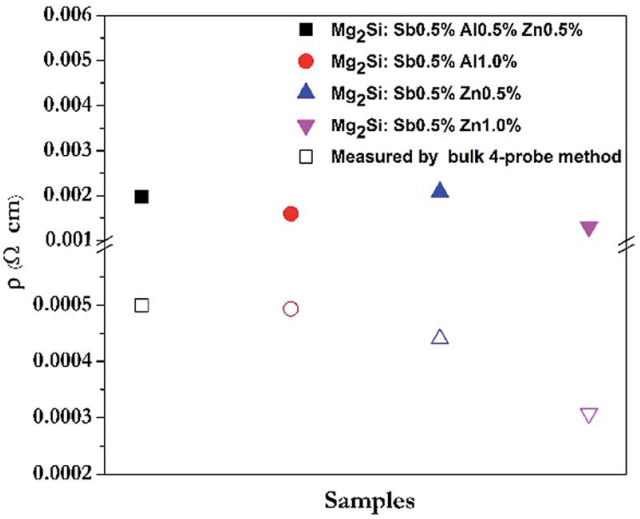

Fig. 5.6 A comparison of electrical resistivity (ρ) extracted from infrared reflectivity spectra and measured by the quasi-four-probe method.

The bulk electrical transport properties of the Zn, Al and Sb multi-doped Mg_2Si samples were determined by temperature dependent electrical resistivity and the Hall coefficient by the quasi-four-probe method. The temperature dependent electrical resistivities (ρ) of doped Mg_2Si samples (Fig. 5.4) were measured with a current of 3 mA and sectional areas between 1.05 × 0.78-1.45 × 1.01 mm^2. It is found that the electrical resistivity of Mg_2Si:Sb0.5%Al1.0% increased from 300 μΩ cm to 500 μΩ cm from 10 K to 300 K. At 300 K, the electrical resistivity in Mg_2Si:Sb0.5%Zn1.0% is smaller than the other doped samples of 430-500 μΩ cm. The results suggest that there are more free electrons in the conduction band of the other samples leading to higher electrical conductivity. Comparing Mg_2Si:Sb0.5%Zn0.5% and Mg_2Si:Sb0.5%Zn1.0%, the

electrical resistivities were found to decrease with concentration of the Zn dopant. Since the concentrations of Sb were the same in these two samples and the Zn atoms were expected to occupy the Mg sites, this conductivity trend suggests that there are more mobile electrons in the conduction band with more Zn dopants.

The measured Hall coefficients (R_H) of Zn, Al, and Sb-doped Mg_2Si samples are shown in Fig. 5.7. The negative and almost constant Hall coefficients show that the multi-doped Mg_2Si materials are *n*-type doped semiconductors. Using the equation $N = 1/(eR_H)$, (where e is the electron charge and R_H is the Hall coefficient) the electron concentrations (N) were calculated and are shown in Table 5.2. Possibly, Mg_2Si:Sb0.5%Al1.0% has the largest electron concentration (N) of 1.78×10^{20} cm^{-3}, due to the high doping concentration. The electron concentration (N) of the multi-doped Mg_2Si samples of $ca.10^{20}$ cm^{-3} is in reasonable agreement with that estimated from the free electron model. Therefore doped-Mg_2Si is a doped semiconductor. [28] The results are supported by the low plasma frequencies of the doped samples. The low plasma frequencies observed in the IR region is also indicative of a doped semiconductor.

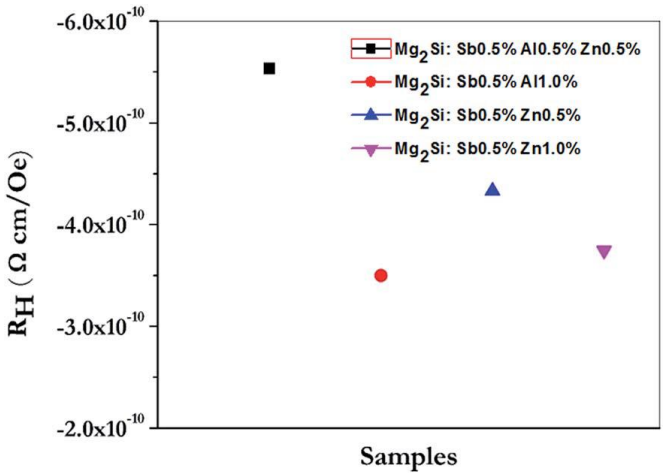

Fig. 5.7 Hall coefficients (R_H) of doped Mg_2Si samples were measured by the quasi-four-probe method.

Table 5.2 Summary of the electron concentration (N) calculated from the Hall coefficient (R_H) of doped Mg_2Si.

Compound	R_H (cm^3C^{-1})	N (cm^{-3})
Mg_2Si:Sb0.5%Al0.5%Zn0.5%	-5.53×10^{-2}	1.17×10^{20}
Mg_2Si:Sb0.5%Al1.0%	-3.50×10^{-2}	1.78×10^{20}
Mg_2Si:Sb0.5% Zn0.5%	-4.33×10^{-2}	1.44×10^{20}
Mg_2Si:Sb0.5%Zn1.0%	-3.75×10^{-2}	1.67×10^{20}

The electron effective mass can be calculated from the plasma frequency observed in the infrared reflectivity and the electron concentration from the Hall coefficient. [33] The plasma frequency ω_p is related to the electron concentration (N) and the electron effective mass in the sample (m^*) by $\omega_p^2 = Ne^2/\varepsilon\varepsilon_0 m^*$, where ε is the dielectric constant of the material, and ε_0 is the vacuum permittivity. [34] Therefore, the electron effective mass (m^*) is inversely proportional to the square of plasma frequency (ω_p). Assuming a constant optical dielectric constant (ε) of 12.82 for doped Mg_2Si samples, [35] the electron effective masses were calculated for all the doped Mg_2Si samples studied. As shown in Table 5.3, the effective masses of electrons in doped Mg_2Si

samples are between $0.255m_e$ and $0.361m_e$, where m_e is the mass of a free electron. The light effective masses found in this work are comparable with previous measurements listed in Table 5.4. Electrons with lighter effective mass are easier to move in the conduction band and therefore contribute to a higher electrical conductivity. The light effective masses *i.e*. $0.255m_e$ to $0.361m_e$ of doped Mg_2Si show the occupation of the free-electron-like conduction band by the excess electron donated by the dopants. [11]

Table 5.3 Summary of the effective mass (m^*) of doped Mg_2Si calculated from the plasma frequency (ω_P) within the infrared reflectivity.

Compound	ω_P (cm^{-1})	m^*/m_e
Mg_2Si:Sb0.5%Al0.5%Zn0.5%	1791	0.255
Mg_2Si:Sb0.5%Al1.0%	1899	0.346
Mg_2Si:Sb0.5% Zn0.5%	1788	0.316
Mg_2Si:Sb0.5%Zn1.0%	1798	0.361

Table 5.4 Summary of the effective masses for pure and *n*-doped Mg_2Si reported in the literature.

Pure Mg_2Si	$0.4m_e$ [36]	$0.5m_e$ [37]	
$Mg_2Si_{0.98}Sb_{0.02}$	$1m_e$ [36]	$1.06m_e$ [10]	$1.1m_e$ [38]
$Mg_2Si_{0.98}Bi_{0.02}$	$0.62m_e$ [10]	$0.5m_e$ [39]	

To define the thermoelectric properties of doped Mg_2Si samples, the temperature dependent electrical conductivity (σ), Seebeck coefficient (S), power factor ($S^2\sigma \times T$), and thermal conductivity (κ) were measured up to 900 K, and the corresponding figure of merit (ZT) was calculated. As shown in Fig. 5.8(a)-(e), the electrical conductivity of doped Mg_2Si decreases

from 2.5 $\times 10^5$ S m^{-1} to 0.8 $\times$ 10^5 S m^{-1} when the temperature is increased from 300 K to 900 K. The highest electrical conductivity obtained in the present study is 2.6 $\times$ 10^5 Sm^{-1} for Mg_2Si:Sb0.5%Zn0.5% at room temperature (300 K). The electrical conductivity of double or multi-doped Mg_2Si is substantially higher when compared to the un-doped Mg_2Si (15 Sm^{-1}). [19] A small amount of dopants (0.5-1.0%) is found to have a dramatic impact on the electrical conductivity. In all four multi-doped Mg_2Si samples, an increase of electrical conductivity was observed. The conductivities derived from infrared reflectivities show that the correct trend expected from the free electron model (*i.e.* the conductivity of Mg_2Si:Sb0.5% Al1.0% is higher than that of Mg_2Si:Sb0.5%Zn0.5%) as Al donates more electrons than Zn when substituted in the Mg sites. The reverse was apparently observed in the bulk measurements (Fig. 5.8). This discrepancy may be attributed to the non-homogeneity of the dopants. Moreover, the free electron model is only a simplification and the true conductivity also depends on the effective mass of the conducting electron, which is related to the dispersion of the occupied conduction band. If the bulk measurements are more representative of the properties of the sample, we may speculate that the effective mass of the conducting electrons in Mg_2Si:Sb0.5%Al1.0% is heavier. In fact, as shown in Table 5.3, the derived effective mass of the electron in Mg_2Si:Sb0.5%Al1.0% of 0.346m_e is heavier than that in Mg_2Si:Sb0.5%Zn0.5% of 0.316m_e. It is interesting to note that there is a distinctive discontinuity in the Mg_2Si:Sb0.5%Al0.5%Zn0.5% at 450-500 K which will be discussed below (*vide supra*).

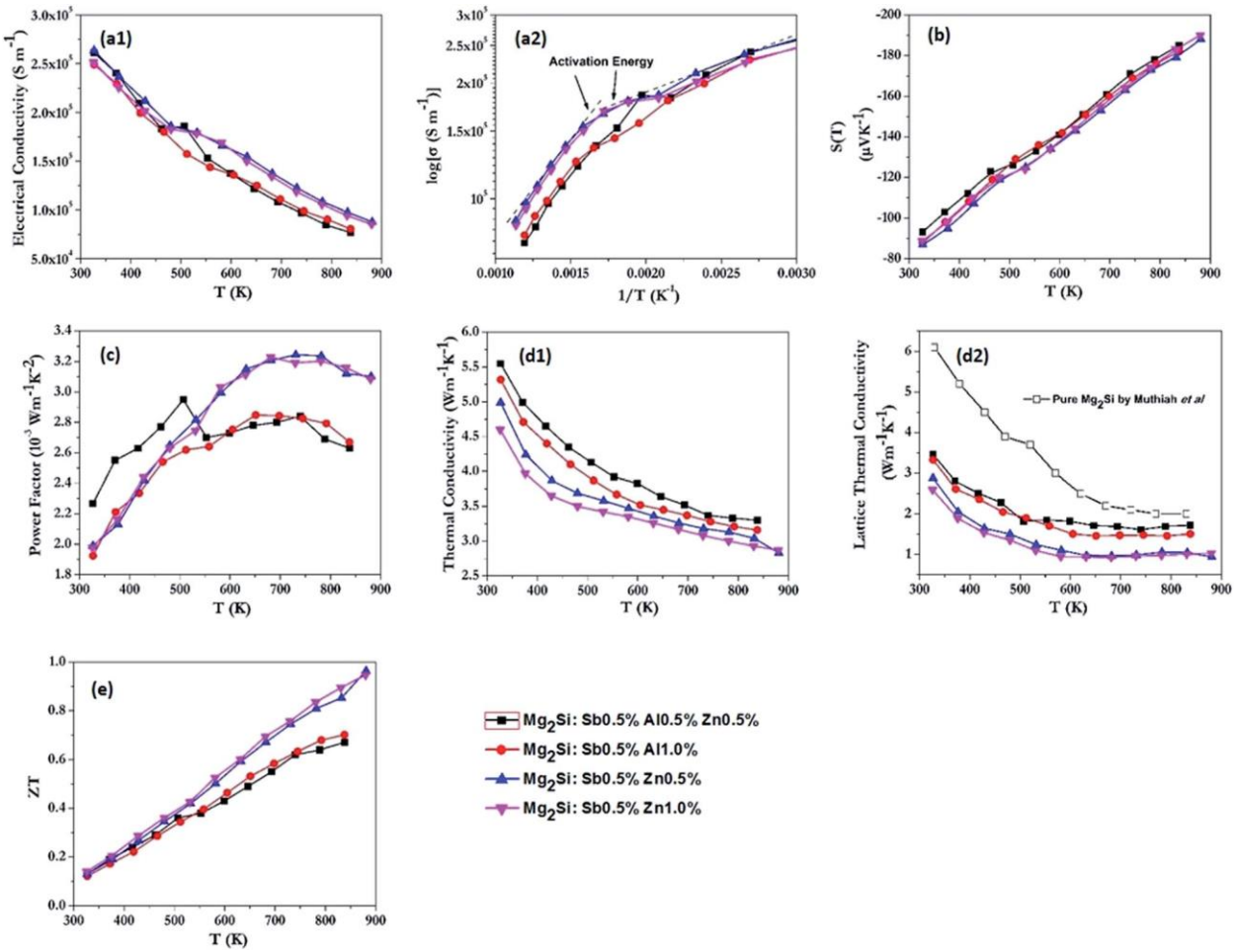

Fig. 5.8 Temperature dependent (a1) & (a2) electrical conductivity, (b) Seebeck coefficient, (c) power factor, (d1) & (d2) thermal conductivity & lattice thermal conductivity, and (e) figure of merit (*ZT*).

The temperature dependence of the electrical conductivity shows a discontinuity at 500 K. Even the material is metallic we used an Arrhenius-like equation $\rho = \rho_0 \exp(-E_t/kT)$ to highlight the discontinuity. In the equation ρ is the electrical resistivity, ρ_0 is the high temperature resistivity, E_t is the "activation" energies, k is the Boltzmann constant, and T is the temperature. The values of E_t are determined from the plot of $\ln(\rho)$ vs. $(1/T)$. As shown in Fig. 5.8(a1) & (a2), between 450 K and 550 K, the trend of Mg_2Si:Sb0.5%Al0.5%Zn0.5% does not follow the relationship with increasing the temperature as the others. The sudden change of activation energy (E_t) further implies that a possible structure change has occurred. [40] Since

the high temperature crystal structure is still unknown, a definitive characterization requires a high temperature X-ray diffraction powder diffraction study.

Throughout the temperature range studied, the Seebeck coefficients (*S*) of Sb, Al, and Zn multi-doped Mg_2Si samples are negative confirming that they are *n*-doped semiconductors, in agreement with the Hall coefficients. The values for the temperature dependent Seebeck coefficient (*S*) are quite similar for all doped samples, suggesting that the dopants play a similar role in enhancing the Seebeck coefficient. The Seebeck coefficient increased from -90 mVK^{-1} to -190 mVK^{-1} with increasing temperature and reached a maximum value at 900 K. The Seebeck coefficients for the doped Mg_2Si samples are comparable with the previously reported Bi, Pb, and Sb double-doped Mg_2Si. [19] For the un-doped Mg_2Si sample, the Seebeck coefficient increased initially with increasing temperature and reached the maximum value at 450 K. Above 450 K, the value of the Seebeck coefficient started to decrease.

Fig. 5.8(c) shows the calculated power factor ($S^2\sigma \times T$) of doped Mg_2Si samples. The general trend of the calculated temperature dependent power factor increased initially and peaked at ~750 K and then decreased with further increase of the temperature. The maximum power factor is due to the effect that the Seebeck coefficient (*S*) increases faster than the decrease in the electrical conductivity (σ). With further increase in temperature, the power factor decreases gradually, as the electrical conductivity (σ) becomes more important to the power factor than the Seebeck coefficient (*S*). A peak power factor of 2.9×10^{-3} $Wm^{-1}K^{-2}$ was found at 500 K in Mg_2Si:Sb0.5%Al0.5%Zn0.5%, close to the possible structural phase transition. Fig. 5.8(d1) shows the temperature dependent thermal conductivity of the doped Mg_2Si samples. The general trend of the thermal conductivities is to decrease with increasing temperature. This is obviously due to the increase in phonon scatterings at higher temperature. At 310 K, the thermal

conductivity of Mg_2Si: Sb0.5%Al0.5% Zn0.5% (5.6 $Wm^{-1}K^{-1}$) is higher than those of other doped Mg_2Si samples. However, all the thermal conductivities of doped Mg_2Si samples are lower than that of un-doped Mg_2Si (6.2 $Wm^{-1}K^{-1}$). Phonon scattering becomes more efficient in the presence of heavier dopants in the lattice. The total thermal conductivity (κ_{total}) can be separated into two contributions: the lattice conductivity (κ_{ph}) and the electronic conductivity (κ_{el}). The electronic conductivity (κ_{el}) can be estimated by the Wiedemann-Franz law, where $\kappa_{el} = L\sigma T$ (the Lorentz number (L) is 2.45×10^{-8} V^2K^{-2}). [41] The lattice thermal conductivity (κ_{ph}) can then be estimated by subtracting the electronic thermal conductivity (κ_{el}) from the total thermal conductivity (κ_{total}). Considering the major contribution of lattice thermal conductivity (κ_{ph}) to the total thermal conductivity (κ_{total}), Fig. 5.8(d2) shows the temperature dependency of the lattice thermal conductivity (κ_{ph}). Compared to Al, the heavier Zn dopants are better phonon scatterers, leading to lower lattice thermal conductivity. The observed trend, Mg_2Si:Sb0.5%Al0.5%Zn0.5% > Mg_2Si:Sb0.5%Al1.0% > Mg_2Si:Sb0.5%Zn0.5% > Mg_2Si:Sb0.5% Zn1.0%, is expected. Similarly, the lattice thermal conductivities of Mg_2Si:Sb0.5%Zn0.5% and Mg_2Si:Sb0.5%Zn1.0% samples are lower than those of others because the phonon scattering becomes more efficient in the presence of heavier Zn dopants. The only exception is Mg_2Si:Sb0.5%Al0.5%Zn0.5% which has a higher thermal conductivity than Mg_2Si:Sb0.5% Al1.0%. At this moment, we cannot provide a satisfactory explanation for this observation. Using the information obtained above, the temperature dependent figure of merits (ZT) were calculated (Fig. 5.8(e)). For each doped-Mg_2Si sample, ZT increased significantly with increasing temperature. A maximum ZT of 0.964 is found in Sb0.5%Zn0.5% doped Mg_2Si at 880 K.

5.4 Conclusions

The structural information of Sb, Al, and Zn multi-doped Mg_2Si powder samples synthesized from spark plasma sintering has been obtained by angle dispersive synchrotron radiation X-ray diffraction, infrared reflectivity, electrical and thermal conductivity measurements. A small concentration of the dopant (0.5-1.0%) did not alter the cubic crystal structure of the host Mg_2Si, but expanded the crystal lattice noticeably. The electrical transport properties were characterized by mid-IR reflectivity and quasi-four probe measurements. Infrared reflectivity shows the doped semiconductor character for all the samples at room temperature. The *dc* conductivities calculated from the analysis of the infrared reflectivity spectra employing the Drude-Lorentz model are in qualitative agreement with the conventional bulk four-probe measurements although the absolute values obtained from IR reflectivities are consistently lower. The electron concentrations (N) were determined from the Hall coefficients and plasma frequencies (ω_P) of the infrared reflectivities. The multi-doped Mg_2Si is within the order 10^{20} cm^{-3}, suggesting that all doped-Mg_2Si are doped semiconductors. The effective masses ranged from $0.255m_e$ to $0.361m_e$ showing that different dopants have a slight effect on the band structure of Mg_2Si. A maximum thermoelectric figure of merit (ZT) of 0.964 was achieved for the Sb0.5%Zn0.5% doped Mg_2Si sample at 880 K. The present study provides new results and insight into the thermoelectric and electrical transport properties of Sb Al Zn multi-doped Mg_2Si in the temperature range of 300 K to 900 K. The information presented here may help to further enhance the performance of Mg_2Si-based thermoelectric materials.

Acknowledgements

Synchrotron work at the Canadian Light Source was made possible by support from NSERC, NRC, CIHR, and the University of Saskatchewan. The use of the U2A beamline was

supported by COMPRES under NSF Cooperative Agreement EAR 11- 57758 and CDAC (DE-FC03 03N00144). The National Synchrotron Light Source, Brookhaven National Laboratory, was supported by the U.S. Department of Energy, Office of Science, Office of Basic Energy Sciences under Contract No. DE-AC02- 98CH10886. The sample preparation and thermoelectric measurements were partly supported by a Grant-in-Aid for Research (A) by the Japanese Ministry of Education, Science, Sports, and Culture. The electrical resistivity measurement was supported by JSPS KAKENHI Grant Number 15F15023. JZ and JST thank AUTO21 for a research grant.

References

[1] T. Sakamoto, T. Iida, S. Kurosaki, K. Yano, H. Taguchi, K. Nishio, and Y. Takanashi, *Journal of Electronic Materials*, 2011, 40, 629-634.

[2] S. Battiston, S. Fiameni, M. Saleemi, S. Boldrini, A. Famengo, F. Agresti, M. Stingaciu, M. S.Toprak, M. Fabrizio, and S. Barison, *Journal of Electronic Materials*, 2013, 42, 1956-1959.

[3] T. Sakamoto, T. Iida, A. Matsumoto, Y. Honda, T. Nemoto, J. Sato, T. Nakajima, H. Taguchi, and Y. Takanashi, *Journal of Electronic Materials*, 2010, 39, 1708-1713.

[4] S. You, K. Park, I. Kim, S. Choi, W. Seo, and S. Kim, *Journal of Electronic Materials*, 2011, 41, 1675-1679.

[5] J. Tani and H. Kido, *Intermetallics*, 2008, 16, 418-423.

[6] N. Wang, H. Chen, H. He, W. Norimatsu, M. Kusunoki, and K. Koumoto, *Scientific Reports*, 2013, 3, 3449.

[7] Q. Chen, Q. Xie, F. Zhao, D. Cui, and X. Li, *Chinese Science Bulletin*, 2010, 55, 2236-2242.

[8] G. J. Snyder, and E. S. Toberer, *Nature Materials*, 2008, 7, 105-114.

[9] G. H. Kim, L. Shao, K. Zhang, and K. P. Pipe, *Nature Materials*, 2013, 12, 719-723.

[10] N. Farahi, M. VanZant, J. Zhao, J. S. Tse, S. Prabhudev, G. A. Botton, J. R. Salvador, F. Borondics, Z. Liu and H. Kleinke, *Dalton Transactions*, 2014, 43, 14983.

[11] M. Akasaka, T. Iida, A. Matsumoto, K. Yamanaka, Y. Takanashi, T. Imai, and N. Hamada, *Journal of Applied Physics*, 2008, 104, 013703.

[12] Y. Isoda, S. Tada, T. Nagai, H. Fujiu, and Y. Shinohara, *Materials Transactions*, 2010, 51, 868-871.

[13] Y. Isoda, S. Tada, T. Nagai, H. Fujiu, and Y. Shinohara, *Journal of Electronic Materials*, 2010, 39, 1531.

[14] H. Gao, T. Zhu, X. Liu, L. Chen, and X. Zhao, *Journal of Materials Chemistry*, 2011, 21, 5933.

[15] Z. Du, T. Zhu, Y. Chen, J. He, H. Gao, G. Jiang, T. M. Tritt, and X. Zhao, *Journal of Materials Chemistry*, 2012, 22, 6838.

[16] X. Liu, T. Zhu, H. Wang, L. Hu, H. Xie, G. Jiang, G. J. Snyder, and X. Zhao, *Advanced Energy Materials*, 2013, 3, 1238.

[17] A. U. Khan, N. Vlachos, and Th. Kyratsi, *Scripta Materialia*, 2013, 69, 606-609.

[18] H. Le-Quoc, S. Bechu, S. Populoh, A. Weidenkaff, and A. Lacoste, *Journal of Alloys and Compounds*, 2013, 546, 138-144.

[19] S. Muthiah, B. Sivaiah, B. Gahtori, K. Tyagi, A. K. Srivastava, B. D. Pathak, A. Dhar, and R. C. Budhani, *Journal of Electronic Materials*, 2014, 43, 2035.

[20] G. Jiang, J. He, T. Zhu, C. Fu, X. Liu, L. Hu, and X. Zhao, *Advanced Functional Materials*, 2014, 24, 3776.

[21] Y. Isoda, M. Held, S. Tada, and Y. Shinohara, *Journal of Electronic Materials*, 2014, 43, 2053.

[22] V. Petricek, M. Dusek, and L. Palatinus, *Z. Kristallogr*., 2014, 229, 345-352.

[23] A. Le Bail, H. Duroy, and J. L. Fourquet, *Materials Research Bulletin*, 1988, 23, 447-452.

[24] R. L. Kronig, *Journal of the Optical Society of America and Review of Scientific Instruments*, 1926, 12, 547-557.

[25] A. B. Kuzmenko, *Review of Scientific Instruments*, 2005, 76, 083108.

[26] N. V. Morozova, S. V. Ovsyannikov, I. V. Korobeinikov, A. E. Karkin, K. Takarabe, Y. Mori, S. Nakamura, and V. V. Shchennikov, *Journal of Applied Physics*, 2014, 115, 213705.

[27] M. Y. Au-Yang, and M. L. Cohen, *Physical Review*, 1969, 178, 1358.

[28] M. Fox, *Optical properties of solids*, 2nd edition, Oxford University Press, 2010.

[29] N. Farahi, S. Prahudev, G. A. Botton, J. Zhao, J. S. Tse, Z. Liu, J. R. Salvador, and H. Kleinke, *Journal of Alloys and Compounds*, 2015, 644, 249-255.

[30] D. M. Larson, K. H. Downing, and R. M. Glaeser, *Journal of Structural Biology*, 2011, 174, 420.

[31] S. Mafe, J. A. Manzanares, and P. Ramirez, *Physical Chemistry Chemical Physics*, 2003, 5, 376.

[32] J. W. L. Wong, A. Mailman, K. Lekin, S. M. Winter, W. Yong, J. Zhao, S. V. Garimella, J. S. John, R. A. Secco, S. Desgreniers, Y. Ohishi, F. Borondics, and R. T. Oakley, *Journal of The American Chemical Society*, 2014, 136, 1070.

[33] P. Perlin, E. Litwin-Staszewska, B. Suchanek, W. Knap, J. Camassel, T. Suski, R. Piotrzkowski, I. Grzegory, S. Porowski, E. Kaminska, and J. C. Chervin, *Applied Physics Letter*, 1996, 68, 1114.

[34] P. E. Blöchl, *Physical Review B*, 1994, 50, 17953.

[35] D. McWilliams, and D. W. Lynch, *Journal of the Optical Society of America*, 1963, 53, 298.

[36] Q. Zhang, *Rare Metal Materials and Engineering*, 2009, 38, 166.

[37] V. K. Zaitsev, M. I. Fedorov, E. A. Gurieva, I. S. Eremin, P. P. Konstantinov, A. Y. Samumin, and M. V. Vedernikov, *Phys. Rev. B: Condens. Matter*, 2006, 74, 045207.

[38] S. K. Bux, M. T. Yeung, E. S. Toberer, G. J. Snyder, R. B. Kaner, and J. P. Fleurial, *J. Mater. Chem.*, 2011, 21, 12259-12266.

[39] G. S. Nolas, D. Wang, and M. Beekman, *Phys. Rev. B: Condens. Matter*, 2007, 76, 235204.

[40] W. Ren, Y. Han, C. Liu, N. Su, Y. Li, B. Ma, Y. Ma, and C. Gao, *Solid State Communications*, 2012, 152, 440-442.

[41] C. Kittel, *Introduction to Solid State Physics*, 8th edition, NJ:Wiley, 2005.

CHAPTER 6

PRESSURE-INDUCED PHASE TRANSITION AND ELECTRICAL PROPERTIES OF THERMOELECTRIC Al-DOPED Mg_2Si

Besides dopants, pressure has also been used to enhance the thermoelectric power factor. Recently, Mg_2Si nominally doped with 1% Al was compressed to 2-3 GPa and the thermal power was found to increase significantly reaching a maximum value of 8×10^{-3} W/(K^2m). In this case, the increase in thermoelectric efficiency was also associated with an increase of electrical conductivity. Therefore it was suggested that the Al-doped sample had become metallic between 5 and 12 GPa. A Raman spectroscopy study also provided tantalizing evidence that two possible structural phase transitions had occurred at 5-7 GPa and 11-12 GPa. [10] To date, the structure and cause for the enhancement of thermal power of the lightly Al-doped Mg_2Si are not known. These form the focus of this investigation.

For this chapter, we investigated the effect of pressure on the thermoelectric performance of a sample of Al-doped Mg_2Si ($Mg_{1.99}Al_{0.01}Si$). Pressure can alter the band structure of a system but it may also induce structural transformation. At ambient pressure and temperature, Mg_2Si has a cubic anti-fluorite structure with the space group of *Fm-3m*. We performed *in-situ* X-ray diffraction and infrared reflectivity measurements up to 17 GPa at room temperature on pure Mg_2Si and Mg_2Si nominally doped with 1% Al. No structural transformation was observed in pure Mg_2Si. In contrast, a phase transition from the cubic anti-fluorite (*Fm-3m*) to an orthorhombic (*Pnma*) structure was observed in the Al-doped Mg_2Si sample at 10 GPa. Experimentally the thermal power was found to increase significantly reaching a maximum value of 8×10^{-3} W/(K^2m) under 2-3 GPa. From our analysis of the infrared reflectivity spectra, we concluded that the enhancement was mainly due to the increase of electrical conductivity associated with the structural phase transition. The results show pressure can affect the structures

and transport properties and helps to improve the electrical conductivity. The experimentally observed maximum thermoelectric power at 1.9 GPa is explained from the increase of the electronic density of states at the Fermi level obtained from DFT calculations.

The results of this investigation has been published in

J. Zhao, Z. Liu, R. A. Gordon, K. Takarabe, J. Reid, and J. S. Tse, "Pressure-induced phase transition and electrical properties of thermoelectric Al-doped Mg_2Si," *Journal of Applied Physics*, vol. 118, pp. 145902, 2015.

The authors' contributions are as follow:

- J. Zhao and J. S. Tse collected ambient and high-pressure powder X-ray diffraction and high-pressure infrared reflectivity spectrum, performed the analysis of all the experimental data, and calculated the electronic structures from ambient to high pressure.
- Z. Liu assisted in performing high-pressure infrared reflectivity experiments at BNL.
- R. A. Gordon assisted in performing high-pressure powder X-ray diffraction experiments at APS.
- K. Takarabe provided the samples in Japan.
- J. Reid assisted in performing ambient pressure powder X-ray diffraction experiments at CLS.
- All authors contributed to the writing and editing of the manuscripts.

Abstract

A recent study has shown the thermoelectric performance of Al-doped Mg_2Si materials can be significantly enhanced at moderate pressure. To understand the cause of this phenomenon, we have performed *in situ* angle dispersive X-ray diffraction and infrared reflectivity measurements up to 17 GPa at room temperature. Contrary to previous experiment, using helium as a pressure transmission medium, no structural transformation was observed in pure Mg_2Si. In contrast, a phase transition from cubic anti-fluorite (*Fm-3m*) to orthorhombic anti-cotunnite (*Pnma*) was observed in the Al-doped sample at 10 GPa. Infrared reflectivity measurements show the electrical conductivity increases with pressure and is further enhanced after the phase transition. The electron density of states at the Fermi level computed form density functional calculations predict a maximum thermoelectric power factor at 1.9 GPa, which is in good agreement with the experimental observation.

6.1 Introduction

Doped Magnesium silicide (Mg_2Si)-based alloys have been suggested as a candidate of a new generation of high performance and environmental friendly thermoelectric materials. [1-4] Compared with other lead-based thermoelectric materials, Mg_2Si-based alloys have the merits of being nontoxic, sustainable, and low cost. It is well known that the efficiency of thermoelectric materials may be increased through *p*- or *n*-type doping at ambient pressure. [5-9] A dopant can increase the carrier concentration and mobility of the conduction electrons. Doping with heavy atoms can affect the lattice vibrations and help to lower the thermal conductivity by increasing the phonon-phonon scatterings. Pressure can also be used to enhance the thermoelectric power factor. Recently, Mg_2Si nominally doped with 1% Al was compressed to 2-3 GPa, and the thermal power was found to increase significantly reaching a maximum value of 8×10^{-3}

$W/(K^2m)$. In this case, the increase in the thermoelectric efficiency is associated with an increase of electrical conductivity, and it was suggested that the Al-doped sample became metallic between 5 and 12 GPa. A Raman spectroscopy study also hinted at two possible structural phase transitions at 5-7 GPa and 11-12 GPa. [10] To date, the structure and the cause for the enhancement of the thermal power of the lightly Al-doped Mg_2Si are still not known. This is the focus of this investigation.

At ambient pressure and temperature, Mg_2Si has a cubic anti-fluorite structure (space group *Fm-3m*) and is a semiconductor with a small indirect band gap of 0.6 eV. [11] Using energy dispersive X-ray diffraction and silicone oil as the pressure medium, it was reported that Mg_2Si underwent a structural transition to an orthorhombic anti-cotunnite structure with space group *Pnma* at 7.5 GPa. Further compression led to a hexagonal Ni_2In-type *P63/mmc* structure at 21.3 GPa. [12,13] The high pressure structural phase transition behavior of pure Mg_2Si was re-investigated by Zhu *et al.* with an angle dispersive diffraction using NaCl as the pressure transmitting medium. [14] A phase transition from the anti-fluorite structure to the monoclinic structure was reported at 11.1 GPa. No further phase transition was found up to 37.5 GPa.

The discrepancy between the two diffraction measurements is unsettling and raises the question on the true identity of compressed Mg_2Si and the role of the pressure transmission medium to the crystal structure. This is further complicated by experimental resistivity measurements of undoped Mg_2Si, where three distinct regimes separated at 7, 12, and 22 GPa were observed, but Mg_2Si remained a semiconductor with the hint of eventual metallization at pressure exceeding 22 GPa. [15] Since theoretical calculations have predicted that the high pressure anti-cotunnite and Ni_2In structures are metallic, [16,17] the resistivity measurements clearly show there is no insulator → metal transition below 7 GPa. As will be shown and

discussed below, and contrary to earlier reports, [12,13] the present study reveals no structural phase transition in pure Mg_2Si up to 18 GPa. However, a structural phase transition was found in Al-doped Mg_2Si at 11 GPa.

Since the reflectivity is related to the dielectric function, frequency dependent optical conductivity can be extracted from the analysis. Static (*dc*) conductivities can be obtained by extrapolation to zero photon energy. *In-situ* high pressure far and mid-infrared reflectivity measurements have been performed on a nominal 1 at. % Al-doped Mg_2Si sample and compared to the results from bulk measurements. [10] The general trend that the electrical conductivity increases with pressure is the same as that found in previous measurements. Data analysis is complemented with theoretical density functional band structure calculations, which reveal a partially filled mid-gap band due to localized electronic interactions between the Al dopant with the surrounding host atoms is responsible for the enhancement of the thermopower.

The objective of this paper is to investigate the high pressure structure and the relationship to the transport properties of Al-doped Mg_2Si. For comparison, we have also examined the structure of pure Mg_2Si. For this purpose, room-temperature high resolution synchrotron angle dispersive synchrotron X-ray diffraction experiments up to 14.7 GPa using helium as the quasi-hydrostatic pressure-transmitting medium. Compared to silicone oil and NaCl, helium has the advantage of remaining in the liquid state at higher pressure and, therefore, able to maintain the isotropic strain of the sample in the diamond anvil cell (DAC).

The layout of the paper is as follows. First, details on the experimental procedure will be described. Diffraction results on pure Mg_2Si will be then compared with earlier studies. New results on the structure and structural transformation of Al-doped Mg_2Si under pressure will then

be presented. This is followed by a discussion on the electrical properties extracted from the analysis of far and mid-IR reflectivity spectra. Comparison of the electrical conductivity with the variation of theoretical electronic density of states (DOS) is then made. The paper concludes with a proposed mechanism for the increase in thermopower under pressure.

6.2 Experiment

Electron microprobe analysis: Powder Mg_2Si with a purity of 99.5% was purchased from Alfa Products. Mg_2Si doped with nominal 1 at. % of Al was synthesized by spark plasma sintering technique. To quantitatively examine the chemical compositions of Al-doped Mg_2Si powder samples, elemental analysis was performed on a JEOL 8600 Superprobe electron microprobe analyzer operating at 15 kV and 50 nA. The beam diameter was 5mm. Dwell time on the peak was 60 s. SPI metals were used as standards for each element. Random sites on a compressed powder sample were selected and analyzed to give an unbiased sampling of compositions.

High-pressure powder x-ray diffraction measurement: The ambient powder diffraction patterns for pure and 1% Al-doped Mg_2Si were measured at the CMCF beamline, Canadian Light Source (CLS). High-pressure X-ray diffraction experiments were performed at Sector 20, Advanced Photon Source (APS) at the Argonne National Laboratory, using synchrotron radiation (λ=0.47685Å). A DAC was used to generate the pressure. The powder sample was placed in the hole of a stainless steel gasket between the diamond anvils and then loaded with helium as the pressure transmitting medium. A ruby sphere was placed with the powder sample with the pressure determined from the peak shift of the ruby R_1 and R_2 fluorescence lines. [18] The maximum pressure studied was 14.7 GPa for pure Mg_2Si and 16.6 GPa for Al-doped Mg_2Si. The

diffraction patterns were analyzed using the JANA 2006 software package and the lattice parameters were determined by Le Bail fit. [19,20]

High-pressure infrared reflectivity measurement: High-pressure infrared reflectance spectra on 1% Al-doped Mg_2Si sample were measured at the side-station of the U2A beamline at the National Synchrotron Radiation Facility, Brookhaven National Laboratory. The mid-infrared spectra were recorded on a Bruker Vertex 80v FTIR spectrometer and a Hyperion 2000 IR microscope attached with a liquid nitrogen cooled HgCdTe detector.

The far-infrared spectra were recorded by a vacuum liquid helium cooled bolometer detector. Powder sample of Al-doped Mg_2Si was prepared and loaded into a stainless steel gasket placed between two 300 μm culets of a Sintek mini type IIa diamond anvil cell. A stainless steel gasket was preindented in the diamond anvil cell, and a 100 μm hole was drilled in the center of the indentation to serve as a sample chamber. Prior to the loading of the sample, the reflected power intensities of air-diamond base (I_d) and air-diamond culet (I_c) interfaces were measured at each pressure point. This process allowed us to minimize the error due to the intensity difference between diamond culet and base. After loading the sample and closing the DAC, the power intensity reflected from the air-diamond base (I_d) was measured again, and subsequently, the power intensity reflected from the sample-diamond interface (I_{sd}) was measured.

The reflectivity of sample-diamond interface (R_{sd}) was calculated as $R_{sd}=(I_{sd}/I_d)\times(I_d/I_c)\times(I_c/I_0)$, where I_0 is the power intensity reflected from gold foil. And I_c/I_0 is a constant of 0.185. All the spectral data were collected at a resolution of 4 cm^{-1} and accumulated for 512 scans. Once again, the fluorescence from a ruby crystal placed in the powder sample was used for pressure calibration.

Frequency dependent optical conductivity was obtained by Kramers-Kronig (K-K) analysis of the data obtained from normal incidence reflectivity measurements. [21] The data were subsequently fitted using a variational K-K constrained dielectric function, as implemented in the RefFIT code. [22] After the correction for the diamond contribution, the frequency dependent optical conductivity is derived from fitting to a Drude-Lorentz (DL) model, and the dc conductivity is obtained from the extrapolation to zero frequency.

Electronic structure calculations: First Principles electronic calculations were performed using density functional theory (DFT) within the Perdew-Burke-Ernzerh (PBE) of parameterization of the generalized gradient approximation (GGA) as implemented in the Vienna *ab initio* simulation package (VASP) code. [23-26] To obtain accurate band gap energy of pure Mg_2Si at ambient and high pressure, additional calculations were performed with the *GW* approximation (*GWA*), which utilized the one-particle Green's function and screened Coulomb interaction *W* to account for the effect of electrons to the electronic band structure. [27,28] For all calculations, the projector-augmented wave (PAW) [29,30] potentials constructed from the generalized PBE functional were used with $3s^2 3p^1$, $3s^2 3p^2$, and $2p^6 3s^2$ as valence electrons for the Al, Si, and Mg atoms, respectively. A 4×4×4 *k*-points mesh was used for total density of states (TDOS) and projected density of states (PDOS) calculations. A 1 at. % Al doped Mg_2Si was constructed from a 2×2×2 supercell of the crystal where one of the Mg atoms is replaced with Al (*i.e.*, $Mg_{63}Si_{32}Al$).

6.3 Results and Discussion

Room-temperature high resolution synchrotron angle dispersive X-ray diffraction patterns of pure Mg_2Si were measured up to 14.7 GPa (Figure 6.1) using helium as the pressure medium. It was shown in a recent report comparing argon and silicone oil as the pressure

transmission medium. [31,32] The linewidth of diffraction pattern in silicone oil is substantially broadened above 10 GPa. Compared to silicone oil and NaCl, helium has the advantage of remaining in the liquid state at higher pressure and, therefore, able to maintain the isotropic strain of the sample in the DAC. Furthermore, the diffraction patterns will be not interfered by the diffraction lines of NaCl. It is unlikely the helium will occupy the empty sites in Mg_2Si. Since Mg_2Si is built from a FCC Si lattice with Mg in the octahedral sites, the only possible site that helium atoms may diffuse into is the tetrahedral site. However, the powder diffraction pattern of pure Mg_2Si was measured independently without a medium. The cubic unit cell parameter determined at ambient pressure agrees well with the results obtained in the DAC extrapolated to zero pressure with helium as the medium. In addition, the lattice constant and volume fitted with the 3rd order Birch-Murnaghan equation of state (red lines) are also in reasonable agreement with results of theoretical calculations (Figure 6.2). Therefore, there is no evidence that the helium can incorporate in the crystal lattice.

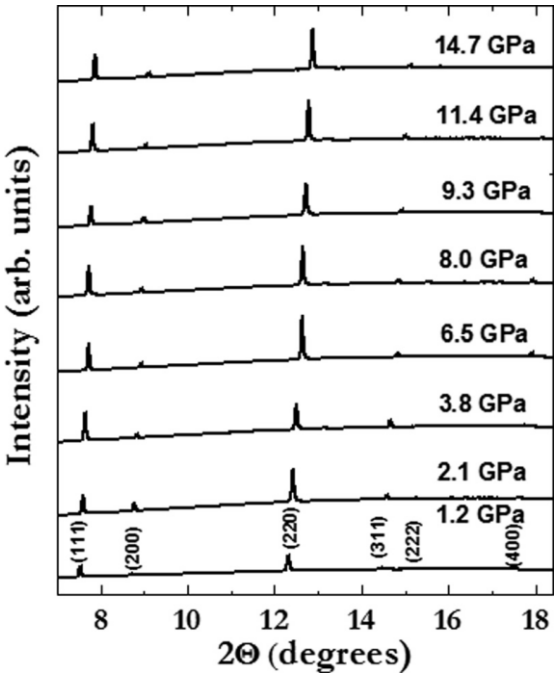

Fig. 6.1 Angle dispersive X-ray diffraction patterns of pure Mg_2Si at selected pressures measured at room temperature.

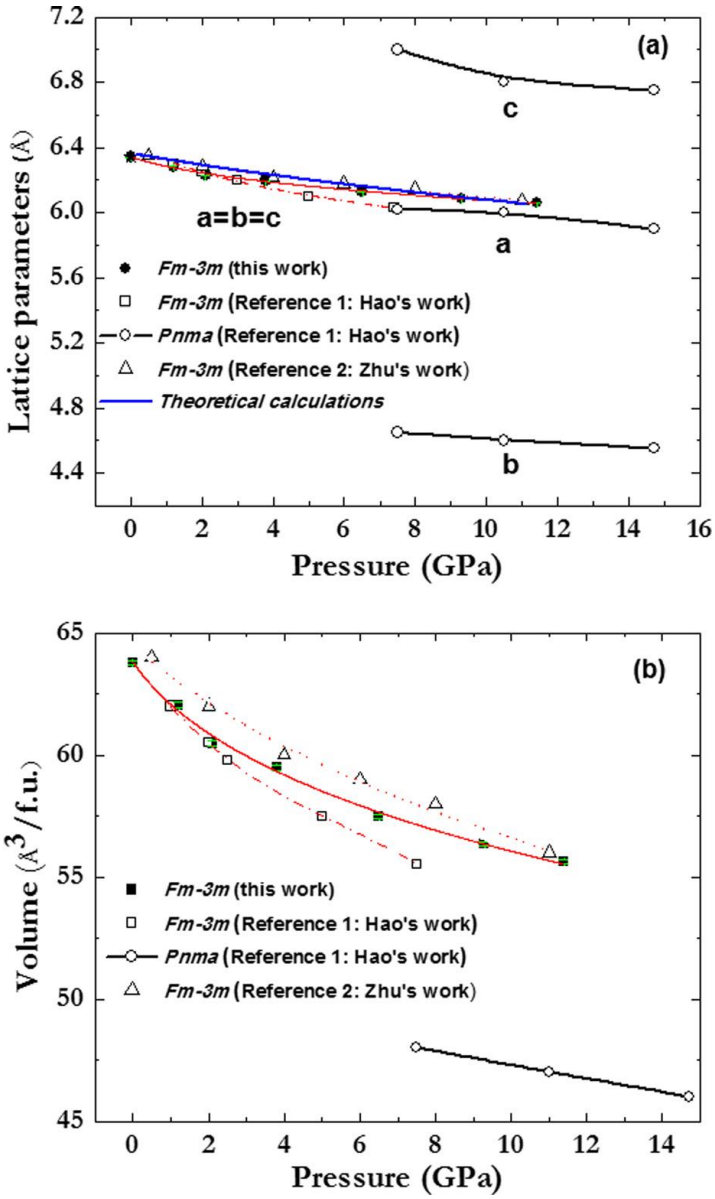

Fig. 6.2 (a) Lattice parameters of pure Mg_2Si as a function of pressure obtained in the present study and compared with previous works. (b) The volume per formula of pure Mg_2Si as a function of pressure and compared with previous works. The red color lines are fits to 3rd order Birch-Murnaghan equation of state.

It is important to point out that we observed no impurity peaks that can be attributed to MgO. The lattice constants were determined from full profile Le Bail fit to the diffraction peaks between 7º to 18º using the JANA 2006 software package. All the X-ray diffraction patterns can be indexed readily to the ambient pressure cubic anti-fluorite (CaF_2) structure with space group *Fm-3m*. The Miller indices (*hkl*) of the Bragg peaks are identified as (111), (200), (220), (311), (222), and (400) reflections with increasing scattering angles. No structural phase transition was found up to 14.7 GPa, the highest pressure studied. All diffraction patterns display the same profile except shifts of the Bragg peaks to higher angles with increasing pressure. The derived lattice parameters and unit cell volumes as a function of pressure were reported in Figures 6.2(a) and 2(b), respectively. The pressure coefficient for the cubic lattice determined from the experiment is -0.045Å/GPa. The lattice parameters are in good accord with previous results by Zhu *et al*. and Hao *et al*. within the overlapping pressure region up to 7.5 GPa. [13]

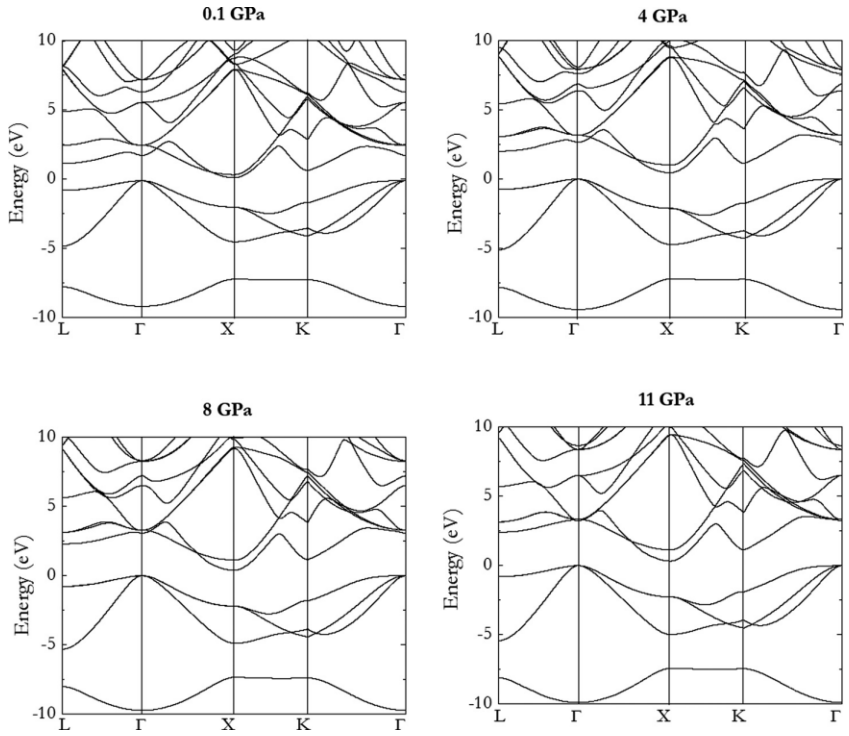

Fig. 6.3 *GW* band structures of pure Mg_2Si at 0.1, 4, 8, and 11 GPa.

To examine the electronic property of Mg_2Si at high pressure, theoretical density functional calculations with the PBE function were performed at 0, 4, 8, and 11 GPa (Figure 6.3). The calculated band structures were corrected for electron correlation effect as *GW*-correction. [40] Obviously, Mg_2Si is a semiconductor with the small band gap over this pressure range. The *GW* band gaps are 0.62, 0.46, 0.41, and 0.30 eV at 0, 4, 8, and 11 GPa, respectively. The theoretical results agree with the resistivity measurements that show Mg_2Si is an insulator at least up to 22 GPa. Together with the electrical measurements, structural transitions to the high pressure anti-cotunnite and Ni_2In phases at 7 and 11 GPa can be ruled out.

Experimental angle dispersive synchrotron radiation X-ray diffraction patterns of 1% Al-doped Mg_2Si were measured as a function of pressure up to 16.6 GPa (Figure 6.4). Again crystal lattice parameters were extracted from full profile of the diffraction patterns. At 0.9 GPa, diffraction peaks located at 7.5º, 8.7º, 12.3º, 14.5º, 15.1º, and 17.5º are indexed to (111), (200),

(220), (311), (222), and (400) reflections of the cubic anti-fluorite structure of Mg_2Si. Below 10.5 GPa, the diffraction patterns of 1% Al-doped Mg_2Si are similar to pristine Mg_2Si. At low pressure, a small amount of Al dopant is not expected to affect the crystal lattice of the host significantly.

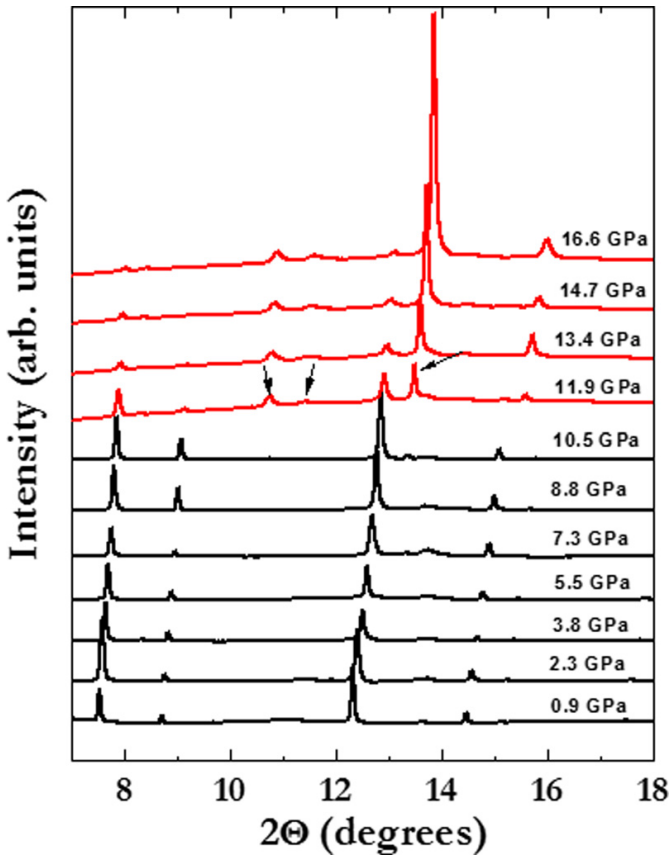

Fig. 6.4 Room temperature angle dispersive x-ray diffraction patterns of 1% Al-doped Mg_2Si at selected pressures.

The unit cell of Al-doped Mg_2Si is slightly larger than the pure Mg_2Si below 2 GPa. This suggests the Al dopants should occupy the Mg sites in the crystal structure. Therefore, under ambient conditions and low Al-doping concentration, Mg_2Si is expected to be an *n*-type semiconductor. This assignment is in agreement with the negative value of Hall coefficient reported. [10] The cubic structure is maintained up to 10.5 GPa. Interestingly, the derived pressure coefficient for the cubic lattice of 0.023 Å/GPa is substantially smaller than in the pure

sample. This observation indicates that even at 1% doping the Al-Mg_2Si crystal lattice is more resilient to compression. Figures 6.5 (a) and (b) show the pressure dependence of the lattice parameters and the unit cell volumes (Figure 6.5). At ambient pressure, the cell parameter of the cubic anti-fluorite structure (*Fm-3m*) of 6.2878(9) Å is reduced to 6.0261(11) Å at 10.5 GPa. Concomitantly, the cell volume per formula unit decreased from 62.15(12) $Å^3$ to 54.71(12) $Å^3$. It is interesting to note that the ambient pressure lattice constant obtained here with high resolution synchrotron radiation is noticeably shorter than the earlier report of 6.396(1) Å. [10] As will be discussed below (*vide supra*), this difference may have important implications on the transport properties. The experimental results conclusively indicated the anti-fluorite structure (*Fm-3m*) of Al-doped Mg_2Si is stable up to 10.5 GPa.

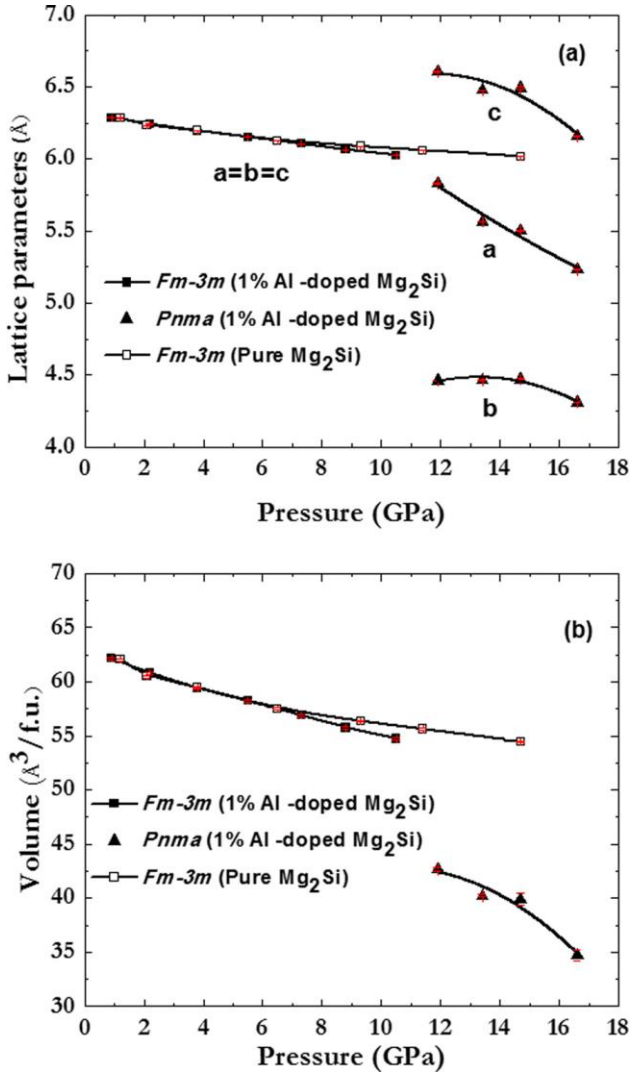

Fig. 6.5 (a) Lattice parameters of anti-fluorite (*Fm-3m*), and anti-cotunnite (*Pnma*) phases for Al-doped Mg_2Si and pure Mg_2Si as a function of pressure. (b) The volume per formula of Al-doped Mg_2Si and pure Mg_2Si as a function of pressure.

Above 11.9 GPa, three new diffraction peaks marked by arrows in Figure 6.4 have emerged, indicating a change in the crystal structure. The new peaks at 10.7º, 11.4º, and 13.5º can be indexed to an orthorhombic anti-cotunnite (*Pnma*) structure with a=5.8282(20) Å, b=4.6313(12) Å, and c=6.6059(23) Å. The strong diffraction peaks at 7.5º, 8.7º, and 12.3º can still be assigned to the cubic anti-fluorite structure (*Fm-3m*), indicating that the orthorhombic anti-cotunnite (*Pnma*) structure co-exists with the cubic anti-fluorite structure (*Fm-3m*) at this pressure. The amount of the cubic structure decreased with increasing pressure and eventually

vanished at 16.6 GPa. Concomitantly, the diffraction peaks around 10.7º, 11.4º, and 13.5º, corresponding to orthorhombic anti-cotunnite (*Pnma*) structure, increased gradually and became dominant. Therefore, the diffraction results show unambiguously a structural phase transition of Al-doped Mg_2Si had occurred around 11.9 GPa and was completed at 16.6 GPa. This structural transformation is accompanied by a large volume reduction of almost 23%. The experimental equation of state (volume *vs*. pressure) shown in Figure 6.5 indicates that the anti-cotunnite phase is more compressible than the cubic structure.

In the previous high energy dispersive X-ray diffraction study of pure Mg_2Si using silicone oil as the pressure medium, the same *Fm-3m* to *Pnma* transition was observed at 7.5 GPa where the volume collapsed from the cubic structure of 56.3 $Å^3$/f.u to *Pnma* of 49.4 $Å^3$/f.u, a reduction of 12.3%. [13] The transition in Al-doped Mg_2Si was observed at a higher pressure of 10 GPa, and the volume reduced by 18% from the cubic phase of 55 $Å^3$/f.u to *Pnma* 45 $Å^3$/f.u. Therefore, the volume changes are comparable.

The behavior of pressure-induced structural phase transition for Al-doped Mg_2Si is different from pristine Mg_2Si which shows no structural transition up to 14.7 GPa. The phase transformation is related to the Al dopant in the crystal structure. A larger atomic size of Al compared to Mg expanded the cubic crystal lattice at low pressure, resulting in a smaller pressure coefficient (*vide supra*). We speculate this mismatch in the atomic size helps to promote the structural transformation at high pressure.

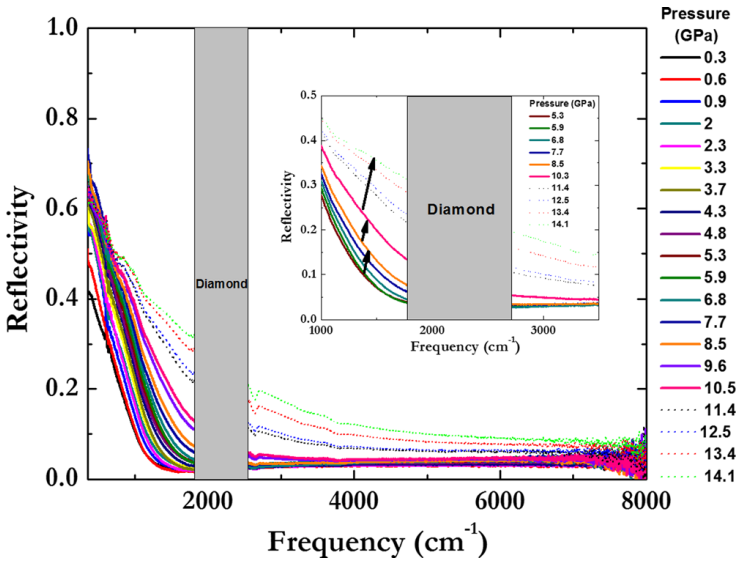

Fig. 6.6 Infrared reflectivity spectra of 1% Al doped Mg_2Si under different pressures.

The measured reflectivities from ambient to 14 GPa are shown in Figure 6.6. Even at ambient pressure, the IR reflectivity shows a Drude-like behavior at a low frequency implying a metallic-like behaviour. In Mg_2Si, the valence bands are completely filled, the electrons provided by the Al dopants must occupy the conduction band. By definition, the partial occupation of the conduction band is a metal. A practical definition for a metal is that the electrical conductivity should decrease with temperature. Previous experiment [10] shows that the electrical conductivity of Al-doped Mg_2Si indeed decreases with temperature, an indication of a metallic-like behaviour. We recognize that doped Mg_2Si are often referred as a semiconductor. However, we believe it is just a matter of semantic. This point is highlighted from a comparison of the reflectivity of pure and Al-doped Mg_2Si at zero pressure (Figure 6.7). In comparison to the flat and featureless reflectivity, typical of a semiconductor of pure Mg_2Si, the extrapolated reflectivity at zero frequency of the doped sample is almost 0.4. On closer examination (inset of Fig. 6.6), it is observed that the reflectivity rose gradually from ambient pressure to about 10.5 GPa. From 8.5 to 10.5 GPa, there is a noticeable jump in the reflectivity from 0.32 to 0.58.

Beyond this pressure, the reflectivities increase rapidly and reach 0.75 at 600 cm^{-1} at 14.1 GPa. This is to be compared with reflectivity close to unity at zero frequency for a good metal, such as copper or aluminum. Qualitatively, the observed trend in the reflectivity parallels that of the bulk measurements reported previously. [10] It was reported that the electrical resistivity decreases (conductivity increases) almost by one order of magnitude from 0 to 1 GPa but became more gradual from 1 to 8 GPa. However, the rapid drop (rise) in the electrical resistivity (conductivity) at low pressure reported earlier by quasi-4-probe method [10] was not so obvious in the infrared reflectivity measurements.

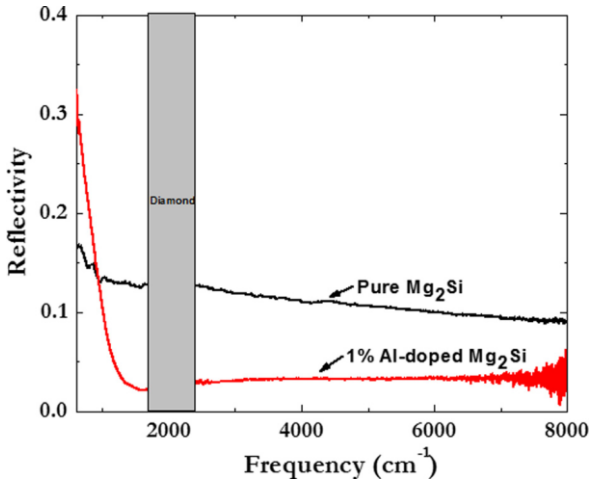

Fig. 6.7 Comparison of the infrared reflectivity spectra of 1% Al-doped Mg_2Si and pure Mg_2Si under ambient conditions.

The frequency dependent conductivity (optical conductivity) can be obtained by performing a K-K analysis of the reflectivity data using the RefFIT code. [22] The procedure is as follows: the optical conductivity obtained from a variational K-K transformation is fitted to a DL model and the *dc* conductivity is estimated by extrapolation to zero frequency. A typical result shows in Figure 6.8, illustrating the quality of the fitting procedure. In the Figure, the original and the fitted infrared reflectivity spectra at 10.5 GPa are compared. The *dc* conductivities are obtained with this procedure (Figure 6.9), where an almost linear dependence

with pressure. The *dc* conductivity is 80 Scm^{-1} at ambient pressure and reaches 300 Scm^{-1} at 14.1 GPa, a fourfold increase. It is apparent that there are two "plateau" regions in the conductivity at *ca.* 6 and 10 GPa. However, due to the simplicity of the Drude-Lorentz model and the limited low frequency range accessible by IR radiation, there is not enough firm data to make a definitive statement. Nevertheless, the results indicate that the conductivity of Al-doped Mg_2Si can be improved significantly by increasing pressure.

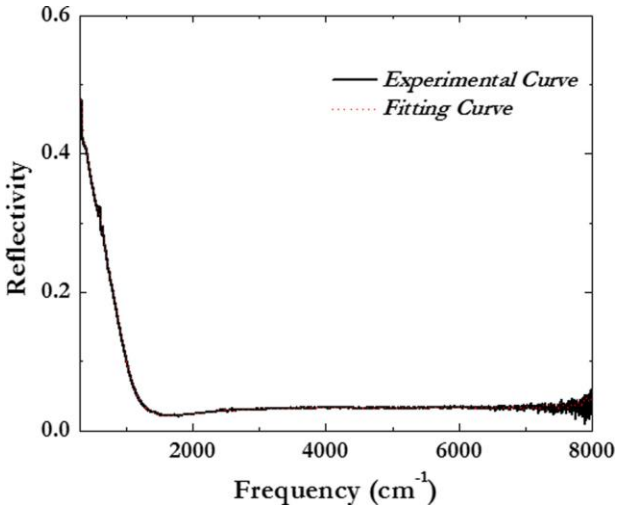

Fig. 6.8 A comparison of measured and fitted infrared reflectivity spectra of 1% Al doped Mg_2Si at 10.5 GPa.

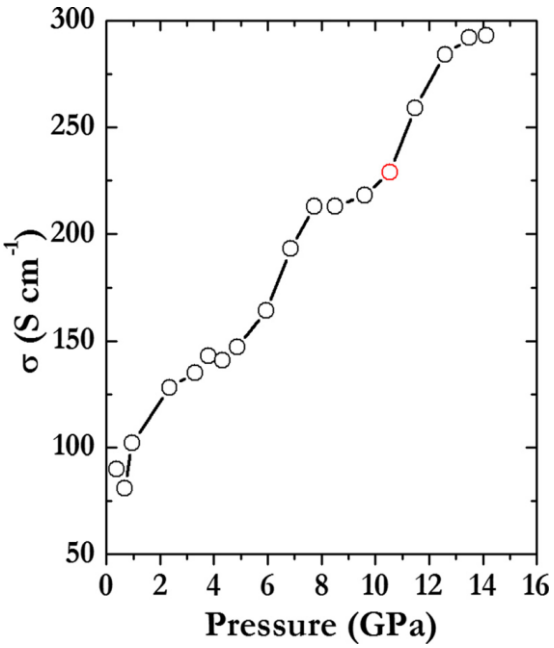

Fig. 6.9 The change in *dc* conductivities of 1% Al-doped Mg_2Si changes with pressure.

In the free electron model, the electron scattering relaxation time (τ) is related to be the electrical conductivity. This parameter can be extracted from the fitting the reflectivity data to the Drude-Lorentz model. [33] The relaxation times obtained at different pressures are summarized in Table 6.1. The derived relaxation times of *ca*. 10^{-14} s is consistent with other doped semiconductors.

To understand the mechanism for the pressure enhancement of the thermoelectric power factor, theoretical density functional calculations were performed at several pressures using a $Mg_{63}Si_{32}Al_1$ supercell model (*vide supra*). No *GW* corrections were needed since the model system is already metallic-like. The aim of the calculations was to investigate the total and projected DOS and how they affect the thermopower with pressure. The results of the calculations are shown in Figure 6.10.

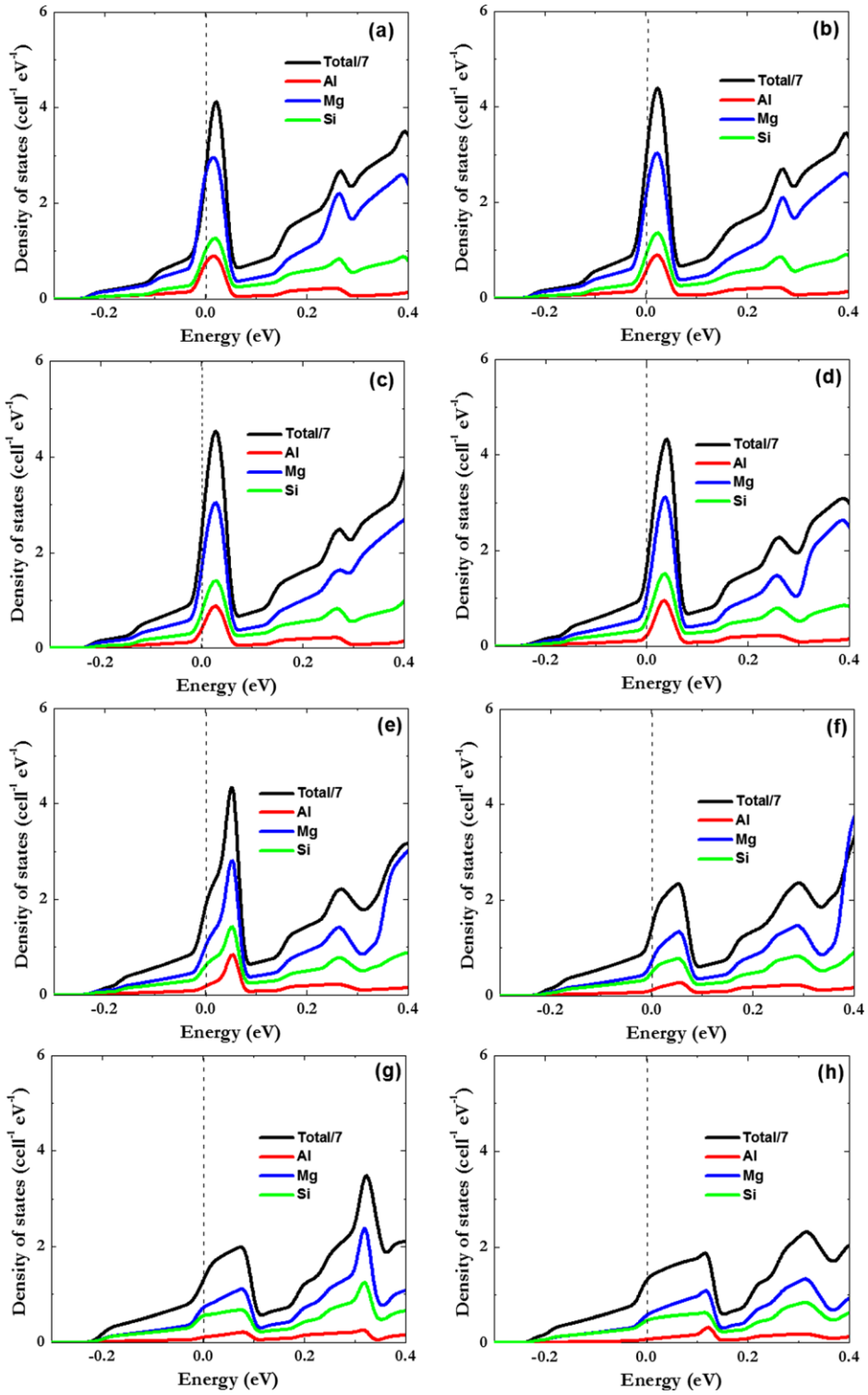

Fig. 6.10 Total density of states and projected density of states for Al-doped Mg_2Si at (a) 0.1 GPa, (b) 0.9 GPa, (c) 1.9 GPa, (d) 3.3 GPa, (e) 4.9 GPa, (f) 6.4 GPa, (g) 8.4 GPa, and (h) 10.3 GPa.

Table 6.1 Summary of *dc* conductivity (σ) and carrier relaxation time (τ) of 1% Al-doped Mg_2Si changing with the function of pressure.

Pressure (GPa)	σ (Scm^{-1})	τ (s)
0.3	90	2.9×10^{-14}
0.6	81	6.1×10^{-14}
0.9	102	6.3×10^{-14}
2.0	134	7.1×10^{-14}
2.3	128	9.3×10^{-14}
3.3	135	7.3×10^{-14}
3.7	143	7.4×10^{-14}
4.3	141	8.0×10^{-14}
4.8	147	6.7×10^{-14}
5.3	143	6.3×10^{-14}
5.9	164	6.2×10^{-14}
6.8	193	6.7×10^{-14}
7.7	213	6.5×10^{-14}
8.5	213	4.6×10^{-14}

9.6	218	2.8×10^{-14}
10.5	229	2.5×10^{-14}
11.4	259	1.4×10^{-14}
12.5	284	0.7×10^{-14}
13.4	292	0.6×10^{-14}
14.1	293	0.4×10^{-14}

At zero pressure, Al-doped Mg_2Si already has a metallic-like behaviour. The Al impurity produced a distinct narrow band with very high DOS located between the valence and conduction band of the Mg_2Si host. The sharp feature is due to localized interactions between the Al dopant with Mg and Si electronic states of the host.

From 0.1 to 3.3 GPa, a localized energy band was predicted to situate between the original gap of pristine Mg_2Si. As the pressure was increased, this electronic band broadened and became more "free-electron" like. This trend explains the observed increase in metal-like behaviour, as well as the higher electrical conductivity and infrared reflectivities. It is known that the thermoelectric power factor is dependent on both the density of states and the derivative at the Fermi energy. [33,34] A significant increase in the thermoelectric power factor is usually caused by the existence of a sharp localized DOS at the Fermi level. [35,36] The calculate DOS at the Fermi level $N(E_f)$ was found to decrease from 19 electronic states/eV/spin at 0.1 GPa to 9 electronic states/eV/spin at 10.3 GPa. In comparison, the slope of the density of states

$(dN(E)/dE)|E_f$ increased from 561 states/eV^2 at zero pressure to a maximum value of 604 states/eV^2 at 1.9 GPa and then decreased rapidly to 104 states/eV^2 at 10.3 GPa (Figure 6.11 and Table 6.2). On theoretical ground, it is expected the effect of $N(E_f)$ and $(dN(E)/dE)|E_f$ will result in an initial increase in the thermopower to 1.9 GPa then followed by a rapid drop. The predicted trend is in qualitative agreement with the measured thermopower, which has a maximum at 2.3 GPa. [10]

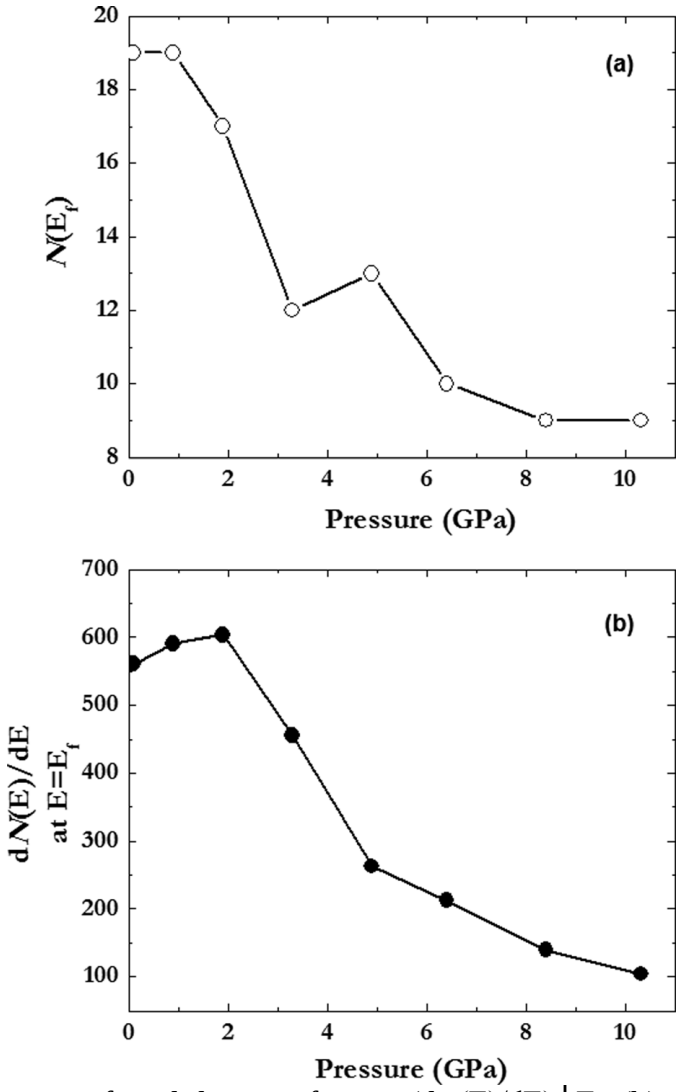

Fig. 6.11 (a) The derivative of total density of states $(dN(E)/dE)|E_f$. (b) The magnitude of total density of states at the Fermi level $N(E_f)$ for Al-doped Mg_2Si as a function of pressure.

Table 6.2 Pressure dependence of total density of states $N(E)$ at Fermi energy (E_f) and the derivative of $N(E)$ at Fermi energy (E_f) of 1% Al-doped Mg_2Si.

Pressure (GPa)	$N(E)$ at $E=E_f$	$dN(E)/dE$ at $E=E_f$
0.1	19	561
0.9	19	591
1.9	17	604
3.3	12	455
4.9	13	263
6.4	10	212
8.4	9	139
10.3	9	104

Although the trend of increasing electrical conductivity with pressure is the same as obtained from IR reflectivities and four-probe conductivity measurements, [10] the comparison of the absolute magnitude is less satisfactory. One contributing factor may be the infrared beam that only surveyed a very small region (20×20 μm^2) and penetrated only a few microns into the sample surface. This process is different from the quasi-four-probe conductivity method, which is a bulk sensitive technique. At the sample surface, the atom density is less than the bulk, and the chemical bonding in the surface is also stronger. [37,38] Therefore, there are fewer free electrons near the sample surface, thus reducing the electrical conductivity. Although plausible, this effect cannot satisfactory explain the discrepancy observed here. Since the *dc* conductivity was obtained from the extrapolation of the frequency dependent conductivity to zero frequency, it is not certain if the omission of reflectivity at very low energy (*i.e.*,<200 cm^{-1}) may have an effect. From past experience, we expect the conductivity derived from an IR measurement should agree within an order of the magnitude of the value obtained from the bulk technique. [39,40] We found no systematic error in the experiment, nor in the treatment of the data. In a previous study, we have compared the *dc* conductivity derived from IR reflectivities to bulk measurements on doped Mg_2Si and the agreements were favorable. [39] We suspect the most likely source of the disagreement may be related to the differences in the concentration of the dopant on the surface. The Al-doped Mg_2Si used in this study was synthesized by plasma spark sintering method. With this technique, this is difficult to control the precise stoichiometry and the homogeneity of the doped samples. As mentioned above, compared to the pure crystal, the cubic lattice constant of doped Mg_2Si is expanded by the inclusion of the Al dopants. The unit cell parameter for the sample used in this study is 6.2878(9) Å, which is noticeably shorter than the

reported lattice constant of 6.396(1) Å on a previous sample. A larger unit cell suggests the concentration of Al in the sample used in the earlier investigate is probably higher.

Since Al-doped Mg_2Si is *n*-doped with the Al atoms providing electrons into the conduction band, a higher Al content will increase the carrier concentration and enhance the electrical conductivity. It is noteworthy that from the diffraction patterns, unlike in the previous study, the Al-doped Mg_2Si sample used in this study is free of MgO and other impurities. Another possible source of the discrepancy may be due to non-uniform distribution of Al in the sample.

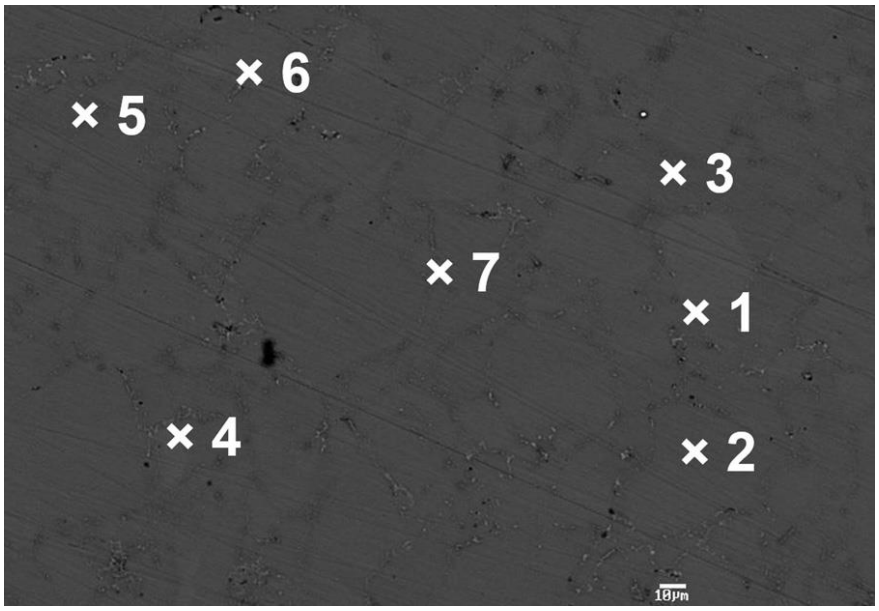

Fig. 6.12 Scanning electron microscopy (SEM) image of Al-doped Mg_2Si powder sample.

In a study of Sb and Bi doped-Mg_2Si, it was found by high resolution transmission microscopy (TEM) that due to the limited solubility excess Sb and Bi atoms are present in the grain boundaries that may enhance the conductivity of the bulk sample. [39] In comparison, IR measurements only examine a very small spot of the sample so this may produce different results. A careful characterization of both samples is critical to resolve the discrepancy. For this purpose, we examined the chemical compositions of the Al-doped Mg_2Si sample using scanning

electron microscopy (SEM). The chemical compositions of several randomly chosen spots on the surface of a compressed sample were analyzed (Figure 6.12). The results of the analysis are summarized in Table 6.3, showing that the doping is highly non-uniform. The concentrations of the doped Al can vary between a minimum of 0.27% at site #4 to a maximum of 1.42% at site #6. The large inhomogeneity in the dopant concentrations will certainly affect the local electronic. Since infrared reflectivity only probes a small spot, we believe that this is the main reason for the discrepancy between the electrical conductivity determined from infrared reflectivities and the bulk measurements.

Table 6.3 The chemical compositions of Al-doped Mg_2Si powder sample were quantitatively determined by the electron microprobe analysis.

Position	Si (wt. %)	Al (wt. %)	Mg (wt. %)
1	35	0.48	63
2	33	0.36	64
3	35	0.57	64
4	34	0.26	65
5	35	0.39	65
6	34	1.4	63
7	32	0.62	65

6.4 Conclusion

The structural transformation and electrical conductivity of a nominally 1 at. % Al-doped Mg_2Si sample synthesized from spark plasma sintering have been investigated by angle dispersive synchrotron radiation X-ray diffraction and infrared reflectivity up to 16.6 GPa at room temperature. Contrary to two earlier reports, no structural transformation was observed in pure Mg_2Si up to 15 GPa when helium was used as the quasi-hydrostatic pressure transmission medium. The electronic band structures of pure Mg_2Si were calculated at selected pressures with density functional theory including the correction for electron correlation effect with the *GW* approximation. It is found that the band gap of Mg_2Si does not close at 11 GPa. The theoretical result is consistent with electrical resistivity measurements, which show that Mg_2Si remains an insulator at least up to 22 GPa. Both studies contradict the reported structural phase transition to metallic anti-cotunnite and Ni_2In phases 7 and 11 GPa, respectively. However, in Al-doped Mg_2Si, a structural phase transition from the cubic anti-fluorite to the anti-cotunnite structure was found to occur around 11.9 GPa. Infrared reflectivity show the Al-doped Mg_2Si already has a metallic-like behavior under ambient conditions.

The *dc* conductivities at high pressure were calculated from the analysis of the infrared reflectivity spectra employing the Drude-Lorentz model. In agreement with bulk four-probe measurements, the electrical conductivity was found to increase with pressure as the sample became more metallic-like. However, the values of the *dc* conductivity derived from IR reflectivities are consistently lower. We attribute this difference to the difference in the stoichiometry of the sample used in the experiment and non-uniform doping. Theoretical density functional calculations reveal the presence of a mid-gap localized electronic band below 3.3 GPa. The sharp mid-gap DOS is the result of hybridization between the electron orbitals of the

host elements with the dopant. As the pressure is increased further, the localized band broadened and the profile became more free-electron like. The derivative of the electron density of states $N(E)$ at the Fermi energy (E_f) is found to maximize at 1.9 GPa. Thus, the theory predicted a maximum thermoelectric power factor, which is in agreement with the experimental observation at 2-3 GPa.

The present study provides new results and insight on the high pressure structures and transport properties of pure and Al-doped Mg_2Si. The diffraction experiments found no phase transition at 6-7 GPa, suggested by the Raman study. [10] However, transformation to an orthorhombic anti-cotunnite (*Pnma*) structure is confirmed at 11 GPa. The information obtained here may help to further enhance the performance of Mg_2Si-based thermoelectric materials.

Acknowledgements

Ambient pressure synchrotron X-ray diffraction experiments were performed at the CMCF beamline, Canadian Light Source, which was made possible by support from NSERC, NRC, CIHR, and the University of Saskatchewan. High pressure synchrotron X-ray diffraction experiments were performed at sector 20 at the Advanced Photon Source, supported by the U.S. Department of Energy-Basic Energy Sciences, the Canadian Light Source and its funding partners, the University of Washington, and the Advanced Photon Source. Use of the Advanced Photon Source, an Office of Science User Facility operated for the U.S. Department of Energy (DOE) Office of Science by Argonne National Laboratory, was supported by the U.S. DOE under Contract No. DE-AC02-06CH11357. The use of U2A beamline was supported by COMPRES under NSF Cooperative Agreement EAR 11-57758 and CDAC (DEFC03 03N00144). The National Synchrotron Light Source, Brookhaven National Laboratory, was supported by the U.S. Department of Energy, Office of Science, Office of Basic Energy Sciences

under Contract No. DE-AC02-98CH10886. The electron microprobe analysis was supported by the Microscopy Lab, Department of Geological Sciences, University of Saskatchewan. J.Z. and J.S.T. thank AUTO21 for a Research Grant and to T. Bonli for the SEM measurements and J. Smith of HPCAT, Advanced Photon Source, for assistance with the high pressure diffraction experiments. We thank S. Tkachev for the help in using the gas-loading system, which is supported by GSECARS and COMPRES. APS is a user facility operated for the DOE Office of Science by ANL under Contract No. DE-AC02- 06CH11357.

References

[1] T. Sakamoto, T. Iida, S. Kurosaki, K. Yano, H. Taguchi, K. Nishio, and Y. Takanashi, *J. Electron. Mater*., 2011, 40, 629-634.

[2] S. Battiston, S. Fiameni, M. Saleemi, S. Boldrini, A. Famengo, F. Agresti, M. Stingaciu, M. S. Toprak, M. Fabrizio, and S. Barison, *J. Electron. Mater*., 2013, 42, 1956-1959.

[3] T. Sakamoto, T. Iida, A. Matsumoto, Y. Honda, T. Nemoto, J. Sato, T. Nakajima, H. Taguchi, and Y. Takanashi, *J. Electron. Mater*., 2010, 39, 1708-1713.

[4] S. You, K. Park, I. Kim, S. Choi, W. Seo, and S. Kim, *J. Electron. Mater*., 2012, 41, 1675-1679.

[5] J. Tani and H. Kido, *Intermetallics*, 2008, 16, 418-423.

[6] N. Wang, H. Chen, H. He, W. Norimatsu, M. Kusunoki, and K. Koumoto, *Sci. Rep*., 2013, 3, 3449.

[7] Q. Chen, Q. Xie, F. Zhao, D. Cui, and X. Li, *IEEE Comput. Soc*., 2009, 22, 338-341.

[8] G. J. Snyder and E. S. Toberer, *Nat. Mater*., 2008, 7, 105-114.

[9] G. H. Kim, L. Shao, K. Zhang, and K. P. Pipe, *Nat. Mater*., 2013, 12, 719-723.

[10] N. V. Morozova, S. V. Ovsyannikov, I. V. Korobeinikov, A. E. Karkin, K. Takarabe, Y. Mori, S. Nakamura, and V. V. Shchennikov, *J. Appl. Phys*., 2014, 115, 213705.

[11] M. Y. Au–Yang and M. L. Cohen, *Phys. Rev*., 1969, 178, 1358.

[12] J. Hao, Z. Guo, and Q. Jin, *Solid State Commun*., 2010, 150, 2299-2302.

[13] J. Hao, B. Zou, P. Zhu, C. Gao, Y. Li, D. Liu, K. Wang, W. Lei, Q. Cui, and G. Zou, Solid *State Commun*., 2009, 149, 689-692.

[14] F. Zhu, X. Wu, S. Qin, and J. Liu, *Solid State Commun*., 2012, 152, 2160-2164.

[15] F. Yu, J. X. Sun, W. Yang, R. G. Tian, and G. F. Ji, *Solid State Commun*., 2010, 150, 620.

[16] W. Ren, Y. Han, C. Liu, N. Su, Y. Li, B. Ma, Y. Ma, and C. Gao, *Solid State Commun*., 2012, 152, 440-442.

[17] B. H. Yu and D. Chen, *Chin. Phys. B*, 2011, 20, 030508.

[18] H. K. Mao, J. Xu, and P. M. Bell, *J. Geophys. Res*., 1986, 91, 4673-4676.

[19] V. Petricek, M. Dusek, and L. Palatinus, *Z. Kristallogr*., 2014, 229, 345-352.

[20] A. Le Bail, H. Duroy, and J. L. Fourquet, *Mater. Res. Bull*., 1988, 23, 447-452.

[21] R. L. Kronig, *J. Opt. Soc. Am. Rev. Sci. Instrum*., 1926, 12, 547-557.

[22] A. B. Kuzmenko, *Rev. Sci. Instrum*., 2005, 76, 083108.

[23] G. Kresse and J. Hafner, *Phys. Rev. B*, 1993, 47, 558.

[24] G. Kresse and J. Hafner, *Phys. Rev. B*, 1994, 49, 14251.

[25] G. Kresse and J. Furthmuller, *Comput. Mater. Sci*., 1996, 6, 15.

[26] G. Kresse and J. Furthmuller, *Phys. Rev. B*, 1996, 54, 11169.

[27] L. Hedin, *Phys. Rev*., 1965, 139, A796-A823.

[28] P. Garcia–Gonzalez and R. W. Godby, *Phys. Rev. B*, 2011, 63, 075112.

[29] P. E. Blochl, *Phys. Rev. B*, 1994, 50, 17953.

[30] G. Kresse and D. Joubert, *Phys. Rev. B*, 1999, 59, 1758.

[31] S. J. You, L. C. Chen, and C. Q. Jin, *Chin. Phys. Lett*., 2009, 26, 096202.

[32] M. Fox, *Optical Properties of Solids*, 2nd ed. (Oxford University Press, 2010).

[33] G. D. Mahan and J. O. Sofo, *Proc. Natl. Acad. Sci. U. S. A*., 1996, 93, 7436.

[34] R. Kim, S. Datta, and M. S. Lundstrom, *J. Appl. Phys*., 2009, 105, 034506.

[35] J. P. Heremans, V. Jovovic, E. S. Toberer, A. Saramat, K. Kurosaki, A. Charoenphakdee, S. Yamanaka, and G. J. Snyder, *Science*, 2008, 321, 554.

[36] J. H. Lee, J. Wu, and J. C. Grossman, *Phys. Rev. Lett*., 2010, 104, 016602.

[37] D. M. Larson, K. H. Downing, and R. M. Glaeser, *J. Struct. Biol*., 2011, 174, 420.

[38] S. Mafe, J. A. Manzanares, and P. Ramirez, *Phys. Chem. Chem. Phys*., 2003, 5, 376.

[39] N. Farahi, M. VanZant, J. Zhao, J. S. Tse, S. Prabhudev, G. A. Botton, J. R. Salvador, F. Borondics, Z. Liu, and H. Kleinke, *Dalton Trans*., 2014, 43, 14983.

[40] J. W. L. Wong, A. Mailman, K. Lekin, S. M. Winter, W. Yong, J. Zhao, S. V. Garimella, J. S. John, R. A. Secco, S. Desgreniers, Y. Ohishi, F. Borondics, and R. T. Oakley, *J. Am. Chem. Soc*., 2014, 136, 1070.

CHAPTER 7

ENHANCED FIGURE OF MERIT IN $Mg_2Si_{0.877}Ge_{0.1}Bi_{0.023}$/MULTI WALL CARBON NANOTUBE NANOCOMPOSITES

One of the strategies to improve thermoelectric performance is through embedding nanomaterials into the bulk matrix. This method is known as "nano-inclusion". [8] Nanostructures are known to reduce thermal conductivity through scattering mid- to long-wavelength phonons, and to sustain electrical conductivity while improving the Seebeck coefficient (thermoelectric power). [8-10] Carbon nanotubes (CNTs), due to their unique electronic properties, are considered to be potential candidates for nano-inclusions in thermoelectric materials. [11-15] Although CNTs have a positive effect on the thermoelectric properties of Bi_2Te_3 [16] and $Bi_2(Se,Te)_3$ [17], reaching a $ZT \sim 1.5$ at 350 K as compared to $ZT \sim 1$ without nanotubes, the presence of rare and toxic tellurium in these materials curtails large scale industrial applications. Furthermore, the temperature at which these materials have the higher performance is well below those of most targeted waste heat recovery applications.

The rationale for this work is to investigate the effect of CNTs on the thermoelectric properties of more cost effective and ecofriendly Mg_2Si-based materials. The objective is to develop this class of material as the next generation of high efficiency thermoelectrics that are suitable for auto industry applications. [18] Thus far, single-wall carbon nanohorns (SWCNHs), [19] TiO_2 [20] and Si nanoparticles [21] have been studied as nano-inclusions in Mg_2Si materials. Embedding SWCNHs improved room temperature electrical conductivity of Bi doped Mg_2Si from around 3 Ω^{-1} cm^{-1} to 100 Ω^{-1} cm^{-1}. An improvement by a factor of 10 was also observed in the electrical conductivity of samples containing TiO_2. Unfortunately, the nano-inclusions were not as effective as tin [22] or germanium [23] solid solutions in reducing the thermal conductivity of Mg_2Si thermoelectrics. The lowest room temperature thermal conductivity of

around 6 $Wm^{-1}K^{-1}$ was achieved for Mg_2Si/Si nanocomposites, which is approximately twice that of a solid solution. [22] The lack of similar investigations of $Mg_2Si_{1-x}Ge_x$ solid solutions motivated this study.

For this chapter, the effect of multi-wall carbon nanotubes (MWCNTs) on the thermoelectric properties of $Mg_2Si_{0.877}Ge_{0.1}Bi_{0.023}$ was examined. The compounds studied were $Mg_2Si_{0.877}Ge_{0.1}Bi_{0.023}$ and $Mg_2Si_{0.877}Ge_{0.1}Bi_{0.023}$ with the addition of 0.5%, 1%, and 1.5% weight MWCNTs, respectively. The reason for introducing MWCNTs is that they are a good conductor and increased electrical conductivity of the doped sample could be expected. Indeed at 323 K the measured electrical conductivity was found to increase from 450 $\Omega^{-1}cm^{-1}$ in $Mg_2Si_{0.877}Ge_{0.1}Bi_{0.023}$ to 500 $\Omega^{-1}cm^{-1}$ in $Mg_2Si_{0.877}Ge_{0.1}Bi_{0.023}$-0.5 wt% MWCNTs. However, this effect diminished at higher temperature where the conductivity dropped back to 470 $\Omega^{-1}cm^{-1}$ at 773 K. The key question was to clarify whether there was a chemical interaction between the MWCNTs and $Mg_2Si_{0.877}Ge_{0.1}Bi_{0.023}$. We performed Raman measurements of the samples and noted the persistence of disorder (D) and tangential (G) mode characteristics of a carbon nanotube. This observation suggested there was no substantial chemical reaction or decomposition of the MWCNTs doped in $Mg_2Si_{0.877}Ge_{0.1}Bi_{0.023}$. Nevertheless, the electrical conductivity was increased by 10% in the doped samples at 300 K. However, the maximum *ZT* of 0.5 in $Mg_2Si_{0.877}Ge_{0.1}Bi_{0.023}$-0.5 wt% MWCNTs at 700 K is not very attractive for practical applications.

The results of this study have been published in

N. Farahi, S. Prabhudev, M. Bugnet, G. A. Botton, J. Zhao, J. S. Tse, J. R. Salvador, and H. Kleinke, "Enhanced figure of merit in $Mg_2Si_{0.877}Ge_{0.1}Bi0._{023}$/multi wall carbon nanotube nanocomposites," *RSC Advances*, vol. 5, pp. 65328-65336, 2015.

- The authors' contributions are as follow:
- N. Farahi and H. Kleinke synthesized the samples and performed the thermoelectric property measurements.
- J. Zhao and J. S. Tse performed micro-Raman spectra measurements and analyzed the data to arrive at the definitive conclusion that there is no decomposition on substantial chemical reaction of the MWCNTs with Mg_2Si.
- S. Prabhudev, M. Bugnet, and G. A. Botton performed the STEM measurement.
- J. R. Salvador performed the Hall measurement.
- All authors contributed to the writing and editing of the manuscript.

Abstract

The effect of multi wall carbon nanotubes (CNT) on the thermoelectric properties of $Mg_2Si_{0.877}Ge_{0.1}Bi_{0.023}$ was examined. While introducing CNTs increases the electrical conductivity from around 450 $\Omega^{-1}cm^{-1}$ to 500 $\Omega^{-1}cm^{-1}$ at 323 K, the increase is neutralized at higher temperature, with the conductivity resulting to be 440 $\Omega^{-1}cm^{-1}$-470 $\Omega^{-1}cm^{-1}$ at 773 K. The Seebeck coefficient of all nanocomposites is enhanced at 773 K due to energy filtering that stems from the introduction of CNTs-$Mg_2Si_{0.877}Ge_{0.1}Bi_{0.023}$ interfaces. The combined effect of CNTs on Seebeck coefficient and electrical conductivity leads to an approximately 20% power factor improvement, with the best sample reaching a maximum value of ~19 $\mu Wcm^{-1}K^{-2}$ at 773 K. The

lattice thermal conductivity of the nanocomposites is reduced due to the phonon scattering by nanodomains and grain boundaries, particularly at medium temperatures, resulting in a slight reduction in total thermal conductivity. According to high resolution transmission electron microscopy studies, bismuth is homogenously distributed within the grains, while germanium is accumulated at the grain boundaries. All in all, the enhanced thermoelectric figure of merit of 0.67 at 773 K for the sample containing 0.5 weight% MWCNT as compared to 0.55 for the pristine sample, demonstrates the promising effect of CNTs on the thermoelectric properties of $Mg_2Si_{0.877}Ge_{0.1}Bi_{0.023}$.

7.1 Introduction

Since the discovery of carbon nanotubes (CNT), [1] numerous studies have been performed to reveal the properties and behaviour of these materials. It is crucial not only to understand their capabilities, but also to be able to manipulate their properties towards the desired application. This manipulation can be done through surface functionalization, [2] chirality control [3] and managing the number of walls [4] for multi wall carbon nanotubes (MWCNT). Since energy is one of the main concerns of our time, it is practical to profit from these modern materials to tackle the energy challenges, such as waste heat recovery. So far, thermoelectric (TE) materials are some of the best candidates for this purpose, due to their exceptional capability to convert waste heat into electricity. Like other newly developed technologies, the quest for increasing the efficiency while mitigating the cost and toxicity of TE materials is still ongoing. The efficiency of a thermoelectric material depends on its figure of merit $ZT = \sigma S^2 T \kappa^{-1}$, where σ, κ, S and T represent electrical conductivity, thermal conductivity, Seebeck coefficient and absolute temperature, respectively. [5-7]

To enhance *ZT* based on the above equation, the electrical conductivity and the Seebeck coefficient need to be increased while maintaining or reducing the thermal conductivity. Unfortunately these properties are entangled in such a way that simultaneous improvements are not always feasible, as for example both the electrical and the thermal conductivity increase with higher charge carrier concentration, while the Seebeck coefficient decreases. One of the strategies to overcome this issue is through embedding nanomaterials into the bulk matrix, which is known as "nano-inclusion". [8] The idea of having nanostructures is to reduce thermal conductivity through scattering mid- to long-wavelength phonons, and to sustain electrical conductivity while improving *S via* energy filtering of carriers. [8-10] Carbon nanotubes, due to their spectacular electronic properties, can be considered as potential candidates for nano-inclusions in thermoelectric materials. [11-15] Even though CNTs had a positive effect on the thermoelectric properties of Bi_2Te_3 [16] and $Bi_2(Se,Te)_3$ [17] by achieving $ZT \sim 1.5$ at 350 K as compared to $ZT \sim 1$ for the sample without nanotubes, the presence of rare and toxic tellurium would not fulfill the criteria for large scale industrial applications, further the temperature at which these materials are most efficient are well below those of most targeted waste heat recovery applications.

The rationale for this work is to investigate the effect of CNTs on the thermoelectric properties of more cost effective and ecofriendly materials. Magnesium silicide based materials, in this regard, are conspicuous as next generation high efficiency TE materials that are suitable for auto industry applications. [18] Thus far, single-wall carbon nanohorns (SWCNH), [19] TiO_2 [20] and Si nanoparticles [21] were studied as nano-inclusions in Mg_2Si materials. Embedding SWCNHs improved room temperature electrical conductivity of Bi doped Mg_2Si from around 3 $\Omega^{-1}cm^{-1}$ to 100 $\Omega^{-1}cm^{-1}$. An improvement by a factor of 10 was also observed in the electrical

conductivity of the samples containing TiO_2. Unfortunately, the nano-inclusions were not as effective as tin [22] or germanium [23] solid solutions in reducing the thermal conductivity of Mg_2Si thermoelectrics. The lowest room temperature thermal conductivity of around 6 $Wm^{-1}K^{-1}$ was achieved for Mg_2Si/Si nanocomposites, which is approximately twice that of a solid solution. [22] The lack of similar investigations of $Mg_2Si_{1-x}Ge_x$ solid solutions motivated this study.

7.2 Experimental section

$Mg_2Si_{0.877}Ge_{0.1}Bi_{0.023}$ samples were synthesized by mixing the elements in tantalum tubes, according to the stoichiometric ratios, in argon filled glove box. Mg chips (99.98%, Sigma Aldrich, 4-30 mesh), Si powder (99.9%, Alfa Aesar, -100 mesh), Ge pieces (99.9999+%, Alfa Aesar, ≤2 cm) and Bi granules (99.99%, Sigma Aldrich) were used for our synthesis. The tantalum tubes were sealed under argon with an arc melter, and put into silica tubes, which were then sealed under vacuum. The tubes were heated in a resistance furnace at 923 K for a week. To achieve pure products, the samples were ground prior to annealing at 1173 K for another week.

To examine the purity of the synthesized samples, an Inel powder X-ray diffractometer with Cu-Ka_1 radiation and a position sensitive detector was used. All samples were pure except for small traces of MgO (Fig. C.1), which is a common side product in Mg_2Si based compounds. [24,25] The powders were manually mixed and divided into four batches. Different amount of carbon nanotubes (Sigma-Aldrich, carbon nanotube, multi-walled; >90% MWCNT basis, outer diameter 10-15 nm, inner diameter 2-6 nm, length 0.1-10 μm) were then added to each batch and mixed for 3 to 5 minutes using a Fisher Scientific vortex mixer until no MWCNT agglomerations were detected.

To perform the physical property measurements, the mixtures were then hot pressed in an Ar atmosphere at 973 K under 56 MPa using an Oxy-Gon hot press. To reduce stress and strain on the pellets during cooling, the pressure was released after sintering. The pressed pellets had 12.7 mm diameter and 2 mm thickness. The thermal conductivity, κ, of the pressed pellets was calculated by measuring the thermal diffusivity, α, under Ar flow using Anter Flashline FL3000 thermal properties analyzer between 300 K and 800 K. The obtained thermal diffusivity values were then multiplied by the density, d, of the pellets, as measured *via* the Archimedes method, and the specific heat, C_p, of the compounds, as calculated from the Dulong–Petit approximation, to yield $\kappa = \alpha d C_p$. The obtained densities together with the calculated specific heat of all the samples are available in Table C.1. Our previous measurements of the specific heat of $Mg_2Si_{0.977-x}Ge_xBi_{0.023}$ samples validated the accuracy of Dulong–Petit approximation for this system. [26] Since adding CNT only changed the Dulong–Petit value of C_p by 2%, within the error range of the measurement, the calculated values were used to obtain the thermal conductivity.

The pressed pellets were thereafter cut into rectangular bars with the dimensions of approximately 12 × 2 × 2 mm^3, the electrical conductivity (σ) and Seebeck coefficient (S) measurements were carried out under helium atmosphere between 300 K and 800 K by using the ULVAC-RIKO ZEM-3 apparatus. Hall effect measurements where performed using a cryostat equipped with a 5 T magnet and with a Linear Research AC resistance bridge. Hall resistance values were measured from -3 T to 3 T from 5 K to 300 K. The carrier concentration (n) was calculated from the Hall coefficient, R_H, using the relationship $n = R_H^{-1} e^{-1}$, where e is the fundamental charge.

To verify the existence and examine the distribution of nanotubes within the samples at the micron level, scanning electron microscopy (SEM) analysis was performed on parts of

selected pressed pellets (Fig. C.2) using a Zeiss ULTRA electron microscope associated with an EDX device, EDAX Pegasus 1200.

7.2.1 Transmission electron microscopy

Atomic-scale structural characterization and elemental analyses were performed using high angle annular dark field imaging (HAADF) and energy dispersive X-ray spectroscopy (XEDS) in an aberration corrected scanning transmission electron microscope (STEM). STEM-HAADF employs a raster scanning electron probe to collect electrons that are elastically scattered at high angles. Upon converging the electron beam into a sub-angstrom probe, an atomic-scale image of materials is possible. The HAADF detector is designed in an annular geometry and placed in a diffraction plane below the sample so as to collect electrons emerging from the specimen at high scattering angles. Since the intensity of these high-angle scattered electrons is directly related to the atomic number of scattering atoms, the resulting image provides an atomic number (Z) contrast with intensities proportional to $Z^{1.6}$. In the case of the Mg_2Si sample doped with Ge and Bi, the atomic columns containing Ge (Z = 32) and Bi (Z = 83) are expected to appear significantly brighter compared to those of Mg (Z = 12) and Si (Z = 14). Further, the EDX elemental mapping and line profiles were based on Mg-*K*, Si-*K*, Ge-*K* and Bi-*L* spectral lines. Both of these analyses were performed on a FEI-Titan cubed microscope equipped with two hexapole-design spherical aberration correctors of the probe and image forming lenses, operated at 300 kV. The sample was thinned down to electron transparency by the wedge-polishing technique using a multiprep apparatus (Allied Inc.), and further argon ion milled using a Gentle Mill (Technoorg Linda Inc.).

7.2.2 Raman spectroscopy

Dispersive Raman microscope (Renishaw Invia Raman Microscope) equipped with a Fourier transform infrared (FTIR) detector for sequential analysis at the same spot was used to measure pure multi-wall carbon nanotube and $Mg_2Si_{0.877}Ge_{0.1}Bi_{0.023}$ samples with additions of 0.5%, 1%, and 1.5% weight MWCNTs. The Raman spectroscopy was operated with a 514 nm argon ion laser (Modu-Laser Stellar Pro laser) and a 1800 line per mm grating. The laser power used was 10%, yielding 0.36 mW at the sample. The laser was focus on the flatten powder sample using a 20× objective, and the Raman signal was collected at 10 s. The measurement was calibrated by using Si (110), which was measured at 520 cm^{-1}. Data processing and analysis were accomplished using software Wire 3.4 (Renishaw, Inc.). The collection wave number range for Raman spectrum was from 100 cm^{-1} to 2000 cm^{-1}.

7.3 Results and discussion

From EDX mapping, we deduce that the additions of Ge and Bi are not localized in the form of precipitates, but are present in the form of a solid solution in the Mg_2Si matrix. Fig. C.3 illustrates EDX elemental mapping carried out over a selected region (the pink box) within the grain with Ge (red) and Bi (green) colour coded maps. Atomic-level characterization work was carried out to confirm this as discussed later. The elemental maps corresponding to Ge (red) and Bi (green) indicate that the Ge and Bi atoms are alloyed with the Mg_2Si matrix in the form of solid solution. Low-magnification STEM imaging as shown in Fig. 7.1a revealed the polycrystalline nature of the sample with larger grain sizes (<12 μm). In addition, the grain-boundaries can be seen as brighter as compared to the bulk of the grain. The reason for the brighter intensities is consistent with the segregation of elements with higher *Z* (in this case, Ge and/or Bi). EDX mapping performed on the area highlighted as a rectangle, *i.e.* including three

different grains and their grain boundaries, revealed a mostly homogenous presence of Mg, Si, and Bi within the grains, while Ge was accumulated along the grain boundaries, but with higher concentration in some of the grains (the top grain in the particular case shown in the map of Fig. 7.1). To further analyze this, additional line scans were performed, as highlighted on the left of Fig. 7.1b and c. Going from the left grain to the bottom grain (Fig. 7.1b), the Ge concentration peaked in the boundary between these two. On the other hand, the line scan from the top to the bottom grain (Fig. 7.1c) revealed a higher Ge concentration in the top grain, while Bi stayed constant within error of the method.

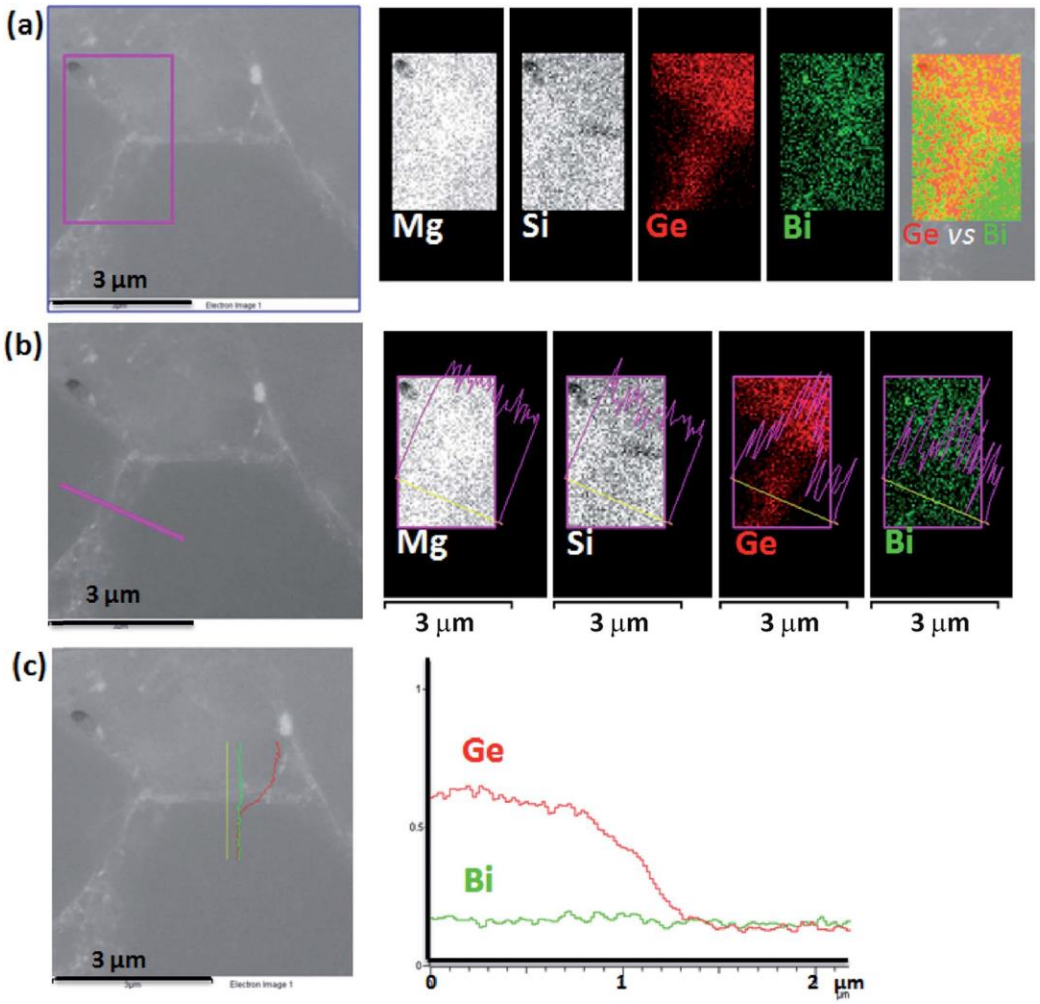

Fig. 7.1 (a) Left: low-magnification STEM-HAADF image; right: EDX elemental maps of Mg, Si, Ge and Bi in the area marked with a rectangle; (b), (c) line profiles of Ge-*K* and Bi-*L* lines along the boundary between different grains. The profiles in red and green correspond to Ge and Bi, respectively.

The low-magnification STEM-HAADF image shown in Fig. 7.2a illustrates an area along the edge of the specimen. The Kikuchi diffraction patterns obtained on two different spots (Fig. 7.2b and c) confirm the presence of two grains with different orientations and, hence, a grain boundary at the interface. In fact, the grain boundary is visible as a bright stripe midway between the spots where the Kikuchi patterns are obtained. EDX line scans were performed for Ge and Bi as shown in the Fig. 7.2d and e to examine the distribution of heavy elements. From the line profile of Ge, it is evident that Ge is segregating along the grain boundary, consistent with the findings discussed above. Again in contrast to Ge, the EDX intensity in the line profile of Bi does not reveal any such segregation, but possibly slightly different concentrations in the two grains. The apparent large width of the Ge segregation profile (Fig. 7.2e) can be explained by the fact that, in this particular region and sample tilt, the grain boundary might not be perfectly parallel to the electron beam. The segregation of Ge at the grain boundaries together with the homogenous distribution of Bi in the grain boundaries could be helpful in blocking the phonons while allowing the electrons to pass. To obtain better statistics, other grain boundaries were analyzed (not shown), and were found to be consistent over all observed ones. Compared to our earlier work (Mg_2Si with Bi and no Ge), the Bi atoms were found to extensively segregate along the grain boundaries. [26,27] Here the segregation, if at all present, would be very small compared to the previously studied samples. This implies that it is possible to tune the segregation/ distribution behaviors of dopants by increasing the unit cell through alloying.

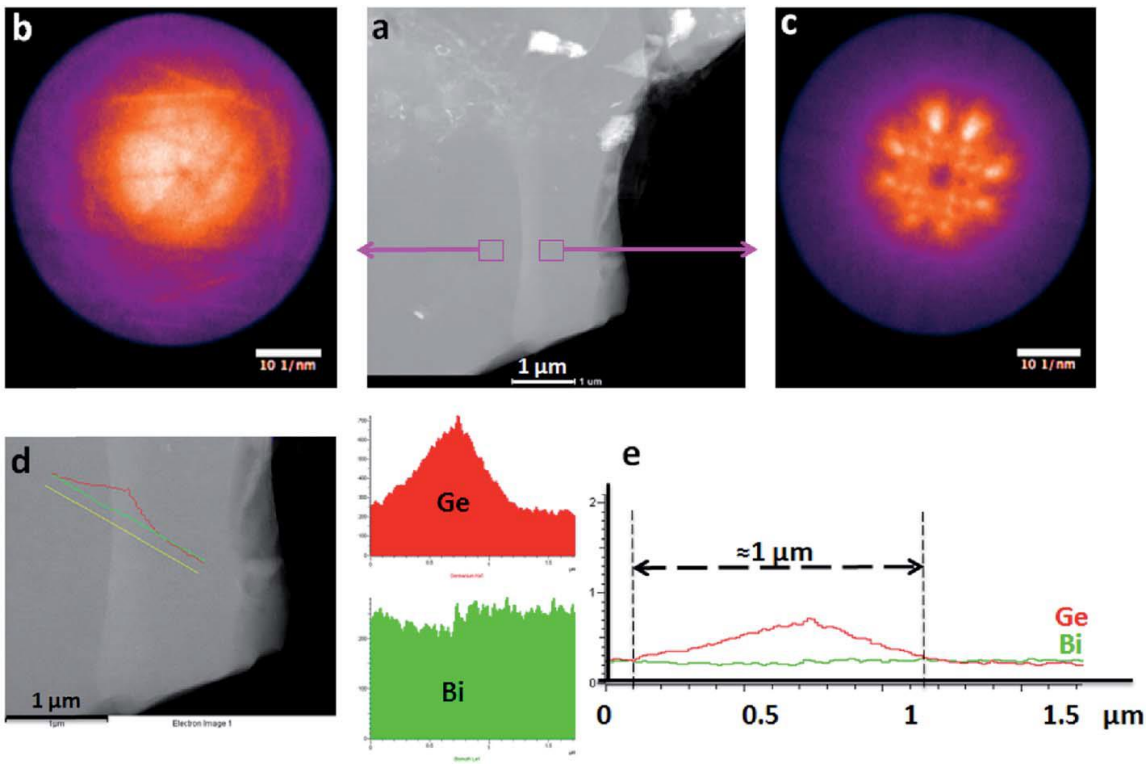

Fig. 7.2 (a) Low-magnification STEM-HAADF image; (b) and (c) Kikuchi patterns confirming two different grains separated by a grain boundary; (d) EDX line scans of Ge-*K* (red) and Bi-*L* (green) lines along the grain boundary; (e) line profiles of Ge (red) and Bi (green) along the grain boundary as shown in (d).

In addition to EDX line scans as well as low-magnification imaging illustrated above, the distribution of dopants within a grain was understood better using STEM-HAADF imaging performed at an atomic resolution, as shown in Fig. 7.3a. For better visibility, a selected region is magnified and shown in Fig. 7.3b. Individual atomic columns of the doped Mg_2Si lattice, oriented along the [111] zone axis, are visible in Fig. 7.3b. In these *Z*-contrast imaging conditions, the brighter atomic columns on the image (identified with pink arrows) are distributed randomly over the entire 2-D projection of the lattice, and contain heavier elements such as Ge and Bi, which are located on substitutional sites replacing Si atoms. [26,27] It is clear that the dopant atoms are rather homogenously distributed within the bulk of the grain. Fig. 7.3c illustrates this in much better clarity where a site with significantly brighter intensity (pink

arrow) can be clearly seen in proximity to another site with relatively weaker intensity (green arrow).

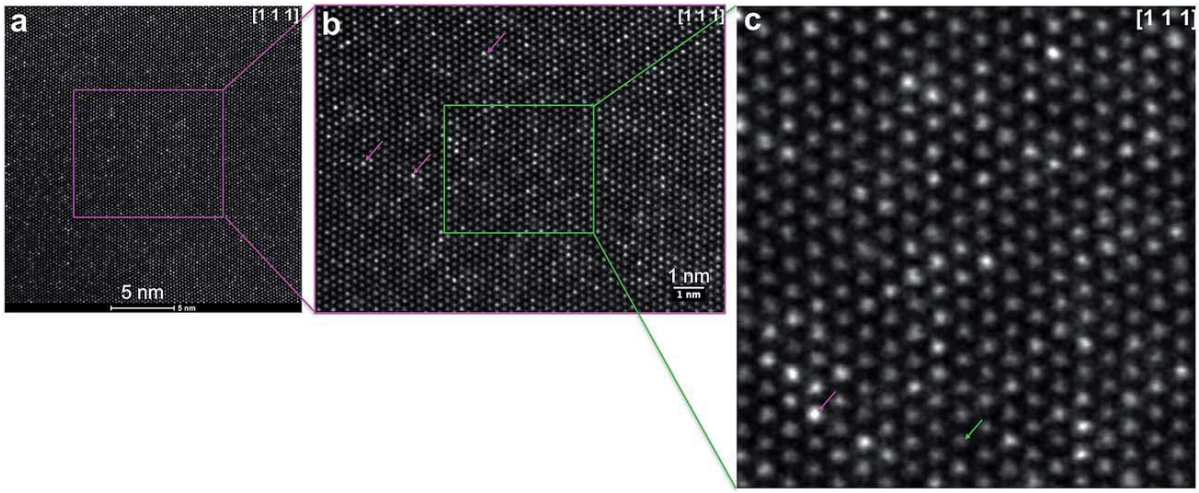

Fig. 7.3 (a and b) Atomic resolution STEM-HAADF images corresponding to a region in the bulk of a grain oriented along [111] zone axis; (c) magnified region from (b), the green arrow indicating an atomic column with no significant brighter intensities as compared to the atomic column highlighted by the pink arrow.

Raman spectra of $Mg_2Si_{0.877}Ge_{0.1}Bi_{0.023}$ with different amounts of MWCNT are shown in Fig. 7.4. The pure MWCNT was also measured as the reference. As can be seen, all the samples demonstrate the higher frequency D mode (disordered) and G mode [28,29] at around 1350 $cm^{-1}$and 1590 cm^{-1}, respectively. No shift is observed in the D and G bands, which indicates the CNTs neither decomposed under pressure used for consolidation nor reacted with the base material. Although the regular breathing mode is specific to CNT, we cannot observe this mode for multi-wall carbon nanotube due to the larger strains of multi wall nanotubes, which hinder its vibration along the radial direction compared to the single wall carbon nanotubes. [30]

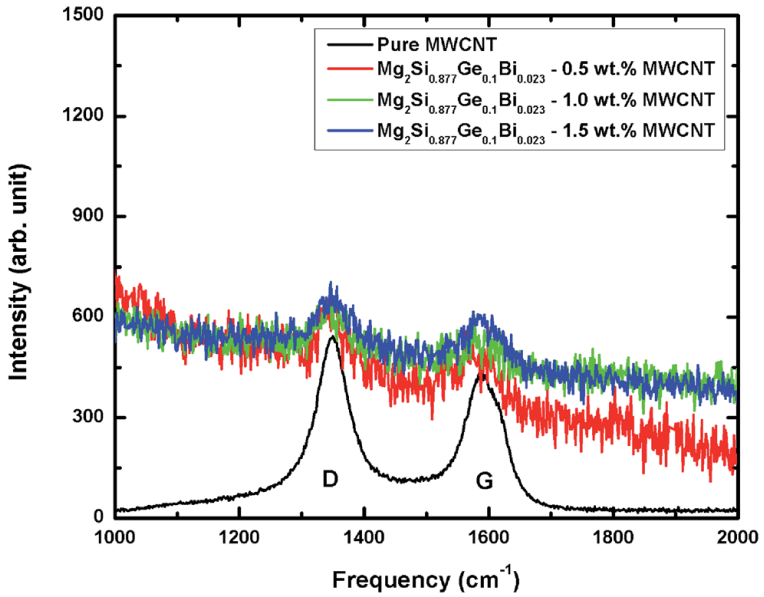

Fig. 7.4 Raman spectra of the $Mg_2Si_{0.877}Ge_{0.1}Bi_{0.023}$/MWCNT samples.

The electrical conductivity of all the nanocomposites is shown in Fig. 7.5. For all samples, the electrical conductivity increases with temperature below 600 K and then decreases due to an increase in electron–phonon interaction, which dominates charge carrier scattering at higher temperature. Adding multi wall carbon nanotubes increases the electrical conductivity from σ = 450 $\Omega^{-1}cm^{-1}$ for the sample without MWCNT to 500 $\Omega^{-1}cm^{-1}$ for the sample containing 0.5 weight% MWCNT at 323 K.

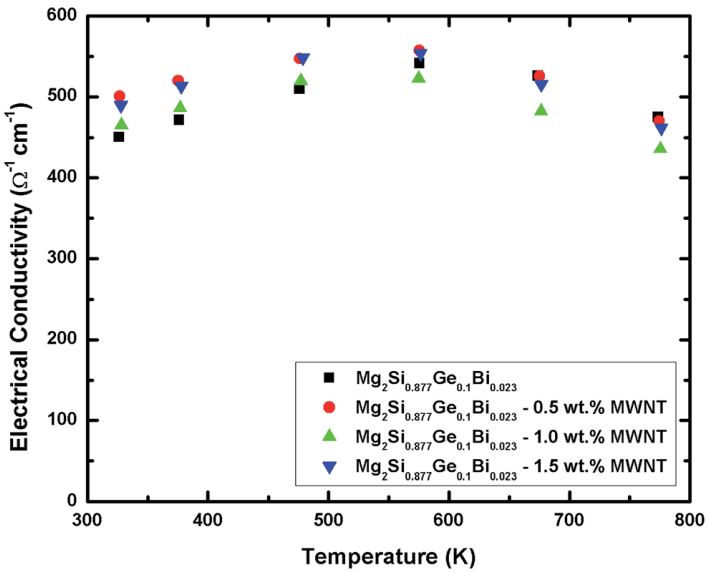

Fig. 7.5 Electrical conductivity of the $Mg_2Si_{0.877}Ge_{0.1}Bi_{0.023}$/MWCNT samples.

The main reason for the increased electrical conductivity is due to the increase in *n* (Fig. 7.6), since the mobility (μ_H) (Fig. 7.7) of all the samples is very similar. The sample containing 0.5 wt% MWCNT shows the highest carrier concentration on average below 300 K with the maximum value of around 8.4×10^{19} per cm^3 at 280 K. Although increasing the amount of carbon nanotubes slightly decreases the carrier concentration, the undoped sample exhibits the lowest on average. The mobility of all samples increases with temperatures, which could be due to the existence of MgO at the grain boundaries, which dominates the grain boundary scattering at lower temperature [27] as also observed in Sb-doped Mg_2Si. [31]

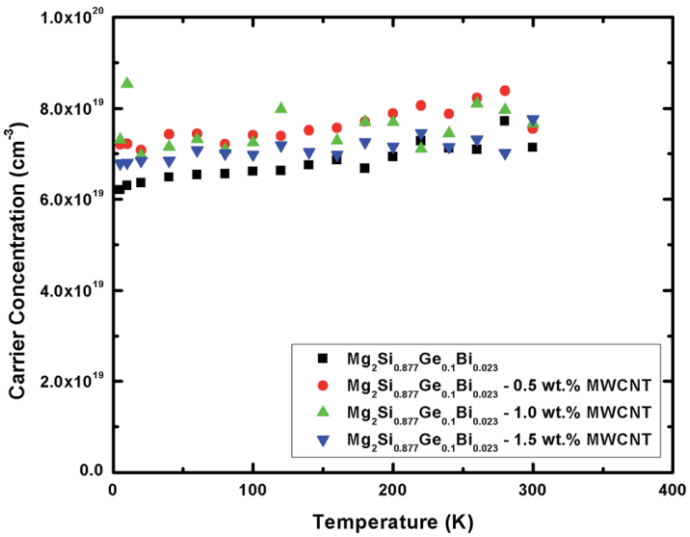

Fig. 7.6 Room temperature carrier concentration of the $Mg_2Si_{0.877}Ge_{0.1}Bi_{0.023}$/MWCNT samples.

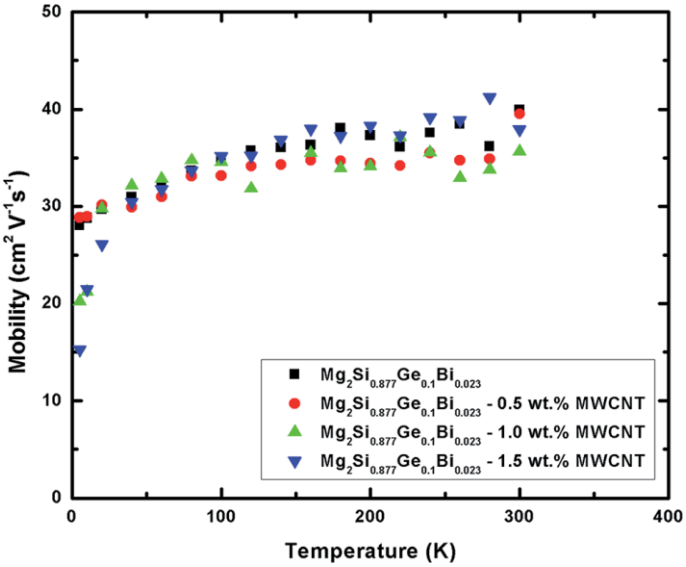

Fig. 7.7 Low temperature Hall mobility of the $Mg_2Si_{0.877}Ge_{0.1}Bi_{0.023}$/MWCNT samples.

A comparison between different Bi-doped Mg_2Si nanocomposites is given in Table 7.1. The 0.5 wt% MWCNT sample shows an electrical conductivity of σ = 470 $\Omega^{-1}cm^{-1}$ at 773 K, which is in between the SWCNH and the Si nanoparticle composite samples with σ = 312 $\Omega^{-1}cm^{-1}$ and 658 $\Omega^{-1}cm^{-1}$, respectively. The main difference between the electrical conductivity of the

MWCNT-containing sample and the one containing Si nanoparticles is due to the 50 percent higher carrier concentration of 11.7×10^{19} per cm^3 of the latter.

Table 7.1 Thermoelectric properties of $Mg_2Si_{0.877}Ge_{0.1}Bi_{0.023}$/0.5% MWCNT at 773 K in comparison to other Mg_2Si-based nanocomposites.

	$Mg_2Si_{0.877}Ge_{0.1}Bi_{0.023}$ / 0.5% MWCNT	Mg_2Si:$Bi_{0.02}$ / SWCNH [19]	Mg_2Si / 2.5 mol% $Si_{1\%Bi}$ [21]
$\sigma(\Omega^{-1}cm^{-1})$	470	312	658
$S/(\mu VK^{-1})$	-200	-216	-204
$\kappa/(Wm^{-1}K^{-1})$	2.2	3.4	3.1
$L/(10^{-8}\ V^2K^{-2})$	1.6	2.5	2.2
$\kappa_L/(Wm^{-1}K^{-1})$	1.6	2.9	2.0
$\mu/(cm^2V^{-1}s^{-1})$ [300 K]	40	n/a	13
$n/(10^{19}\ cm^{-3})$ [300 K]	7.6	n/a	11.7
ZT	0.67	0.32	0.67

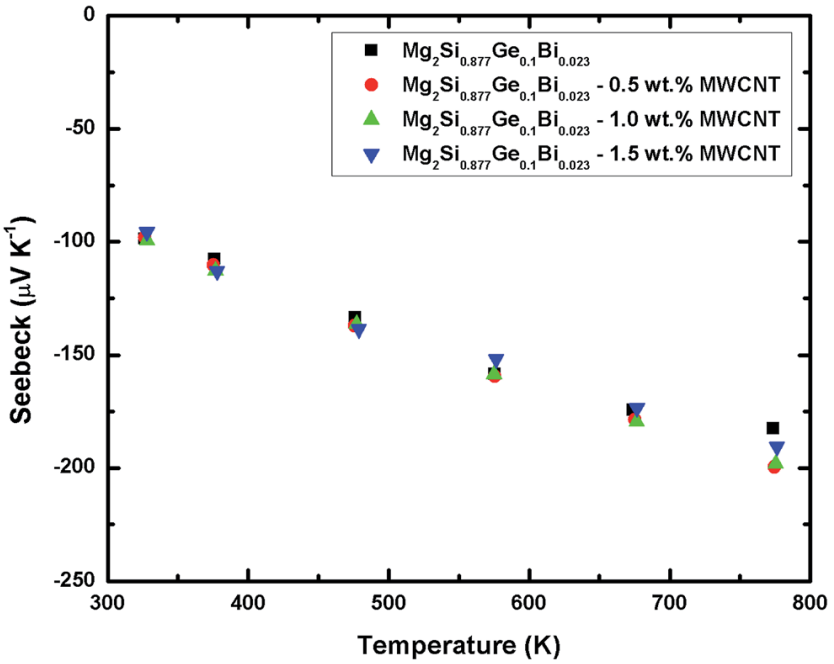

Fig. 7.8 Seebeck coefficient of the $Mg_2Si_{0.877}Ge_{0.1}Bi_{0.023}$/MWCNT samples.

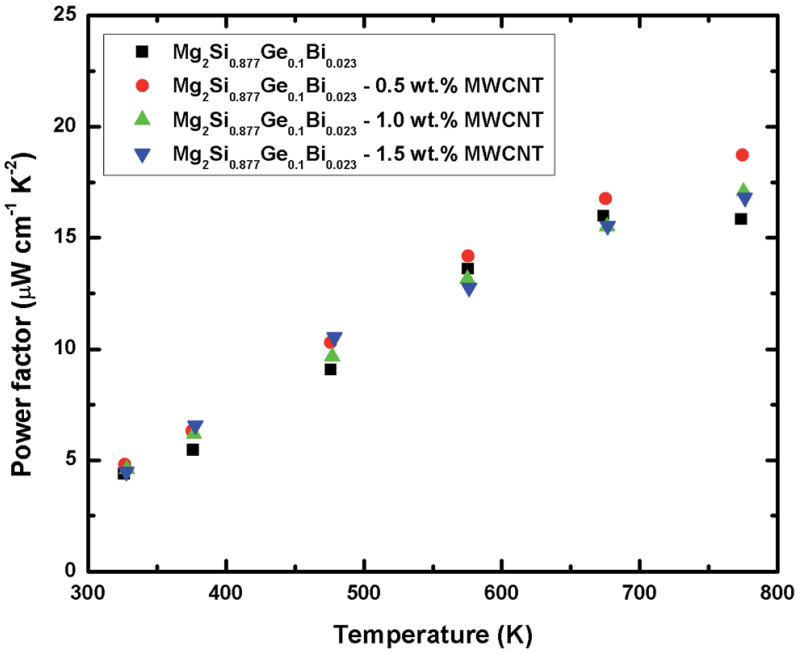

Fig. 7.9 Power factor of MWCNT/$Mg_2Si_{0.877}Ge_{0.1}Bi_{0.023}$ samples.

Fig. 7.8 exhibits the temperature dependence of the Seebeck coefficient. All the composites show a negative Seebeck value, indicative of electrons as the major charge carriers. The Seebeck value is around S = -100 μVK^{-1} at 323 K in every case, and it increases with increasing temperature. For the samples containing MWCNT, the increase is more noticeable, at 773 K with S = -200 μVK^{-1} for the 0.5 wt% MWCNT composite compared to S = -180 μVK^{-1} for the pristine sample. Thus, adding MWCNT resulted in an enhancement in Seebeck coefficient while maintaining the electrical conductivity. This phenomenon was also observed in $(Bi_{0.2}Sb_{0.8})_2Te_3$/MWCNT nanocomposites, [17] and can be attributed to the energy filtering of the low energy charge carriers, [32-35] which is a common phenomenon in nanocomposites due to the nanophase-matrix interface. [36] On the other hand, the SWCNH sample has a slightly higher (absolute) Seebeck coefficient (S = -215 μVK^{-1}), which is related to its noticeably low electrical conductivity (Table 7.1).

The capability of a thermoelectric material to generate electrical power is measured by the power factor, P.F. = $S^2\sigma$, which is demonstrated in Fig. 7.9. The power factor of all samples starts around 5 $\mu Wcm^{-1}K^{-2}$ at 323 K and increases with temperature. Except for the pristine sample, which reaches its maximum power factor of roughly 16 $\mu Wcm^{-1}K^{-2}$ at around 673 K, all the nanocomposites show their highest value at around 773 K, with the 0.5 wt% MWCNT sample attaining ~19 $\mu Wcm^{-1}K^{-2}$. Obtaining higher power factors would lead to higher output power density which makes the material more suitable for practical use. [37]

Fig. 7.10 shows the thermal conductivity of all nanocomposites studied in this work, which was calculated based on the measured thermal diffusivity data. Because of the dominant acoustic phonon scattering, the thermal conductivity of all samples decreases with increasing temperature. The 1.5 wt% MWCNT sample demonstrates the lowest thermal conductivity of

2.07 $Wm^{-1}K^{-1}$, which is substantially lower than that of the samples containing SWCNH and Si nanoparticle composites. This reduction in thermal conductivity can come from the combination of having both Ge and MWCNT in the sample. Since the thermal conductivity of MWCNT is increasing with temperature, [38] the propitious effect of MWCNT on thermal conductivity of nanocomposites is more dominant in the medium temperature range (Fig. C.4).

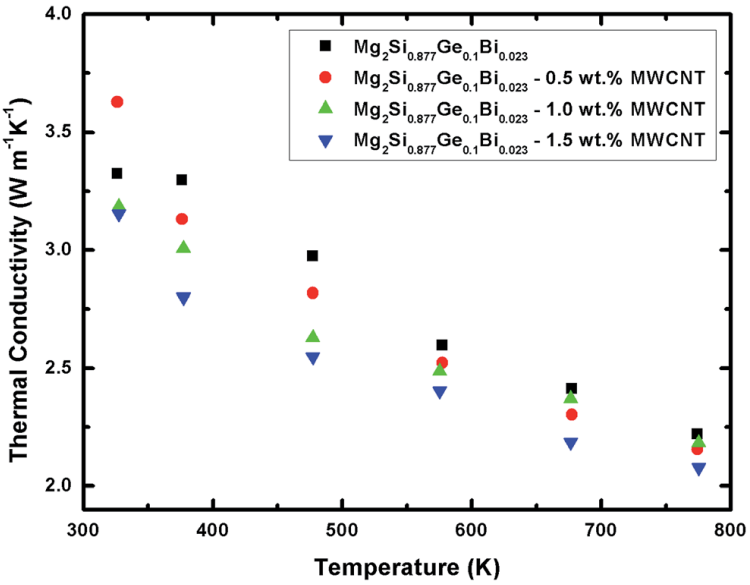

Fig. 7.10 Thermal conductivity of the $Mg_2Si_{0.877}Ge_{0.1}Bi_{0.023}$/MWCNT samples.

The electronic thermal conductivity, κ_e, was calculated by applying the Wiedemann-Franz law $\kappa_e = L\sigma T$. The Lorenz numbers, L, that were used in calculating κ_e are shown in Fig. C.5 and were obtained from eqn (7.1) by utilizing the single parabolic band and elastic carrier scattering estimation:

$$L = \left(\frac{k_B}{e}\right)^2 \left\{\frac{(1+\lambda)(3+\lambda)F_\lambda(\eta)F_{2+\lambda}(\eta) - (2+\lambda)^2 F_{1+\lambda}^2(\eta)}{(1+\lambda)^2 F_\lambda^2(\eta)}\right\} \quad (7.1)$$

where k_B and e are the Boltzmann constant and the electron charge, respectively. The Fermi integral of order j is depicted as $F_j(\eta)$, where η is the reduced Fermi energy (E_F) and is equal to $E_F/(k_BT)$. By assuming acoustic phonon scattering of the carriers (λ = 0), [39] The temperature dependence of η can be determined from the experimental Seebeck coefficient using eqn (7.2):

$$S = \frac{k_B}{e}\left\{\frac{(2+\lambda)F_{1+\lambda}(\eta)}{(1+\lambda)F_{\lambda}(\eta)} - \eta\right\} \quad (7.2)$$

The electronic thermal conductivity of all samples is nearly the same and it increases approximately from 0.3 $Wm^{-1}K^{-1}$ at 323 K to 0.6 $Wm^{-1}K^{-1}$ at 773 K, which leads us to the conclusion that the reduction in thermal conductivity is chiefly coming from changes in the lattice contribution (Fig. 7.11). The sample containing 1.5 wt% MWCNT depicts the lowest lattice thermal conductivity of 1.49 $Wm^{-1}K^{-1}$ at 773 K, compared to 2.85 $Wm^{-1}K^{-1}$ and 2 $Wm^{-1}K^{-1}$ determined for the SWCNH and Si nanoparticle composites, respectively.

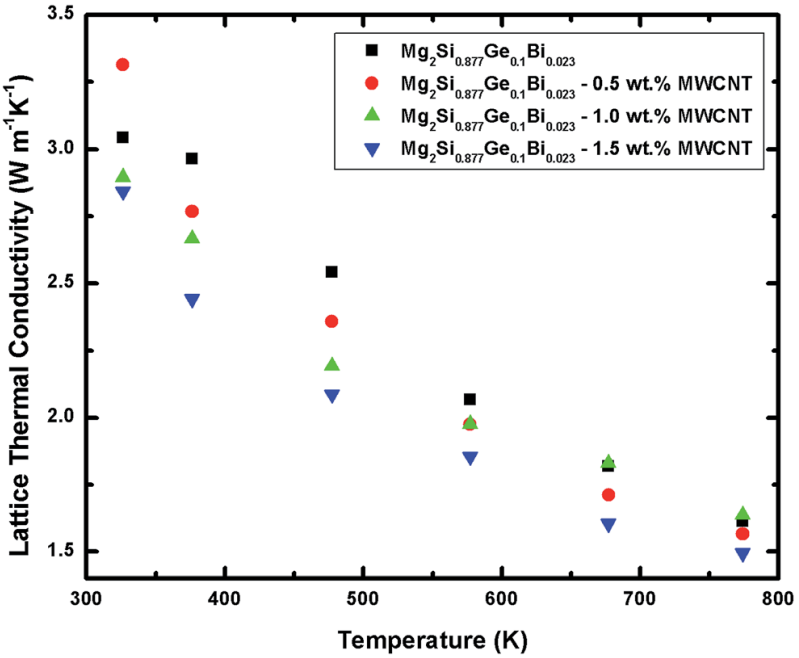

Fig. 7.11 Lattice thermal conductivity of the $Mg_2Si_{0.877}Ge_{0.1}Bi_{0.023}$/MWCNT samples.

After measuring all the thermoelectric properties, the thermoelectric figure of merit *ZT* was computed (Fig. 7.12). The *ZT* of all composites increases with increasing temperature. While all the nanocomposites show higher *ZT* than the pristine sample, the 0.5 wt% MWCNT sample reaches a maximum value of *ZT* = 0.67 at 773 K among all MWCNT. This matches *ZT* of the Si nanoparticle counterpart, and is more than twice of what was achieved for the Bi doped SWCNH composites.

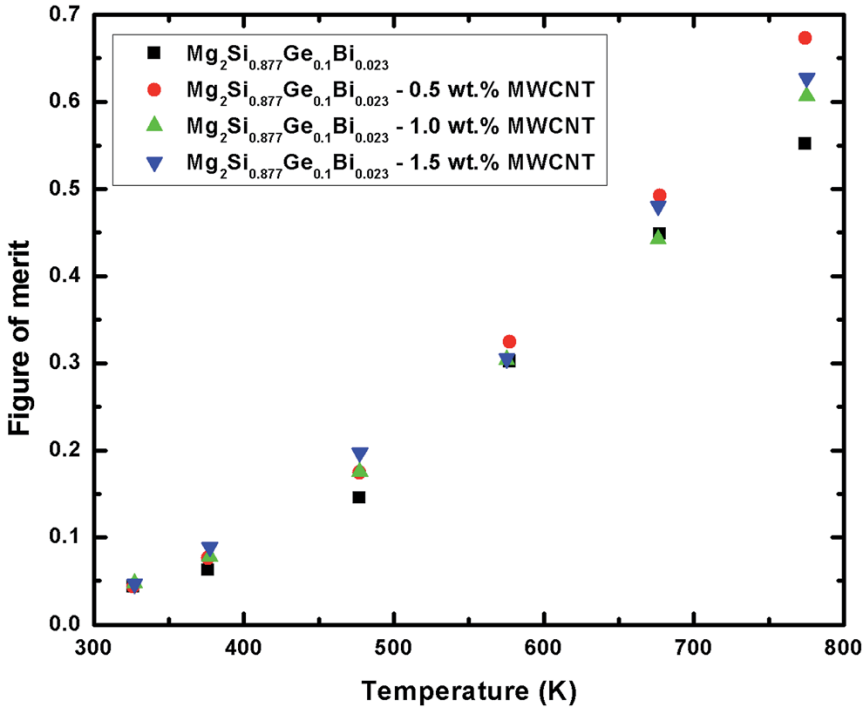

Fig. 7.12 Figure of merit of the $Mg_2Si_{0.877}Ge_{0.1}Bi_{0.023}$/MWCNT samples.

One of the main issues in thermoelectric nanocomposites research is the homogeneity of the distributed nano phase in the matrix and its effect on the properties of the nanocomposites. To examine the reliability of the presented data, a second bar was cut from a different part of the 0.5 wt% MWCNT pellet, and the obtained power factor (Fig. C.6) is equal within experimental error.

7.4 Conclusions

Atomic resolution imaging and EDX analyses on $Mg_2Si_{0.877}Ge_{0.1}Bi_{0.023}$/0.5 wt% MWCNT sample revealed a rather homogenous distribution of Ge and Bi in the bulk of the grains, although Ge partially segregates along the grain boundaries. With *Z*-contrast imaging, we have shown the random distribution in solid solution of Bi and Ge atoms in the Mg_2Si lattice ultimately leading to local lattice distortions of the lattice due to size effects. The inclusion of multi wall carbon nanotubes into $Mg_2Si_{0.877}Ge_{0.1}Bi_{0.023}$ matrix at low concentration not only maintained the high temperature electrical conductivity, but also led to a 10% improvement of the high temperature Seebeck coefficient, which could be due to energy filtering that originated from the $Mg_2Si_{0.877}Ge_{0.1}Bi_{0.023}$-MWCNT matrix interfaces.

Although the existence of MWCNT enhanced phonon scattering especially at medium temperature lowered the lattice thermal conductivity, this reduction is compensated at higher temperature due to the thermal transport behavior of MWCNT. The positive effect of MWCNT on thermoelectric properties of $Mg_2Si_{0.877}Ge_{0.1}Bi_{0.023}$ is manifested by the enhanced thermoelectric figure of merit, *ZT*, with all the nanocomposites achieving higher *ZT* values than the pristine sample. The highest improvement of more than 20% belongs to the sample containing 0.5 wt% MWCNT with its *ZT* of 0.67 at 773 K. Comparing with the other nano inclusions that were applied to Mg_2Si based thermoelectrics, MWCNT exhibited the most promising effect on TE properties, and further development may be implemented through adding tin or *in situ* nanostructuring *via* ball milling.

Acknowledgements

The authors would like to thank AUTO21 (Network Centres of Excellence) and General Motors for financial support of this work. The STEM and EDX work was performed at the

Canadian Centre for Electron Microscopy, a national facility supported by NSERC, the Canada Foundation for Innovation and McMaster University.

References

[1] S. Iijima, *Nature*, 1991, 354, 56-58.

[2] K. Balasubramanian and M. Burghard, *Small*, 2005, 1, 180-192.

[3] F. Yang, X. Wang, D. Zhang, J. Yang, D. Luo, Z. Xu, J. Wei, J.-Q. Wang, Z. Xu, F. Peng, X. Li, R. Li, Y. Li, M. Li, X. Bai, F. Ding and Y. Li, *Nature*, 2014, 510, 522-524.

[4] K. M. Choi, S. Augustine, J. H. Choi, J. H. Lee, W. H. Shin, S. H. Yang, J. Y. Lee and J. K. Kang, *Angew. Chem. Int. Ed. Engl.*, 2008, 47, 9904-9907.

[5] M. V. Vedernikov and E. K. Iordanishvili, in *Seventeenth International Conference on Thermoelectrics. Proceedings ICT98*, IEEE, 1998, pp. 37-42.

[6] T. M. Tritt, *Annu. Rev. Mater. Res.*, 2011, 41, 433-448.

[7] H. Kleinke, *Chem. Mater.*, 2010, 22, 604-611.

[8] S. V Faleev and F. Léonard, *Phys. Rev. B*, 2008, 77, 214304/1-214304/9.

[9] M. Zebarjadi, K. Esfarjani, A. Shakouri, J.-H. Bahk, Z. Bian, G. Zeng, J. Bowers, H. Lu, J. Zide and A. Gossard, *Appl. Phys. Lett.*, 2009, 94, 202105.

[10] M. S. Dresselhaus, G. Chen, M. Y. Tang, R. G. Yang, H. Lee, D. Z. Wang, Z. F. Ren, J.-P. Fleurial and P. Gogna, *Adv. Mater.*, 2007, 19, 1043-1053.

[11] T. Ando, *NPG Asia Mater.*, 2009, 1, 17-21.

[12] C. Qin, X. Shi, S. Q. Bai, L. D. Chen and L. J. Wang, *Mater. Sci. Eng. A*, 2006, 420, 208-211.

[13] D. Suh, D. Lee, C. Kang, I.-J. Shon, W. Kim and S. Baik, *J. Mater. Chem.*, 2012, 22, 21376-21381.

[14] F. Ren, H. Wang, P. A. Menchhofer and J. O. Kiggans, *Appl. Phys. Lett.*, 2013, 103, 221907.

[15] Y. Zhang, X. L. Wang, W. K. Yeoh, R. K. Zheng and C. Zhang, *Appl. Phys. Lett.*, 2012, 101, 031909.

[16] K. T. Kim, S. Y. Choi, E. H. Shin, K. S. Moon, H. Y. Koo, G.-G. Lee and G. H. Ha, *Carbon N. Y.*, 2013, 52, 541-549.

[17] Y. H. Yeo and T. S. Oh, *Mater. Res. Bull.*, 2014, 58, 54-58.

[18] J. Yang and F. R. Stabler, *J. Electron. Mater.*, 2009, 38, 1245-1251.

[19] S. Fiameni, S. Battiston, S. Boldrini, A. Famengo, F. Agresti, S. Barison and M. Fabrizio, *J. Solid State Chem.*, 2012, 193, 142-146.

[20] D. Cederkrantz, N. Farahi, K. A. Borup, B. B. Iversen, M. Nygren and A. E. C. Palmqvist, *J. Appl. Phys.*, 2012, 111, 023701.

[21] T. Yi, S. Chen, S. Li, H. Yang, S. Bux, Z. Bian, N. a. Katcho, A. Shakouri, N. Mingo, J.-P. Fleurial, N. D. Browning and S. M. Kauzlarich, *J. Mater. Chem.*, 2012, 22, 24805.

[22] V. K. Zaitsev, M. I. Fedorov, E. A. Gurieva, I. S. Eremin, P. P. Konstantinov, A. Y. Samunin and M. V Vedernikov, *Phys. Rev. B*, 2006, 74, 045207/1-045207/5.

[23] R. J. LaBotz, D. R. Mason and D. F. O'Kane, *J. Electrochem. Soc.*, 1963, 110, 127-134.

[24] E. Ratai, M. P. Augustine and S. M. Kauzlarich, *J. Phys. Chem. B*, 2003, 107, 12573-12577.

[25] T. Ikeda, L. Haviez, Y. Li and G. J. Snyder, *Small*, 2012, 8, 2350-2355.

[26] N. Farahi, S. Prabhudev, G. Botton, J. Zhao, J. S. Tse, Z. Liu, J. R. Salvador and H. Kleinke, *J. Alloy. Compd.*, 2015, 644, 249-255.

[27] N. Farahi, M. VanZant, J. Zhao, J. S. Tse, S. Prabhudev, G. Botton, J. R. Salvador, F. Borondics, Z. Liu and H. Kleinke, *Dalt. Trans.*, 2014, 43, 14983-14991.

[28] M. S. Dresselhaus, G. Dresselhaus, P. C. Eklund and A. M. Rao, *in The Physics of Fullerene-Based and Fullerene-Related Materials SE - 9*, ed. W. Andreoni, Springer Netherlands, 2000, vol. 23, pp. 331-379.

[29] A. M. Rao, A. Jorio, M. A. Pimenta, M. S. S. Dantas, R. Saito, G. Dresselhaus and M. S. Dresselhaus, *Phys. Rev. Lett.*, 2000, 84, 1820-1823.

[30] J. H. Lehman, M. Terrones, E. Mansfield, K. E. Hurst and V. Meunier, *Carbon N. Y.*, 2011, 49, 2581-2602.

[31] J. de Boor, T. Dasgupta, H. Kolb, C. Compere, K. Kelm and E. Mueller, *Acta Mater.*, 2014, 77, 68-75.

[32] Y. Zhang, J.-H. Bahk, J. Lee, C. S. Birkel, M. L. Snedaker, D. Liu, H. Zeng, M. Moskovits, A. Shakouri and G. D. Stucky, *Adv. Mater*., 2014, 26, 2755-2761.

[33] A. Shakouri, Annu. *Rev. Mater. Sci*., 2011, 41, 399-431.

[34] A. Soni, Y. Shen, M. Yin, Y. Zhao, L. Yu, X. Hu, Z. Dong, K. A. Khor, M. S. Dresselhaus and Q. Xiong, *Nano Lett*., 2012, 12, 4305-4310.

[35] N. D. Y. Truong, H. Kleinke and F. Gascoin, *Dalt. Trans*., 2014, 43, 15092-15097.

[36] D. L. Medlin and G. J. Snyder, *Curr. Opin. Colloid Interface Sci*., 2009, 14, 226-235.

[37] W. Liu, H. S. Kim, S. Chen, Q. Jie, B. Lv, M. Yao, Z. Ren, C. P. Opeil, S. Wilson, C.-W. Chu and Z. Ren, *Proc. Natl. Acad. Sci. U. S. A*., 2015, 112, 3269-3274.

[38] R. Prasher, *Phys. Rev. B*, 2008, 77, 075424.

[39] V. I. Fistul', *Heavily Doped Semiconductors*, Springer New York, Boston, MA, 1995.

CHAPTER 8

CHARGE DENSITIES OF MULTI-DOPED Mg_2Si THERMOELECTRIC MATERIALS USING THE MAXIMUM ENTROPY METHOD

The Maximum Entropy Method (MEM) is a powerful tool to determine the most probable electron density distributions from X-ray diffraction measurements using a limited number of Bragg reflections. [12-14] This method has been successfully applied to the characterization of the electron density and bonding of a variety of materials including semiconductor, metals, and ionic systems. [15] A good example is manganites $La_{0.67}Sr_{0.22}Mn_{1.11-x}Co_xO_3$. From MEM analysis, the charge density distribution in the perovskite structure was reconstructed and the effect of Co^{3+} doping in the Mn-O matrix was investigated. [16] Francis *et al*. reported the effect of Co doping on the electronic, structural, magnetic and optical properties of ZnO bulk samples. [17] The electron density distribution of $NaCoO_2$ has also been studied by the MEM using single-crystal X-ray diffraction data obtained at 298 K. In this work, the strong covalent bonding was clearly observed between Co and O atoms, but no bonding around Na atom. [18] Previously, a similar technique has been applied to thermoelectric materials: Saravanan *et al*. have used the MEM to extract the electron density distribution and local structure of PbTe, pure Mg_2Si and other crystalline systems. [19-21] The electron density of the high performance thermoelectric material Zn_4Sb_3 has also been determined from synchrotron X-ray powder diffraction data. [22] Ohno *et al*. revealed three types of charge density overlap between atoms in $CoSb_3$, and the four Sb atoms form an Sb_4 ring. [23] Recently, Kastbjerg *et al.* found strong anharmonicity and large cation disorder are present in both PbTe and PbS thermoelectric materials. [24] Compared to the traditional Fourier analysis, MEM avoids the series termination errors on the extraction of electron density in the crystal. Therefore, with a limited diffraction data set, it is possible to extract the gross feature in the bonding and electron

density distribution of a crystal. We hope that this technique can be useful to reveal the charge density topology of the host atoms as well as for the doped samples.

In this Chapter, we investigated the valence charge density distribution of Mg_2Si thermoelectric materials multi-doped with Al, Zn and Sb using data from synchrotron X-ray powder diffraction experiments. The compounds studied were $Mg_{1.99}Al_{0.005}Zn_{0.005}Si_{0.995}Sb_{0.005}$, $Mg_{1.995}Zn_{0.005}Si_{0.995}Sb_{0.005}$, $Mg_{1.99}Zn_{0.01}Si_{0.995}Sb_{0.005,}$ and $Mg_{1.99}Al_{0.01}Si$. The results show the valence electron topologies are correctly calculated. However, due to the limited number of Bragg diffraction peaks in the experimental patterns, the finer details on the effect of the dopants to the core charge density may not be too reliable. An error analysis on the contributions of the high angle obtained data for a diffraction pattern of Al-doped Mg_2Si was performed. We concluded that since the electron density differences for pure Mg_2Si were located far away from the atomic sites the results and conclusions are qualitatively correct.

The results of this study are under preparation for submission

J. Zhao, J. Reid, K. Takarabe, and J. S. Tse, "Charge Densities of Multi-doped Mg_2Si Thermoelectric Materials using the Maximum Entropy Method".

- The authors' contributions are as follow,
- J. Zhao and J. S. Tse performed the diffraction experiments and MEM analysis to determine the charge density distribution of doped Mg_2Si thermoelectric materials and calculated the electronic structures.
- J. Reid assisted in performing powder X-ray diffraction experiments at CLS.
- K. Takarabe provided the samples in Japan.

- All authors contributed to the writing and editing of the manuscript.

Abstract

In this chapter, we present the valence electron topologies of Mg_2Si multi-doped with Al, Zn and Sb thermoelectric materials determined by the Maximum Entropy Method (MEM) using synchrotron X-ray powder diffraction data. In spite of the very lower concentration, the cubic unit cells were found to expand in the doped samples. Using pure Mg_2Si as reference, charge density difference maps revealed qualitative features on the distributions of the electrons contributed by the doped atoms. The presences of excess electrons show all doped samples are *n*-type semiconductors and they are shared among the atomic sites. We evaluated the reliability of the MEM calculated charge density by considering the effect of successively increasing the number of high angle Bragg reflections used in the analysis on the diffraction pattern of a single doped Al-Mg_2Si sample.

8.1 Introduction

Magnesium silicide (Mg_2Si) doped with heavy elements are potentially high performance and environmental friendly thermoelectric materials. [1-4] Compared to conventional lead-based thermoelectric materials, Mg_2Si-based alloys have merit as they are non-toxic, sustainable, light and low cost. A figure of merit for the efficiency of a thermoelectric material at temperature T is given by $ZT=S^2T\sigma/\kappa$, where S is the Seebeck coefficient, σ is the electrical conductivity and κ is the thermal conductivity. Therefore, a good candidate material must possess high Seebeck coefficient, high electrical conductivity, and low thermal conductivity. Previously research have shown that *p*- or *n*-type doping enhances the efficiency of thermoelectric materials. [5-10] The electron-rich dopants can increase the carrier concentration and mobility of the conduction electrons thus enhancing the electrical conductivity. In addition, doping with heavy atoms affects

lattice vibrations and helps to lower the thermal conductivity by increasing phonon-phonon scatterings. Recently, Zhao *et al*. found the thermoelectric and electrical transport properties of Mg_2Si thermoelectric materials were enhanced significantly after doping with Al, Zn and Sb. Within this class of compounds, the best *ZT* of 0.964 at 880 K has been achieved, a value comparable to those of PbTe-based thermoelectric materials. [11] Here, we wish to study the effect of dopants on the valence charge density using powder diffraction patterns. This investigation is relevant as the exact locations of the dopants in Mg_2Si are still ambiguous. In the case of single doping by Al or Sb, it is generally believed that since the doped samples are *n*-type semiconductors the dopants Al should replace the Mg sites thus increasing the electron concentration. [12,13] However, there is no concrete experimental evidence to substantiate this assignment. A recent electronic structure calculation has shown that the site preference of Al at lower concentration in Mg_2Si is ambiguous. [14] This theoretical study was also not able to determine conclusively the site preference of Sb at the doping level of 1% and 3%. Finally, no experimental data is available for the Zn-doping although it is expected Zn atoms should substitute the Mg sites.

The Maximum Entropy Method (MEM) is a powerful tool for determining the most probable valence electron density distributions from X-ray diffraction measurements using a limited number of low angle Bragg reflections and without the prior knowledge of the atomic positions. [15-17] The MEM has been successfully applied to evaluate the electron density and bonding of a variety of materials including semiconductors, metals, and ionic systems. [18] For example, the MEM was used to reconstruct the charge density distribution in the perovskite structure of the manganite $La_{0.67}Sr_{0.22}Mn_{1.11-x}Co_xO_3$ to evaluate the effect of Co^{3+} doping in the Mn-O matrix. [19] Francis *et al*. reported the effect of Co doping on the electronic, structural,

magnetic, and optical properties of ZnO bulk samples. [20] The electron density distribution of $NaCoO_2$ has been studied by using single-crystal X-ray diffraction data obtained at 298 K and the results show strong covalent bonding between Co and O atoms but no bonding around the Na atom. [21] Previously, a similar technique was applied to the study of thermoelectric materials. Saravanan *et al*. used the MEM and pair distribution functions to extract the electron density distribution and local structure of PbTe, pure Mg_2Si and other crystalline systems. [22-24] The electron density of the high performance thermoelectric material Zn_4Sb_3 has also been determined from synchrotron powder diffraction data. [25] In $CoSb_3$, Ohno *et al*. revealed three types of charge density overlap between atoms in particular, it was found that four Sb atoms formed a ring structure. [26] Recently, Kastbjerg *et al.* found strong anharmonicity and large cation disorder are present in both PbTe and PbS thermoelectric materials. [27] Compared to the traditional Fourier analysis, the MEM avoids the series-termination errors on the extraction of electron density in the crystal. Therefore, with a limited diffraction data set, it may be possible to extract qualitative bonding and electron density distribution of the host atoms as well as the dopant atoms in thermoelectric materials.

The objective of this paper is to characterize and better understand the effect of the electron density distribution of the dopants in Mg_2Si crystals. For this purpose, we studied Mg_2Si samples multi-doped with Al, Zn and Sb synthesized by spark plasma sintering technique. Synchrotron X-ray powder diffraction experiments were performed at the Canadian Macromolecular Crystallography Facility (CMCF) and Hard X-ray MicroAnalysis (HXMA) beamlines of the Canadian Light Source under ambient pressure and temperature. The electron density distributions in the crystal were investigated from the analysis of X-ray diffraction patterns using the Maximum Entropy Method implemented within the Dysnomia code. [28]

The layout of this paper is as follows: First, details on the experimental procedure are described. The diffraction patterns of the Mg_2Si samples multi-doped with Al, Zn and Sb are compared with pure Mg_2Si. This is followed by a discussion on the trend of electron density distributions in the crystal. The paper concludes with an investigation on the dependence of the evaluated charge density with respect to the number of Bragg reflections as illustrated from the analysis of a high angle diffraction pattern of Al-doped Mg_2Si.

8.2 Experimental details

8.2.1 Synthesis and Sintering Process for Preparation of Doped Mg_2Si Samples

Polycrystalline Mg_2Si was synthesized from stoichiometric melts with Mg:Si = 2:1 using an electric furnace by lowering the temperature from slightly beyond the melting point (1378 K) of Mg_2Si. The starting materials, Mg and Si, were placed in an alumina crucible under argon-hydrogen forming gas (0.08MPa). Intentional impurities, antimony (Sb) aluminium (Al) and zinc (Zn) were incorporated in order to increase the electronic carrier concentrations and to promote phonon scattering. The dopants were incorporated during the synthesis process at 1378 K. The resultant polycrystalline Mg_2Si, pulverized into powder with a granule size ranging from 25 to 75μm, was then placed into a graphite die and sintered by a plasma-activated sintering (PAS) technique using an ELENIX Ed-PAS-III-Es. The sintering was performed at 1123 K for 10 min. at a pressure of 40 MPa in an Ar atmosphere. Depending on the dopant, the sintering temperature and time were varied in order to obtain a dense material. The compositions of the samples were analysed by electron-probe microanalysis (EPMA) using JEOL JXA-8900. The concentrations of the dopant impurities in the samples were estimated by grow discharge mass spectrometry (GDMS) using a V.G. Scientific VG-9000. Previous studies have focused that the Sb and Al doped Mg_2Si are *n*-type semiconductors and therefore the dopants should predominantly

substitute in the Si and Mg, respectively. On the other hand, Zn is expected to show no significant contribution to carrier generation but influence over the phonon scattering behaviour, leading to a reduction in the thermal conductivity.

8.2.2 X-ray Powder Diffraction Measurements

The reference pure powder Mg_2Si with a purity of 99.5%, was purchased from Alfa Products. Powder diffraction patterns of three Mg_2Si-doped samples were measured by synchrotron X-ray at the CMCF beamline of the Canadian Light Source [29], with an X-ray wavelength of λ=0.68880 Å. The nominal concentrations of the samples were 0.5 at. % of Sb, 0.5 at. % of Al, 0.5~1.0 at. % of Zn at. % of Sb0.5% Al0.5% Zn0.5%, Sb0.5% Zn0.5%, and Sb0.5% Zn1.0%. The compounds studied were $Mg_{1.995}Zn_{0.005}Si_{0.995}Sb_{0.005}$, $Mg_{1.99}Zn_{0.01}Si_{0.995}Sb_{0.005}$ and $Mg_{1.99}Al_{0.005}Zn_{0.005}Si_{0.995}Sb_{0.005}$. In addition, in order to obtain diffraction data at higher scattering angles, the measurement of 1% Al-doped Mg_2Si ($Mg_{1.99}Al_{0.01}Si$) sample was performed at the HXMA beamline [30] using a shorter synchrotron X-ray wavelength of λ=0.50917 Å. All diffraction patterns were analyzed with the JANA 2006 software package with the lattice parameters determined by Le Bail fit. [31,32] The structure factors used in the maximum entropy analysis were extracted from Le Bail fit of the Bragg's intensities of the diffraction patterns.

8.2.3 Maximum Entropy Method (MEM)

The Maximum Entropy Method, based on the information theory, [15] can be used to determine the electron density distribution from the analysis of the structure factors obtained from a powder diffraction pattern. In this work, the charge density distributions were analyzed using the Dysnomia software package. [28] In the MEM analysis, the unit cell was partitioned into 128×128×128 pixels. The initial charge density used a uniform distribution. The total

scattering factor ($F(000)$) was scaled to the nominal concentration of the dopants. Thus, the $F(000)/a^3$ are 152 $e/Å^3$ for pure Mg_2Si, 153.1 $e/Å^3$ for $Mg_{1.995}Zn_{0.005}Si_{0.995}Sb_{0.005}$, 153.46 $e/Å^3$ for $Mg_{1.99}Zn_{0.01}Si_{0.995}Sb_{0.005}$, 153.12 $e/Å^3$ for $Mg_{1.99}Al_{0.005}Zn_{0.005}Si_{0.995}Sb_{0.005}$, and 152.04 $e/Å^3$ for $Mg_{1.99}Al_{0.01}Si$. The three-dimensional (3D) and two-dimensional (2D) visualization charge densities were plotted using the VESTA program. [33-36]

8.2.4 Electronic Structure Calculations

First principles electronic calculations were performed using density functional theory (DFT) within the Perdew-Burke Ernzerhof (PBE) parameterization of the generalized gradient approximation (GGA) as implemented in the Vienna ab initio simulation package (VASP) code. [37-40] For all calculations, the projector-augmented wave (PAW) [41,42] potentials were used with the following valence configurations: $3s^2 3p^1$ for Al, $3d^{10} 4s^2$ for Zn, $5s^2 5p^3$ for Sb, $3s^2 3p^0$ for Mg and $3s^2 3p^2$ for Si.

For Al, Zn, and Sb substitutions, two models with different substitution sites were considered. Two models with 0.6% at Al Zn Sb doped Mg_2Si were constructed from a 3×3×3 supercell of the pure crystal. In the first, Zn atoms were put on the Mg sites with Si sites substituted by Al and Sb (*i.e.* $(Mg_{214}Zn_2)(Si_{104}Al_2Sb_2)$). In the second model, some Mg atoms were replaced by Al and Zn with Si sites substituted by Sb (*i.e.* $(Mg_{212}Zn_2Al_2)(Si_{106}Sb_2)$). A 2×2×2 *k*-point mesh was used for the calculation of the projected density of states (pdos) on the supercells.

8.3 Results and Discussion

High-resolution synchrotron angle dispersive X-ray diffraction patterns of pure Mg_2Si and doped Mg_2Si samples were measured under ambient conditions (Fig. 8.1 (a) and (b)). The lattice parameters were determined from full profile Le Bail to the diffraction patterns using

angular data with range from 5° to 40°. The X-ray diffraction patterns of pure Mg_2Si can be indexed readily to the cubic anti-fluorite (CaF_2) structure with space group *Fm-3m*. In increasing diffraction angle, the Miller indices (*hkl*) of the Bragg peaks were assigned to (111), (200), (220), (311), (222), (400), (331), (420), (422), (511), (440), (531) and (600) reflections. The diffraction patterns of all the multi-doped Mg_2Si samples share the same profile as pure Mg_2Si except the positions of the Bragg peaks shifted noticeably to lower angles. (See Fig. 8.1 (a)) This indicates that even with small dopant concentrations (0.5%~1.0%) the cubic lattice of Mg_2Si was expanded. This is clearly seen in the expanded region 9°-12° of the (111) peak. (See Fig. 8.1 (b)) The cubic cell parameter of pure Mg_2Si a = 6.2843(9) Å is increased to 6.3571(9) Å to 6.3634(9) Å by the substitutions of the dopants Zn, Al, and Sb, respectively. This trend can be rationalized from the fact that the atomic sizes of Zn and Al dopants that are larger than Mg, and Sb is larger than Si. A more detailed examination of the lattice constants of the doped Mg_2Si samples shows, for instance, compared with $Mg_{1.995}Zn_{0.005}Si_{0.995}Sb_{0.005}$, the lattice constant of $Mg_{1.99}Zn_{0.01}Si_{0.995}Sb_{0.005}$ is larger, possibly due to the higher doping concentration of Zn. In comparison, the lattice parameter of $Mg_{1.995}Zn_{0.005}Si_{0.995}Sb_{0.005}$ is similar to $Mg_{1.99}Al_{0.005}Zn_{0.005}Si_{0.995}Sb_{0.005}$, suggesting that Al has a weaker effect on the expansion of the crystal lattice, probably due to the similar atomic sizes of Al and Mg atoms.

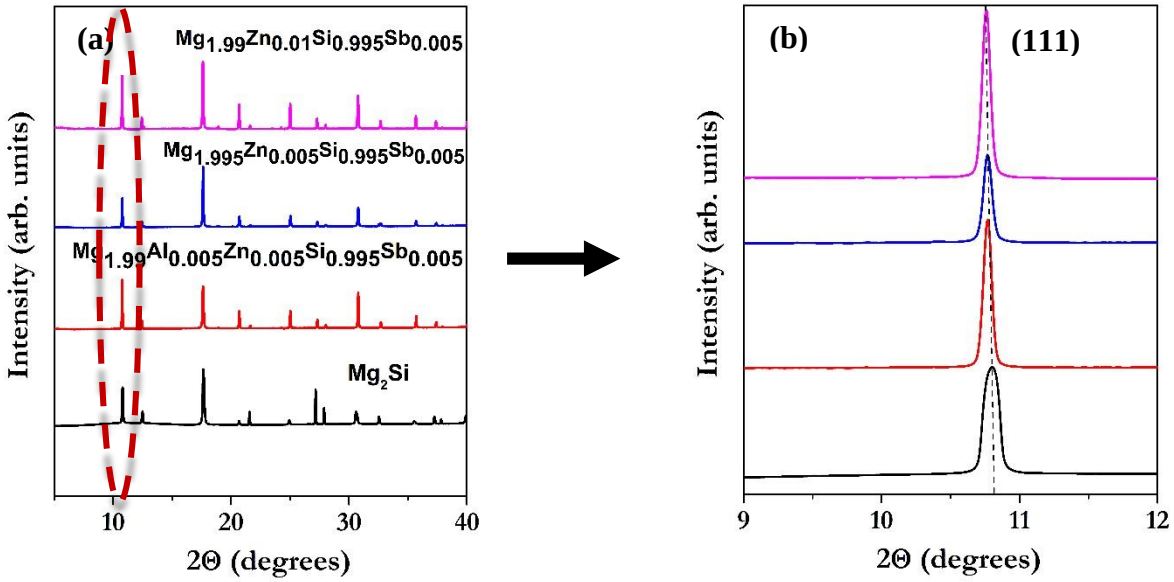

Fig. 8.1 (a) Angle dispersive X-ray diffraction patterns of pure Mg_2Si and doped Mg_2Si measured at ambient conditions; (b) The expanded diffraction patterns between 9° to 12° of the (111) peak.

The intensities of the Bragg reflections of pure and doped Mg_2Si were determined from Le Bail fit to the diffraction profiles. The background was represented by a 15 terms Legendre polynomial function. The lineshape of the Bragg peaks was assumed to be a pseudo-Voigt function, a combination of Gaussian and Lorentzian profile functions. Fig. 8.2 (a)-(d) shows the measured and refined profiles of pure and doped Mg_2Si samples, respectively. The measured data (crosses) and calculated diffraction profiles (continuous solid line) are in reasonable agreement with each other. In addition, the vertical lines below the diffraction pattern indicate the calculated positions of Bragg peaks. The calculated structure factors (F_{cal}), the observed structure factors (F_{obs}), and the standard derivation ($\sigma(F_{obs})$) are summarized in Table 8.1. The small standard derivation errors (0.5~3) in $\sigma(F_{obs})$ indicate the goodness of the fitted intensities.

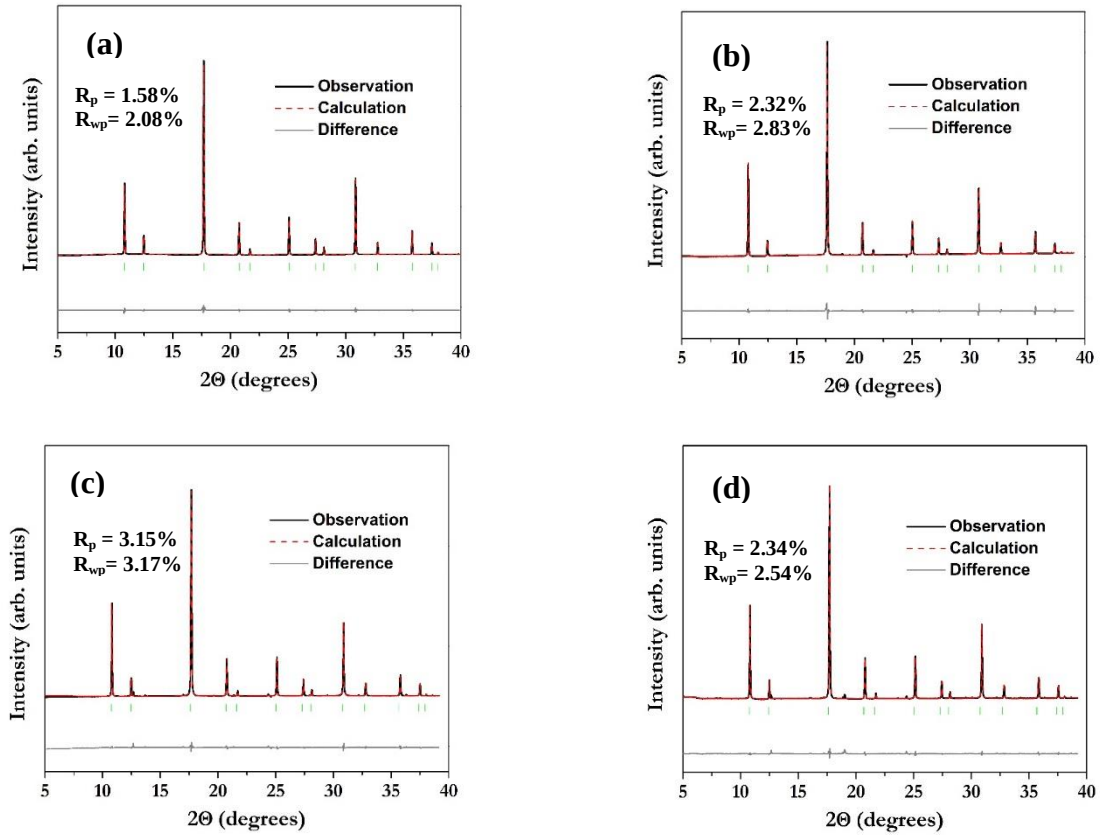

Fig. 8.2 Le Bail fit to the experimental X-ray diffraction patterns for (a) pure Mg_2Si; (b) $Mg_{1.99}Al_{0.005}Zn_{0.005}Si_{0.995}Sb_{0.005}$; (c) $Mg_{1.995}Zn_{0.005}Si_{0.995}Sb_{0.005}$; and (d) $Mg_{1.99}Zn_{0.01}Si_{0.995}Sb_{0.005}$.

Table 8.1 The structure factor of pure & doped Mg_2Si obtained from diffraction data.

Pure Mg_2Si			
h k l	F_{obs}	F_{cal}	σ (F_{obs})
1 1 1	45.61	44.07	0.71
0 0 2	-31.15	-31.51	0.84
2 0 2	100.00	100.08	1.23
1 1 3	33.97	35.51	0.70
2 2 2	-26.81	-26.40	0.90
0 0 4	87.36	87.49	1.71
3 1 3	30.76	31.48	0.90
2 0 4	-21.82	-20.91	0.97
2 2 4	75.60	74.42	1.16
3 3 3	27.17	27.26	0.83
1 1 5	27.17	27.45	0.83
4 0 4	68.14	65.73	1.64
3 1 5	24.68	24.48	0.52
0 0 6	-13.43	-13.43	0.27
4 2 4	-13.43	-13.49	0.27

$Mg_{1.99}Al_{0.005}Zn_{0.005}Si_{0.995}Sb_{0.005}$			
h k l	F_{obs}	F_{cal}	σ (F_{obs})
1 1 1	47.17	46.60	0.91
0 0 2	-26.05	-25.90	0.86
2 0 2	100.00	97.78	1.54
1 1 3	33.00	32.93	0.95
2 2 2	-23.39	-23.22	0.57
0 0 4	82.94	80.94	2.33
3 1 3	31.17	29.96	1.30
2 0 4	-18.40	-18.09	0.58
2 2 4	72.62	70.10	1.49
3 3 3	27.33	26.61	1.41
1 1 5	27.33	25.79	1.41
4 0 4	66.94	61.73	2.40
3 1 5	24.39	22.93	1.37
0 0 6	-10.54	-10.63	1.18
4 2 4	-10.54	-10.81	1.18

$Mg_{1.995}Zn_{0.005}Si_{0.995}Sb_{0.005}$			
h k l	F_{obs}	F_{cal}	$\sigma (F_{obs})$
1 1 1	47.67	46.72	1.09
0 0 2	-28.16	-27.68	1.13
2 0 2	100.00	98.33	1.66
1 1 3	34.64	32.81	1.22
2 2 2	-23.64	-23.16	0.95
0 0 4	89.51	84.99	2.99
3 1 3	31.83	29.64	1.73
2 0 4	-18.82	-18.46	0.61
2 2 4	74.72	71.38	1.87
3 3 3	28.06	27.64	0.98
1 1 5	28.06	26.97	0.98
4 0 4	65.40	61.09	3.27
3 1 5	25.36	22.82	1.88
0 0 6	-11.36	-11.26	1.13
4 2 4	-11.36	-11.37	1.13

$Mg_{1.99}Zn_{0.01}Si_{0.995}Sb_{0.005}$			
h k l	F_{obs}	F_{cal}	$\sigma (F_{obs})$
1 1 1	47.60	46.69	0.88
0 0 2	-29.02	-28.59	0.81
2 0 2	100.00	100.08	1.40
1 1 3	36.67	35.10	0.89
2 2 2	-24.64	-23.90	0.91
0 0 4	90.71	88.22	2.18
3 1 3	31.36	30.01	0.98
2 0 4	-19.86	-19.25	0.57
2 2 4	74.47	73.19	1.42
3 3 3	28.57	27.92	1.23
1 1 5	28.57	27.03	1.23
4 0 4	64.88	63.22	2.16
3 1 5	25.49	23.76	1.16
0 0 6	-11.52	-11.56	1.12
4 2 4	-11.52	-11.63	1.12

The charge densities of the samples were determined from the structure factors extracted from the X-ray diffraction patterns using the MEM. For pure Mg_2Si, convergence in the MEM refinement was reached when the Lagrange parameter (λ)=0.001 and reliability indices R_{MEM}=1.58% and wR_{MEM}=2.08% were achieved (where R_{MEM} is the unweighted index and wR_{MEM} is the weighted index). For the doped Mg_2Si samples, similar analyses with comparable accuracy were obtained. The 3D MEM charge density surface contour plot for pure Mg_2Si showed the correct positions of charge density in Mg and Si sites (Fig. 8.3) in the unit cell. Electron densities are concentrated at the equivalent 4*a* sites of Si (0,0,0) and the 8*c* (1/4,1/4,1/4) sites of Mg. This picture is consistent with the face-centered cubic crystal structure of pure Mg_2Si with an *Fm-3m* space group. Furthermore, visualization of the charge density shows the ionic of the chemical bonding indicating the electron charges distribution are visually very similar at the Si and Mg sites as the size of the charge clouds were comparable between the Mg and Si atoms. The results obtained here are similar to those previously reported. [22]

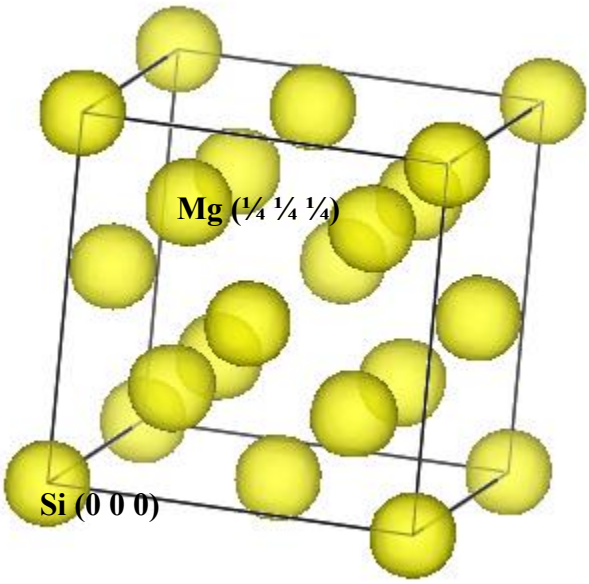

Fig. 8.3 3D charge density of pure Mg_2Si in the unit cell (The value of the contour surface is 0.5 e/Å^3.)

To reveal the distribution of the excess electrons donated by the dopants, three-dimensional (3D) and two-dimensional (2D) electron densities difference (Δρ) maps in which the electron density of pure Mg_2Si was subtracted from the doped samples were calculated. The 3D electron distribution differences are shown in Fig. 8.4 (a) and (b). In Fig. 8.4 (a) and (b), positive and negative differences were plotted with surface contours of ±0.5 e/Å^3, respectively. It is surprising that both positive and negative density difference were found in the atomic core regions. It might suggest there may be core polarization. However, as will be discussed below, this explanation is untenable as the inherent errors in the analysis are very large in the atomic core region.

A strategy to analyze the MEM results is to fix the unit cells of the doped Mg_2Si samples to that of pure Mg_2Si. In this case, for the doped Mg_2Si samples, the only difference is the number of electrons added in the unit cell. As mentioned above, we always found spurious positive and negative electron density (-0.5~0 e/Å^3) inside the core region of Mg atoms. This

observation is unrealistic as we have only used X-ray diffraction data up to a *d*-spacing of 1 Å, therefore, it is not expected that reliable density with $r<1$ Å can be obtained. We therefore ignored the core electron density and only analyzed the positive electron density difference. In Fig. 8.5, the electron density difference maps of the doped samples projected in the (100) and (110) planes of the unit cell are compared by using the experimental unit cells for the analysis of the MEM for the doped samples. The (100) plane contains only the Si atoms and the (110) plane contains both Si and Mg atoms. The results show the obvious trend that all the doped samples gained electrons in the crystal with the addition of the dopants (Sb, Al and Zn). The most important observation is that, even though doped atoms are expected to locate at specific atom sites, the extra electrons are not localized in specific spatial regions, but both Mg and Si sites gain electrons. This observation will be explained later with the DFT-calculated density of states.

Examination of the MEM derived electron densities of the doped Mg_2Si samples shows the charge accumulation on the Si sites increased in the order of $Mg_{1.99}Al_{0.005}Zn_{0.005}Si_{0.995}Sb_{0.005}$ (Sb0.5%Al0.5%Zn0.5%)<$Mg_{1.995}Zn_{0.005}Si_{0.995}Sb_{0.005}$ (Sb0.5%Zn0.5%)<$Mg_{1.99}Zn_{0.01}Si_{0.995}Sb_{0.005}$ (Sb0.5%Zn1.0%). (See Fig. 8.5(a) and (b)) Comparing the charge density difference maps containing only the Si atoms in the (100) plane (Fig. 8.5 (a)), we found that $Mg_{1.995}Zn_{0.005}Si_{0.995}Sb_{0.005}$ and $Mg_{1.99}Zn_{0.01}Si_{0.995}Sb_{0.005}$ are similar, indicating that the increase of Zn concentration does not affect the charge distribution, so it is likely that Zn does not occupy the Si sites. The charge density difference of $Mg_{1.99}Al_{0.005}Zn_{0.005}Si_{0.995}Sb_{0.005}$ is different from those of $Mg_{1.995}Zn_{0.005}Si_{0.995}Sb_{0.005}$ and $Mg_{1.99}Zn_{0.01}Si_{0.995}Sb_{0.005}$. Since the only difference in chemistry is the addition of the Al atom in $Mg_{1.99}Al_{0.005}Zn_{0.005}Si_{0.995}Sb_{0.005}$, we may conclude Al occupies the Si sites. An additional evidence is that the charge density on the Si sites in $Mg_{1.99}Al_{0.005}Zn_{0.005}Si_{0.995}Sb_{0.005}$ is lower than the other two compounds

($Mg_{1.995}Zn_{0.005}Si_{0.995}Sb_{0.005}$ and $Mg_{1.99}Zn_{0.01}Si_{0.995}Sb_{0.005}$), since Al has one less electron that Si. If the Zn atoms indeed is situated at the Mg sites, as suggested above one would expect when the concentration of Zn is increased from 0.5% to 1.0%, there will be more electrons at the sites. This description is indeed confirmed by the difference in electron topology around the Mg sites showing an increase of electron density from 0.5% to 1.0% Zn. Finally, unlike Si sites, the electrons distribution around Mg sites is not spherical, but show additional features. The apparent difference can be explained by the fact the both Mg and Si atoms are sp^3 hybridized. The Mg atoms are tetrahedrally arrayed around Si and *vice versa*. However, in the (100) plane showing the Si atoms, there is no projection of the electron density of the Si-Mg bond on this plane. On the other hand, the (110) plane cuts into the Mg-Si sp^3 hybrid orbitals and therefore resulting in the addition feature. Therefore, from the MEM charge density analysis, we can conclude that the Zn dopants should occupy the Mg sites. The increase in electron density suggests both Al and Sb occupied the Si sites. This suggestion is at odd with the *n*-type semiconductor property of the synthesized samples, which indicate Al dopants substitute the Mg and the extra electrons are in the valence band. However, a recent theoretical calculation suggested that the conclusion on the Al substitution site in Mg_2Si is still ambiguous, in particular at low Al concentration. [14] The present results provide a new perspective on the possible locations of the dopants in the crystal: Al and Sb substituted the Si sites but only Zn occupied the Mg sites.

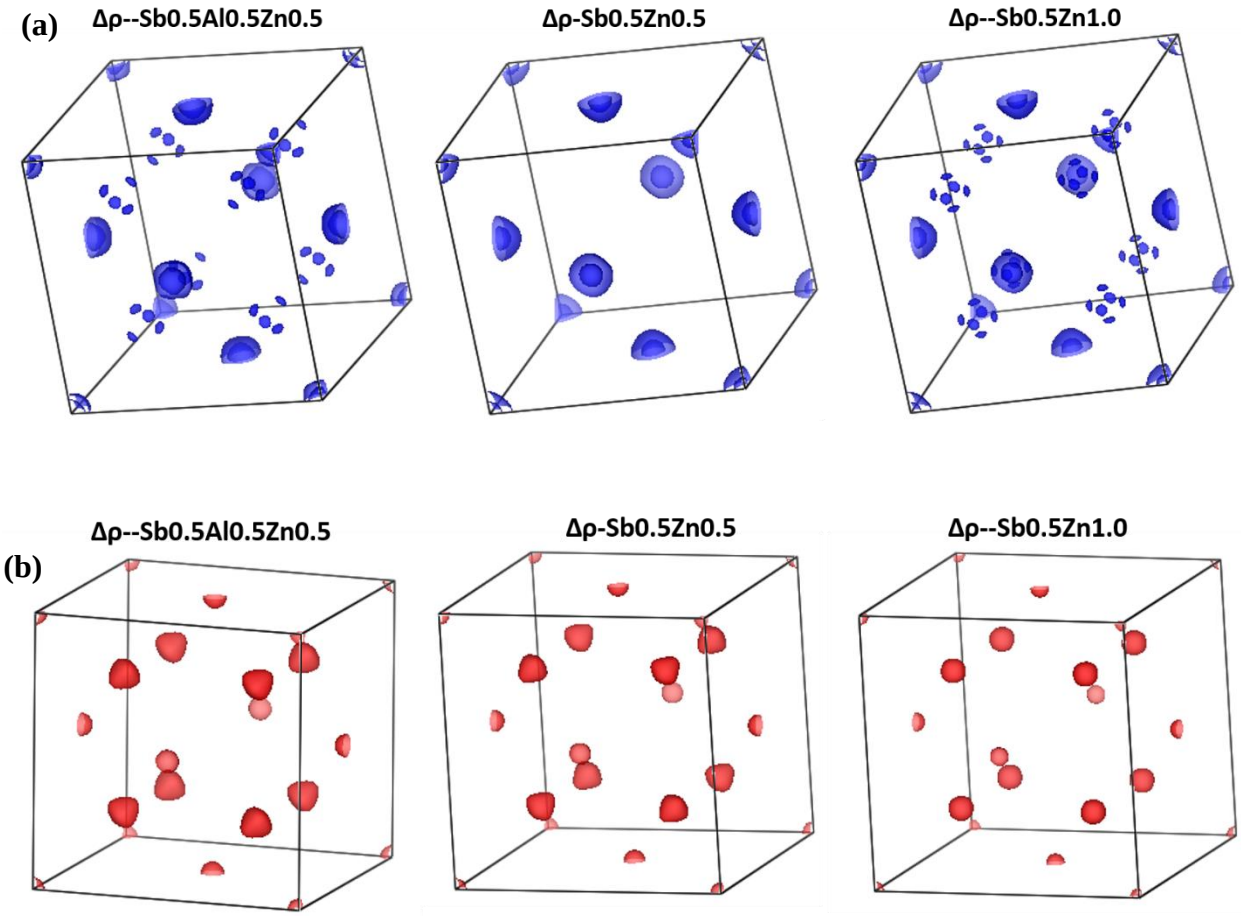

Fig. 8.4 3D electron density difference (Δρ) of doped Mg_2Si samples ($Mg_{1.99}Al_{0.005}Zn_{0.005}Si_{0.995}Sb_{0.005}$ (Sb0.5%Al0.5%Zn0.5%), $Mg_{1.995}Zn_{0.005}Si_{0.995}Sb_{0.005}$ (Sb0.5%Zn0.5%), and $Mg_{1.99}Zn_{0.01}Si_{0.995}Sb_{0.005}$ (Sb0.5%Zn1.0%)) relative to pure Mg_2Si with isosurface contour values of (a) 0.5 e/Å^3 and (b) -0.5 e/Å^3.

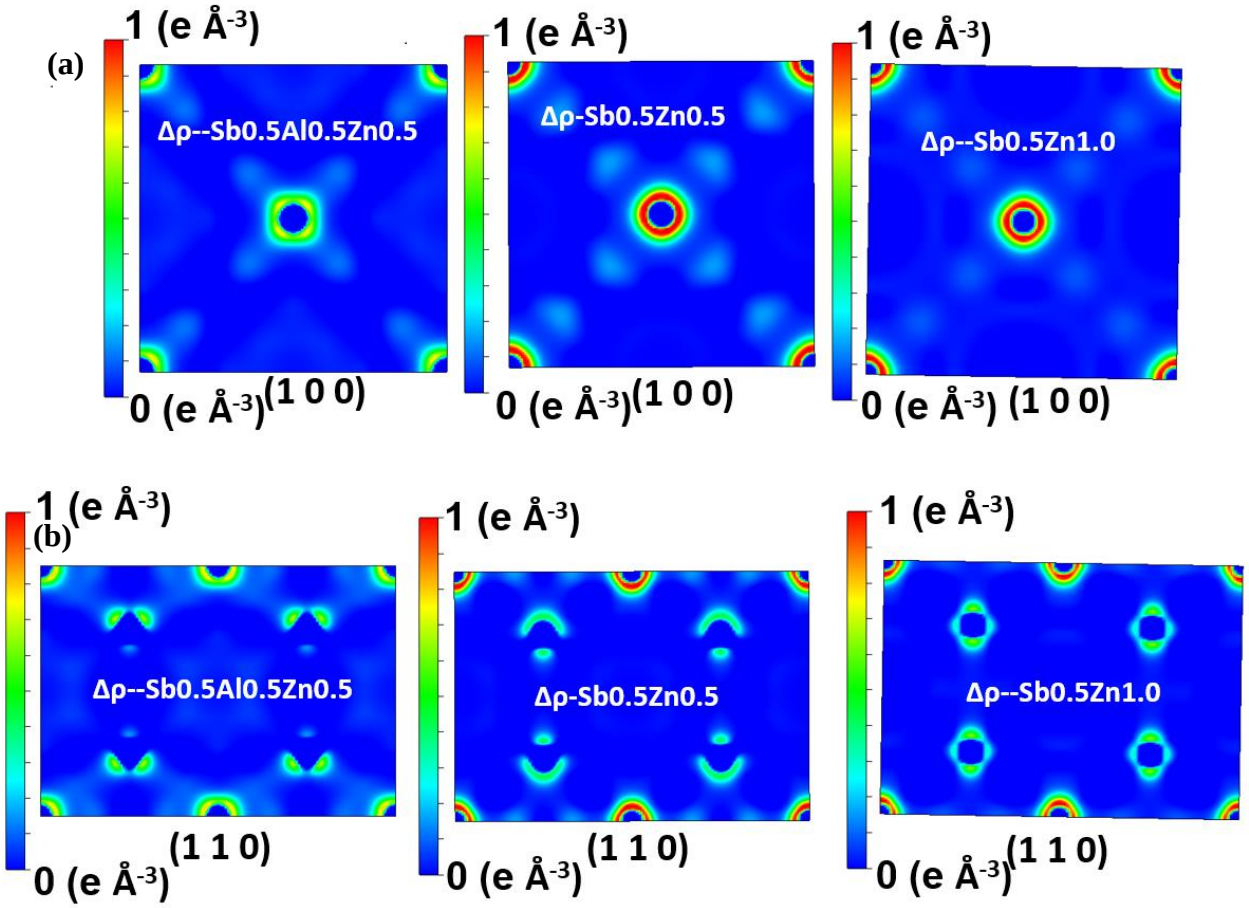

Fig. 8.5 2D electron density difference (Δρ) of doped Mg_2Si samples ($Mg_{1.99}Al_{0.005}Zn_{0.005}Si_{0.995}Sb_{0.005}$ (Sb0.5%Al0.5%Zn0.5%), $Mg_{1.995}Zn_{0.005}Si_{0.995}Sb_{0.005}$ (Sb0.5%Zn0.5%), and $Mg_{1.99}Zn_{0.01}Si_{0.995}Sb_{0.005}$ (Sb0.5%Zn1.0%)) relative to pure Mg_2Si in (a) (100) and (b) (110) planes. The contour levels are shown in the side bars.

Since the exact locations of the dopants are not certain, we performed theoretical DFT calculations on two different multi-doped Mg_2Si models in order to clarify the situation. In the first model, we assumed that the Zn atoms substituted the Mg sites, and Al and Sb resided at the Si sites. (*i.e.* $(Mg_{214}Zn_2)(Si_{104}Al_2Sb_2)$). In the second model, Mg atoms were replaced with Al and Zn and Si atoms were replaced with Sb (*i.e.* $(Mg_{212}Zn_2Al_2)(Si_{106}Sb_2)$). In Fig. 8.6 (a) and (b), we observed no localized mid gap band and the electrons are delocalized over the entire crystal structure. It should be noted that both structural models resulted in an *n*-type semiconductor. (Fig. 8.6 (a)) The first model shows below and at the Fermi level the dominant contributions are from Si, Mg and Al atoms with very small participation of Zn and Sb atoms. In Fig. 8.6 (b), the

density of states is projected into individual atomic orbitals. The *p*-type atomic orbitals of both Mg and Si atoms contribute to the density of states near the Fermi level is clear and supporting the suggestion that both Mg and Si are sp^3 hybridized.

The calculated projected densities of states (pdos) of the second multi-doped $(Mg_{212}Zn_2Al_2)(Si_{106}Sb_2)$ model are shown in Fig. 8.7 (a) and (b). The only difference of this model with the previous one is that Al atoms now substituted the Mg sites instead of the Si. If this was the case, there will be more free electrons available with this substitution. Comparing to the $(Mg_{214}Zn_2)(Si_{104}Al_2Sb_2)$ model, the Fermi level indeed shifts to a higher energy as more free electrons should contribute to the conduction band. The same observation is made that the calculated projected orbital densities of states for all atoms show that, although the dopants replace the Mg and Si sites, the dopant electrons are spread over the entire crystal and not localized in specific regions.

To conclude, the electronic structures of two theoretical structural models, *i.e* with Al substituting either the Mg or Si sites, cannot differentiate the preference sites of the dopants. However, the results also do not contradict the observed electron density difference discussed above, indirectly showing the present assignments of the substitution sites are plausible.

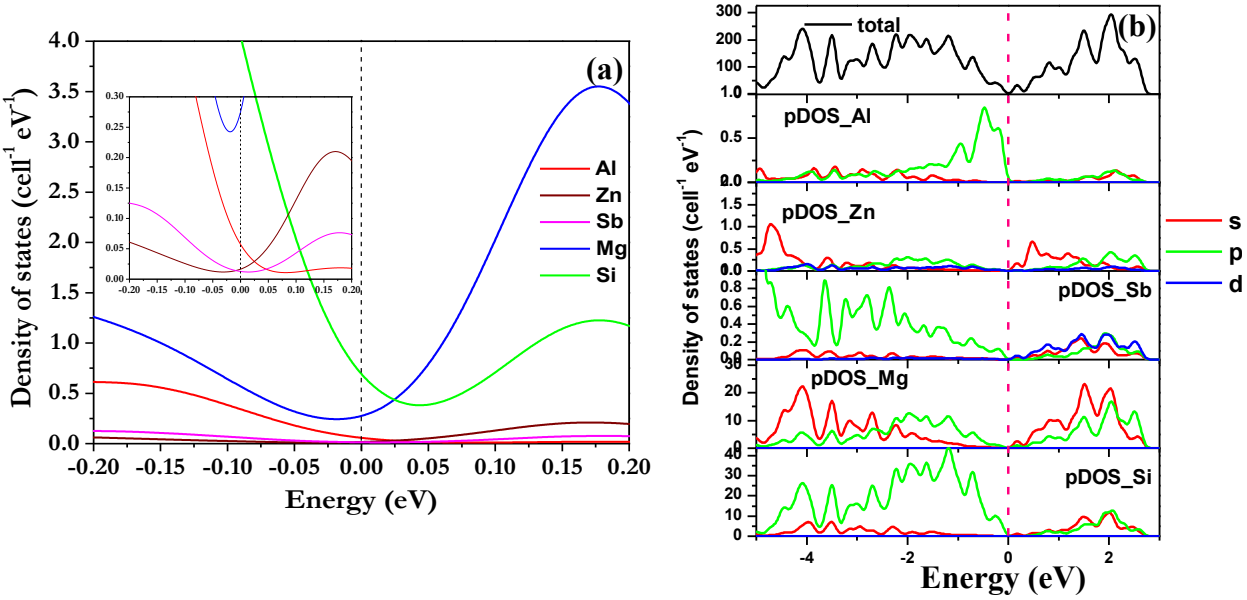

Fig. 8.6 Projected density of states (pdos) of $Mg_{214}Zn_2Si_{104}Al_2Sb_2$ model (a) into atomic composition; (b) into atomic orbitals.

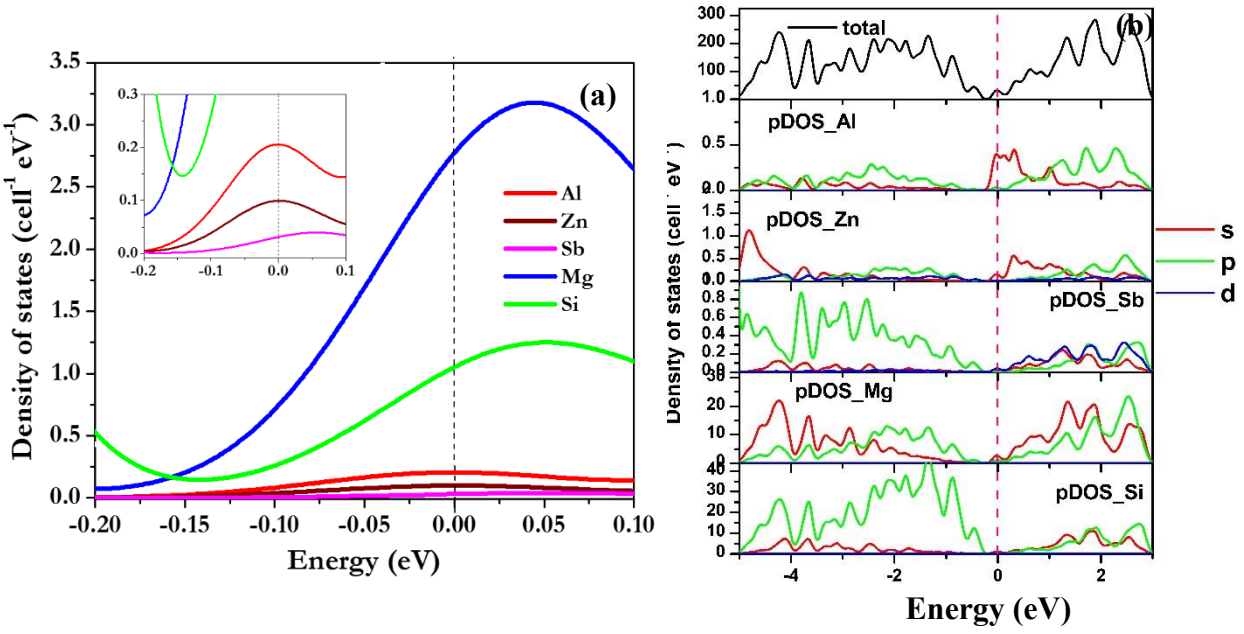

Fig. 8.7 Projected density of states (pdos) of $Mg_{212}Zn_2Al_2Si_{106}Sb_2$ model (a) into atomic composition; (b) into atomic orbitals.

The maximum entropy method (MEM) is a powerful technique to determine the electron density distribution if only a limited set of diffraction data is available. However, it does have limitations. First, the quality of the experimental data is an important factor, this is particularly important for the intensities extracted from powder patterns. Second, the calculated electron density is dependent on the numbers of Bragg reflections considered in the MEM analysis (*i.e.* errors introduced by the limited maximum scattering angle). We investigated this effect on a 1% Al-doped Mg_2Si sample ($Mg_{1.99}Al_{0.01}Si$) using synchrotron radiation measured with a shorter wavelength (λ=0.50917 Å), in which higher angle Bragg reflections were collected. From 5° to 52°, a total of 55 non-overlapping reflections can be indexed and their intensities extracted (Fig. 8.8). To study the errors introduced to the computed charge density due to the restricted number of reflections included in the calculations, MEM charge density maps were constructed with 15, 20, 30, 45 and 55 Bragg reflections. Deviations of the charge density were examined from the difference with the full data set (*i.e.* 55 reflections). As shown in Fig. 8.9, the major discrepancy is concentrated at the atomic sites with a radial spread of *ca.* ~1 Å. This is not surprising as the high angle structure factors are more sensitive to the core electrons. In the worst possible case (*i.e.* using 15 Bragg reflections) the largest difference in the electron density is at most 14 e/Å^3 with a spread of the electron density about 1 Å. Since the positive electron density differences are located away from the atomic sites in the density maps of the doped samples, we believe the results are qualitatively correct. Although the errors of electron density in the core regions become smaller as an increasing number of Bragg reflections are introduced, we conclude that it is difficult to obtain highly accurate measurements of the electron density distribution for the doped samples with small doping concentrations by using the MEM.

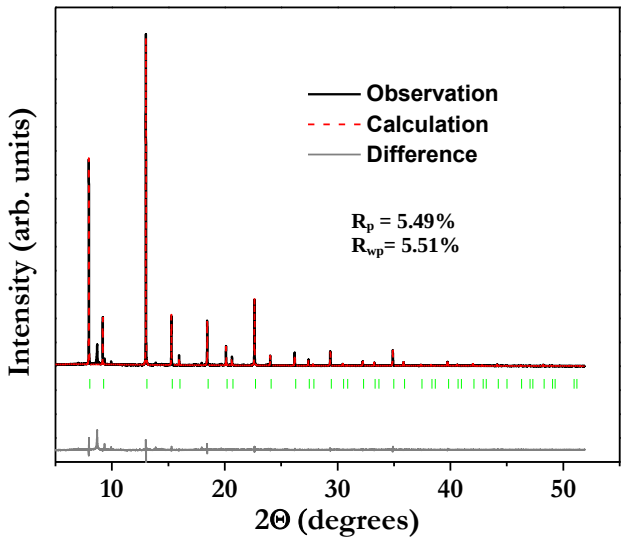

Fig. 8.8 Refined X-ray diffraction pattern for 1% Al-doped Mg_2Si ($Mg_{1.99}Al_{0.01}Si$).

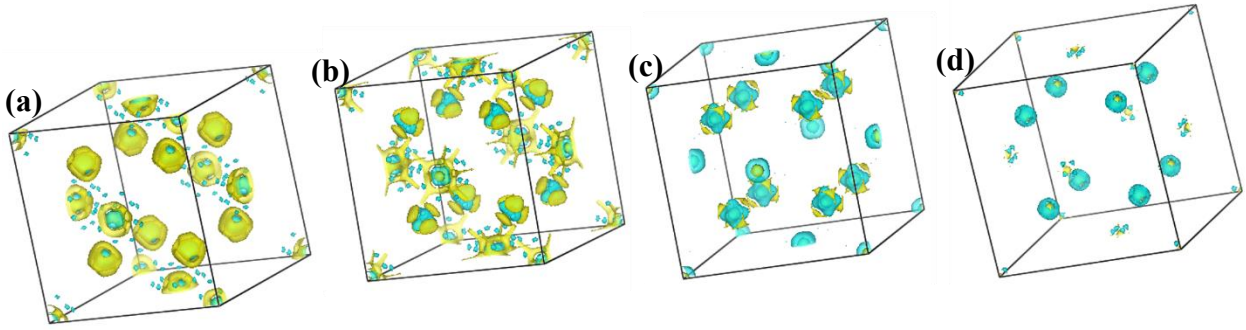

Fig. 8.9 3D electron density difference of 1% Al-doped Mg_2Si ($Mg_{1.99}Al_{0.01}Si$) (a) between 15 and 55 reflection peaks used; (b) between 20 and 55 reflection peaks used; (c) between 30 and 55 reflection peaks used; and (d) between 45 and 55 reflection peaks used. (Yellow: positive charge density; Green: negative charge density)

8.4 Conclusion

High resolution powder diffraction patterns of pure and multi-doped Mg_2Si have been measured by synchrotron X-ray. Analyses show the addition of the dopants expanded the unit cells from pure Mg_2Si. It is gratifying that even using a limited set of low angle Bragg reflections the charge density distribution of pure Mg_2Si can be reconstructed using the Maximum Entropy Method (MEM). Analysis also revealed subtle differences in the valence electron topologies between doped and pure samples. It is found that the electrons contributed by the dopants populated the conduction band and are not localized on the dopant sites. This observation is supported by results of theoretical DFT calculations on two different doping models showing that these electrons occupied the conduction bands and are delocalized. In contrast to the electron density difference profile in (100) plane showing only the Si atoms, in the (110) plane, the electrons distribution around Mg sites is found to have additional features. These features can be explained by electrons on the Mg polarized along the Mg-Si bond direction in the (110) plane but have no projection in the (100) plane. Studies on the charge density difference maps strongly suggest that the Zn dopant should occupy the Mg sites whilst Al and Sb occupied the Si sites. Comparisons of MEM charge densities calculated with systematic increase in the number of high angle Bragg reflections included in the analysis on Al-doped Mg_2Si indicate that the electron density maps for the multi-doped samples are denominated by the valence electrons and should be qualitatively correct.

Acknowledgments

Synchrotron X-ray diffraction experiments were performed at the CMCF and HXMA beamlines of the Canadian Light Source, which were made possible by support from NSERC, NRC, CIHR, and the University of Saskatchewan. The sample preparation was partly supported

by a Grant-in-Aid for Research (A) by the Japanese Ministry of Education, Science, Sports, and Culture. JZ and JST thank AUTO21 for a research grant.

References

[1] T. Sakamoto, T. Iida, S. Kurosaki, K. Yano, H. Taguchi, K. Nishio, and Y. Takanashi, *Journal of Electronic Materials*, 2011, 40, 629-634.

[2] S. Battiston, S. Fiameni, M. Saleemi, S. Boldrini, A. Famengo, F. Agresti, M. Stingaciu, M. S. Toprak, M. Fabrizio, and S. Barison, *Journal of Electronic Materials*, 2013, 42, 1956-1959.

[3] T. Sakamoto, T. Iida, A. Matsumoto, Y. Honda, T. Nemoto, J. Sato, T. Nakajima, H. Taguchi, and Y. Takanashi, *Journal of Electronic Materials*, 2010, 39, 1708-1713.

[4] S. You, K. Park, I. Kim, S. Choi, W. Seo, and S. Kim, *Journal of Electronic Materials*, 2011, 41, 1675-1679.

[5] J. Tani and H. Kido, *Intermetallics*, 2008, 16, 418-423.

[6] N. Wang, H. Chen, H. He, W. Norimatsu, M. Kusunoki, and K. Koumoto, *Scientific Reports*, 2013, 3, 3449.

[7] Q. Chen, Q. Xie, F. Zhao, D. Cui, and X. Li, *IEEE Computer Society*, 2009, 22, 338-341.

[8] G. J. Snyder and E. S. Toberer, *Nature Materials*, 2008, 7, 105-114.

[9] G. H. Kim, L. Shao, K. Zhang, and K. P. Pipe, *Nature Materials*, 2013, 12, 719-723.

[10] M. Christensen, N. Lock, J. Overgaard, and B. B. Iversen, *J. Am. Chem. Soc*., 2006, 128, 15657.

[11] J. Zhao, Z. Liu, J. Reid, K. Takarabe, T. Iida, B. Wang, U. Yoshiya, and J. S. Tse, *Journal of Materials Chemistry A*, 2015, 3, 19774-19782.

[12] N. Farahi, M. VanZant, J. Zhao, J. S. Tse, S. Prabhudev, G. A. Botton, J. R. Salvador, F. Borondics, Z. Liu, and H. Kleinke, *Dalton Transactions*, 2014, 43, 14983-14991.

[13] J. Zhao, Z. Liu, R. A. Gordon, K. Takarabe, J. Reid, and J. S. Tse, *Journal of Applied Physics*, 2015, 118, 145902.

[14] P. Zwolenski, J. Tobola, and S. Kaprzyk, *Journal of Electronic Materials*, 2011, 40, 889-897.

[15] D. M. Collins, *Nature*, 1982, 298, 49-51.

[16] N. K. Hansen and P. Coppens, *Acta. Cryst*., 1978, A34, 909-921.

[17] S. V. Smaalen and J. Netzel, *Phys. Scr*., 2009, 79, 048304.

[18] R. Saravanan and M. P. Rani, *Metal and Alloy Bonding- An Experimental Analysis*, Springer-Verlag London Press, 2012.

[19] K. S. S. Ali, R. Saravanan, A. V. Pashchenko, and V. P. Pashchenko, *Journal of Alloys and Compounds*, 2010, 501, 307-312.

[20] S. Francis, R. Saravanan, and L. J. Berchmans, *Journal of Electronic Materials*, 2013, 42, 701.

[21] Y. Takahashi, Y. Gotoh, and J. Akimoto, *Journal of Solid State Chemistry*, 2003, 172, 22-26.

[22] R. Saravanan and M. C. Robert, *Journal of Alloys and Compounds*, 2009, 479, 26-31.

[23] R. Saravanan and M. C. Robert, *Journal of Physics and Chemistry of Solids*, 2009, 70, 159-163.

[24] R. Saravanan, *Phys. Scr*., 2009, 79, 048303.

[25] F. Gargnoni, E. Nishibori, P. Rabiller, L. Bertini, G. J. Snyder, M. Christensen, C. Gatti, and B. B. Iversen, *Chem. Eur. J*., 2004, 10, 3861-3870.

[26] A. Ohno, S. Sasaki, E. Nishibori, S. Aoyagi, M. Sakata, and B. B. Iverson, *Physical Review B*, 2007, 76, 064119.

[27] S. Kastbjerg, N. Bindzus, M. SØndergaard, S. Johnsen, N. Lock, M. Christensen, M. Takata, M. A. Spackman, and B. B. Iversen, *Advanced Functional Materials*, 2013, 23, 5477-5483.

[28] K. Momma, T. Ikeda, A. A. Belik and F. Izumi, *Powder Diffraction*, 2013, 28, 184-193.

[29] http://cmcf.lightsource.ca/beamlines/08b1-1/

[30] T. D. Jiang, N. Chen, and W. Sheng, Wiggler-based Hard X-ray spectroscopy beamline at CLS, AIP Proc. (Accelerators and Beams), 2009, 879, 800-803.

[31] V. Petricek, M. Dusek, and L. Palatinus, *Z. Kristallogr*., 2014, 229, 345-352.

[32] A. Le Bail, H. Duroy, and J. L. Fourquet, *Materials Research Bulletin*, 1988, 23, 447-452.

[33] F. Izumi and K. Momma, *Proc. XX Conf. Appl. Crystallogr., Solid State Phenom*., 2007, 130, 15-20.

[34] K. Momma and F. Izumi, *Commission on Crystallogr. Comput., IUCr Newslett*., 2006, 7, 106-119.

[35] K. Momma and F. Izumi, *J. Appl. Crystallogr*., 2008, 41, 653-658.

[36] K. Momma and F. Izumi, *J. Appl. Crystallogr*., 2011, 44, 1272-1276.

[37] G. Kresse and J. Hafner, *Physical Review B*, 1993, 47, 558.

[38] G. Kresse and J. Hafner, *Physical Review B*, 1994, 49, 14251.

[39] G. Kresse and J. Furthmller, *Computational Materials Science*, 1996, 6, 15.

[40] G. Kresse and J. Furthmller, *Physical Review B*, 1996, 54, 11169.

[41] P. E. Blöchl, *Physical Review B*, 1994, 50, 17953.

[42] G. Kresse and D. Joubert, *Physical Review B*, 1999, 59, 1758.

CHAPTER 9

SUMMARY AND PERSPECTIVES

The research reported in this thesis has fulfilled its initial objectives: to characterize the electronic, electrical, and structural properties of doped Mg_2Si thermoelectric materials using state-of-the-art synchrotron radiation techniques (infrared reflectivity/absorption spectra and powder X-ray diffraction) and theoretical density functional (DFT) calculations. However, there are still opportunities for improvements and future investigation. In this chapter, the major results and contributions are summarized, and opportunities for future work are presented.

9.1 Summary

We studied Mg_2Si doped with a variety of elements and obtained the samples' transport properties using infrared reflectivity measurements. DFT calculations were performed to explain the electronic structures and electrical properties. We demonstrated that the Seebeck coefficients of doped Mg_2Si samples can be reproduced by the rigid band approximation using the Boltzmann transport theory. We found the thermoelectric performances of samples single-doped with Sb and Bi could indeed be enhanced with electron donating dopants. We further replaced Si in Bi-doped Mg_2Si with heavier Ge atoms in order to decrease the lattice thermal conductivity. From the analysis of IR reflectivity data, a significant decrease in the electrical conductivity was found with increasing Ge content. However, Ge helped to reduce the lattice thermal conductivity. As a result, the overall effect was the enhancement of the thermoelectric figure of merit.

Doping was found to affect the crystal structure of Mg_2Si. Angle-dispersive synchrotron radiation X-ray powder diffraction provided structural information on Sb, Al, and Zn multi-doped Mg_2Si powder samples, synthesized by spark plasma sintering. Small concentrations of the dopants (0.5-1.0%) did not alter the overall cubic crystal symmetry of the host lattice but

expanded the unit cell sizes noticeably by 1.1%-1.2%. Electrical transport properties were characterized by mid-IR reflectivity and compared to bulk quasi-four probe measurements. The infrared reflectivities show the doped samples were semiconductors at room temperature. The trend in the *dc* conductivities derived from the analysis of the infrared reflectivity spectra employing the Drude-Lorentz model is in qualitative agreement with the conventional bulk measurements. However, the absolute values obtained from IR reflectivities were found to be consistently lower. We attribute the discrepancy to non-uniform distributions of the doped atoms in the sample. The carrier electron concentrations (N) can be determined from Hall coefficients obtained from the bulk measurements, and the plasma frequencies (ω_p) can be obtained from the infrared reflectivity spectra. From the values of N and ω_p, the electron effective masses were found to be between $0.255m_e$ and $0.361m_e$. The lighter effective masses reflect a higher electrical conductivity in the doped Mg_2Si. A best thermoelectric performance figure of merit (ZT) of 0.964 was achieved for the $Mg_{1.995}Zn_{0.005}Si_{0.995}Sb_{0.005}$ at 880 K, very close to the ZT of PbTe that is the present choice in many commercial products.

We investigated the mechanism for the observed enhancement of thermal power of Al-doped Mg_2Si under pressure. The structures of a nominally 1 at. % Al-doped Mg_2Si sample ($Mg_{1.99}Al_{0.01}Si$) were measured by angle dispersive synchrotron radiation X-ray diffraction and the electrical conductivity by infrared reflectivity. All measurements were performed at room temperature up to 16.6 GPa. Contrary to previous reports, no structural transformation was observed in pure Mg_2Si up to 15 GPa when helium was used here as the pressure transmission medium. This is substantiated by the electronic band structures of pure Mg_2Si with density functional theory including the correction for the electron correlation effect with the *GW* approximation showing the band gap of Mg_2Si does not close at 11 GPa. The theoretical

electronic density of states is consistent with electrical resistivity measurements showing that Mg_2Si did not transform to a metal at least up to 22 GPa. The present diffraction and theoretical results contradict reports on the structural phase transition to metallic anti-cotunnite and Ni_2In structures at 7 and 11 GPa, respectively. In contrast, a structural phase transition from the cubic anti-fluorite to the anti-cotunnite structure was found in Al-doped Mg_2Si at 11.9 GPa. The *dc* conductivities at high pressure calculated from the analysis of infrared reflectivity spectra employing the Drude-Lorentz model were found to increase after the phase transition. The results also show the Al-doped Mg_2Si already exhibited semi-metallic-like behaviour under ambient conditions. The results from synchrotron IR reflectivity agree with bulk four-probe measurements, in which the electrical conductivity was found to increase with pressure. From the theoretical density of electronic states, a maximum thermoelectric power factor was predicted at 2-3 GPa, which is in good agreement with the experimental observation.

We investigated the possibility of mixing multi-wall carbon nanotubes (MWCNTs), a good conductor, to enhance the electrical conductivity and, therefore, the thermoelectric properties of $Mg_2Si_{0.877}Ge_{0.1}Bi_{0.023}$. Indeed, we found the addition of MWCNTs increased the electrical conductivity. At 323 K, the measured electrical conductivity was increased from 450 $\Omega^{-1}cm^{-1}$ (undoped $Mg_2Si_{0.877}Ge_{0.1}Bi_{0.023}$) to 500 $\Omega^{-1}cm^{-1}$ (doped $Mg_2Si_{0.877}Ge_{0.1}Bi_{0.023}$-0.5 wt% MWCNTs), an increase of about 10%. However, the positive effect diminished at higher temperature where the conductivity dropped back to 470 $\Omega^{-1}cm^{-1}$ at 773 K. To clarify whether the enhancement was due to chemical interaction between the MWCNTs and $Mg_2Si_{0.877}Ge_{0.1}Bi_{0.023}$, we performed Raman measurements on the samples. The persistence of disorder (D) and tangential (G) vibrational mode characteristics of a carbon nanotube suggested there was no decomposition or substantial chemical reaction of the MWCNTs doped in

$Mg_2Si_{0.877}Ge_{0.1}Bi_{0.023}$. The final result is that the best *ZT* of 0.5 obtained in $Mg_2Si_{0.877}Ge_{0.1}Bi_{0.023}$-0.5 wt% MWCNTs at 700 K is not very attractive for practical applications.

The charge-densities of pure Mg_2Si and multi-doped Mg_2Si samples were constructed by the Maximum Entropy Method (MEM) using synchrotron X-ray powder diffraction patterns. The atomic positions were correctly located. We found the extra electrons contributed by the dopants populated the conduction band but were not localized on the substituted dopant sites. This observation is supported by results of theoretical DFT calculations showing there were no mid-gap localized electron bands and the electrons were delocalized over the unit cell. In the (110) plane of both the Mg and Si sites, the distribution of electrons around Mg sites was not spherical, but showed additional features. The apparent difference can be explained by the fact that both Mg and Si atoms were sp^3 hybridized. The Mg atoms were tetrahedrally arranged around Si and *vice versa*. However, in the (100) plane showing the Si atoms, there was no projection of the electron density of the Si-Mg bond on this plane. On the other hand, the (110) plane cut into the Mg-Si sp^3 hybrid orbitals resulting in the additional feature. Therefore, from the MEM charge density analysis, we can conclude that the Zn dopants should have occupied the Mg sites. The increase in electron density suggests both Al and Sb occupied the Si sites. However, due to the limited Bragg diffraction peaks measured, we conclude the effect of the dopants to the core charge density cannot be reliably obtained from this data and only qualitative features of the valence electron topology can be revealed. This conclusion is further confirmed from the analysis of the diffraction pattern of an Al-doped Mg_2Si ($Mg_{1.99}Al_{0.01}Si$) sample: The errors of electron density in the core regions became smaller as the number of high angle Bragg reflections included in the analysis was increased.

9.2 Perspectives

Several studies reported in this thesis can be further expanded and improved. As discussed in Chapter 8, we found the error of the derived electron density in the atomic core regions became smaller as the number of Bragg reflections included in the MEM analysis increased. Despite many successes, MEM has its limitations in the quantitative determination of the electron density distribution using just the low angle diffraction data. Another important factor is the quality of the experimental data. This is particularly important for powder samples. One way to further improve the accuracy of identifying electron density distribution using MEM would be to re-visit these problems through the examination of single-crystal data. Using higher angle X-ray single-crystal diffraction data, we might obtain more accurate results on electron density distribution for the doped samples even with low doping concentrations.

We show the trends of the electrical conductivity obtained from IR reflectivity are similar to the four-probe conductivity measurements of the bulk samples, however, the agreements on the absolute magnitudes are not satisfactory. Since an infrared reflectivity measurement only probes a very small spot of *ca*. 20 × 20 μm^2 of the highly non-uniform doped sample, we speculate that this is the main reason for the discrepancies. In further work, careful characterization of the samples would be critical to resolve the discrepancy. It is possible to measure IR reflectivities on different spots on the sample. Transmission electron microscopy (TEM) would also complement the characterization of the locations of the dopants, particularly around the grain boundaries.

In this research, the highest $ZT_{max} \approx 1$ was achieved in $Mg_{1.995}Zn_{0.005}Si_{0.995}Sb_{0.005}$ at 880K. This value is still far from that needed for commercial applications. The thermoelectric samples we studied were all in bulk form. However, low dimensional and nanocomposite thermoelectric

materials are known to dramatically enhance thermoelectric performance. [1-2] For example, *ZT* was found to exceed 2 by using a 2D electron gas thin layer of $SrTi_{0.8}Nb_{0.2}O_3$. [1] Previous studies have also found 2D quantum-well, 1D quantum-wire of Bi_2Te_3 or PbTe-based thermoelectric materials and bulk samples containing nanoparticles have the promising potential to further increase thermoelectric performance. [3-7] For example, a nanostructural layer of Bi_2Te_3 sample has been fabricated by electrochemical deposition from a solution. [8] Investigations of thermoelectric performance of thin layer or nanostructural Mg_2Si samples would be interesting to undertake in the future. We expect that the effect of low dimensionality and nanocomposites can significantly improve thermoelectric performance of doped Mg_2Si-based thermoelectric materials.

References

[1] H. Ohta, S. Kim, Y. Mune, T. Mizoguchi, K. Nomura, S. Ohta, T. Nomura, Y. Nakanishi, Y. Ikuhara, M. Hirano, H. Hosono, and K. Koumoto, *Nature Materials*, 2007, 6, 129-134.

[2] L. D. Hicks and M. S. Dresselhaus, *Physical Review B*, 1993, 47, 12727.

[3] M. S. Dresselhaus, G. Chen, M. Y. Tang, R. Yang, H. Lee, D. Wang, Z. Ren, J. P. Fleurial, and P. Gogna, *Advanced Materials*, 2007, 19, 1043-1053.

[4] R. R. Bourassa, D. Lazarus, and D. A. Blackburn, *Physical Review*, 1968, 165, 853.

[5] M. J. Yang, Q. Shen, and L. M. Zhang, *China Phys. B*, 2011, 20, 106202.

[6] M. J. Yang, W. J. Luo, and Q. Shen, *Rare Met. Mater. Eng.*, 2009, S2, 1055-1059.

[7] S. Fiameni, S. Battiston, S. Boldrini, A. Famengo, F. Agresti, S. Barison, and M. Fabrizio, *Journal of Solid State Chemistry*, 2012, 193, 142-146.

[8] S. Li, M. S. Toprak, H. M. A. Soliman, J. Zhou, M. Muhammed, D. Platzek, and E. Müller, *Chem. Mater.*, 2006, 18, 3627-3633.

APPENDIX A

Supplementary data for Chapter 3

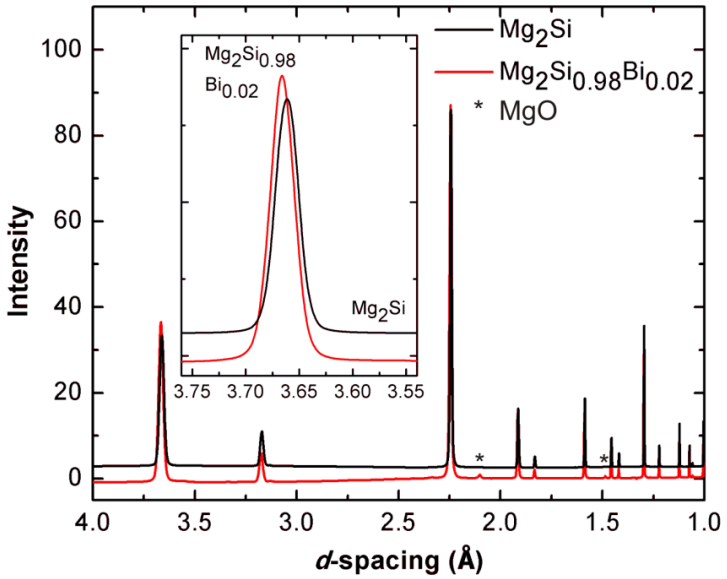

Fig. A.1 Experimental powder diagrams of Mg_2Si and $Mg_2Si_{0.98}Bi_{0.02}$.

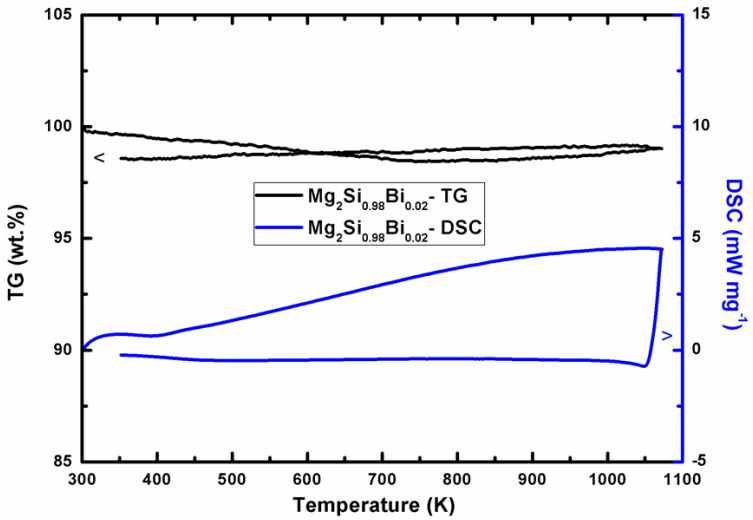

Fig. A.2 DSC and TG of $Mg_2Si_{0.98}Bi_{0.02}$.

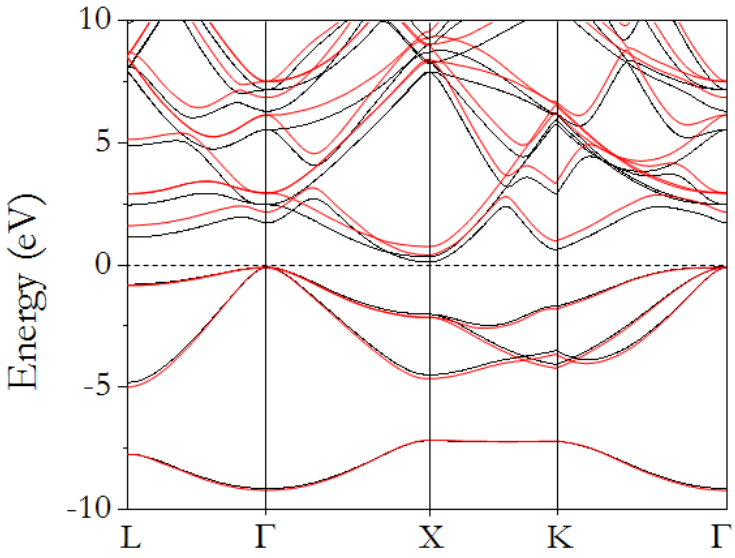

Fig. A.3 Band structure of Mg_2Si. Black: GGA, red: *GW* method.

APPENDIX B

Supplementary data for Chapter 4

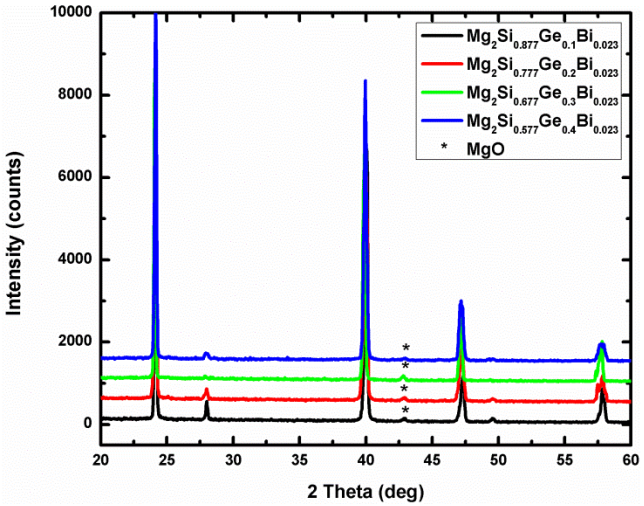

Fig. B.1 Experimental powder diagrams of $Mg_2Si_{0.977-x}Ge_xBi_{0.023}$ ($0.1 \leq x \leq 0.4$).

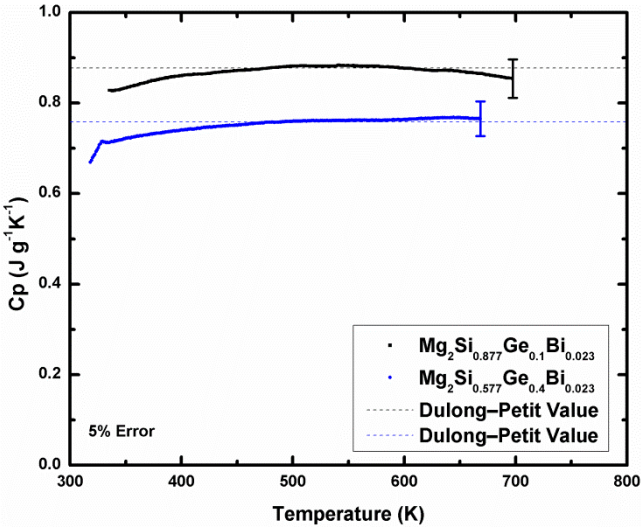

Fig. B.2 Specific heat of $Mg_2Si_{0.977-x}Ge_xBi_{0.023}$ (x = 0.1, 0.4).

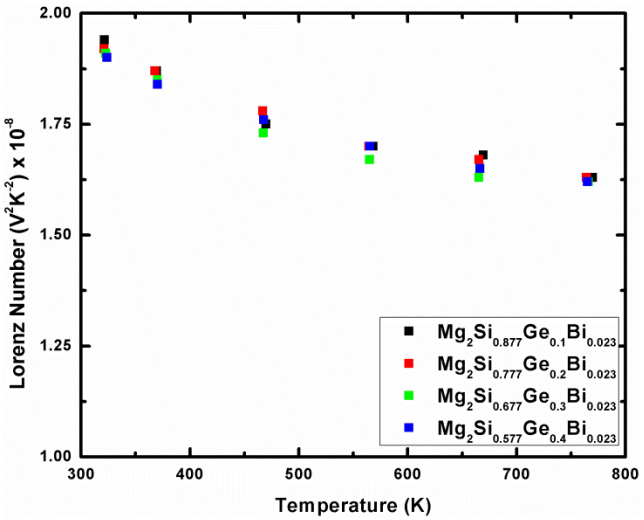

Fig. B.3 Calculated Lorenz number of $Mg_2Si_{0.977-x}Ge_xBi_{0.023}$ ($0.1 \leq x \leq 0.4$).

APPENDIX C

Supplementary data for Chapter 7

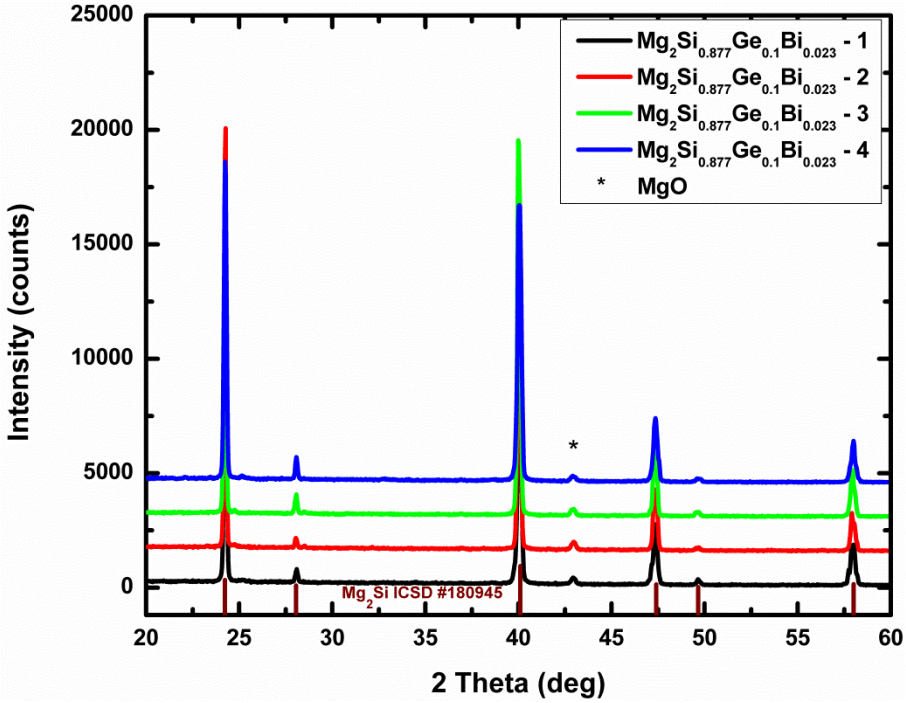

Fig. C.1 Powder XRD patterns of $Mg_2Si_{0.877}Ge_{0.1}Bi_{0.023}$ samples.

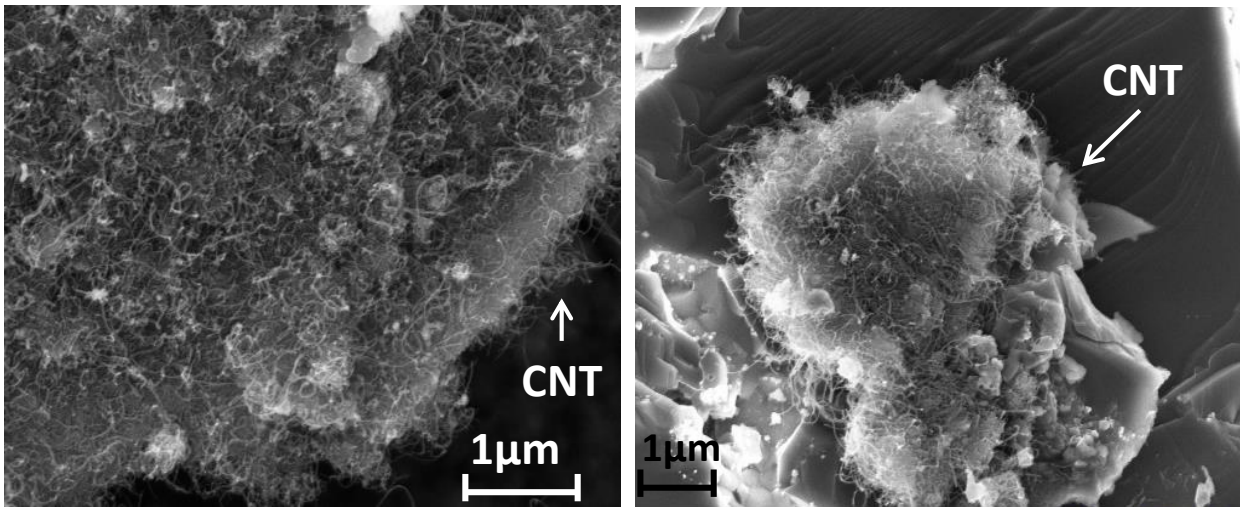

Fig. C.2 SEM images of the $Mg_2Si_{0.877}Ge_{0.1}Bi_{0.023}$/1 wt.-% MWCNT sample.

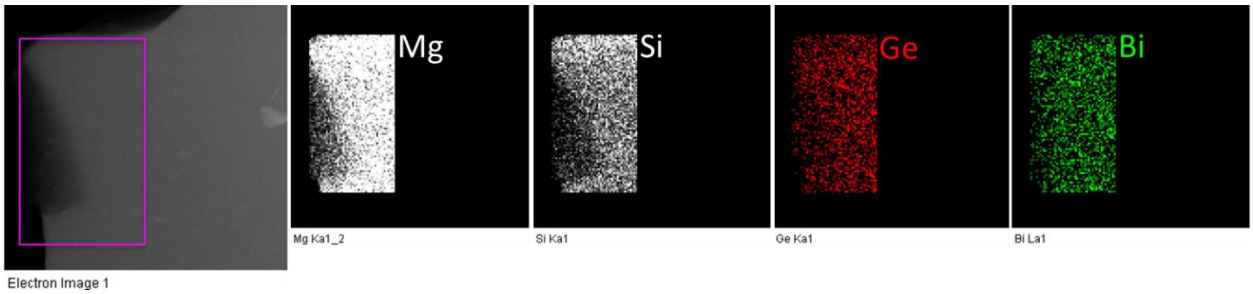

Fig. C.3 Low-magnification structural and compositional analyses of the edge of a grain. EDXelemental mapping over a selected area showing the distribution of Mg, Si, Ge and Bi.

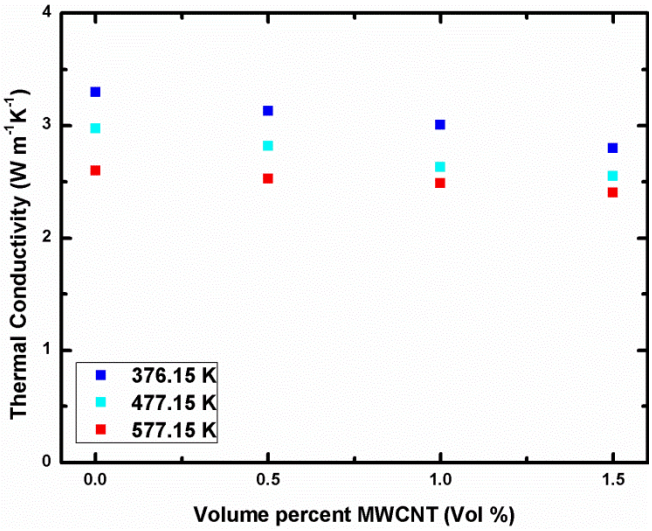

Fig. C.4 Medium temperature thermal conductivity of all samples with respect to MWCNT content.

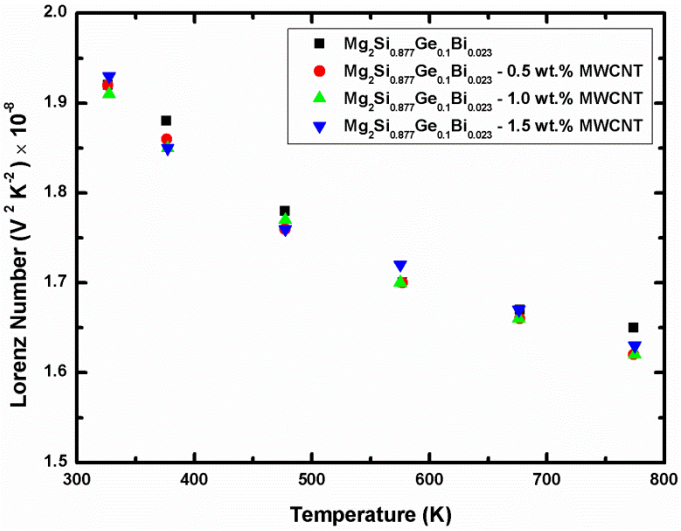

Fig. C.5 Lorenz number of all samples with regard to temperature.

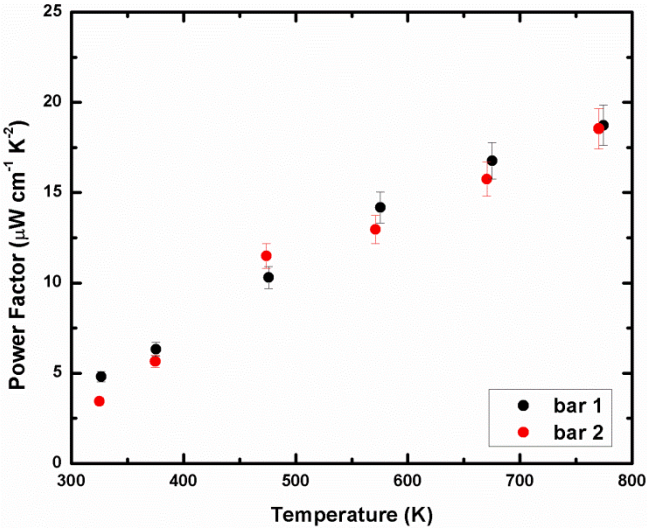

Fig. C.6 Power factor of two bars obtained from 0.5% MWCNT/$Mg_2Si_{0.877}Ge_{0.1}Bi_{0.023}$ nanocomposite (6% error is considered).

Table C.1 Densities and specific heat of the $Mg_2Si_{0.877}Ge_{0.1}Bi_{0.023}$/MWCNT samples.

Sample	Density (gcm^{-3})	Relative density	C_p ($Jg^{-1}K^{-1}$)
$Mg_2Si_{0.877}Ge_{0.1}Bi_{0.023}$	2.10	96%	0.877
$Mg_2Si_{0.877}Ge_{0.1}Bi_{0.023}$ - 0.5 wt.-% MWCNT	2.10	96%	0.882
$Mg_2Si_{0.877}Ge_{0.1}Bi_{0.023}$ - 1.0 wt.-% MWCNT	2.04	93%	0.888
$Mg_2Si_{0.877}Ge_{0.1}Bi_{0.023}$ - 1.5 wt.-% MWCNT	2.06	94%	0.894

Theoretical densities of the composite (d_C) were calculated using the mixture rule:

$$\frac{1}{d_C} = \frac{w_{MWCNT}}{d_{MWCNT}} + \frac{w_{Matrix}}{d_{Matrix}}$$

where d_{MWCNT}, d_{Matrix}, W_{MWCNT} and W_{Matrix} are the densities and mass fractions of the nanotubes and $Mg_2Si_{0.877}Ge_{0.1}Bi_{0.023}$, respectively.

Sb- and Bi-doped Mg_2Si: location of the dopants, micro- and nanostructures, electronic structures and thermoelectric properties

N. Farahi, M. VanZant, J. Zhao, J. S. Tse, S. Prabhudev, G. A. Botton, J. R. Salvador, F. Borondics, Z. Liu and H. Kleinke, Dalton Trans., 2014, 43, 14983
DOI: 10.1039/C4DT01177E

- For reproduction of material from NJC:
  [Original citation] - Reproduced by permission of The Royal Society of Chemistry (RSC) on behalf of the Centre National de la Recherche Scientifique (CNRS) and the RSC
- For reproduction of material from PCCP:
  [Original citation] - Reproduced by permission of the PCCP Owner Societies
- For reproduction of material from PPS:
  [Original citation] - Reproduced by permission of The Royal Society of Chemistry (RSC) on behalf of the European Society for Photobiology, the European Photochemistry Association, and RSC
- For reproduction of material from all other RSC journals:
  [Original citation] - Reproduced by permission of The Royal Society of Chemistry

If you are the author of this article you still need to obtain permission to reproduce the whole article in a third party publication with the exception of reproduction of the whole article in a thesis or dissertation.

Information about reproducing material from RSC articles with different licences is available on our Permission Requests page.

ELSEVIER LICENSE
TERMS AND CONDITIONS

Jan 05, 2016

This is a License Agreement between Jianbao Zhao ("You") and Elsevier ("Elsevier") provided by Copyright Clearance Center ("CCC"). The license consists of your order details, the terms and conditions provided by Elsevier, and the payment terms and conditions.

All payments must be made in full to CCC. For payment instructions, please see information listed at the bottom of this form.

Supplier	Elsevier Limited The Boulevard,Langford Lane Kidlington,Oxford,OX5 1GB,UK
Registered Company Number	1982084
Customer name	Jianbao Zhao
Customer address	#40-330 Haight Crescent Saskatoon, SK S7H4V9
License number	3782710615337
License date	Jan 05, 2016
Licensed content publisher	Elsevier
Licensed content publication	Journal of Alloys and Compounds
Licensed content title	Local structure and thermoelectric properties of Mg2Si0.977−xGexBi0.023 (0.1⩽x⩽0.4)
Licensed content author	Nader Farahi,Sagar Prabhudev,Gianluigi A. Botton,Jianbao Zhao,John S. Tse,Zhenxian Liu,James R. Salvador,Holger Kleinke
Licensed content date	25 September 2015
Licensed content volume number	644
Licensed content issue number	n/a
Number of pages	7
Start Page	249
End Page	255
Type of Use	reuse in a thesis/dissertation
Portion	full article
Format	electronic
Are you the author of this Elsevier article?	Yes
Will you be translating?	No
Title of your thesis/dissertation	STUDY OF Mg2Si-BASED THERMOELECTRIC MATERIALS

Expected completion date	Apr 2016
Estimated size (number of pages)	202
Elsevier VAT number	GB 494 6272 12
Permissions price	0.00 CAD
VAT/Local Sales Tax	0.00 CAD / 0.00 GBP
Total	0.00 CAD

Terms and Conditions

INTRODUCTION

1. The publisher for this copyrighted material is Elsevier. By clicking "accept" in connection with completing this licensing transaction, you agree that the following terms and conditions apply to this transaction (along with the Billing and Payment terms and conditions established by Copyright Clearance Center, Inc. ("CCC"), at the time that you opened your Rightslink account and that are available at any time at http://myaccount.copyright.com).

GENERAL TERMS

2. Elsevier hereby grants you permission to reproduce the aforementioned material subject to the terms and conditions indicated.
3. Acknowledgement: If any part of the material to be used (for example, figures) has appeared in our publication with credit or acknowledgement to another source, permission must also be sought from that source. If such permission is not obtained then that material may not be included in your publication/copies. Suitable acknowledgement to the source must be made, either as a footnote or in a reference list at the end of your publication, as follows:
"Reprinted from Publication title, Vol /edition number, Author(s), Title of article / title of chapter, Pages No., Copyright (Year), with permission from Elsevier [OR APPLICABLE SOCIETY COPYRIGHT OWNER]." Also Lancet special credit - "Reprinted from The Lancet, Vol. number, Author(s), Title of article, Pages No., Copyright (Year), with permission from Elsevier."
4. Reproduction of this material is confined to the purpose and/or media for which permission is hereby given.
5. Altering/Modifying Material: Not Permitted. However figures and illustrations may be altered/adapted minimally to serve your work. Any other abbreviations, additions, deletions and/or any other alterations shall be made only with prior written authorization of Elsevier Ltd. (Please contact Elsevier at permissions@elsevier.com)
6. If the permission fee for the requested use of our material is waived in this instance, please be advised that your future requests for Elsevier materials may attract a fee.
7. Reservation of Rights: Publisher reserves all rights not specifically granted in the combination of (i) the license details provided by you and accepted in the course of this licensing transaction, (ii) these terms and conditions and (iii) CCC's Billing and Payment terms and conditions.
8. License Contingent Upon Payment: While you may exercise the rights licensed immediately upon issuance of the license at the end of the

licensing process for the transaction, provided that you have disclosed complete and accurate details of your proposed use, no license is finally effective unless and until full payment is received from you (either by publisher or by CCC) as provided in CCC's Billing and Payment terms and conditions. If full payment is not received on a timely basis, then any license preliminarily granted shall be deemed automatically revoked and shall be void as if never granted. Further, in the event that you breach any of these terms and conditions or any of CCC's Billing and Payment terms and conditions, the license is automatically revoked and shall be void as if never granted. Use of materials as described in a revoked license, as well as any use of the materials beyond the scope of an unrevoked license, may constitute copyright infringement and publisher reserves the right to take any and all action to protect its copyright in the materials.

9. Warranties: Publisher makes no representations or warranties with respect to the licensed material.

10. Indemnity: You hereby indemnify and agree to hold harmless publisher and CCC, and their respective officers, directors, employees and agents, from and against any and all claims arising out of your use of the licensed material other than as specifically authorized pursuant to this license.

11. No Transfer of License: This license is personal to you and may not be sublicensed, assigned, or transferred by you to any other person without publisher's written permission.

12. No Amendment Except in Writing: This license may not be amended except in a writing signed by both parties (or, in the case of publisher, by CCC on publisher's behalf).

13. Objection to Contrary Terms: Publisher hereby objects to any terms contained in any purchase order, acknowledgment, check endorsement or other writing prepared by you, which terms are inconsistent with these terms and conditions or CCC's Billing and Payment terms and conditions. These terms and conditions, together with CCC's Billing and Payment terms and conditions (which are incorporated herein), comprise the entire agreement between you and publisher (and CCC) concerning this licensing transaction. In the event of any conflict between your obligations established by these terms and conditions and those established by CCC's Billing and Payment terms and conditions, these terms and conditions shall control.

14. Revocation: Elsevier or Copyright Clearance Center may deny the permissions described in this License at their sole discretion, for any reason or no reason, with a full refund payable to you. Notice of such denial will be made using the contact information provided by you. Failure to receive such notice will not alter or invalidate the denial. In no event will Elsevier or Copyright Clearance Center be responsible or liable for any costs, expenses or damage incurred by you as a result of a denial of your permission request, other than a refund of the amount(s) paid by you to Elsevier and/or Copyright Clearance Center for denied permissions.

LIMITED LICENSE

The following terms and conditions apply only to specific license types:

15. Translation: This permission is granted for non-exclusive world English rights only unless your license was granted for translation rights. If you licensed translation rights you may only translate this content into the languages you requested. A professional translator must perform all translations and reproduce the content word for word preserving the integrity of the article.
16. Posting licensed content on any Website: The following terms and conditions apply as follows: Licensing material from an Elsevier journal: All content posted to the web site must maintain the copyright information line on the bottom of each image; A hyper-text must be included to the Homepage of the journal from which you are licensing at http://www.sciencedirect.com/science/journal/xxxxx or the Elsevier homepage for books at http://www.elsevier.com; Central Storage: This license does not include permission for a scanned version of the material to be stored in a central repository such as that provided by Heron/XanEdu.
Licensing material from an Elsevier book: A hyper-text link must be included to the Elsevier homepage at http://www.elsevier.com . All content posted to the web site must maintain the copyright information line on the bottom of each image.

Posting licensed content on Electronic reserve: In addition to the above the following clauses are applicable: The web site must be password-protected and made available only to bona fide students registered on a relevant course. This permission is granted for 1 year only. You may obtain a new license for future website posting.
17. For journal authors: the following clauses are applicable in addition to the above:
Preprints:
A preprint is an author's own write-up of research results and analysis, it has not been peer-reviewed, nor has it had any other value added to it by a publisher (such as formatting, copyright, technical enhancement etc.).
Authors can share their preprints anywhere at any time. Preprints should not be added to or enhanced in any way in order to appear more like, or to substitute for, the final versions of articles however authors can update their preprints on arXiv or RePEc with their Accepted Author Manuscript (see below).
If accepted for publication, we encourage authors to link from the preprint to their formal publication via its DOI. Millions of researchers have access to the formal publications on ScienceDirect, and so links will help users to find, access, cite and use the best available version.
Please note that Cell Press, The Lancet and some society-owned have different preprint policies. Information on these policies is available on the journal homepage.
Accepted Author Manuscripts: An accepted author manuscript is the manuscript of an article that has been accepted for publication and which typically includes author-incorporated changes suggested during submission, peer review and editor-author communications.
Authors can share their accepted author manuscript:

- immediately
  - via their non-commercial person homepage or blog
  - by updating a preprint in arXiv or RePEc with the accepted manuscript
  - via their research institute or institutional repository for internal institutional uses or as part of an invitation-only research collaboration work-group
  - directly by providing copies to their students or to research collaborators for their personal use
  - for private scholarly sharing as part of an invitation-only work group on commercial sites with which Elsevier has an agreement
- after the embargo period
  - via non-commercial hosting platforms such as their institutional repository
  - via commercial sites with which Elsevier has an agreement

In all cases accepted manuscripts should:

- link to the formal publication via its DOI
- bear a CC-BY-NC-ND license - this is easy to do
- if aggregated with other manuscripts, for example in a repository or other site, be shared in alignment with our hosting policy not be added to or enhanced in any way to appear more like, or to substitute for, the published journal article.

Published journal article (JPA): A published journal article (PJA) is the definitive final record of published research that appears or will appear in the journal and embodies all value-adding publishing activities including peer review co-ordination, copy-editing, formatting, (if relevant) pagination and online enrichment.
Policies for sharing publishing journal articles differ for subscription and gold open access articles:
Subscription Articles: If you are an author, please share a link to your article rather than the full-text. Millions of researchers have access to the formal publications on ScienceDirect, and so links will help your users to find, access, cite, and use the best available version.
Theses and dissertations which contain embedded PJAs as part of the formal submission can be posted publicly by the awarding institution with DOI links back to the formal publications on ScienceDirect.
If you are affiliated with a library that subscribes to ScienceDirect you have additional private sharing rights for others' research accessed under that agreement. This includes use for classroom teaching and internal training at the institution (including use in course packs and courseware programs), and inclusion of the article for grant funding purposes.
Gold Open Access Articles: May be shared according to the author-selected end-user license and should contain a CrossMark logo, the end user license, and a DOI link to the formal publication on ScienceDirect.
Please refer to Elsevier's posting policy for further information.
18. For book authors the following clauses are applicable in addition to

the above: Authors are permitted to place a brief summary of their work online only. You are not allowed to download and post the published electronic version of your chapter, nor may you scan the printed edition to create an electronic version. Posting to a repository: Authors are permitted to post a summary of their chapter only in their institution's repository.

19. Thesis/Dissertation: If your license is for use in a thesis/dissertation your thesis may be submitted to your institution in either print or electronic form. Should your thesis be published commercially, please reapply for permission. These requirements include permission for the Library and Archives of Canada to supply single copies, on demand, of the complete thesis and include permission for Proquest/UMI to supply single copies, on demand, of the complete thesis. Should your thesis be published commercially, please reapply for permission. Theses and dissertations which contain embedded PJAs as part of the formal submission can be posted publicly by the awarding institution with DOI links back to the formal publications on ScienceDirect.

Elsevier Open Access Terms and Conditions

You can publish open access with Elsevier in hundreds of open access journals or in nearly 2000 established subscription journals that support open access publishing. Permitted third party re-use of these open access articles is defined by the author's choice of Creative Commons user license. See our open access license policy for more information.

Terms & Conditions applicable to all Open Access articles published with Elsevier:

Any reuse of the article must not represent the author as endorsing the adaptation of the article nor should the article be modified in such a way as to damage the author's honour or reputation. If any changes have been made, such changes must be clearly indicated.

The author(s) must be appropriately credited and we ask that you include the end user license and a DOI link to the formal publication on ScienceDirect.

If any part of the material to be used (for example, figures) has appeared in our publication with credit or acknowledgement to another source it is the responsibility of the user to ensure their reuse complies with the terms and conditions determined by the rights holder.

Additional Terms & Conditions applicable to each Creative Commons user license:

CC BY: The CC-BY license allows users to copy, to create extracts, abstracts and new works from the Article, to alter and revise the Article and to make commercial use of the Article (including reuse and/or resale of the Article by commercial entities), provided the user gives appropriate credit (with a link to the formal publication through the relevant DOI), provides a link to the license, indicates if changes were made and the licensor is not represented as endorsing the use made of the work. The full details of the license are available at http://creativecommons.org/licenses/by/4.0.

CC BY NC SA: The CC BY-NC-SA license allows users to copy, to create extracts, abstracts and new works from the Article, to alter and revise

the Article, provided this is not done for commercial purposes, and that the user gives appropriate credit (with a link to the formal publication through the relevant DOI), provides a link to the license, indicates if changes were made and the licensor is not represented as endorsing the use made of the work. Further, any new works must be made available on the same conditions. The full details of the license are available at http://creativecommons.org/licenses/by-nc-sa/4.0.
CC BY NC ND: The CC BY-NC-ND license allows users to copy and distribute the Article, provided this is not done for commercial purposes and further does not permit distribution of the Article if it is changed or edited in any way, and provided the user gives appropriate credit (with a link to the formal publication through the relevant DOI), provides a link to the license, and that the licensor is not represented as endorsing the use made of the work. The full details of the license are available at http://creativecommons.org/licenses/by-nc-nd/4.0. Any commercial reuse of Open Access articles published with a CC BY NC SA or CC BY NC ND license requires permission from Elsevier and will be subject to a fee.
Commercial reuse includes:

- Associating advertising with the full text of the Article
- Charging fees for document delivery or access
- Article aggregation
- Systematic distribution via e-mail lists or share buttons

Posting or linking by commercial companies for use by customers of those companies.

20. Other Conditions:

v1.8

Questions? customercare@copyright.com or +1-855-239-3415 (toll free in the US) or +1-978-646-2777.

Thermoelectric and electrical transport properties of Mg_2Si multi-doped with Sb, Al and Zn

J. Zhao, Z. Liu, J. Reid, K. Takarabe, T. Iida, B. Wang, U. Yoshiya and J. S. Tse, J. Mater. Chem. A, 2015, 3, 19774
DOI: 10.1039/C5TA03751D

Chemistry (RSC) on behalf of the Centre National de la Recherche Scientifique (CNRS) and the RSC

- For reproduction of material from PCCP:
  [Original citation] - Reproduced by permission of the PCCP Owner Societies
- For reproduction of material from PPS:
  [Original citation] - Reproduced by permission of The Royal Society of Chemistry (RSC) on behalf of the European Society for Photobiology, the European Photochemistry Association, and RSC
- For reproduction of material from all other RSC journals:
  [Original citation] - Reproduced by permission of The Royal Society of Chemistry

If you are the author of this article you still need to obtain permission to reproduce the whole article in a third party publication with the exception of reproduction of the whole article in a thesis or dissertation.

Information about reproducing material from RSC articles with different licences is available on our Permission Requests page.

AIP PUBLISHING LLC LICENSE TERMS AND CONDITIONS

Jan 05, 2016

All payments must be made in full to CCC. For payment instructions, please see information listed at the bottom of this form.

License Number	3782711246326
Order Date	Jan 05, 2016
Publisher	AIP Publishing LLC
Publication	Journal of Applied Physics
Article Title	Pressure-induced phase transition and electrical properties of thermoelectric Al-doped Mg2Si
Author	Jianbao Zhao,Zhenxian Liu,Robert A. Gordon, et al.
Online Publication Date	Oct 14, 2015
Volume number	118
Issue number	14
Type of Use	Thesis/Dissertation
Requestor type	Author (original article)
Format	Electronic
Portion	Excerpt (> 800 words)
Will you be translating?	No
Title of your thesis / dissertation	STUDY OF Mg2Si-BASED THERMOELECTRIC MATERIALS
Expected completion date	Apr 2016
Estimated size (number of pages)	202
Total	0.00 CAD

Terms and Conditions

AIP Publishing LLC -- Terms and Conditions: Permissions Uses

AIP Publishing LLC ("AIPP"") hereby grants to you the non-exclusive right and license to use and/or distribute the Material according to the use specified in your order, on a one-time basis, for the specified term, with a maximum distribution equal to the number that you have ordered. Any links or other content accompanying the Material are not the subject of this license.

1. You agree to include the following copyright and permission notice with the reproduction of the Material:"Reprinted with permission from [FULL CITATION]. Copyright [PUBLICATION YEAR], AIP Publishing LLC." For an article, the copyright and permission notice must be printed on the first page of the article or book chapter. For photographs, covers, or tables, the copyright and permission notice may appear with the Material, in a footnote, or in the reference list.
2. If you have licensed reuse of a figure, photograph, cover, or table, it is your responsibility to ensure that the material is original to AIPP and does not contain the copyright of another entity, and that the copyright notice of the figure, photograph, cover, or table does not indicate that it was reprinted by AIPP, with permission, from another source. Under no circumstances does AIPP, purport or intend to grant permission to reuse material to which it does not hold copyright.
3. You may not alter or modify the Material in any manner. You may translate the Material into another language only if you have licensed translation rights. You may not use the Material

for promotional purposes. AIPP reserves all rights not specifically granted herein.

4. The foregoing license shall not take effect unless and until AIPP or its agent, Copyright Clearance Center, receives the Payment in accordance with Copyright Clearance Center Billing and Payment Terms and Conditions, which are incorporated herein by reference.
5. AIPP or the Copyright Clearance Center may, within two business days of granting this license, revoke the license for any reason whatsoever, with a full refund payable to you. Should you violate the terms of this license at any time, AIPP, AIP Publishing LLC, or Copyright Clearance Center may revoke the license with no refund to you. Notice of such revocation will be made using the contact information provided by you. Failure to receive such notice will not nullify the revocation.
6. AIPP makes no representations or warranties with respect to the Material. You agree to indemnify and hold harmless AIPP, AIP Publishing LLC, and their officers, directors, employees or agents from and against any and all claims arising out of your use of the Material other than as specifically authorized herein.
7. The permission granted herein is personal to you and is not transferable or assignable without the prior written permission of AIPP. This license may not be amended except in a writing signed by the party to be charged.
8. If purchase orders, acknowledgments or check endorsements are issued on any forms containing terms and conditions which are inconsistent with these provisions, such inconsistent terms and conditions shall be of no force and effect. This document, including the CCC Billing and Payment Terms and Conditions, shall be the entire agreement between the parties relating to the subject matter hereof.

This Agreement shall be governed by and construed in accordance with the laws of the State of New York. Both parties hereby submit to the jurisdiction of the courts of New York County for purposes of resolving any disputes that may arise hereunder.

Questions? customercare@copyright.com or +1-855-239-3415 (toll free in the US) or +1-978-646-2777.

Enhanced figure of merit in $Mg_2Si_{0.877}Ge_{0.1}Bi_{0.023}$/multi wall carbon nanotube nanocomposites

N. Farahi, S. Prabhudev, M. Bugnet, G. A. Botton, J. Zhao, J. S. Tse, J. R. Salvador and H. Kleinke, RSC Adv., 2015, 5, 65328
DOI: 10.1039/C5RA12225B

Chemistry (RSC) on behalf of the Centre National de la Recherche Scientifique (CNRS) and the RSC
- For reproduction of material from PCCP:
  [Original citation] - Reproduced by permission of the PCCP Owner Societies
- For reproduction of material from PPS:
  [Original citation] - Reproduced by permission of The Royal Society of Chemistry (RSC) on behalf of the European Society for Photobiology, the European Photochemistry Association, and RSC
- For reproduction of material from all other RSC journals:
  [Original citation] - Reproduced by permission of The Royal Society of Chemistry

If you are the author of this article you still need to obtain permission to reproduce the whole article in a third party publication with the exception of reproduction of the whole article in a thesis or dissertation.

Information about reproducing material from RSC articles with different licences is available on our Permission Requests page.